Test of the Equivalence Principle in an Einstein Elevator

Final Report

NASA Grant NAG8-1780

For the period 30 April 2001 through 1 May 2003

Principal Investigator
Irwin I. Shapiro

April 2004

Prepared for
National Aeronautics and Space Administration
Office of Biological and Physical Research
Washington, DC

Smithsonian Institution
Astrophysical Observatory
Cambridge, Massachusetts 02138

The Smithsonian Astrophysical Observatory
is a member of the
Harvard-Smithsonian Center for Astrophysics

Test of the Equivalence Principle in an Einstein Elevator

Final Report

NASA Grant NAG8-1780

For the period 30 April 2001 through 1 May 2003

Principal Investigator
Irwin I. Shapiro

Co-Investigators
S. Glashow
E.C. Lorenzini
M.L. Cosmo
P. Cheimets
N. Finkelstein (E/PO)
M. Schneps (E/PO)

Non-US Partners (IFSI/CNR)
V. Iafolla (non-US PI)
S. Nozzoli
M. Fiorenza

Ph.D. Students
A. Turner
C. Bombardelli
G. Parzianello

Collaborators
J. Ashenberg

SAO Engineering
M. Freeman
M. Burke
R. Eng

April 2004

Prepared for
National Aeronautics and Space Administration
Office of Biological and Physical Research
Washington, DC

Smithsonian Institution
Astrophysical Observatory
Cambridge, Massachusetts 02138

The Smithsonian Astrophysical Observatory
is a member of the
Harvard-Smithsonian Center for Astrophysics

TABLE OF CONTENTS

LIST OF FIGURES

LIST OF TABLES

INTRODUCTION

The scientific goal of the experiment is to test the equality of gravitational and inertial mass (i.e., to test the Principle of Equivalence) by measuring the independence of the rate of fall of bodies from the composition of the falling body. The measurement is accomplished by measuring the relative displacement (or equivalently acceleration) of two falling bodies of different materials which are the proof masses of a differential accelerometer. The goal of the experiment is to measure the Eötvös ratio $\delta g/g$ (differential acceleration/common acceleration) with an accuracy goal of several parts in 10^{15}. The estimated accuracy is about two orders of magnitude better than the present state of the art.

The main goal of the study to be carried out under this grant is part of the flight definition of the experiment and laboratory testing of key components. The project involves an international cooperation in which the responsibility of the US side is the flight definition of the experimental facility while the responsibility of the non-US partners is the flight definition and laboratory prototyping of the differential acceleration detector.

In summary, the experiment to be designed is for taking differential acceleration measurements with a high-sensitivity detector (the sensor) during free fall conditions lasting up to 30 s in a disturbance-free acceleration environment. The experiment strategy consists in letting the sensor free fall inside a few meters long (in the vertical direction) evacuated capsule that is falling simultaneously in the rarefied atmosphere after release from a helium balloon flying at a stratospheric altitude.

DESCRIPTION OF EXPERIMENT CONCEPT

Need for Picogravity Environment

The accuracy of the Weak Equivalence Principle (WEP) tests with laboratory proof masses on the ground is limited by the Earth's seismic noise and the weakness of suitable signal sources. Previous experiments include the famous torsion balance experiments of Eötvös (1890-1922)[i] [ii] as well as the classical tests of the Equivalence Principle by Roll-Krotkov-Dicke (1964)[iii] utilizing a torsion balance which had an accuracy of 3 parts in 10^{11} and the I.I. Shapiro et al. (1976)[iv] and Williams et al. (1976)[v] lunar laser ranging experiment with an accuracy of 3 parts in 10^{12}. The present state of the art is at a few parts in 10^{13} both for lunar laser ranging tests (Williams et al., 1996)[vi] and for torsion balance tests (Adelberger et al., 1999)[vii].

By conducting the experiment in free fall, the signal strength increases by about three orders of magnitude because the full strength of the Earth's gravity is sensed in free fall. Seismic noise is also absent in free fall. Seismic noise is replaced in orbit by the noise sources of the space environment which require drag free stages or drag compensation in order to achieve the promised improvements in the test accuracy. An orbital free fall, with a "drag-free" satellite, is one approach that has been under development for many years. A small number of orbital tests of the WEP has been proposed with estimated accuracies of 10^{-15} [viii], 10^{-17} [ix], and 10^{-18} [x]. An alternative to the free fall in space is the vertical free fall inside a drag-shielding capsule released from a balloon at a stratospheric altitude as proposed in this experiment[xi].

An orbital free-fall has advantages and disadvantages with respect to vertical free fall. On the one hand, orbital free-fall tests can achieve an even higher accuracy than vertical free-fall tests thanks to the longer integration time and lower resonance frequency of the detector. On the other hand, vertical free fall tests have some key advantages over orbital tests. First of all, in a vertical free fall (from a balloon) the experiment can be repeated at relatively short intervals of time (a few weeks) and at a more affordable cost. The ability to repeat the experiment is important for the success because these high-accuracy differential detectors can not be tested on the ground at the accuracy that they can achieve in free fall conditions. Therefore, modifications and improvements have to be expected before the detector/experiment performs at the estimated free-fall accuracy.

Both orbital and vertical free fall are Galilean experiments in which the differential displacement or rate of fall or acceleration is measured between two bodies of different materials falling in a gravitational field. However, classic Galilean experiments, in which the relative displacement of two bodies falling side by side is measured (with drops ranging from 1m to 140m) have yielded an accuracy[xii] in testing the WEP of order 10^{-10}. The limitation mostly stems from relative errors in initial conditions at release which propagate over time due to gravity gradients. This problem can be overcome in orbital and long vertical free falls (i.e., from stratospheric heights) thanks to two provisions: (1) the initial relative motion of the two sensing masses inside the detector is abated during a damping phase preceding the measurement phase and (2) the detector is rotated with respect to the gravity field in order to modulate the signal (at a frequency f_S) and move the frequency of key gravity gradient components to $2f_S$.

The test of the Equivalence Principle requires a differential measurement of acceleration. This fact has a positive consequence in terms of the rejection of accelerations that affect the two proof masses equally (common-mode type) and their effects on the differential acceleration. Typical values of the common-mode rejection factor of differential accelerometers are of order 10^{-4}. Consequently, for an experiment that aims at measuring differential acceleration of order 10^{-15} g, the common-mode acceleration perturbations external to the detector must be of order 10^{-12} g or less.

Drop Facility

The following is a preliminary description of the drop facility the design of which will evolve as a result of the analyses carried out during the flight definition phase. The free fall facility (see Fig. 1) consists of: (1) the *gondola* that stays attached to the balloon; (2) a leveling mechanism that keeps the capsule vertical before release; (3) the *capsule*, which houses a large vacuum chamber/cryostat; (4) the *instrument package* which free falls inside the cryostat and contains a small, high-vacuum chamber which in turn houses the detector; and (5) the *parachute system* to decelerate the capsule at the end of the free fall run.

The capsule is kept vertically leveled and stabilized in azimuth by the gondola before release. Upon reaching an altitude higher than 40 km, the capsule is released from the gondola and immediately afterwards ($\leq$ 1 s) the instrument package is released from the top of the capsule. The analysis indicates (see later on) that with a 1-3 m long vertical space available inside the capsule, the instrument package will span that space in 25-30 s while the capsule, that is slightly decelerated by the rarefied atmosphere, falls by a few km over the same time. The capsule shields the instrument package from external perturbations and allows it to free fall under acceleration conditions which are close to ideal. The differential acceleration between the two falling test masses is measured during the free fall time. At the end of the free-fall run the capsule is decelerated by a parachute system for recovery in water or, alternatively, over land.

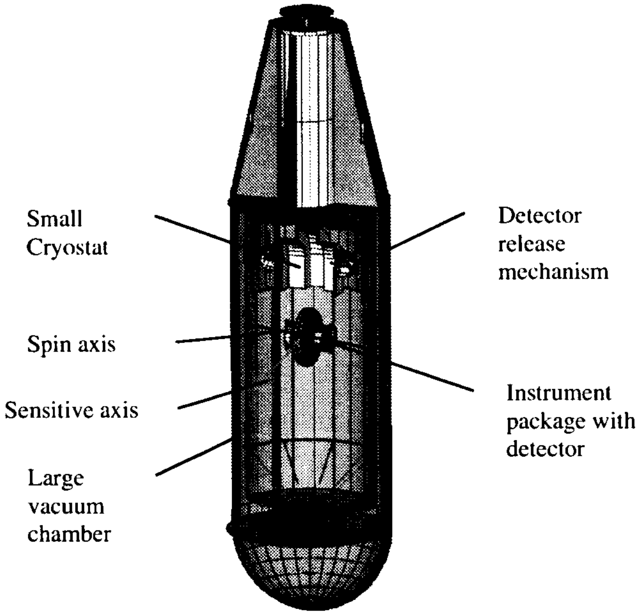

Figure 1 Pre-definition-study configuration of capsule in free fall after detector release

Detector Concept

The following is a preliminary description of a differential acceleration detector concept, the design of which (carried out in cooperation with our non-US partners) will evolve as a result of the analyses conducted during the flight definition phase.

The detector that we plan to use for the experiment is a differential accelerometer that will be developed at the Institute of Space Physics (IFSI) in Rome (Italy), under the sponsorship of the Italian Space Agency in the framework of the participation in this project of non-US investigators (with V. Iafolla, PI). This detector technology[xiii] has been pioneered by V. Iafolla and the late F. Fuligni and applied to the construction of a number of high-sensitivity, low-frequency accelerometers over several years. In the following we give a brief description of the detector conceptual design at this stage of the project.

The differential-acceleration detector (see Fig. 2) measures the relative displacement, along the sensitive axis, between two sensing masses of different materials. The centers of mass of the sensing masses are made to coincide within the attainable values in order to minimize the effect of gravity gradients, rotational motions and linear accelerations upon the differential output signal.

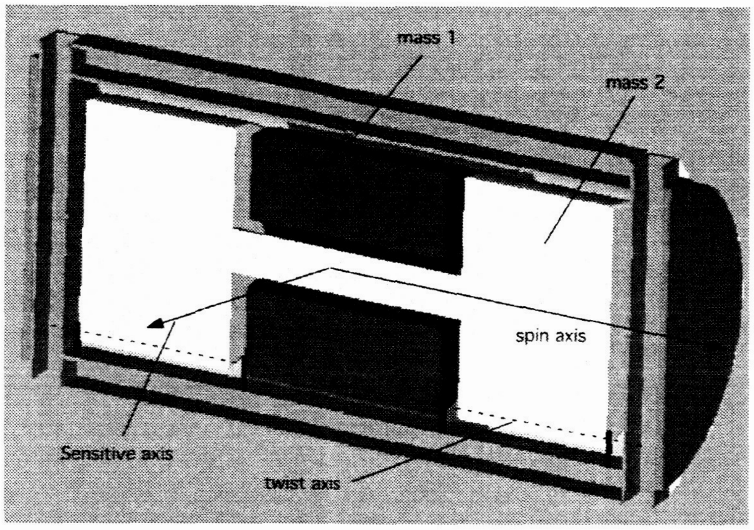

Figure 2 Longitudinal section of conceptual instrument and sensing masses.

The two sensing masses are constrained by torsion springs to rotate independently about the twist axis (which is parallel to the spin axis of the instrument) and their resonant frequencies are electrostatically controlled for frequency matching. The displacements generated by the rotations are sensed by the capacitive pick-ups of the instrument as explained later on. Sensing mass 1 (in dark color) is a hollow cylinder mostly made of a given material while sensing mass 2 (in light color) is a dumbbell-shaped cylinder made of a different material. Each sensing mass constitutes the moving part of a capacitor with symmetric fixed plates on either side of the sensing mass (see Fig. 3). Capacitor 1 is formed by sensing mass 1 and the fixed plates marked A and B while capacitor 2 is formed by sensing mass 2 and the fixed plates marked C and D. The fixed plates A and C are used for signal pick-up and the fixed plates B and D for feed-back control. The displacement of sensing mass 1, for example, is detected by the series capacitances As (one fixed plate on each side of the sensing mass). These plates form one branch of a capacitive bridge in which two additional reference capacitors form the other branch. The bridge is pumped by a quartz oscillator at a stable frequency of 10-20 kHz, reducing the relevant noise temperature of the preamplifier. The difference between the output signals from capacitors 1 and 2 is amplified by a low-noise preamplifier, sent to a lock-in amplifier for phase-detection, and then to a low-pass filter.

The cross sections of the ellipsoids of inertia about the spin axis of the instrument are circular so as to minimize, within the construction tolerance, the mass-moment torques[xiv]. In the detector shown in Figs. 2 and 3, the inner cylindrical mass is made mostly of a high-density material (e.g., Platinum-Iridium) while the outer dumbbell-mass is made of a low-density material (e.g., Aluminum).

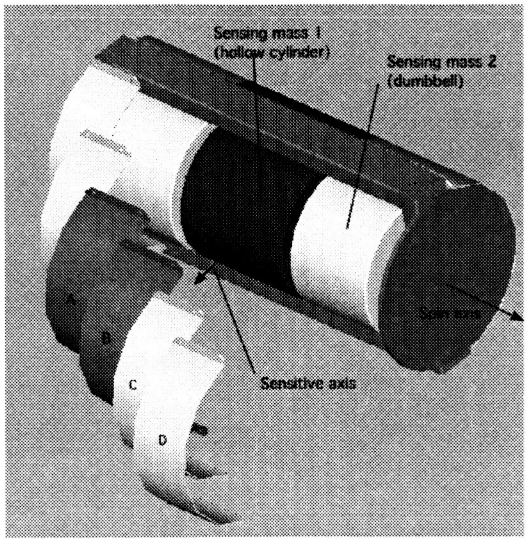

Figure 3 Interior of conceptual differential acceleration detector.

In order to achieve an experimental accuracy of several parts in 10^{15} in 25-30 s integration time, the detector must have an intrinsic noise (expressed in terms of acceleration) of about 10^{-14} g/Hz$^{1/2}$. Earlier analyses indicate that this level of noise is attainable with an instrument refrigerated to a temperature close to that of liquid Helium and with state-of-the-art low-noise preamplifiers.

Experiment Sequence and Communication Links

Figure 4 shows the preliminary timetable of the experiment sequence. The experiment starts with the loading of the sensor into the vacuum chamber/cryostat about 2 weeks before the planned launch. This operation is then followed by the pumping down of the chamber and the refrigeration of the sensor. After connecting the capsule to the gondola and the balloon, the balloon is launched. The estimated time to reach altitude is of order 3 hours. Upon reaching altitude, the attitude of the capsule is stabilized by the leveling mechanism attached to the gondola, the sensor is spun up, and the dynamics of the system is analyzed. When the dynamics is within the acceptable bounds, the capsule is released from the gondola and the sensor is released from the top of the chamber/cryostat immediately afterwards. The science data is taken during the free-fall phase in which the sensor spans the length of the chamber. Shortly after the sensor has reached the bottom of the capsule, the blut (first stage of the deceleration system) is released and, when the speed has decreased below the required value, the parachute is deployed. The chamber is vented before the capsule hits the surface/water and the locator beacon is turned on.

Event	Prelaunch					
	T-2wks				T-1Day	Launch
Mount Sensor in Chamber	■					
Close Chamber	■					
Pump Down Chamber	■					
Chill Sensor	■	■	■	■	■	
Connect to Balloon					■	
Launch						■
	To Float					
	T+30m	T+60m	T+90m	T+120m	T+150m	T+180m
Rise to Altitude	■	■	■	■	■	
Study Dynamic conditions						■
Spin up Sensor						■
Check out full comm path						■
	Release		Measurement			
	R+1s	R+2s	R+10s	R+20s	R+25s	R+30s
Release Capsule	■					
Release Sensor		■				
Take Data		■	■	■	■	■
Sensor at Bottom of Capsule						■
	Post Measurement Fall					
	R+40s	R+70s	R+100s	R+130s	R+150s	R+TBD
Release Blut	■					
Fall under Blut Drag	■	■	■			
Release Main Chute			■			
Fall under Chute Drag			■	■	■	
Vent Capsule				■	■	
Deploy Landing Isolators					■	
Turn on Locator Beacons					■	
Touchdown						■
Valve down balloon						■

Figure 4 Preliminary timeline of experiment

Figure 5 is a schematic of the communication system between the ground, the gondola and the capsule through radio links and the communication between the sensor (during free fall) and the capsule through an infra-red link.

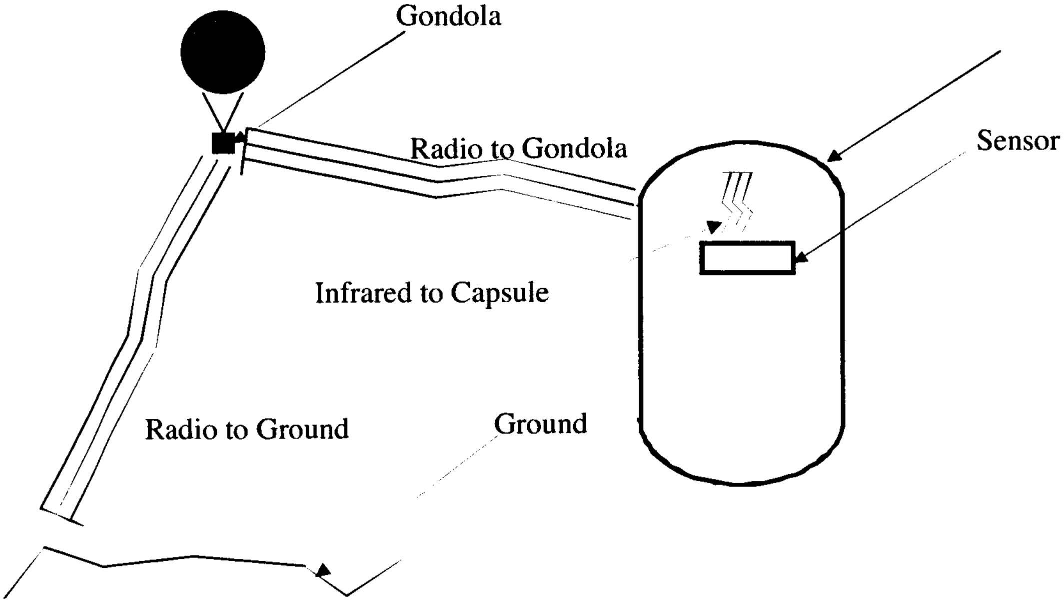

Figure 5 Schematic of communication links.

ANALYSIS OF FREE FALL PHASE

The free fall time of the instrument package inside the capsule can be computed after considering that the capsule is slowly decelerated by the air drag while the instrument package (after release) moves inside the vacuum chamber at low relative speed and consequently it is unaffected by air drag (it is indeed in free-fall conditions).

Free fall time

The free fall time and vertical size of the vacuum chamber/cryostat can be computed from the equations of motion of the instrument package in free fall and the capsule in decelerated fall. The equations of motion are as follows:

$$\ddot{z}_1 = g$$
$$\ddot{z}_2 = g - \frac{1}{2m_2} C_D S \rho \dot{z}_2^2 \qquad (1)$$

where z is the vertical distance from the time of release (the subscript 1 stands for instrument package and 2 for capsule), S is the frontal cross section of the capsule, C_D the air drag coefficient of the capsule and $\rho = f(h)$ is the air density with h the altitude above the Earth's surface. Equations (1) can be solved analytically only if C_D is assumed constant and the atmospheric density exponential. We will not spend time on the analytic solution because it is valid only for relatively-short drops.

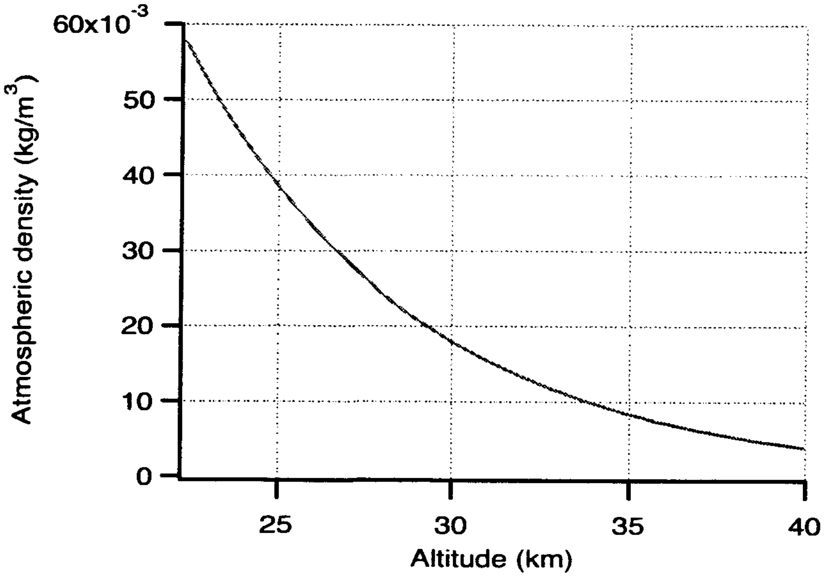

Figure 6 Atmospheric density in the stratosphere per US Standard Atmosphere 1976

After adopting a density profile from the US Standard 1976 Atmospheric Model (as shown in Fig. 6) the exponential fit of the density for the altitudes of interest is:

$$\rho = \rho_0 e^{-h/H} \tag{2}$$

Where H is the scale height, ρ_0 is the reference density which is taken at the Earth's surface and h the altitude above the Earth's surface. The relative distance can be obtained as the double integral of the acceleration difference between the capsule and the instrument package $\delta\ddot{x} = \ddot{x}_2 - \ddot{x}_1$ which is equal to the deceleration of the capsule due to aerodynamic drag:

$$\delta\ddot{x} = \frac{1}{2}\frac{\rho_0}{\beta} e^{(z-h_D)/H} g^2 t^2 \tag{3}$$

where $\beta = m/(C_D S)$ is the frontal ballistic coefficient of the capsule, h_D is the drop altitude, $z \approx (1/2)gt^2$ the distance traveled by the capsule and g the Earth's gravitational acceleration. The drop velocity of the capsule is assumed equal to the free fall velocity *gt only* for the purpose of computing the air drag deceleration (which is a valid approximation at high altitudes).

The air drag coefficient C_D is fairly constant in the non-compressible regime but then it grows substantially with the Mach number for speeds approaching the transonic regime as shown in Fig. 7 for an aerodynamically-shaped cylinder with fineness ratio $D/L = \delta \approx 0.25$. The Mach number M is the ratio between the actual speed of the capsule and the speed of sound at the local altitude:

$$M = \frac{V}{\sqrt{\gamma R T}} \tag{4}$$

where $R = 287$ J/(kg-K) is the gas constant of air, T the local air temperature and $\gamma \approx 1.4$. The Mach number vs. the drop time is shown in Fig. 8 together with the drop distance vs. time.

As a result of the functional dependence $C_D = f(\text{Mach})$, we can separate the ballistic coefficient into two components as follows:

$$\beta = \beta_0(1 + \Delta\beta') \tag{5}$$

where $\beta_0 = m/(C_{D0}A)$ is the low-speed ballistic coefficient (i.e., its minimum value) and $\Delta\beta'$ is the fractional variation of the ballistic coefficient due to the increase of the Mach number.

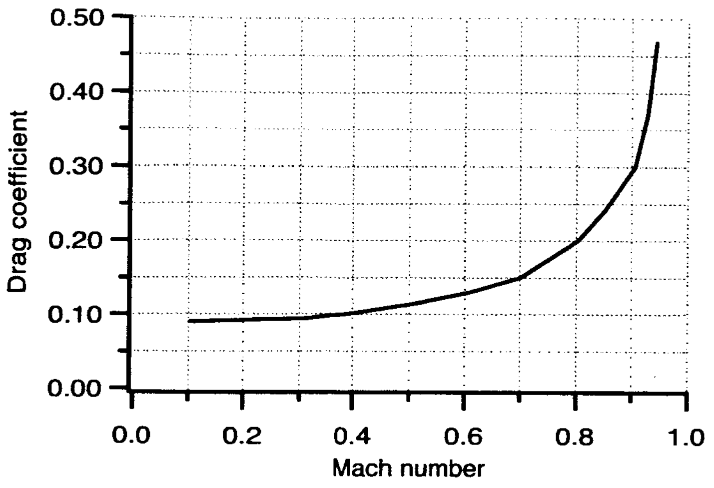

Figure 7 C_D vs. Mach number for an aerodynamically-shaped cylinder with $\delta = 0.25$ (see text)

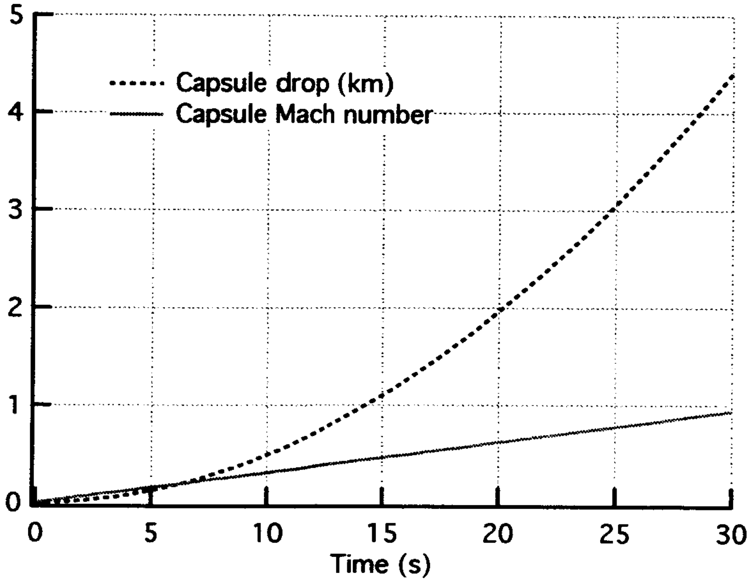

Figure 8 Mach number and capsule drop distance vs. time

After taking into account the functional dependence C_D = f(Mach) and integrating eqn. (3) twice for different values of the ballistic coefficient, we obtain the numerical results shown in Fig. 9, for a fineness ratio $\delta \approx 0.25$, a drop altitude of 40 km and a (low-speed) ballistic coefficient β_0 ranging from 2000 kg/m^2 to 10000 kg/m^2.

The numerical results clearly indicate that it is possible to attain a free fall time between 25 s and 30 s with very reasonable lengths of the chamber and capsule. Appropriate values of the (low-speed) ballistic coefficient in the range of greater interest of 6000-10000 kg/m^2 can be readily obtained with capsule masses ≤1500 kg and external diameters smaller than 1.8 m. Designs options will be investigated later on in this report.

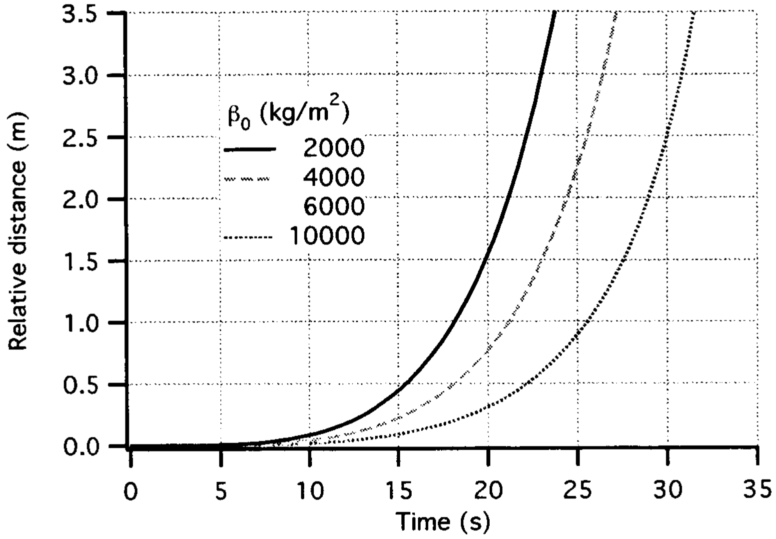

Figure 9 Relative distance for various initial ballistic coefficients

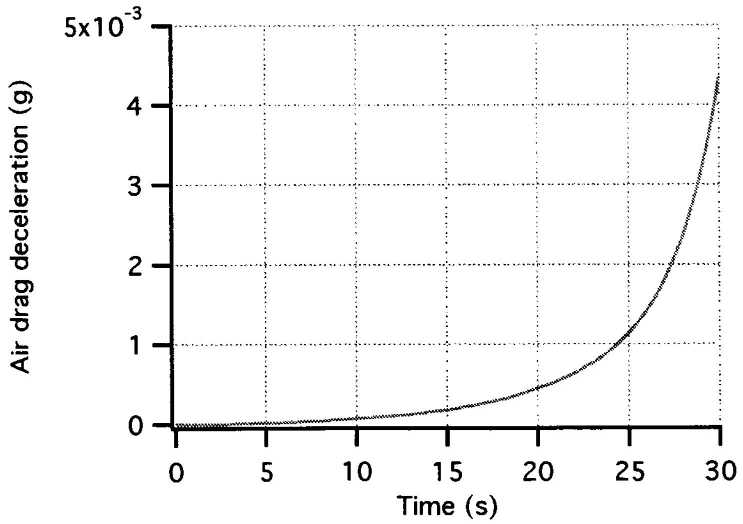

Figure 10 Capsule deceleration due to air drag (β_0 = 6000 kg/m^2)

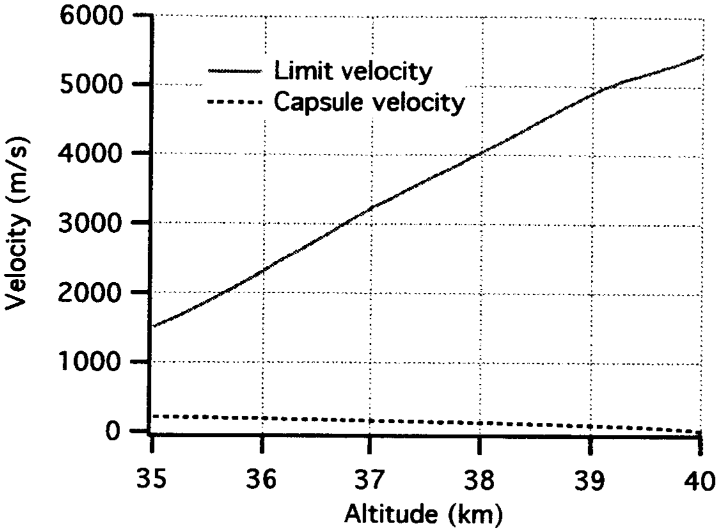

Figure 11 Limit velocity and actual velocity of capsule vs. altitude ($\beta_0 = 6000$ kg/m^2)

For completeness the deceleration of the capsule caused by air drag is shown in Fig. 10 for $\beta_0 = 6000$ kg/m^2. Figure 11 depicts the limit velocity and the capsule actual velocity vs. altitude for the same case. The limit velocity is the velocity at which the gravitational and air drag force are equal and, consequently, for a limit velocity much greater than the actual velocity the air-drag deceleration is very small.

Effect of Wind Shear

The horizontal velocities of the capsule and the instrument package (attached to the capsule) are the same at the start of the fall. The inertial horizontal velocity is determined by the rotational velocity of the Earth at the latitude of capsule release and by the local wind. The former (which is much bigger than the latter) simply makes the falling bodies follow a parabolic trajectory rather than a fall along the local vertical. The maximum lateral displacement is of order a couple of hundred meters over a fall distance of 4.4 km which is consistent with a 30-s fall time. It is also worth pointing out that this lateral displacement does not generate any acceleration on board because the displacement is due to an initial non-null velocity and not to external acceleration acting on the falling body.

The diameter of the capsule is important for tolerating vertical gradients (wind shear) of the lateral wind without the need for a propulsion system to compensate for their effect. The balloon will move at the speed of the local wind once the floating altitude has been reached, i.e., the capsule will be at zero relative speed with respect to the local wind. If the wind vertical profile were constant, the capsule and the instrument package would move laterally during the fall with the same initial lateral velocity and hence maintain the same lateral distance with respect to one another. But, if the wind vertical profile changes, the capsule will experience a lateral force that will change its lateral speed while the instrument package will not experience such force.

The lateral displacement *y* of the capsule due to the wind shear $V_Z = \partial V/\partial z$ over the vertical drop distance ($Z = 1/2gt^2$) is as follows:

$$y = \frac{1}{30}\frac{\bar{\rho} Z^3}{\beta_l \; g} V_z^2 \tag{8}$$

where ρ is the atmospheric density, $\beta_l = m/(C_{Dl}S_l)$ is the lateral ballistic coefficient of the capsule, S_l the lateral area of the capsule, and g the Earth's surface gravity. Equation (8) is simplified because the atmospheric density has been assumed constant over the drop. The equation, however, provides a good estimate of the lateral displacement of the capsule due to wind shear after adopting the average value $\bar{\rho}$ of the density along the drop. After calling S the frontal area of the capsule and assuming that $C_{Dl} \approx 10C_D$, $S_l \approx 3S/(\pi\delta)$, which are valid in approximation for a cylinder with aerodynamically-shaped nose and tail, we can relate the lateral ballistic coefficient to the frontal (low-speed) ballistic coefficient as follows:

$$\beta_l = \frac{\pi\delta}{30}\beta_0 \tag{9}$$

Consequently, eqn. (8) yields:

$$y = \frac{1}{\pi\delta}\frac{\bar{\rho} Z^3}{\beta_0 \; g} V_z^2 \tag{10}$$

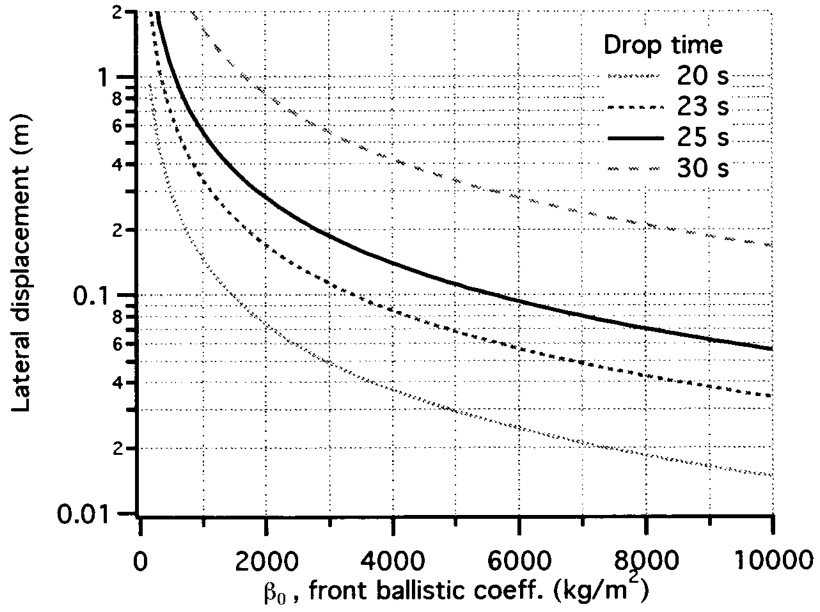

Figure 12 Lateral displacement due to wind shear vs. β_0

For $\bar{\rho} = 6 \times 10^{-3}$ kg/m^3 (i.e., average atmospheric density between 40 km and 35 km of altitude), $V_Z = 0.005$ s^{-1}, and $\delta = 0.25$, we obtain the results shown in Fig. 12. The accuracy of eqns. (8) and (10) was also checked through numerical integration of the equation of lateral motion after assuming an exponential air density profile. The displacement error is less than 5% by using the average density value. The value adopted for the wind shear of 0.005 s^{-1} is equivalent to a vertical gradient of 10 knots per km. This value is twice as high as the maximum wind shear reported[xv] for the Air Force balloon base at Holloman, New Mexico.

The lateral displacements due to wind shear are relatively small for rather conservative values of wind shear, free-fall times and ballistic coefficients greater than 6000 kg/m^2, which are easy to obtain. These results show that there is no need for a thruster system to compensate for the effect of the lateral wind acting on the capsule. The geometry and mass of the capsule can be chosen in a way to accommodate the presence of wind shear. Furthermore, if the balloon is launched during the periodically-occurring wind reversal times (in April-May and September-October) the vertical wind gradient is much smaller than the value adopted for the computations shown here.

The capsule displacement due to wind shear has to be taken into account when computing the internal diameter of the capsule (where the instrument package falls). However, it will be shown later on that other factors (e.g., gravity gradients) are more important in determining the capsule internal diameter.

The error analysis has been extended with respect to what is reported in Ref.[xvi] to include a thorough analysis of the gravity gradient generated by the distributed mass of the capsule, the concentrated masses on board the capsule, and the Earth's mass for generic positions and orientations of the sensor. The acceleration noise inside the capsule has also been revisited after considering that in the new reference design (see later on) the chamber is fully cryogenic. The intrinsic noise components of the detector (Brownian and preamplifier noise) were also recomputed based on new information from the IFSI laboratory. As a results of these new analyses, requirements have been derived for: (a) the mass distribution of the capsule; (b) the tolerable mass and location of equipment on board the capsule; (c) the orientation of the sensor during free fall and the centering of the two sensing masses; and (d) the characteristics parameters of the detector that affects its intrinsic noise level.

Acceleration Noise inside Capsule

The experimental package moves at very low speed inside the capsule. Consequently, the residual gas inside the vacuum chamber produces a minute force on the free-falling package with a frequency content centered at $f = 1/t_f\ s^{-1}$ where t_f is the free-fall time. This gas thus affects the acceleration of the instrument package in a frequency range well removed from the signal frequency. The acceleration, as a function of pressure inside the chamber, is as follows:

$$a_D = \frac{C_D A}{2m}\frac{V^2 p}{RT} \qquad (11)$$

where A and m are the frontal area and mass of the instrument package, respectively, V is the maximum velocity of the instrument package with respect to the falling capsule, R is the gas constant, T the temperature of the residual gas, and p the pressure inside the chamber. Because of the new reference design (see later on) with a fully cryogenic vacuum chamber, the residual gas in the chamber is refrigerated Helium. After assuming $C_D = 2.2$ (for a free-molecular regime), $A = 0.1\ m^2$, $m = 30$ kg, $V = 0.5$ m/s (obtained by integrating eqn. 3 once up to 30 s), $R = 2078$ J/(kg-K), $T \approx 5$ K, and $p = 10^{-6}$ mBar, eqn. (11) yields $a_D = 10^{-12}$ g. The spectrum of this acceleration is centered at a frequency 0.033-0.05 Hz for free-fall times t_f in the range 20-30 s. Consequently, the magnitude of the acceleration at the signal frequency f_s, which is in the range 0.2-0.5 Hz, is well smaller than 10^{-12} g. This acceleration is a common-mode acceleration which is further reduced by the common-mode rejection factor (CMRF) of order 10^{-4}.

Furthermore, the vacuum strongly attenuates the propagation of perturbations from the walls of the capsule to the free-falling instrument package. The estimate of the acceleration at the falling instrument package produced by the vibrating walls of the capsule are based on the experimental data measured on board the system Mikroba[xvii]. This system shares the fall from a stratospheric altitude; it is not, however, a free-falling experimental package inside the shielding capsule. In Mikroba, the measurement package or experiment is solidly attached to the walls of the falling capsule. Moreover, Mikroba is not propelled during the first 30 s (like our experiment) although it is propelled downwards during the next 30 s. Once the magnitude of the acceleration at the walls $|a_{wall}|$ is known, the magnitude of the acceleration at the falling package $|a|$ can be readily computed as explained in the following. The motion of the vibrating walls increase the kinetic energy of the gas molecules above the thermal velocity. The kinetic energy variation is then expressed as a pressure variation Δp of the gas after equating the increase in kinetic energy to the work done on the gas molecules by the vibrating walls. We then assume, conservatively, that the pressure perturbation Δp acts on one side only of the instrument package in order to compute an upper bound of the acceleration disturbance imparted to the package. The upper bound of the acceleration at the instrument package is as follows:

$$|a| = \frac{Ap}{mv}|u_{wall}| = \frac{Ap}{m\omega v}|a_{wall}| \qquad (12)$$

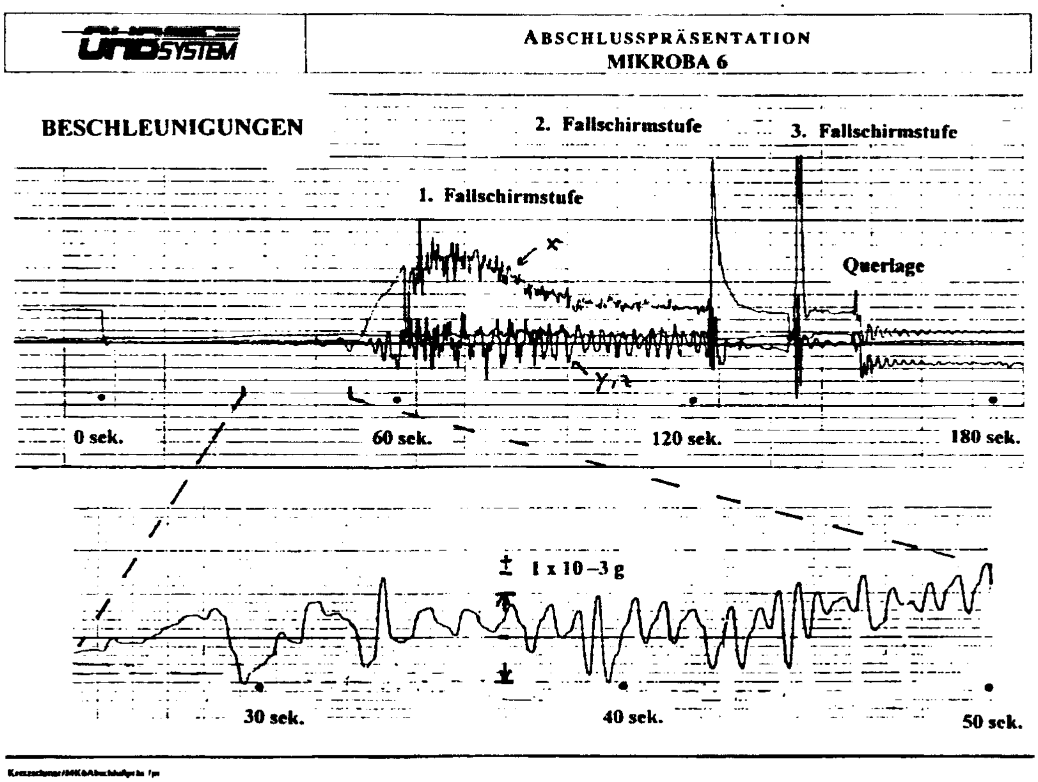

Figure 13 Acceleration measured on board the Mikroba capsule (with accelerometer solidly attached) during the fall [Kretzchmar, 1999]

In equation (12), A and m are the cross section and mass of the instrument package, v is the thermal velocity of the residual gas, a and a_{wall} are the accelerations of the package and the wall, respectively, p is the pressure inside the capsule, $u_{wall} = a_{wall}/\omega$ is the velocity and ω the angular frequency of the vibrating walls. If, for example, $p = 10^{-6}$ mBar and the temperature of the gas inside the capsule is slightly higher than LHe, we obtain an attenuation factor $a/a_{wall} = 6 \times 10^{-10}$ at the signal frequency of our experiment (~0.5 Hz). In other words, the high vacuum provides an excellent attenuation of the wall vibrations. Moreover, the capsule walls do not necessarily vibrate at the signal frequency of the instrument. The cryostat will be designed with structural frequencies much higher than the experiment signal frequency. However, in this early stage of the design and for conservativeness, we assume that the wall acceleration has a component at the signal frequency with an intensity equal to the largest magnitude of the acceleration recorded on Mikroba during the first 30-s of fall, that is, $a_{wall} < 10^{-4}$ g (although not very visible in Fig. 13). We then obtain an acceleration at the instrument package of order 10^{-13} g under rather conservative assumptions. Consequently, the free-falling capsule reduces the acceleration noise to values unmatched by any other Earth-based drop facility and comparable to values achieved on board the Triad drag-free satellite[xviii].

The acceleration components above are common-mode-type (i.e., they affect equally both sensing masses) thus they can be further reduced by the common-mode rejection fact of the differential accelerometer. With a typical value of 10^{-4} for the CMRF, the influence of these accelerations on the differential measurement is made negligible.

The acceleration noise components produced by the residual gas in the capsule are proportional to the pressure inside the capsule. The pressure can be reduced in successive flights if, for any unanticipated reasons, its influence on the measurement proves to be greater than expected. It is, in fact, well within the state of the art to obtain pressures at room temperature as low as 10^{-8} mBar in large volumes.

Internal noise of detector

The most important internal noise sources for a high accuracy mechanical detector like the one proposed for this WEP test are: (1) preamplifier noise; and (2) thermal noise (Braginsky, 1974[xix]; Giffard, 1976[xx]). The combined effect of these two noise components upon the acceleration spectral density S_a of the detector's output is given by the following equation for an instrument with the measurement frequency smaller than the resonant frequency ω_0, a measurement bridge pumped at the frequency ω_P (of typically tens of kHz) and a preamplifier that matches the transducer impedance[xxi]:

$$S_a = \frac{1}{g}\left[\frac{4k_B\omega_0}{m_{eff}}\left(\frac{T}{Q} + T_n\frac{2\omega_0}{\lambda\omega_P}\right)\right]^{1/2} \quad g/\sqrt{Hz} \tag{13}$$

In equation (13), the two terms in round parentheses correspond to the Brownian noise and the preamplifier noise, respectively; ω_0 is the detector resonant frequency; k_B the Boltzmann's constant; T the ambient temperature; T_n the preamplifier noise temperature; Q the quality factor; m_{eff} the effective mass of the sensing mass; and λ the electromechanical transducer factor. The effective mass is used to convert a rotation of the sensing mass into a translation of equal energy. Its relationship to the mass *m* is: m_{eff}

$= m(\eta_t/l)^2$ where η_t and l are, respectively, the radius of inertia and the lever arm with respect to the rotation axis of the sensing mass. With the geometry of the sensing masses in our detector $m_{eff} \approx 1.8m$.

Clearly, from eqn (13), we see that the sensitivity of the detector increases by decreasing the resonant frequency and the temperature, and by increasing the mass of the sensing masses and the Q-factor. Liquid He (4.2 K) refrigeration will be used to provide low Brownian noise and a high Q-factor. These are necessary conditions to achieve the desired measurement accuracy. In order to derive requirements for the detector, we assume that the contribution of the Brownian noise is about equal to the contribution of the preamplifier noise. In this case, if we set our experiment accuracy goal to several parts in 10^{15} (with 95% confidence level and a 20-s integration time) each one of the two noise components should be about $10^{-14}\ g/\sqrt{Hz}$ or smaller. These noise requirements imply the following (see also the section on Requirements Development):

$$T < 10\ K;\ T_n < 60\ mK;\ m > 2\ kg;\ \omega_0/Q < 6\pi/\ 10^5\ rad/s \qquad (14)$$

These requirements do not exceed the state-of the-art but they do require a very careful construction of the detector with low dissipation and the use of very-low-noise preamplifier. Key quantities like the Q-factor at low temperature and the preamplifier noise will be measured experimentally by our partners at IFSI once a prototype laboratory detector is built and operated at LHe temperature. Noise contributions other than the intrinsic noise components of the detector should be kept at a lower level in order to make them smaller than the intrinsic noise.

Gravity Gradients

Capsule Gravity Gradients

The gravity gradients generated by the distributed mass of the chamber/cryostat and their effects on the differential measurement are analyzed in the following for a generic position of the detector inside the capsule and a generic orientation of its spin axis with respect to the gradient field.

Gravity gradient for a mass distribution with cylindrical symmetry

For a mass distributed with cylindrical symmetry, the resultant gravitational acceleration has two components:

a_z= acceleration component along the cylinder axis
a_r = acceleration component along the cylinder radius

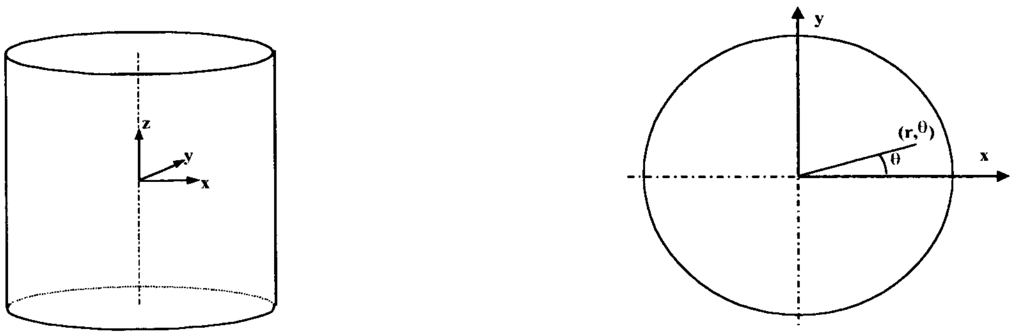

Figure 14 Reference frames for gravity gradient analysis

After erecting a Cartesian reference system xyz as depicted in Figure 14, the components of the gravity gradient tensor are computed according to the following transformation formulas:

$$\begin{aligned}
dx &= \cos(\theta)\cdot dr - r\cdot sin(\theta)\cdot d\theta \\
dy &= sin(\theta)\cdot dr + r\cdot\cos(\theta)\cdot d\theta \\
da_x &= \cos(\theta)\cdot da_r - a_r\cdot sin(\theta)\cdot d\theta \\
da_y &= sin(\theta)\cdot da_r + a_r\cdot\cos(\theta)\cdot d\theta
\end{aligned} \tag{15}$$

Setting θ = 0 and indicating the spatial derivative with a second subscript:

$$a_x = a_r$$

$$a_y = 0$$

and

$$\begin{aligned}
a_{xx} &= a_{rr} \\
a_{xy} &= 0 \\
a_{yy} &= a_r / r \\
a_{xz} &= a_{zx} = a_{rz} \\
a_{yz} &= a_{zy} = 0
\end{aligned} \tag{16}$$

Hence the gravity gradient tensor has the form:

$$\Gamma = \begin{bmatrix} a_{rr} & 0 & a_{rz} \\ 0 & a_r / r & 0 \\ a_{rz} & 0 & a_{zz} \end{bmatrix} \tag{17}$$

As a result of the Laplace equation, the trace of the gravity gradient tensor is equal to zero, that is

$$a_{rr} + a_r / r + a_{zz} = 0 \tag{18}$$

In the singular case of r = 0 the limit calculation yields:

$$\Gamma_{(r=0)} = \begin{bmatrix} a_{rr} & 0 & 0 \\ 0 & a_{rr} & 0 \\ 0 & 0 & -2a_{rr} \end{bmatrix} \tag{19}$$

Gravity gradient matrix of a rotating body

In general a gravity gradient matrix has the form:

$$\Gamma = \begin{bmatrix} \Gamma_{xx} & \Gamma_{xy} & \Gamma_{xz} \\ \Gamma_{yx} & \Gamma_{yy} & \Gamma_{yz} \\ \Gamma_{zx} & \Gamma_{yz} & \Gamma_{zz} \end{bmatrix} \tag{20}$$

The rotated matrix Γ' after a $\theta = \omega t$ rotation is:

$$\Gamma\copyright = R_\theta \Gamma R_\theta^T \tag{21}$$

where R_θ is the rotation matrix and R_θ^T its transpose.

After a rotation about an axis (i.e., the x axis), the rotated matrix has four components modulated at ω, four components modulated at 2ω and one component that is not modulated.

The ω-modulated components of the transformed matrix are:

$$\Gamma'_{12} = \Gamma'_{21} = \Gamma_{xz} \sin(\omega \cdot t) + \Gamma_{xy} \cos(\omega \cdot t) \tag{22.1}$$

$$\Gamma'_{13} = \Gamma'_{31} = \Gamma_{xz} \cos(\omega \cdot t) - \Gamma_{xy} \sin(\omega \cdot t) \tag{22.2}$$

where the rotated axes are labelled x' = 1, y' = 2, z' = 3. In summary, the *off-diagonal components* $\Gamma'_{12} = \Gamma'_{21}$ and $\Gamma'_{13} = \Gamma'_{31}$ of the gravity gradient matrix produce components that are modulated at the rotation frequency.

Gravity gradient matrix projected onto body axes

In a general case the body reference frame placed at the CM of a sensing mass of the detector can be identified with respect to the cryostat frame by means of 3 successive rotations as follows:

1 - Rotation +α around z axis (azimuth rotation)
2 - Rotation +β around y' axis (elevation rotation)
3 - Rotation +ωt around x'' axis (spin rotation)

In the computation of gravity gradients, these rotations can either be rotations of the sensing mass with respect to the cryostat or, equivalently, rotations of the cryostat with respect to the sensing mass. In the former case, and solely for the reason of pointing out a typical geometrical situation, the first and second rotations could, for example, be caused by the detector dynamics during free-fall (e.g., precession of its body axes) while the third rotation is the ωt rotation of the detector about its longitudinal axis aimed at modulating the signal.

Clearly, we are mostly concerned about the components of the gravity gradient matrix that contain a frequency ω equal to the modulation frequency of the signal. We can choose the body axis y' = 2 to coincide with the sensitive axis of the accelerometer and, consequently, we are only concerned with the component Γ'_{21} of eqn. (22.1). In general, the moduli of the two components Γ'_{12} and Γ'_{13} are the same and they can be written as follows:

$$\chi = \sqrt{\Gamma_{xy}^2 + \Gamma_{xz}^2} \qquad (23)$$

After rotating the original matrix by two rotations α and β (where α is the azimuth of the spin axis with respect to the radial and β is the elevation with respect to the capsule equatorial plane) the expressions of Γ_{xy} and Γ_{xz} in eqn. (23) are as follows

$$\Gamma_{xy} = k_1 \sin(\beta)\sin(\alpha) - k_2 \cos(\beta)\sin(2\alpha) \qquad (24.1)$$

$$\Gamma_{xz} = k_3 \sin(2\beta) + k_1 \cos(\alpha)\cos(2\beta) + k_2 \sin(2\beta)\cos^2(\alpha) \qquad (24.2)$$

$$k_1 = a_{xz} \qquad (24.3)$$

$$k_2 = \frac{1}{2}(a_{xx} - a_{yy}) \qquad (24.4)$$

$$k_3 = \frac{1}{2}(a_{yy} - a_{zz}) \qquad (24.5)$$

where the a_{ij} are the matrix components before the rotations are carried out. In the case of a body with cylindrical symmetry and for cylindrical coordinates, eqn. (16) yields $a_{xx} = a_{rr}$, $a_{yy} = a_r/r$, $a_{zz} = a_{zz}$, $a_{xz} = a_{rz}$ and the other components are null.

After carrying out a numerical analysis of eqns. (24) and taking into account that inside a cylinder k_2 is always at least one order of magnitude less than k_1 and k_3, we find that the maximum value for χ occurs for $\alpha = 0$ (where α is the azimuth). This result implies that the maximum disturbance of the capsule gravity field on the differential accelerometer is produced when the capsule moves radially with respect to the sensor (see Figure 15) in such a way that the spin axis is oriented along the radius of the cylinder through the sensor and the capsule has been displaced radially with respect to the sensor (e.g., by wind shear).

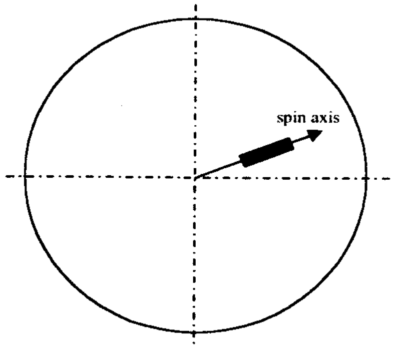

Figure 15 Geometry of sensor and capsule (viewed from the top) for strongest gravity gradient affecting the measurement

On the opposite end, if the motion of the capsule is such as to keep α close to 90°, that is the spin axis is orthogonal to the radial, the disturbance is minimum. In any case since the translational motion of the capsule is not predictable nor controlled, the worst condition is analyzed setting α equal to zero and varying the angle β. After doing so eqns. (23) and (24) yield:

$$\chi = (k_3 + k_2)\sin(2\beta) + k_1\cos(2\beta) \tag{25}$$

Equation (25) summarizes the disturbances induced by the cryostat mass modulated at the measurement frequency. This equation is important for the cryostat/capsule design. The variations of the quantities k_1, k_2, k_3 inside the cryostat for different shapes and sizes are analyzed numerically in the following subsection.

Variation of k_1, k_2, k_3 in the cryostat/capsule

A numerical code has been developed in Matlab to compute the gravity gradient matrix inside a distributed, massive cylinder. The program, which uses a very large (of order 10^4) number of mass points, can map the desired components of the gravity gradient matrix inside the enclosed surface. The code has been applied to a number of cylinders with different H/D ratios (where D is the diameter and H the height) and different shapes of caps. Each run takes a couple of hours on a Pentium III PC.

Cylindrical cryostat without caps

We first analyzed the gradient field for various cases of cylinders with various H/D (height over diameter) ratios to conclude that the gradient field is strongly reduced (for the components of interest) for H/D > 1

The following results are for a cylinder of uniform mass distribution with the following characteristics:

Cylinder mass = 500 kg; Dimensions: 1 m (dia) x 1 m (height)

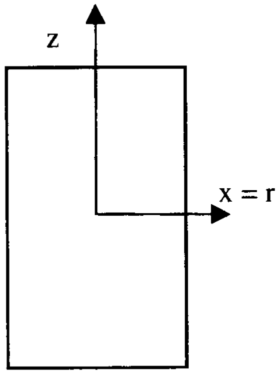

Figure 16 Schematic of cylinder and reference frame

Vertical profiles at r = 0 (along centerline)

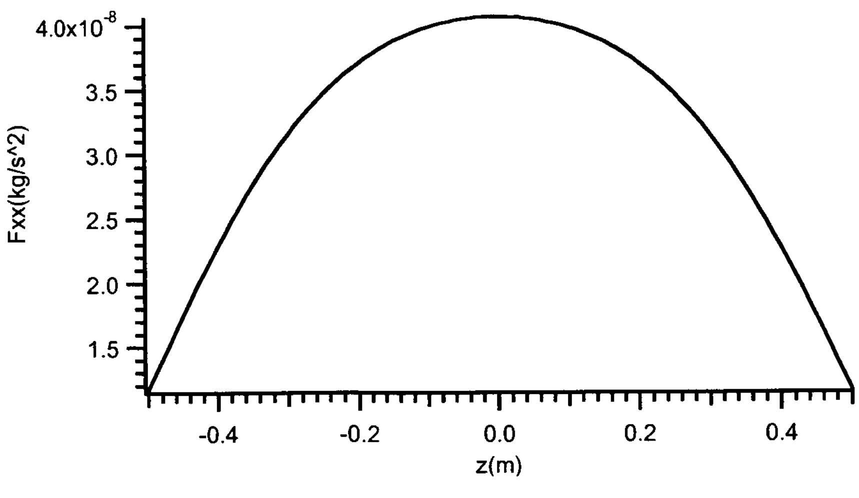

(continued)

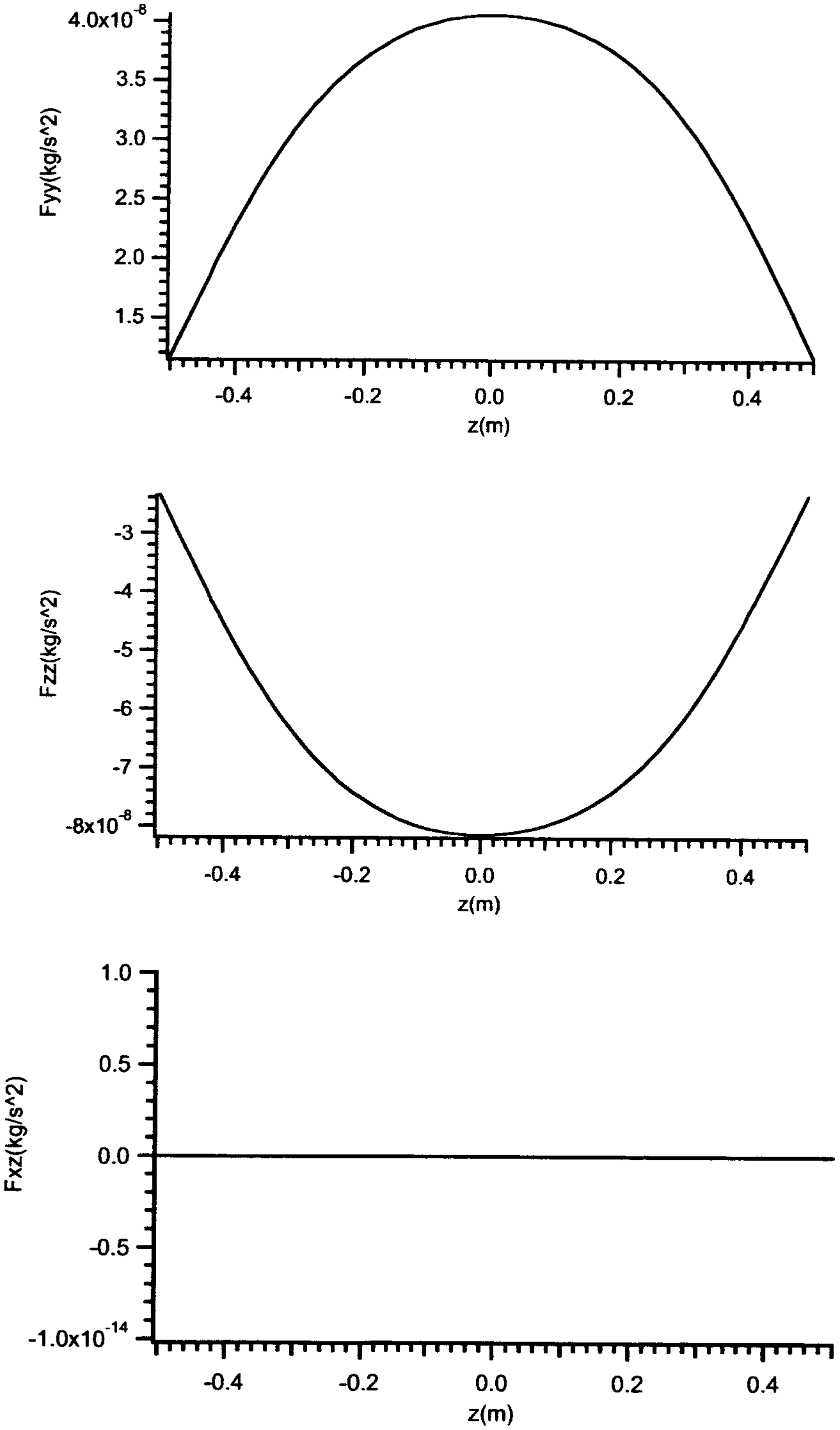

Figure 17 All components of gravity gradient along a vertical profile at r = 0 (units are $f_{rz} = ma_{rz}$ in kg/s^2 = s^{-2} for 1-kg test mass)

Vertical profiles at r = 10 cm

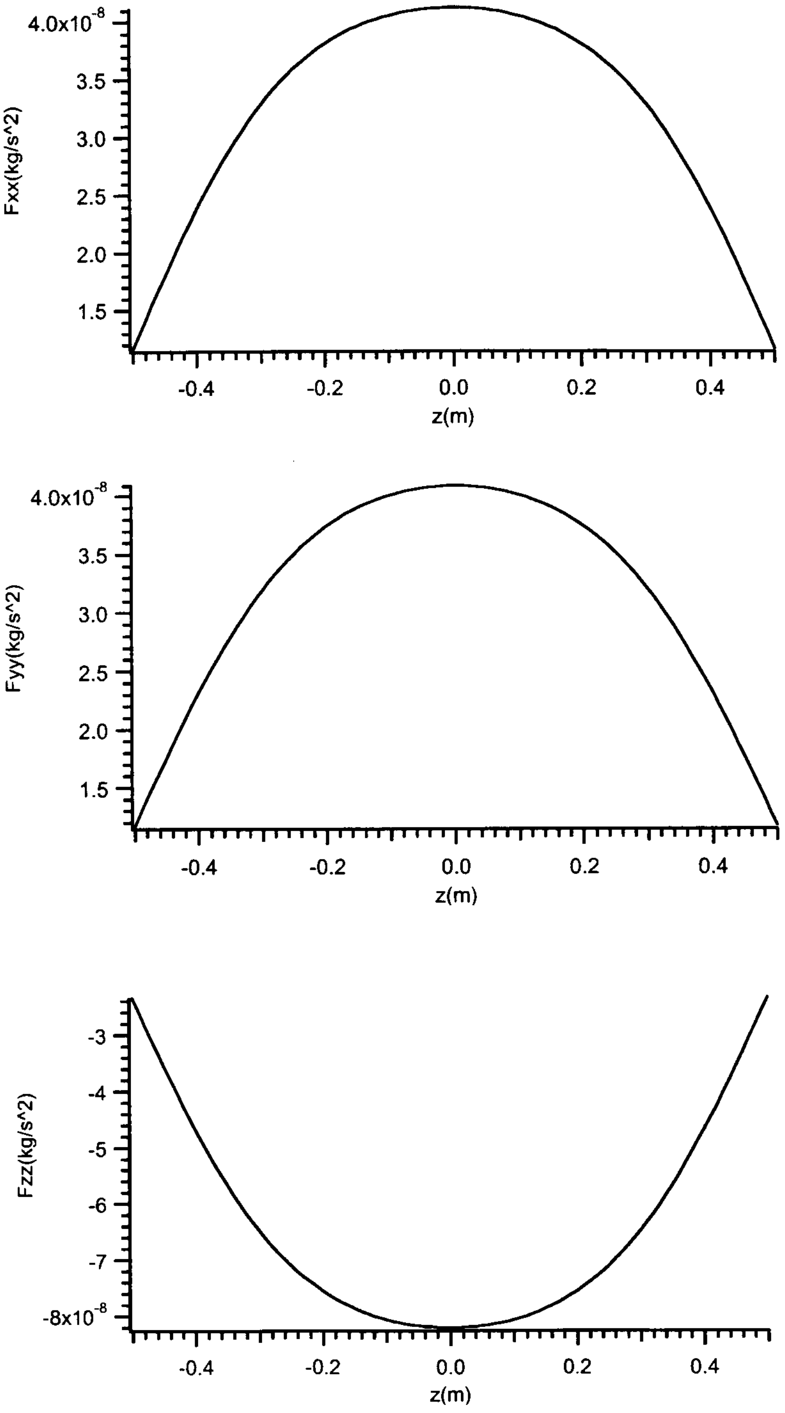

(continued)

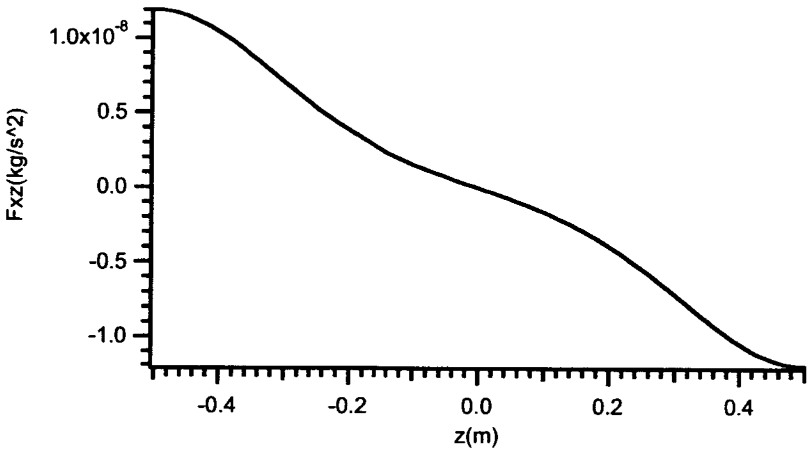

Figure 18 All components of gravity gradient along a vertical profile at r = 10 cm (units are $f_{rz} = ma_{rz}$ in kg/s^2 = s^{-2} for 1-kg test mass)

Vertical profiles at r = 20 cm

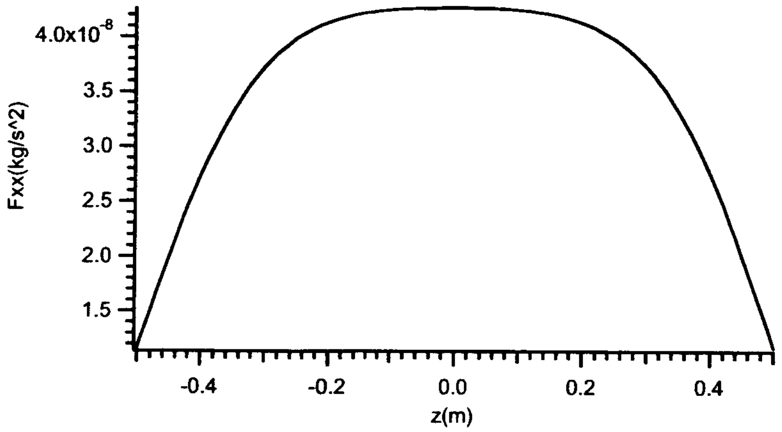

(continued)

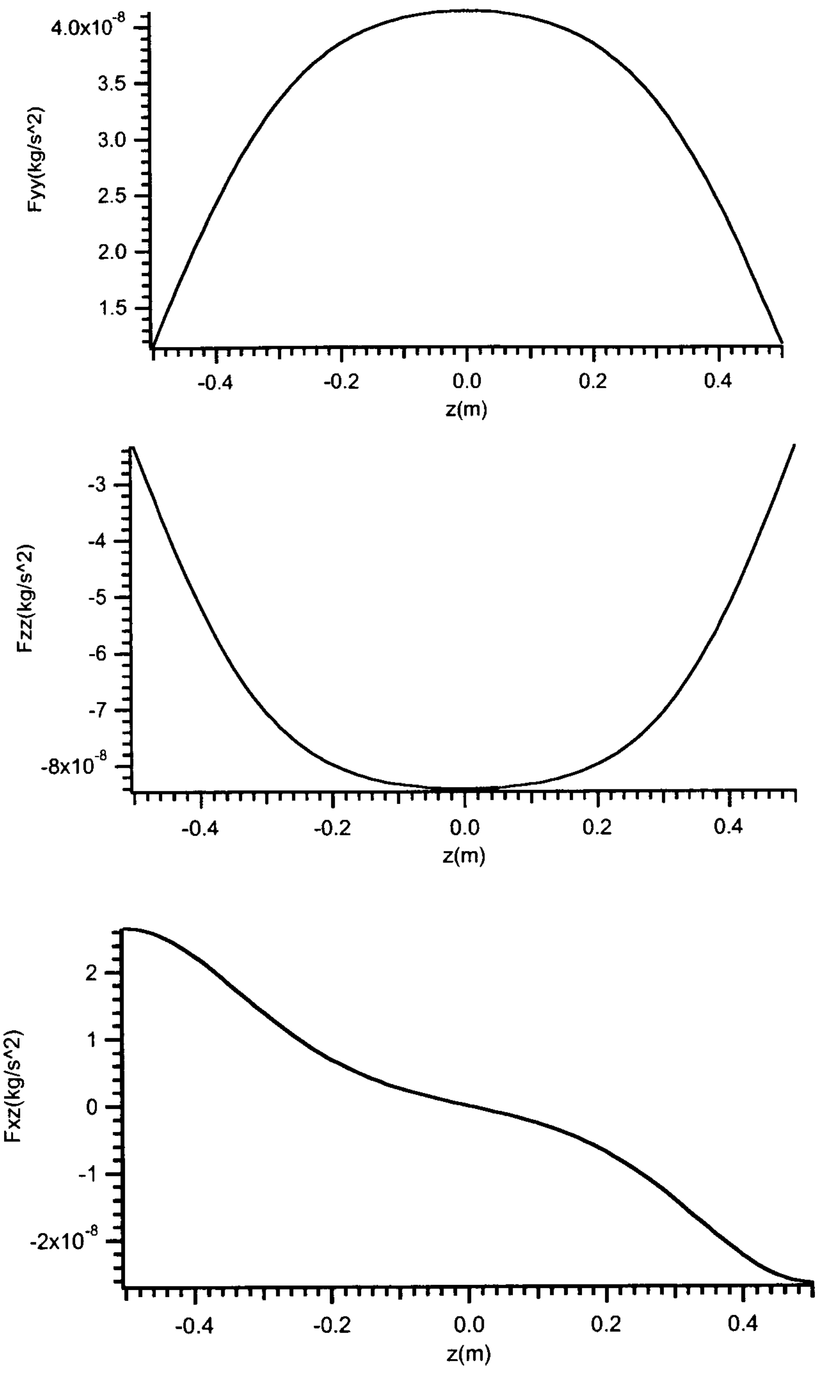

Figure 19 All components of gravity gradient along a vertical profile at r = 20 cm (units are $f_{rz} = ma_{rz}$ in kg/s^2 = s^{-2} for 1-kg test mass)

Vertical profile at r = 30 cm

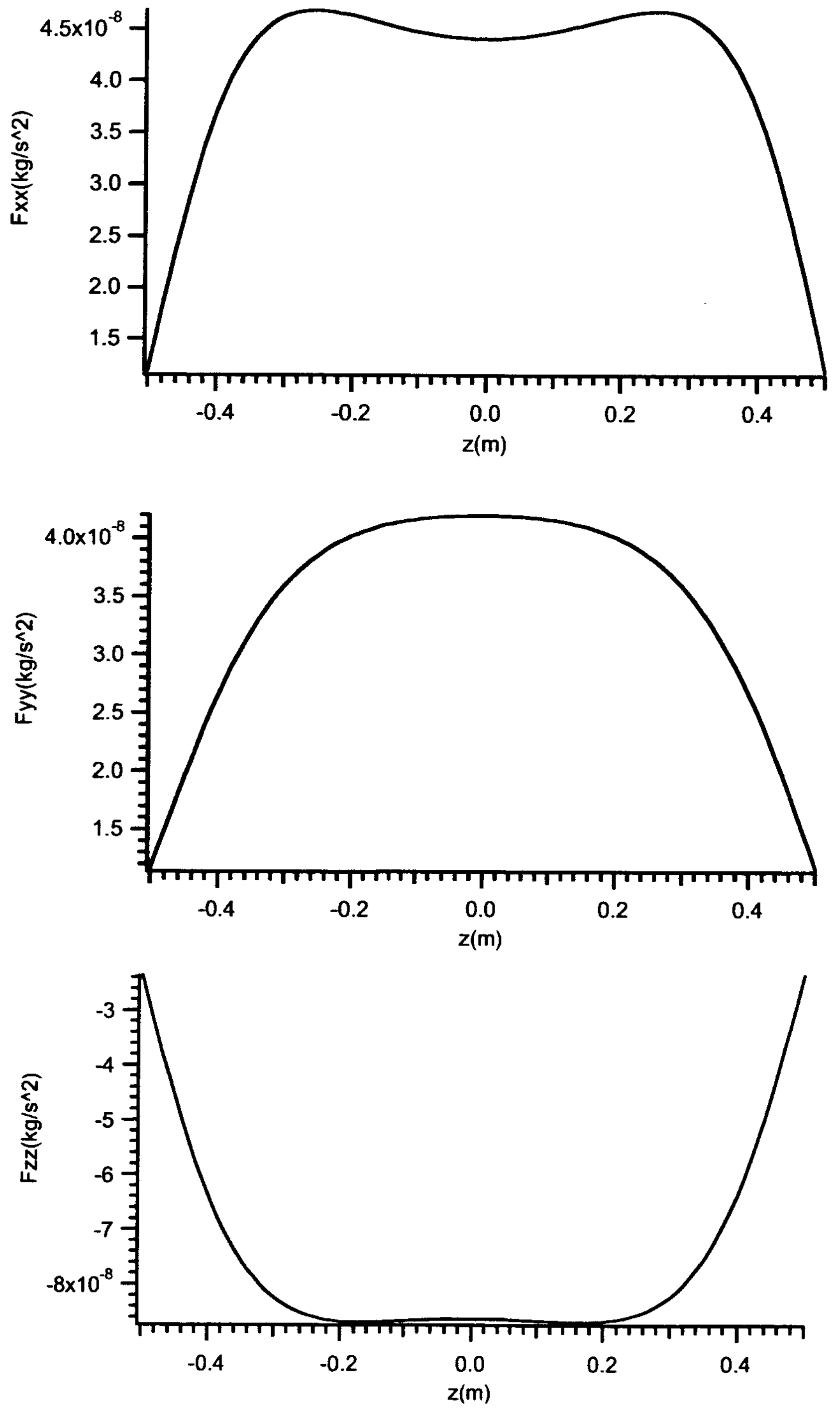

(continued)

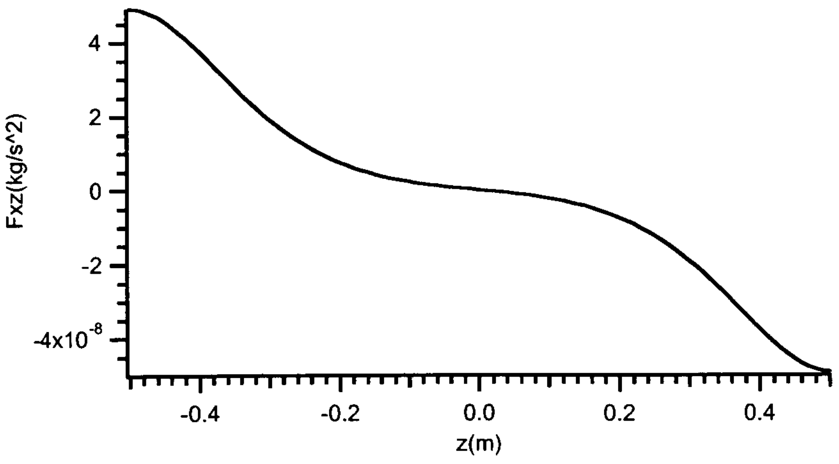

Figure 20 All components of gravity gradient along a vertical profile at r = 30 cm (units are $f_{rz} = ma_{rz}$ in kg/s^2 = s^{-2} for 1-kg test mass)

Vertical profiles at r = 40 cm

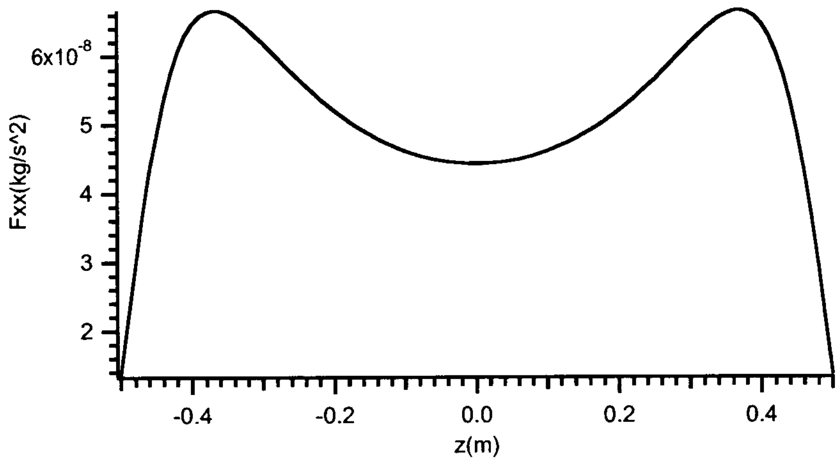

(continued)

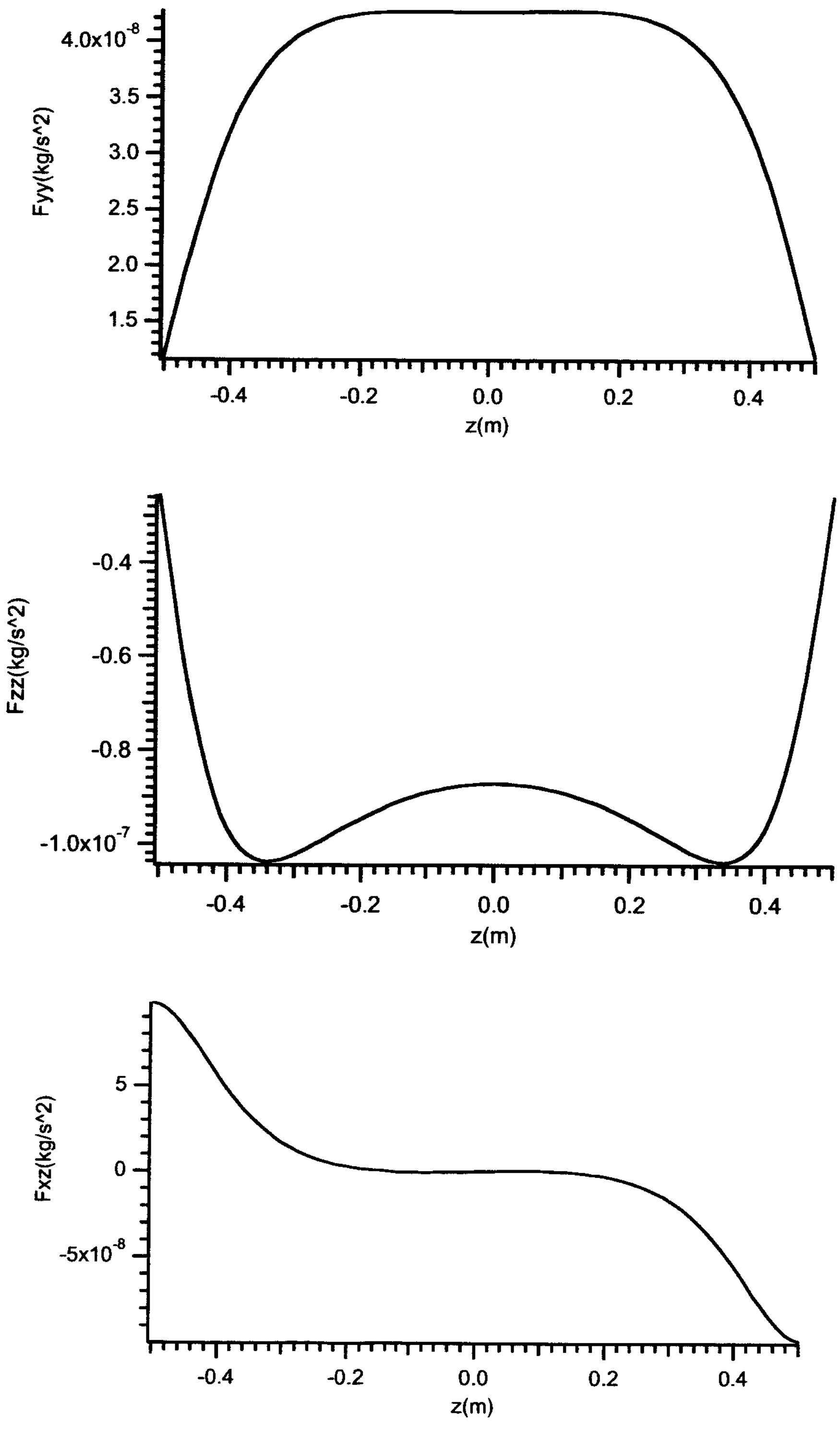

Figure 21 All components of gravity gradient along a vertical profile at r = 40 cm (units are $f_{rz} = ma_{rz}$ in kg/s^2 = s^{-2} for 1-kg test mass)

The following is a contour plot of the k_1 component inside the cylinder and the radial profiles of this component along radii at various distances from the cylinder's equatorial plane.

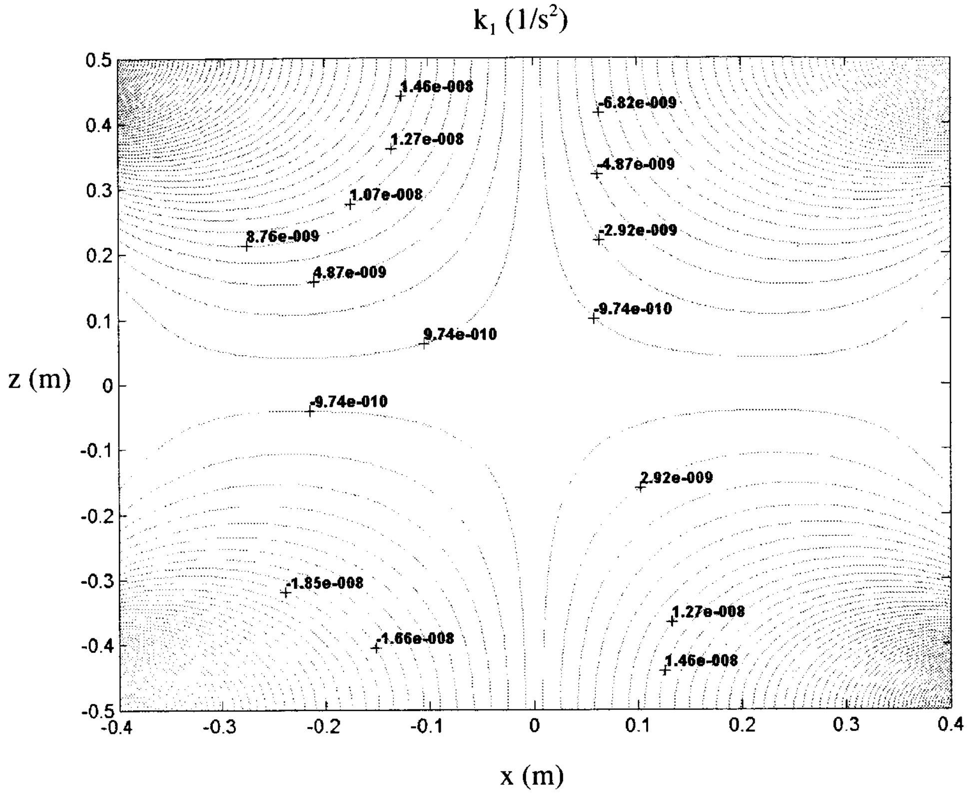

Figure 22 Contour plot of capsule gravity gradient component $k_1 = a_{rz}$ (s^{-2}) for a cylinder with H/D = 1-m/1-m

z = 10 cm (above cylinder's equatorial plane)

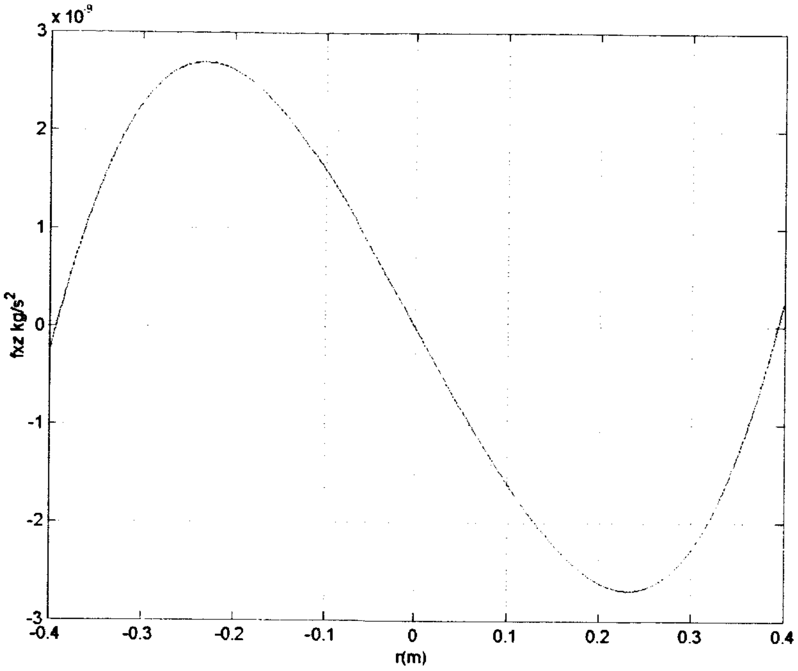

z = 20 cm (above cylinder's equatorial plane)

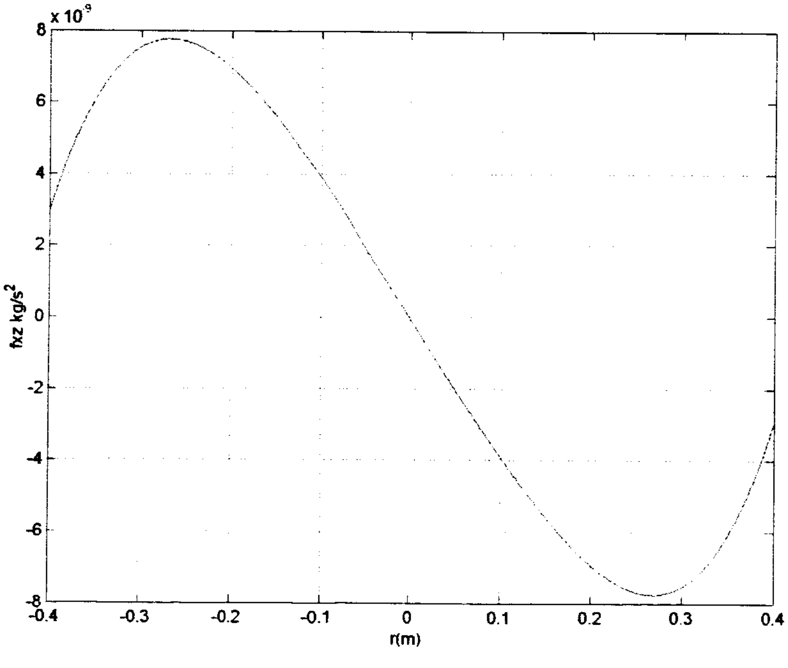

(continued)

z = 30 cm above cylinder's equatorial plane

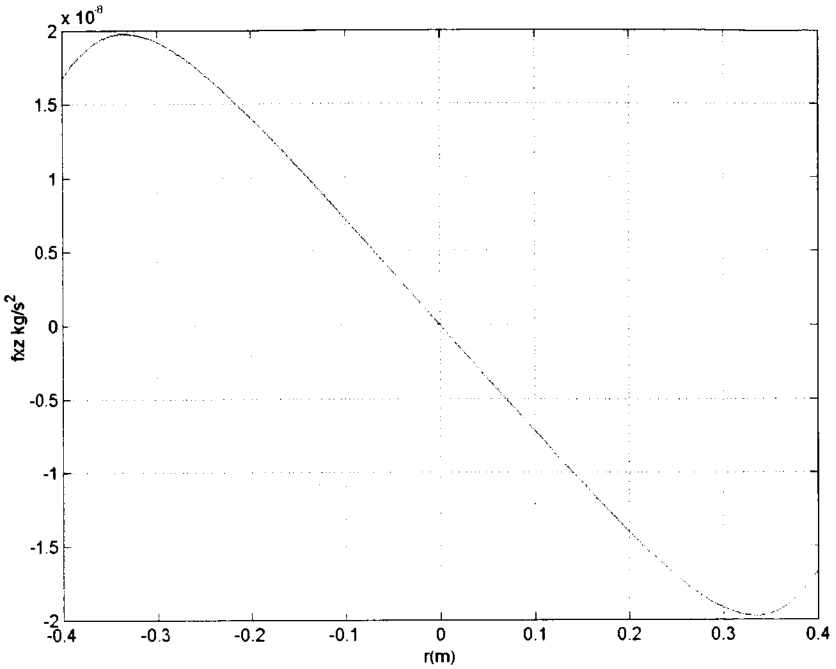

z = 40 cm above cylinder's equatorial plane

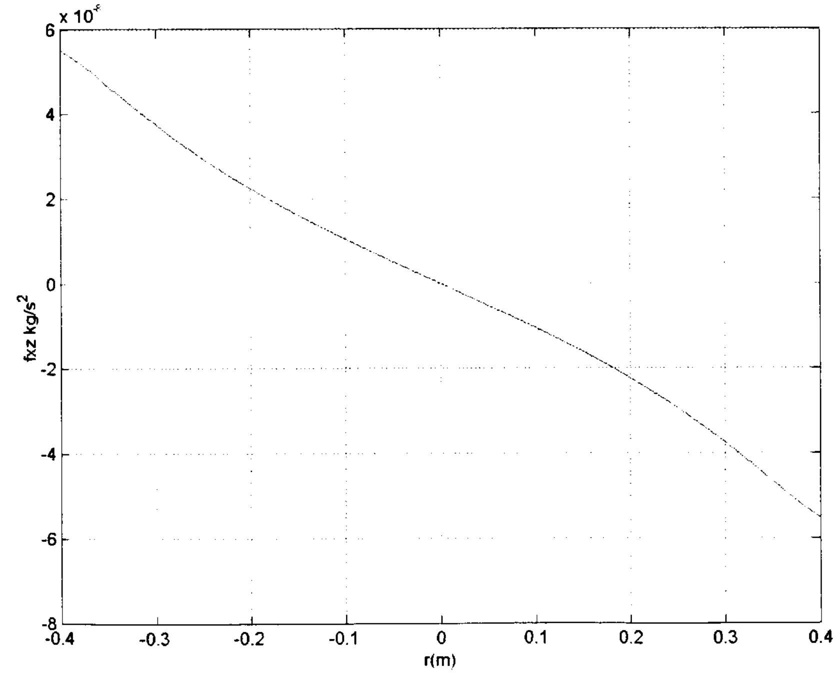

Figure 23 Gravity gradient ($a_{rz} = k_1$ component) for latitudinal sections at different distances above the cylinder's equator (units are $f_{rz} = ma_{rz}$ in $kg/s^2 = s^{-2}$ for 1-kg test mass)

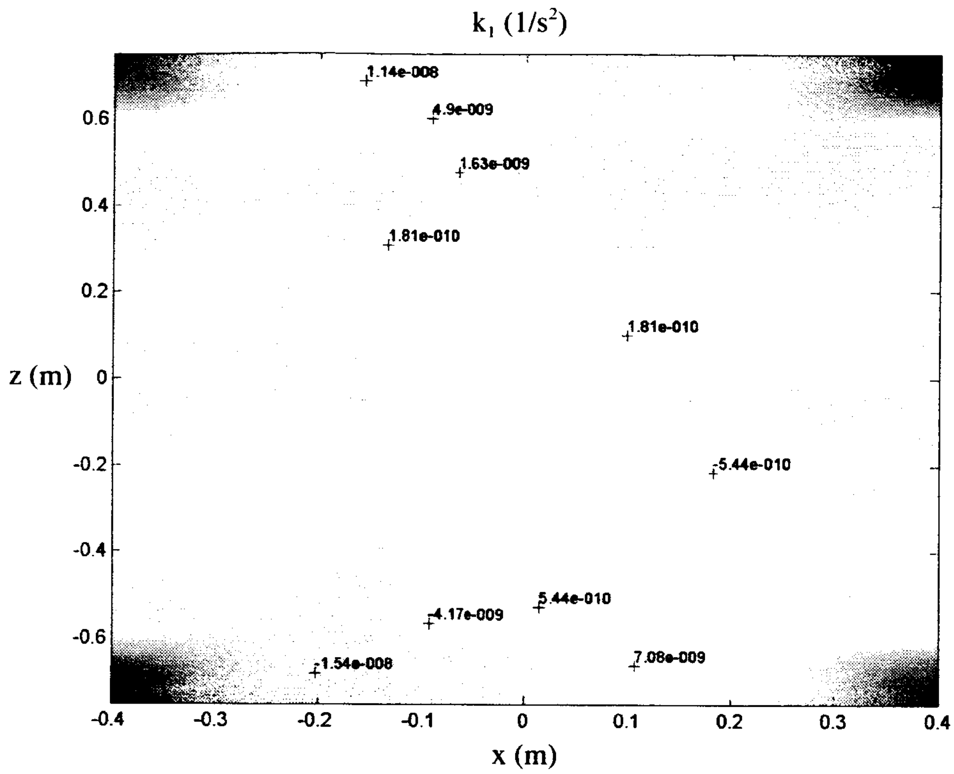

Figure 24 Contour plot of capsule gravity gradient component a_{rz} (s^{-2}) for a cylinder with H/D = 1.5-m/1-m

Figure 24 shows the contour plot of the $k_l = a_{rz}$ component for a cylinder with H/D = 1.5-m/1-m. Note that the strength of the gravity gradient in the area of interest (near the cylinder's centerline) is strongly decreased thanks to the lengthening of the cylinder in the vertical direction.

As the cylinder is stretched along the vertical, the effect of the cylinder edges (which produce stronger gravity gradients) is smaller the closer the detector is to the cylinder's centerline, where the detector free falls. In the following plots we will show all the gravity gradient terms k_1, k_2 and k_3 (modulated at ω) inside a cylinder with dimensions close to those that we are considering at the present stage of development of the design.

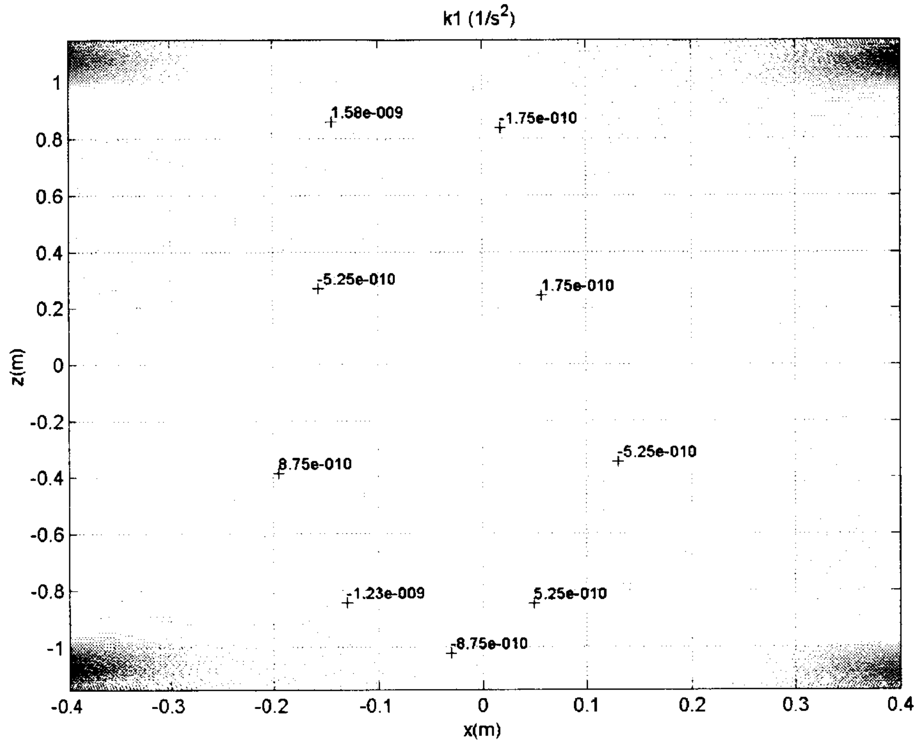

(continued)

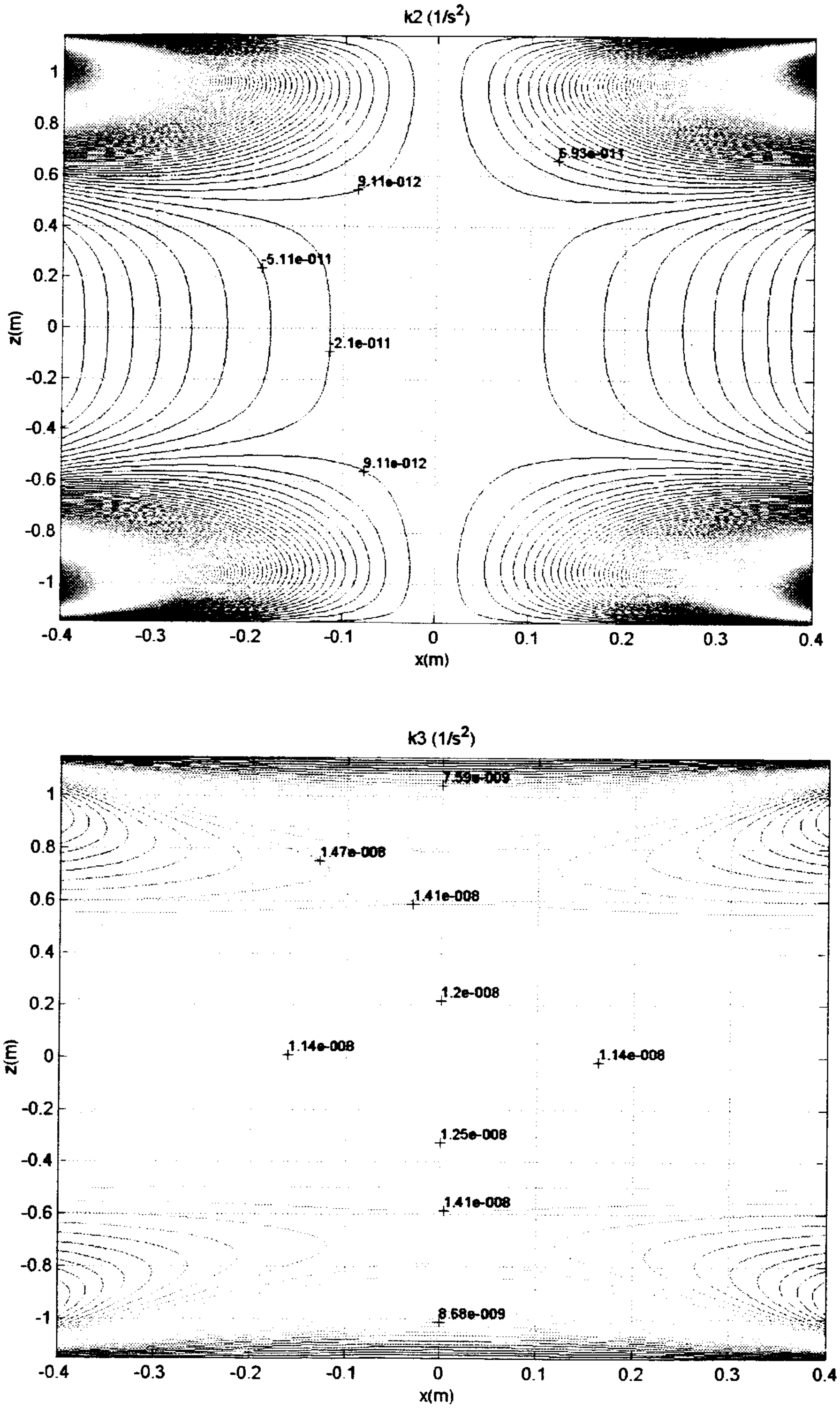

Figure 25 Cylinder without caps and H = 2.3 m; D = 1.2 m; overall mass = 500 kg.

Variation of k_1, k_2, and k_3 along free-fall trajectories

Based on the evaluation of the dynamics of the instrument package relative to the capsule (see also later on), we can map trajectories of the instrument package inside the capsule and evaluate the maximum values of the gravity gradients that the detector will experience during the fall.

It is important to evaluate the strength of the gravity gradient field inside the cryostat along a worst-case trajectory of the instrument package (sensor) that moves with respect to the cryostat/capsule during free fall. Based on worst-case wind shear conditions the trajectory (in z-r coordinates) of the sensor with respect to the cryostat can be expressed as follows:

$$\begin{aligned} z &= z_0 - \frac{a}{\beta_0} t^b \exp(ct^2) \\ r &= r_0 - \frac{dg^2t^6}{8\pi\beta_0} + (z - z_0)\sin\gamma \end{aligned} \qquad (26)$$

with a = 0.149636, b = 0.001692, c = 3.084, and d = 6×10^{-7} (see section on Optimization). In equation (26), β_0 is the low-speed ballistic coefficient, z_0 and r_0 are the coordinates of the point of release in the cryostat coordinate frame and γ is the angle of the capsule's longitudinal axis with respect to the local vertical which (at this stage of the project) represents a reasonable upper limit for the verticality error of the capsule during the fall. This trajectory will beused in the next subsections.

Cylindrical cryostat with flat caps

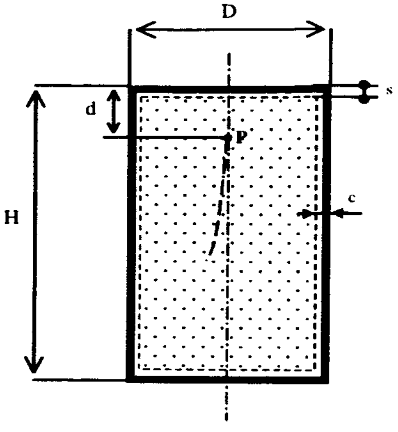

The Matlab routine has been modified to include cryostat caps of different shapes. The routine creates a two-dimensional mesh of point masses uniformly distributed on the average surface of the cylinder and its caps. In the case of flat caps the mass distribution results in a closed cylindrical surface of height H and diameter D. The gravity gradient field has been mapped on the z-x plane where x coincides with the cylinder's radial and z with the longitudinal axis, as far as s = 10 cm from the top and bottom and c = 20 cm from the side walls.

The point of release P lies on the symmetry axis of the cylinder and at d = 40 cm from the top. The sensor trajectory obeys eqns. (26) with β_0 = 10000 kg/m^2 and the capsule verticality error $\gamma = 5°$ has been conservatively assumed to produce a lateral displacement of the sensor in the same direction of the wind shear. The other parameters in eqns. (26) also represent a worst-case scenario for lateral displacements. The key quantities k_1, k_2 and k_3 are plotted as contour plots on the x-z plane in Figs. 26.

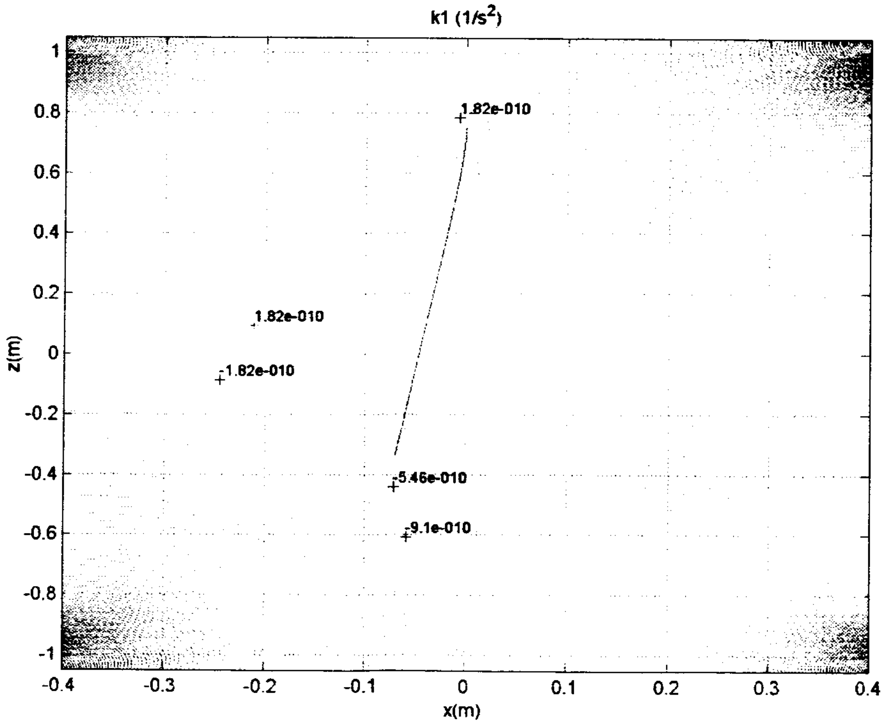

(continued)

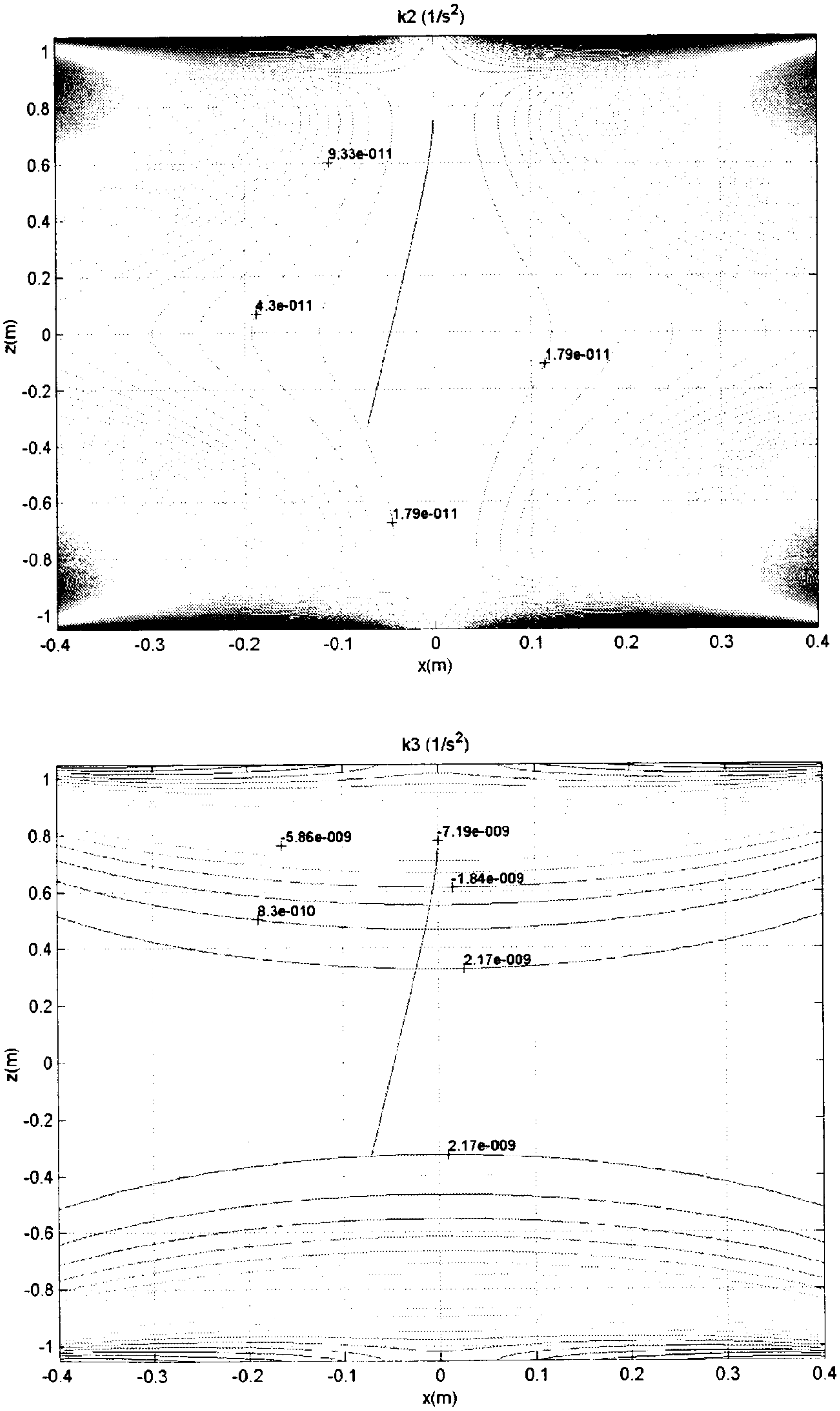

Figure 26 Contour plots of k_1, k_2, k_3 for a cryostat with flat caps and H = 2.3 m, D = 1.2 m and total mass = 500 kg.

The quantities k_1, k_2, k_3 are then computed along the trajectory of the instrument package and the power spectral densities are computed over the free-fall time of 26 s. Results are shown in Fig. 27 where the peaks with frequency $1/t_f = 1/26$ Hz due to the free-fall duration, are clearly visible in the spectra.

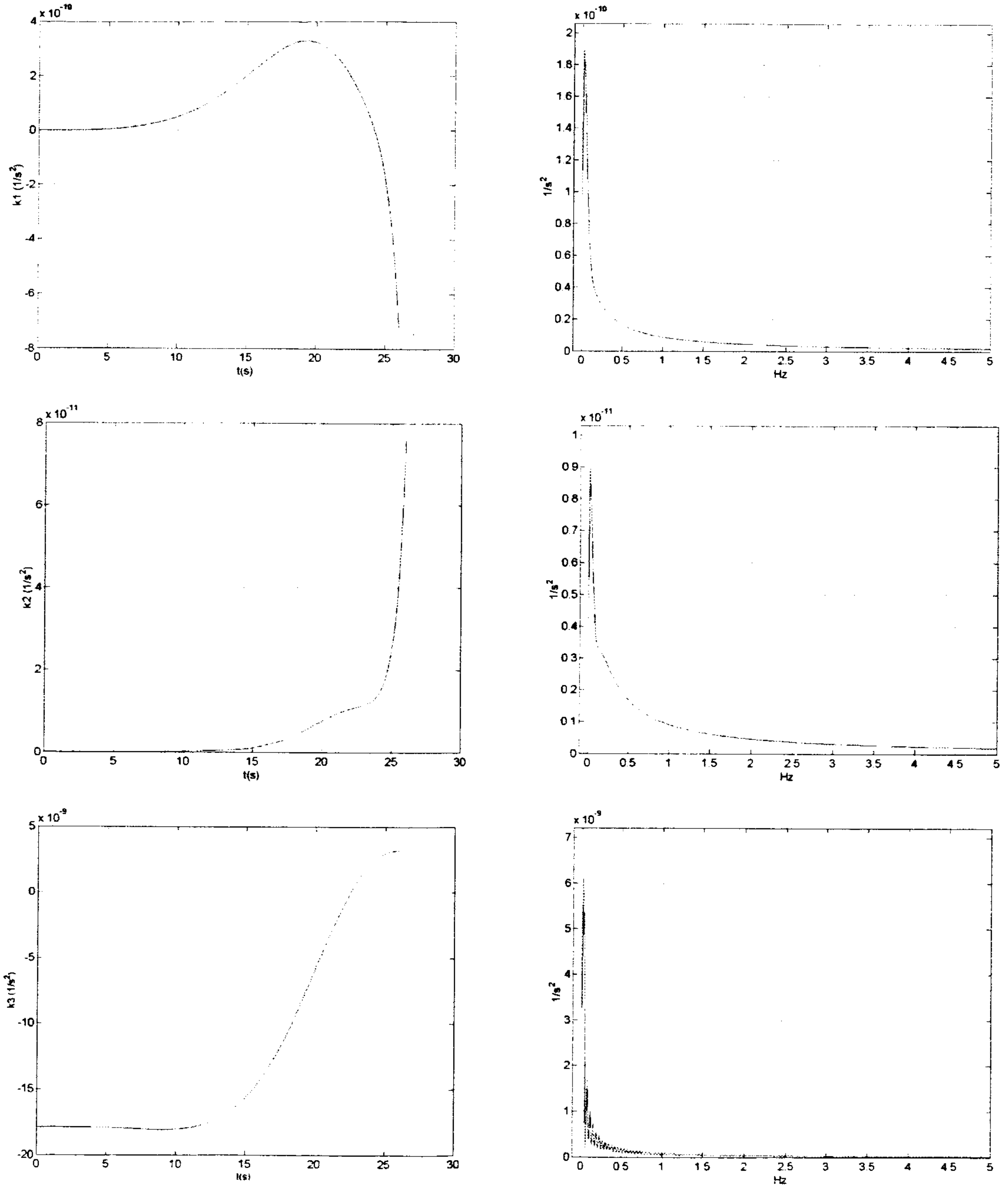

Figure 27 k_1,k_2,k_3 along the trajectory and their spectra.

Figure 26 shows that the quantity k_3 is relatively larger than k_1 and k_2. Consequently, eqn. (25) poses a limit for the angle β that defines the capsule attitude with respect to the spin axis of the sensor. After neglecting the much smaller k_2 (and k_1 which depends on $\cos(2\beta)$) we find that the maximum allowable β is:

$$\beta_{\max} = \frac{1}{2}\sin^{-1}\left(\frac{\chi_{\max}}{k_3}\right) \tag{27}$$

With a $\chi_{\max}$ of 10^{-9} s^{-2} and the results shown in Fig. (27), we obtain a limit of 4.8 deg for β, which is a relatively large value.

Cylindrical cryostat with hemispherical caps

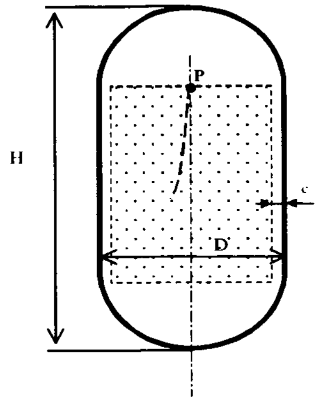

A cylindrical cryostat with hemispherical caps has also been analyzed. The gravity gradient distribution has been mapped on the x-z plane, where x is the cylinder's radial and z the longitudinal axis, between the base of the upper and lower hemispheres and as close as c = 20 cm from the side wall.

The release point P (and starting point for the simulation) lies on the symmetry axis of the cylinder and at the base of the upper hemisphere. The sensor trajectory is the same as in the previous case.

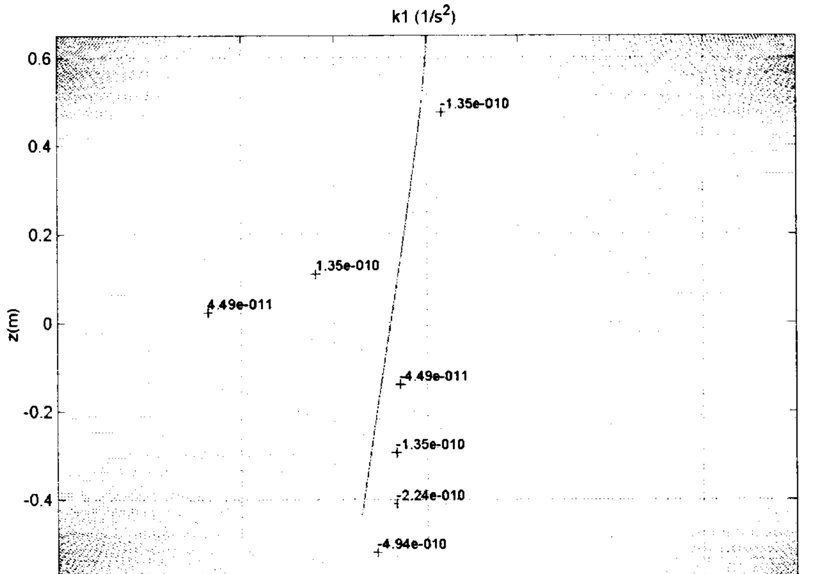

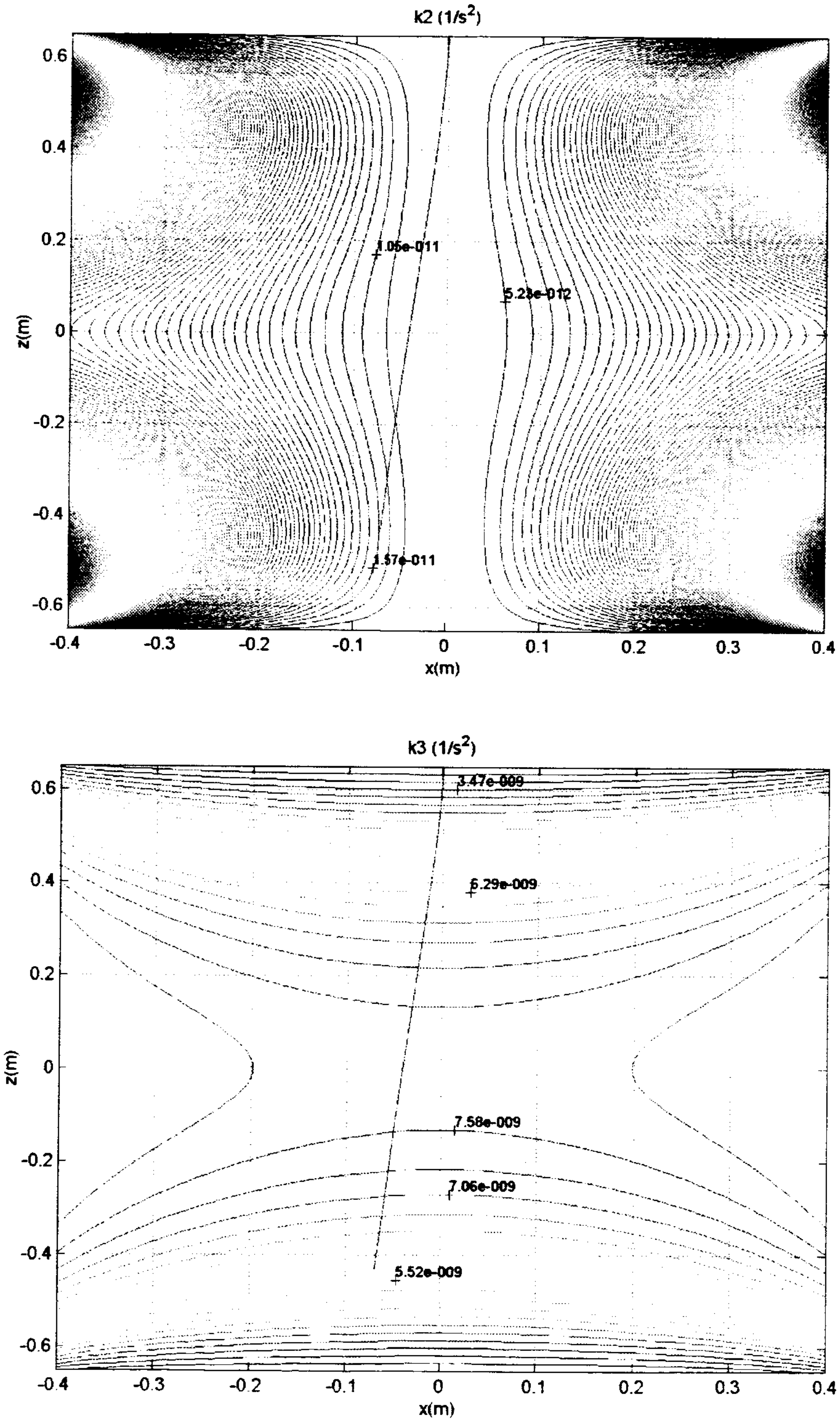

Figure 28 Contour plots of k_1, k_2, k_3 for cryostat with hemispherical caps and H = 2.5 m, D = 1.2 m and total mass = 500 kg.

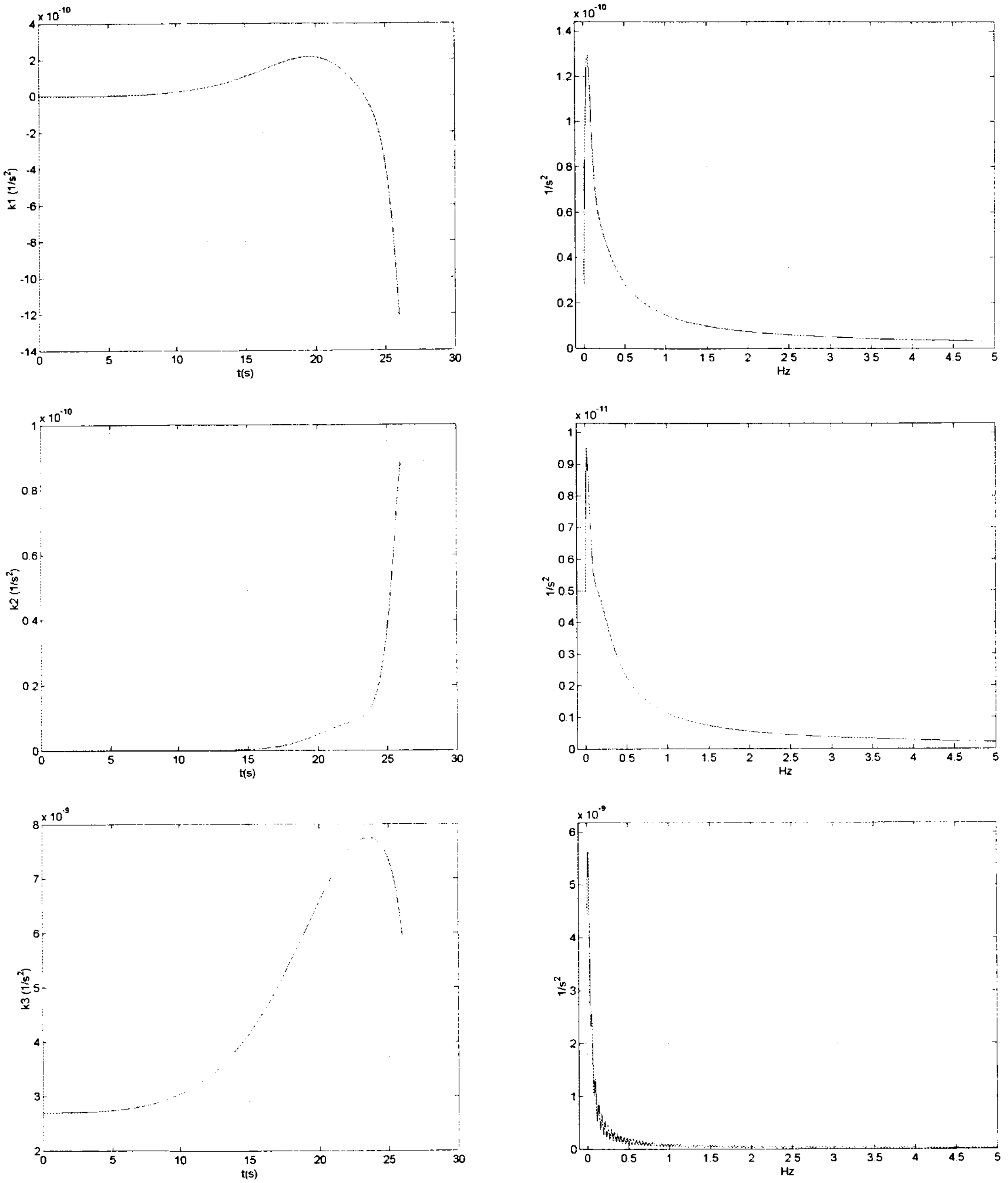

Figure 29 k_1, k_2, k_3 along the trajectory and their spectra.

The analysis carried out here and additional results not shown in this report lead to the definition of a stand-off distance of about 40 cm between the sensor CM and the heavy part of the cryostat walls to provide ω-modulated components of the gravity gradient that are sufficiently low for the sizes and masses relevant to this project.

Earth's gravity gradient

We compute here the Earth's gravity gradient tensor and we analyze the effects of Earth's gravity gradient components on a rotating detector with a generic orientation of its spin axis with respect to the gravity gradient field. Let us consider the gravitational potential per unit mass at a point (x, y, z) with respect to the detector's center of mass:

$$V = -\frac{\mu}{\sqrt{(x-R_X)^2 + (y-R_Y)^2 + (z-R_Z)^2}} \tag{28}$$

where R_X, R_Y, R_Z are the components of the radius vector R from the Earth's center to the detector's CM (in which Z is the local vertical) and μ is the Earth's gravitational constant. After projecting about the detector's body axes in which x is the spin axis and calling $\theta = \omega t$ the rotation about the spin axis and ϕ the elevation angle of the spin axis with respect to the horizontal plane:

$$\begin{aligned} R_x &= R(t)\sin(\phi) \\ R_y &= R(t)\cos(\phi)\sin(\omega t) \\ R_z &= R(t)\cos(\phi)\cos(\omega t) \end{aligned} \tag{29}$$

The gravitational acceleration in body axes is obtained by substituting eqns (29) into eqn. (28) and computing the gradient:

$$\{g_x, g_y, g_z\}^T = -\nabla V \tag{30}$$

The components of the gravity gradient matrix in body axes are finally computed by taking a further derivative with respect to the spatial coordinates, to yield

$$g_{xx} = -\frac{\mu}{R^3}[-2 + 3\cos^2(\phi)] \tag{31.1}$$

$$g_{xy} = 3\frac{\mu}{R^3}\sin(\omega t)\cos(\phi)\sin(\phi) \tag{31.2}$$

$$g_{xz} = 3\frac{\mu}{R^3}\cos(\omega t)\cos(\phi)\sin(\phi) \tag{31.3}$$

$$g_{yy} = -\frac{\mu}{R^3}[1 - 3\cos^2(\phi) + 3\cos^2(\omega t)\cos^2(\phi)] \tag{31.4}$$

$$g_{yz} = 3\frac{\mu}{R^3}\cos(\omega t)\sin(\omega t)\cos^2(\phi) \tag{31.5}$$

$$g_{zz} = \frac{\mu}{R^3}[-1 + 3\cos^2(\omega t)\cos^2(\phi)] \qquad (31.6)$$

Here again, the components modulated at ω are g_{xy} and g_{xz} (in which x is the spin axis). In other words, if the spin axis lies on the horizontal plane, the detector only sees components modulated at 2ω but if it is not, components modulated at the frequency ω appear. The strengths of these components are proportional to the tilt angle with respect to the local horizon. Note also that the effect of the Earth's gravity gradient on a rotating body can be readily applied to the space-based tests of the Equivalence Principle in which the only difference from the balloon-based experiment is the slightly larger value of the radial distance from the space-based sensor to the Earth's center.

An alternative way of portraying the origin of the ω-modulated components of the Earth's gravity gradient field is by considering the following. If the z-axis of the body reference frame is directed along the local vertical (that is the spin axis x of the sensor is on the horizontal plane) then the gravity gradient tensor is

$$\Gamma^E_{(z \equiv r)} = \frac{GM_E}{R^3}\begin{bmatrix} -1 & 0 & 0 \\ 0 & -1 & 0 \\ 0 & 0 & 2 \end{bmatrix} \qquad (32)$$

The tensor does not change under a rotation about the z-body axis due to its structure which reflects a symmetry about the radial line. Consequently, we can choose the azimuth orientation of the spin axis at will (let us call it the y-body axis). A rotation ϕ about an axis perpendicular to the spin axis produces terms $g'_{xz} = g'_{zx}$ in the transformed tensor:

$$\Gamma^E_\phi = R_\phi \Gamma^E R^T_\phi = \frac{GM_E}{R^3}\begin{bmatrix} g\copyright_{xx} & 0 & g\copyright_{xz} \\ 0 & -1 & 0 \\ g\copyright_{zx} & 0 & g\copyright_{zz} \end{bmatrix} \qquad (33)$$

where

$$\begin{aligned} g\copyright_{xx} &= -1 + 3\sin^2\phi \\ g\copyright_{zz} &= -1 + 3\cos^2\phi \qquad (34) \\ g\copyright_{xz} &= g_{zx} = -3\sin\phi\cos\phi \end{aligned}$$

The g'_{xz} and g'_{zx} terms are subsequently modulated at the frequency ω by the rotation θ = ωt about the spin axis as shown previously.

Since there are terms modulated at the signal frequency ω, we have to make sure that they are kept lower than the accuracy with which we want to measure the signal. From the detector point of view, there will be requirements imposed on the centering of the sensing masses and their orientation with respect to the Earth's gravity field as shown later on.

Disturbances induced by concentrated masses on board the capsule

Let us consider the reference system (x, y, z) fixed to the sensor with origin at the center of mass and with x oriented along the spin axis and let us indicate the position of a point mass m_p in proximity of the sensor in spherical coordinates (δ,γ,ρ) (see Fig. 30).

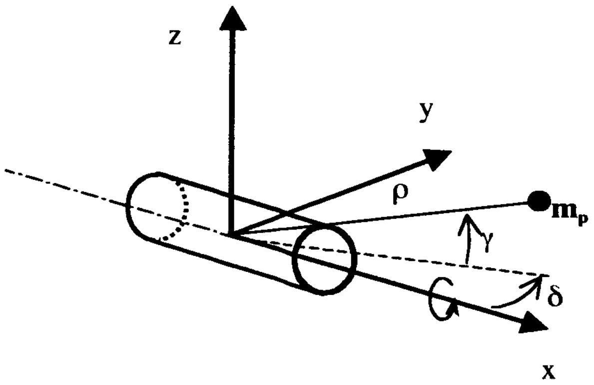

Figure 30 Geometry of the sensing mass and reference frame

The position of m_p is then expressed as:

$$\begin{aligned} x_p &= \rho\cos\delta\cos\gamma \\ y_p &= \rho\sin\delta\cos\gamma \\ z_p &= \rho\sin\gamma \end{aligned} \qquad (35)$$

The gravity gradient matrix at the detector due to the gravity field induced by a mass point m_p is:

$$\Gamma_{m_p} = \frac{G\cdot m_p}{\rho^5}\begin{bmatrix} 3x^2-\rho^2 & 3xy & 3xz \\ 3yx & 3x^2-\rho^2 & 3yz \\ 3zx & 3yz & 3x^2-\rho^2 \end{bmatrix} \qquad (36)$$

Considering a sensor that rotates with respect to a fixed point mass in its proximity we obtain the two ω-modulated components already shown in the previous paragraphs:

$$\Gamma'_{12} = \Gamma'_{21} = \Gamma_{13}\sin(\omega\cdot t) + \Gamma_{12}\cos(\omega\cdot t) \qquad (37.1)$$

$$\Gamma'_{13} = \Gamma'_{31} = \Gamma_{13}\sin(\omega\cdot t) - \Gamma_{12}\cos(\omega\cdot t) \qquad (37.2)$$

The moduli of the two ω-modulated gravity gradient components Γ'_{12} and Γ'_{13} are the same and can be expressed as follows:

$$\chi = \frac{G \cdot m_p}{\rho^5}|x|\sqrt{z^2 + y^2} \tag{38}$$

which shows that the masses located on the plane y-z (i.e., x = 0) do not generate disturbances with the same frequency as the measured signal. Substituting eqn. (35) into (38) and extracting ρ yields the minimum distance for a point mass to produce a disturbing gradient equal to or less than the critical gradient $a_{gg\text{-}max}$:

$$\rho_{\min} = \left(\frac{G \cdot m_p}{a_{gg-\max}}|\cos\delta\cos\gamma|\sqrt{\sin^2\delta\cos^2\gamma + \sin^2\gamma}\right)^{1/3} \tag{39}$$

Setting a limit of 10^{-9} s^{-2} for a_{max} we plot the locus f(ρ,γ,δ) = 0 of the points in space with $a_{gg} = a_{gg\text{-}max}$ in Figure 31 for a disturbing point mass of 1 kg. Next, meridian sections (rotated about the z-axis by the meridian angle δ) of the same locus are plotted for different values of the angle δ in Fig. 32 where r is the radial direction.

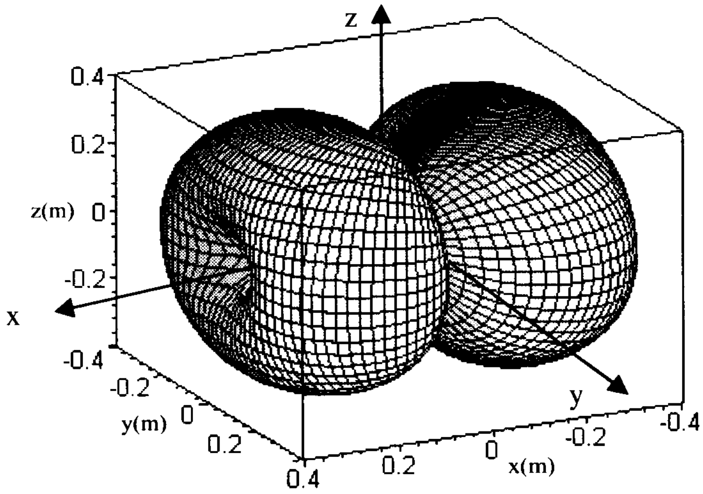

Figure 31 Locus of ω-modulated gravity gradient component with strength = 10^{-9} s^{-2}

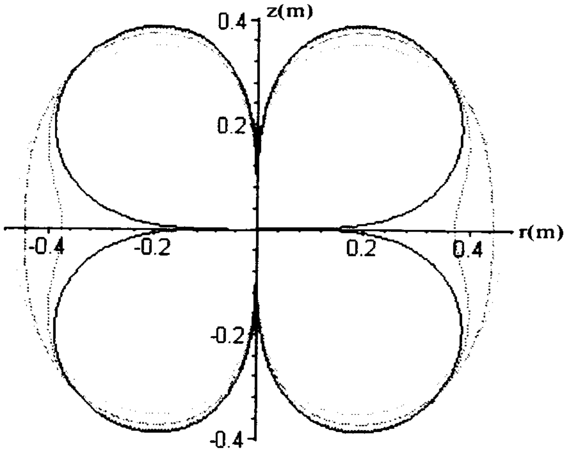

Figure 32 Meridian sections of locus in Fig. 31 for different angles δ [$\delta = 0$ (i.e., y-z plane) - solid black line; $\delta = 15°$ - blue dots; $\delta = 30°$ - red dash; $\delta = 45°$ - gray dash dot]

The worst case meridian section at $\delta = 45°$ is plotted for different values of the perturbing mass in Fig. 33.

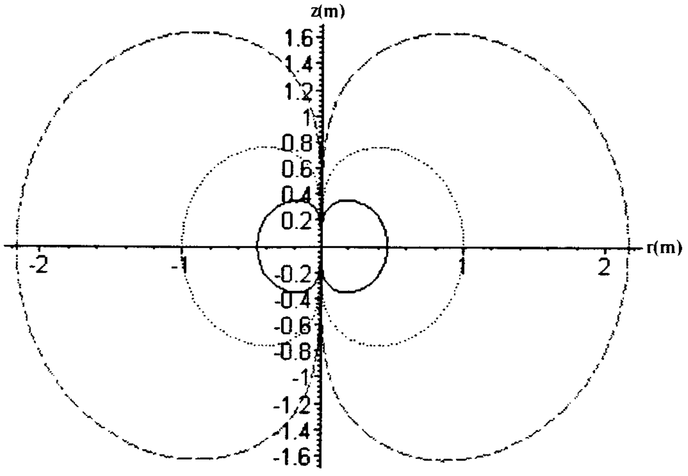

Figure 33 Meridian sections for $\delta = 45°$ and different values of perturbing mass m_p ($m_p = 1$ kg - solid black line; $m_p = 10$ kg – blue dots; $m_p = 100$ kg - red dash)

The previous analysis defines exclusion zones for concentrated masses on board the capsule. In general, masses can be placed rather freely on the y-z plane (perpendicular to the sensor spin axis). Masses lying on this plane generate only 2ω-modulated components whose strength only needs to be reasonably smaller than the upper bound of the dynamic range of the sensor. The Earth itself produces such 2ω-modulated components with a strength equal to 3×10^{-6} s^{-2} that is well stronger than the sensor sensitivity (for realistic values of the sensing mass CMs errors), but is about 3-orders of magnitude lower than the upper bound of the sensor dynamic range. For the 2ω-modulated term, the equivalent Earth is a mass of 22,500 kg at 1-m or a 22.5 kg at 10 cm from the sensor.

Requirements related to the ω-modulated components are more stringent and, consequently, we will concentrate on these components which have been dealt with in this analysis. In summary, concentrated masses should be placed as close as possible to the y-z plane (perpendicular to the sensor spin axis). For masses away from the y-z plane, Fig. 33 defines the exclusion zones from the sensor for different mass values under the worst possible condition of masses placed on the 45° meridian plane.

Effect of Gravity Gradients on Differential Acceleration Measurement

The differential accelerometer consists (from the mechanical point of view) of two sensing masses with ideally coincident centers of mass (CM). The equivalence violation signal is measured as a differential displacement along the y-body axis of the sensor which is orthogonal to the spin axis along the x-body axis. In reality the two centers of mass (or more appropriately centers of gravity) do not coincide and CM_2 (i.e., the CM of mass 2) is displaced by a position error vector δ with respect to CM_1 as follows

$$\delta = \begin{bmatrix} \delta_x \\ \delta_y \\ \delta_z \end{bmatrix} \tag{40}$$

We can place the body reference frame at CM_1 and compute the differential acceleration due to gravity gradients by simply multiplying the gravity gradient matrix in body axis , that is

$$\begin{bmatrix} \delta a_x \\ \delta a_y \\ \delta az \end{bmatrix} = \left(\Gamma^E + \Gamma^C + \Gamma^M\right) \begin{bmatrix} \delta_x \\ \delta_y \\ \delta_z \end{bmatrix} \tag{41}$$

where Γ^E, Γ^C, Γ^M are the gravity gradient matrices of the Earth, the distributed capsule mass and concentrated masses on board the capsule, respectively. Since the differential accelerometer measures only the component along the y-body axis, we obtain finally:

$$\delta a_y = (\Gamma^E_{yx} + \Gamma^C_{yx} + \Gamma^M_{yx})\delta_x + (\Gamma^E_{yy} + \Gamma^C_{yy} + \Gamma^M_{yy})\delta_y + (\Gamma^E_{yz} + \Gamma^C_{yz} + \Gamma^M_{yz})\delta_z \tag{42}$$

in which Γ^E_{yx}, Γ^C_{yx}, and Γ^M_{yx} are the components modulated at the signal frequency ω while the other terms in eqn. (42) are modulated at 2ω. In conclusion, the disturbing differential acceleration along y produced by gravity gradients can be expressed as follows:

$$\delta a_y < 3\frac{\mu}{R^3}\cos(\phi)\sin(\phi)\sin(\omega t)\delta_x + \left[(k_2+k_3)\sin(2\beta)+k_1\cos(2\beta)\right]\sin(\omega t)\delta_x + a_M(\omega) + f_y(2\omega,\delta_y) + f_z(2\omega,\delta_z) \tag{43}$$

where k_1, k_2, and k_3 are the gravity gradient terms (see previous subsections) generated by the capsule in the capsule-body reference frame, ϕ is the elevation of the spin axis with respect to the local horizon, β is the elevation of the spin axis with respect to the equatorial plane of the capsule, $a_M(\omega)$ is the ω-modulated disturbing acceleration (in functional form) produced by concentrated mass on board the capsule (see previous subsection) and $f_y(2\omega, \delta_y)$ and $f_z(2\omega, \delta_z)$ represent all the other 2ω-modulated components which have been separated in eqn. (43), according to the centering error components. Note that the 2ω-components depend on the centering errors δ_y and δ_z while the ω-components depend only on the centering error δ_x. The less-than sign in eqn. (43) is due to the fact that, on the right hand side of the equation, we have adopted the strongest value of the ω-modulated gravity gradient component of the capsule, that is, for $\alpha = 0$ (see Fig. 15). Moreover, from the analysis of the capsule gravity gradients, we have concluded that if we keep the sensor (at the CM) about 40 cm away from the heavy part of the chamber/cryostat walls, the ω-modulated gravity gradients are well below the critical value of about 10^{-9} s^{-2}. Based on similar reasoning, we assume that the concentrated masses on board the capsule are placed outside of the exclusion zones (defined in the previous subsection) in order to keep them below the critical value. In other words, an appropriate design and a careful mechanical construction of the sensing masses (δ_x of order microns) will make the gravity gradient contribution of the capsule and the concentrated masses on board the capsule negligible.

To attenuate the effect of the gravity gradient of the Earth we have to make sure that the product $\sin(\phi)\cos(\phi)\delta_x$ is sufficiently small. In other words we can trade the position error between the CMs of the sensing masses along the spin axis δ_x for the tolerable angle ϕ of the spin axis with respect to the local horizontal. For small values of ϕ, we readily compute that for the first term on the right hand side of eqn. (34) to be smaller than, let us say, 10^{-15} g, the product $\phi\delta_x$ must be smaller than 0.1 deg-µm. This requirement must be considered in the design of the detector, the release mechanism, and the capsule leveling system of the capsule. The complexity of some subsystems can be traded for the simplicity of other subsystems among those three devices.

THEORETICAL IMPACTS

Contribution of Parity Non-conserving Weak Interactions

Introduction

A theoretical question that we sought to address can be simply stated: What is the contribution to the mass-energy of each material due to the parity non conserving part of the weak interaction? The reason that we sought an answer to this question was to find out if our experiment would be sensitive enough to determine whether or not this contribution obeys the weak principle of equivalence.

Unfortunately, the present level of development of physics does not allow us to address our question reliably. Knowledge of the physics of nuclear matter is too primitive. We have therefore had to make a number of "reasonable," but nonetheless somewhat arbitrary, assumptions to carry out the calculations. The discussion below mentions each of these assumptions. The results of the calculations indicate that our experiment will not be sensitive to the contribution to mass-energy of the parity non conserving part of the weak interaction.

Evaluation of contribution

The materials to be compared in the experiment should have binding energies stored in forms which are as different as possible. For example, if gravity couples differently to protons and neutrons, we should compare elements with different proton to neutron ratios. A new long range force could also be detected by comparing such elements. A force coupling to baryon number would cause an acceleration proportional to the total number of protons and neutrons divided by the mass, or for a single nucleus, to $(Z+N)/(m_p Z + m_n N) \sim 1/m_N(1-\frac{(m_p - m_n)}{m_N} x)$. Here x is the ratio Z/A and Z, N and A are the number of protons, neutrons, and combined nucleons. The mass m_N is used for the common mass of protons and neutrons. In order to observe this effect, it is best to compare heavy elements with $x \sim 1/3$ to light elements with $x \sim 1/2$.

As we will see below, the energy of a nucleus can depend very sensitively on the wave functions of the protons and neutrons. We will discuss a force coupling to the product of proton and neutron densities. Such a force is more significant for nuclei in which proton and neutron wave functions have greater overlaps. This suggests choosing a nucleus with a magic number to compare to a less stable nucleus. The filled shell structure of a nucleus with a magic number may imply greater overlap of the wave functions of the protons and neutrons.

Suppose gravity couples differently to the energy produced by the parity violating part of the weak force. We must calculate what fraction of a nucleus's energy is stored in this form, although we will see that it is not very well defined. First of all, right-handed neutrinos do not appear to exist, so it is not just the weak force which violates parity. The model used in Ref [xxii] to calculate the total weak force energy of a nucleus is a current-current interaction. To discuss this, let us consider the Lagrangian for the interaction of the weak force with quarks and leptons. Schematically, it is $A_\mu(J_5^\mu + J^\mu)$, where J and J_5 are the weak vector and axial currents, and A is the field of the weak force. (This expression must be summed over the three types of W particles; this formula ignores the fact that the observed W and Z particles are actually linear combinations of these three fields with a fourth field.) By including both terms, we ensure that the coupling to right-handed particles cancels. The first term here is the parity violating term. However, if we use a contact interaction, taking into account the large mass of the W particles, we find an interaction of the form $L_{eff} = (J_\mu + J_\mu^5)(J^\mu + J^{5\mu})$. Multiplying this out, we get four terms—only the terms coupling the axial current to the vector current seem to violate parity in this description of the weak force. Another difficulty is that the separate vector and axial currents are not actually well defined if right-handed neutrinos do not exist.

Since the parity conserving parts of L_{eff} contribute one part in 10^8 to the mass of a nucleus, current limits imply that gravity's coupling to these terms must differ by less than 10^{-4} from its coupling to other matter. The parity violating terms of L_{eff} contribute much less to the mass of a nucleus. If $|i>$ is the state of the nucleus with weak forces neglect, then the first order perturbation of its energy due to these terms is $<i|J^\mu J_\mu^5|i>$, which vanishes by symmetry. ($|i>$ is a parity eigenstate, so the operator changes its parity, and gives a state orthogonal to $<i|$.) This ensures that the contribution of the parity violating terms is second order in perturbation theory, and therefore small enough to be unconstrained by previous experiments. However, L_{eff} is only useful for calculations. It would be strange for gravity to couple differently to the parity violating part of the weak force unless it coupled differently to $J_\mu^5 A^\mu$ in the original Lagrangian. In this case $J_\mu^5 J^{5\mu}$ would also couple differently to gravity, and this would be a much larger effect.

While we are deciding which terms of the effective Lagrangian will be considered to be parity violating, we should notice that there are other parity violating interactions involving pion exchange[xxiii,xxiv]. Ref. xxiv probably overestimated the contribution of $J_\mu J^\mu$ to the weak energy of a nucleus, because of the assumption that the nucleons are distributed independently of one another in a nucleus. In fact, protons and neutrons are generally not closer to one another than their radius of 10^{-15} m, or $(160\text{ MeV})^{-1}$ as compared to the range 1 GeV^{-1} of the weak force. Thus, the weak interaction of nucleons occurs only very rarely. The pion exchange force has a range larger than the size of a nucleon, so the assumption that nucleons are independently distributed is more accurate when considering this force.

The interaction between nucleons and pions is described by the Lagrangian

$$L_{\text{int}} = -ig_{\pi NN}\overline{N}\gamma_5\vec{\tau}\cdot\vec{\pi}N - \tfrac{i}{2}f_\pi\overline{N}(\vec{\tau}\times\vec{\pi})_3N$$

(Ref xxv) where we have used isospin notation, so that N is an isospinor of proton and neutron fields: $N=\begin{pmatrix} p \\ n \end{pmatrix}$, $\vec{\tau}$ is a vector of three Pauli matrices, and $\vec{\pi}$ is the vector of pion fields, which are usually written as $(\frac{\pi^+ + \pi^-}{\sqrt{2}}, i\frac{\pi^+ - \pi^-}{\sqrt{2}}, \pi^0)$. The first term in the Lagrangian represents pion exchange due to the strong force ($g_{\pi NN}=13.45$), the second to the weak force ($f_\pi = 4.54\times10^{-7}$). This term violates parity. We will calculate contributions to the energy of a nucleus arising from this term.

Any interaction in which a light particle like the pion is exchanged can be approximated by interaction potentials. For example, we begin with a simplified model of spin zero protons and neutrons which can exchange a neutral spin 0 pion (of mass m_π). Let the interaction Hamiltonian be $g(n^\dagger n+p^\dagger p)\pi$. Then the amplitude for pion emission is $-ig$. Let us calculate the potential acting between protons and neutrons. The Feynman diagram is:

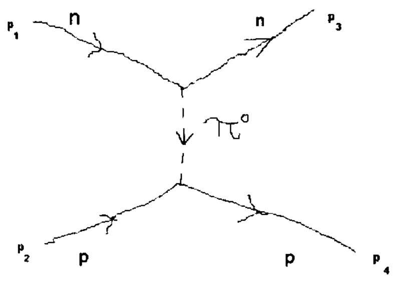

The amplitude associated with this is $A = \frac{1}{i}(-ig)^2\frac{i}{q^2 - m_\pi^2} \approx \frac{g^2}{\vec{q}^2 + m_\pi^2}$. We have omitted the time-like component of q, since this is the energy transferred between the nucleons, and is small compared to the momentum in the non-relativistic limit.

Compare this to the calculation of scattering under the influence of a potential V. Let the initial and final states be $|\psi_i> = \frac{e^{i(\vec{p}_1\cdot\vec{r}_n + p_2\cdot\vec{r}_p)}}{(2\pi)^3}$ and $|\psi_f> = \frac{e^{i(\vec{p}_3\cdot\vec{r}_n + p_4\cdot\vec{r}_p)}}{(2\pi)^3}$. In time independent perturbation theory, we solve for the coefficient $c_f = <f|T(-\infty,t)|i> \approx \int_{-\infty}^{t}<f|V|i>e^{i(E_f-E_i)t'}dt' \xrightarrow{t\to\infty} V_{fi}2\pi\delta(E_f - E_i)$.

It is not hard to check that $V_{fi} = \frac{1}{(2\pi)^3}\delta(\vec{p}_1 + \vec{p}_2 - \vec{p}_3 - \vec{p}_4)\int d^3\vec{x}V(\vec{x})e^{i\vec{q}\cdot\vec{x}}$.

The Feynman amplitude is closely related to this coefficient; however, it is calculated with the wave functions normalized so that $< p_3p_4 \,|\, p_1p_2 >= 4E_1E_2(2\pi)^3\delta(\vec{p}_1 - \vec{p}_3)\delta(\vec{p}_2 - \vec{p}_4) \approx 4m_N^{\,2}(2\pi)^6\delta(\vec{p}_1 - \vec{p}_3)\delta(\vec{p}_2 - \vec{p}_4)$. Thus we must multiply our value for c_f by $4m_N^{\,2}(2\pi)^6$. The relationship between c_f and A is thus

$$iA(2\pi)^4\delta(E_3 + E_4 - E_1 - E_2)\delta(\vec{p}_1 + \vec{p}_2 - \vec{p}_3 - \vec{p}_4) = 4m_N^{\,2}(2\pi)^6 c_f\,.$$

Therefore

$A = -4m_N^{\,2}i\int V(\vec{x})e^{i\vec{q}\cdot\vec{x}}d^3\vec{x}$, and the inverse Fourier transform of this gives V. We find that $V(\vec{x}) = \dfrac{-g^2e^{-m_\pi|\vec{x}|}}{(4m_N^{\,2})4\pi\,|\,\vec{x}\,|}$, where the transform is evaluated using spherical coordinates. This is the Yukawa potential, but it is not actually the true interaction potential of the protons and neutrons, since protons and neutrons really have spin 1/2, and have axial couplings to the pions.

Expanding the Hamiltonian given above, we find the parity conserving and parity violating pion-nucleon interactions

$$H_{PC} = ig_{\pi NN}\int d^3\vec{x}(\bar{p}\gamma_5p - \bar{n}\gamma_5n)\pi^0 + \sqrt{2}(\bar{p}\gamma_5n\pi^+ + \bar{n}\gamma_5p\pi^-)$$

and

$$H_{PV} = \tfrac{if_\pi}{\sqrt{2}}\int d^3\vec{x}\,\bar{p}n\pi^+ - \bar{n}p\pi^-\,.$$

The π's are pseudoscalar particles and $\bar{p}\gamma_5p$ and similar terms are scalars, and so it is the first of these interactions which is parity conserving. This is actually a convention, since if the second interaction had been discovered first, the pions would have been called scalar particles. A consequence is that an interaction between nucleons by exchange of pions is equivalent to a parity conserving potential as long as both pion-nucleon vertices are governed by the same interaction. If the pion is emitted according to the parity conserving interaction and absorbed according to the parity violating interaction, then the equivalent potential distinguishes between left and right. We call the three potentials

$V_{PCPC}, V_{PVPV}, V_{PVPC}$, where the subscripts indicate the nature of the pion exchanges (parity violating or parity conserving).

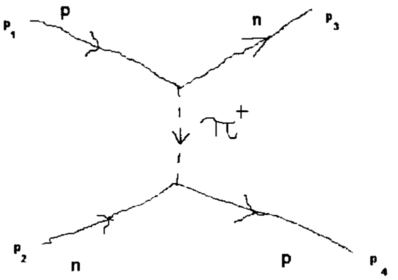

Since the PVPV interaction is mediated only by charged pions, the only possible interaction is the above. The proton turns into a neutron when it emits the π^+ in order to conserve charge. The calculation of the potential associated with this interaction is very similar to the calculation above for the simplified model. There are two differences. First, the extra factors proportional to the mass which arise from normalization conventions do not occur for spinors. Second, since the proton and neutron have two spin states, we must determine how the interactions affect their spins. Since the pions are spinless, a nucleon's spin does not flip when it emits a pion. Thus if the proton initially has spin up and the neutron is spin down, then the scattered proton has spin down and the scattered neutron has spin up. The effective potential for this interaction is

$V(\vec{r}_1 - \vec{r}_2) = \frac{f_\pi^2}{2} \frac{e^{-m_\pi |\vec{r}_1 - \vec{r}_2|}}{4\pi |\vec{r}_1 - \vec{r}_2|} X$, where X is an operator which turns protons into neutrons and neutrons into protons.

Since particles can change types, we will use second quantization. The operator $n_\uparrow^+(\vec{r}_1)p_\uparrow(\vec{r}_1) + n_\downarrow^+(\vec{r}_1)p_\downarrow(\vec{r}_1)$ turns a proton at point r_1 into a neutron at the same point with the same spin. So the operator X is equal to $[\, p_\uparrow^+(\vec{r}_1)n_\uparrow(\vec{r}_1) + p_\downarrow^+(\vec{r}_1)n_\downarrow(\vec{r}_1)\,][n_\uparrow^+(\vec{r}_2)p_\uparrow(\vec{r}_2) + n_\downarrow^+(\vec{r}_2)p_\downarrow(\vec{r}_2)\,]$.

The interaction Hamiltonian is therefore

$$H_{PVPV} = -\iint d^3\vec{r}_1 d^3\vec{r}_2 \, \tfrac{f_\pi^2}{8\pi} \frac{e^{-m_\pi |\vec{r}_1 - \vec{r}_2|}}{|\vec{r}_1 - \vec{r}_2|} [\, p_\uparrow^+(\vec{r}_1)n_\uparrow(\vec{r}_1) + p_\downarrow^+(\vec{r}_1)n_\downarrow(\vec{r}_1)\,][n_\uparrow^+(\vec{r}_2)p_\uparrow(\vec{r}_2) + n_\downarrow^+(\vec{r}_2)p_\downarrow(\vec{r}_2)\,].$$

This interaction does not seem to mediate a force between two separated nucleons, since the nucleons can't retain their identity. In particular, it cannot mediate a force between two separate nuclei, even though it does contribute to the binding energy of a single nucleus. Suppose the nucleus can be modeled as consisting of two Fermi seas, one of protons and one of neutrons. (Of course H_{PCPC}, which is much larger than any parity violating interactions, produces correlations in nuclei.) There are protons of both spins and of every momentum less than k_p, and there are neutrons up to k_n. We will assume the nucleus is very large so that we can approximate the waves by plane waves, and we will calculate the energy density due to H_{PVPV}. Then since the proton and neutron which interact are in the same nucleus, the interaction does not change the nucleus type.

The energy shift is <i| H_{PVPV} |i>. Consider the action of H_{PVPV} on the Fermi sea. It acts on two particles—a proton of momentum $\vec{k}_1$ and a neutron of momentum $\vec{k}_2$, changing their momentum and interchanging their particle types. Since the resulting state is multiplied by <i|, it must have the same occupied states as |i> in order to give a nonzero contribution to the energy. Thus the final proton must have the same momentum as the initial proton, as in the following diagram:

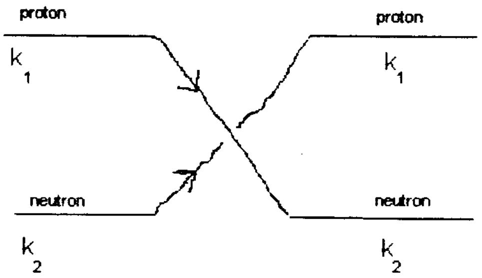

Also, the particles must have the same spin, since the interaction does not flip spin.

In order to see at least one failure of our approximations, we consider two general wave functions for a proton and neutron and calculate their interaction in these states. We ignore the spin wave function, and set

$$|\psi>=\frac{1}{\sqrt{2}}(f_1(\vec{r}_1)f_2(\vec{r}_2)\,|\,pn> - f_2(\vec{r}_1)f_1(\vec{r}_2)\,|\,np>).$$

The wave function here is antisymmetric in space and isospin, according to the Pauli exclusion principle for multiple types of fermions. Thus neither $\vec{r}_1$ nor $\vec{r}_2$ is the coordinate of the proton. But f_1 must be the wave function of the proton. Assuming both spins are up,

$$\begin{aligned}H_{PVPV}\,|\psi>&=-\frac{f_\pi^{\,2}}{2\sqrt{2}}\iint V(\vec{x}_1-\vec{x}_2)d^3\vec{x}_1 d^3\vec{x}_2\, p_\uparrow^+(\vec{x}_1)n_\uparrow(\vec{x}_1)n_\uparrow^+(\vec{x}_2)p_\uparrow(\vec{x}_2)[f_1(\vec{r}_1)f_2(\vec{r}_2)\,|\,pn> - f_2(\vec{r}_1)f_1(\vec{r}_2)\,|\,np>]\\ &=-\frac{f_\pi^{\,2}}{2\sqrt{2}}[V(\vec{r}_2-\vec{r}_1)f_1(\vec{r}_1)f_2(\vec{r}_2)\,|\,np> - V(\vec{r}_1-\vec{r}_2)f_2(\vec{r}_1)f_1(\vec{r}_2)\,|\,pn>].\end{aligned}$$

In evaluating the integrals, we must choose $\vec{x}_1$ and $\vec{x}_2$ to coincide with $\vec{r}_1$ and $\vec{r}_2$ in one order, so that $\vec{x}_1$ represents the location of the initial neutron. Now, noticing that <pn|pn>=<np|np>=1 while <pn|np>=<np|pn>=0, we obtain

$$\begin{aligned}<\psi\,|\,H_{PVPV}\,|\psi>&=\frac{f_\pi^{\,2}}{4}\iint d^3\vec{r}_1 d^3\vec{r}_2\, V(\vec{r}_1-\vec{r}_2)[f_1(\vec{r}_1)^* f_2(\vec{r}_2)^* f_2(\vec{r}_1)f_1(\vec{r}_2)+f_2(\vec{r}_1)^* f_1(\vec{r}_2)^* f_1(\vec{r}_1)f_2(\vec{r}_2)]\\ &=\frac{f_\pi^{\,2}}{2}\iint d^3\vec{r}_1 d^3\vec{r}_2\, V(\vec{r}_1-\vec{r}_2)f_1(\vec{r}_1)^* f_2(\vec{r}_1)f_1(\vec{r}_2)f_2(\vec{r}_1)^*,\end{aligned}$$

where the two terms can be combined by exchanging $\vec{r}_1$ and $\vec{r}_2$ in the second term.

This has the form of an exchange force—notice that if f_1 and f_2 are never nonzero at the same point, then the integrand vanishes. This is why we claimed above that the shell structure might affect the parity violating energy; a simple form with plane wave states ignores all the structure of the nucleus.

In order to find the total energy, we must sum over all occupied proton and neutron states f_1 and f_2 respectively. There is also a self-interaction due to H_{PVPV} in which a nucleon changes type and then changes back. This gives an infinite contribution to the energy, and is also more significant because a particle is certain to be at the same location as itself, so the comment about overlap at the end of the last paragraph doesn't apply. We will discuss self-energy contributions at the end.

Substituting $V(\vec{r}_1-\vec{r}_2)=\frac{1}{4\pi}\frac{e^{-m_\pi|\vec{r}_1-\vec{r}_2|}}{|\vec{r}_1-\vec{r}_2|}$ and plane waves which are normalized so that their integral over the volume V of the nucleus is 1, we obtain an energy proportional to the Fourier transform of the Yukawa potential. It is equal to

$<H_{PVPV}>=\frac{f_\pi^{\;2}}{2V}\frac{1}{m_\pi^{\;2}+|\vec{k}_1-\vec{k}_2|^2}$, and the sum over all pairs of nucleons is

$$\delta E_{PV}=2\frac{f_\pi^{\;2}}{2V}\sum_{|\vec{k}_1|<k_p}\sum_{|\vec{k}_2|<k_n}\frac{1}{m_\pi^{\;2}+|\vec{k}_1-\vec{k}_2|^2}$$

where the factor of 2 arises because the proton and neutron can be both spin up or both spin down. Converting the sum to an integral in the usual way, we obtain

$$\delta E_{PV}=\frac{f_\pi^{\;2}}{V}\left(\frac{V}{(2\pi)^3}\right)^2\int\int_{|\vec{k}_1|<k_p,|\vec{k}_2|<k_n}\frac{d^3\vec{k}_1d^3\vec{k}_2}{m_\pi^{\;2}+|\vec{k}_1-\vec{k}_2|^2}\,.$$

First integrate over $\vec{k}_2$, taking the z-axis along $\vec{k}_1$.

$$\begin{aligned}\int d^3\vec{k}_2\frac{1}{m_\pi^{\;2}+|\vec{k}_1-\vec{k}_2|^2}&=2\pi\int_0^{k_n}k_2^{\;2}dk_2\int_0^{\pi}\frac{\sin\theta d\theta}{m_\pi^{\;2}+k_1^{\;2}+k_2^{\;2}-2k_1k_2\cos\theta}\\&=2\pi\int_0^{k_n}k_2^{\;2}dk_2\frac{\ln(m_\pi^{\;2}+k_1^{\;2}+k_2^{\;2}-2k_1k_2\cos\theta)}{2k_1k_2}\Big|_0^{\pi}\\&=\pi\int_0^{k_n}\frac{k_2}{k_1}dk_2\ln\left(\frac{m_\pi^{\;2}+(k_1+k_2)^2}{m_\pi^{\;2}+(k_1-k_2)^2}\right)\end{aligned}$$

We now integrate over the direction of $\bar{k}_1$, giving a factor of 4π, and then give the expression for the integral:

$$\begin{aligned}\frac{\delta E_{PV}}{V} &= \frac{f_\pi^2}{16\pi^4}\int_0^{k_p}\int_0^{k_n} dk_2 dk_1 k_1 k_2 \ln\left(\frac{m_\pi^2+(k_1+k_2)^2}{m_\pi^2+(k_1-k_2)^2}\right) \\ &= \frac{f_\pi^2}{16\pi^4}\{[-\tfrac{1}{8}(k_p^2-k_n^2)^2+\tfrac{1}{4}m_\pi^2(k_p^2+k_n^2)+\frac{m_\pi^4}{24}]\ln\left(\frac{m_\pi^2+(k_1+k_2)^2}{m_\pi^2+(k_1-k_2)^2}\right) \qquad (44) \\ &\quad -\frac{2m_\pi}{3}(k_p^3+k_n^3)\arctan\frac{k_p+k_n}{m_\pi}+\frac{2m_\pi}{3}(k_p^3-k_n^3)\arctan\frac{k_p-k_n}{m_\pi} \\ &\quad -\frac{m_\pi^2 k_p k_n}{6}+\tfrac{1}{2}k_p k_n(k_p^2+k_n^2)\}\end{aligned}$$

The integral is evaluated by repeated integrations by parts.

We would now like to evaluate this expression as a function of x = Z/A. The volume of a nucleus is proportional to A; that is, each nucleon occupies a fixed volume. The volume is given by $\frac{4}{3}\pi r_0^3 A$ where r_0 =1.2 fm[xxv]. As usual, the Fermi momenta are given by $k_p=(3\pi^2 n_p)^{1/3}$ where n_p is the proton number density, so $k_p=\frac{1}{r_0}\sqrt[3]{\frac{9\pi}{4}x}=320\sqrt[3]{x}\,MeV$ and similarly $k_n=320\sqrt[3]{1-x}\,MeV$. Furthermore, the mass of a nucleus is roughly Am_N, so

$\frac{\delta E_{PV}}{M}=\frac{V}{Am_N}\frac{\delta E_{PV}}{V}=\frac{\frac{4}{3}\pi r_0^3}{m_N}\frac{\delta E_{PV}}{V}=(1.0\times10^{-9}MeV^{-4})\frac{\delta E_{PV}}{V}$. (Notice that our estimates, for x = 1/2, give a Fermi momentum of 250 MeV, which is somewhat small compared to the nucleon mass, so our nonrelativistic approximations (in particular, neglecting the time-like component of q in the derivation of the effective interaction) seem reasonable.)

The following figure shows $\frac{\delta E_{PV}}{M}$ as a function of x; it is on the order of 10^{-16} and is almost exactly equal to $\frac{\delta E_{PV}}{M}=9x(1-x)\times10^{-16}$, which is much easier to interpret than the formula given above; for a contact force, the number of interactions occurring in the nucleus is proportional to the product of the densities, which is proportional to x(1-x). (The suggested derivation of this formula—assume the mass of the pion is very large and replace the interaction by a contact interaction—gives an incorrect answer, $30x(1-x)\times10^{-16}$. The mass of the pion is not large enough to regard V_{PV} as a contact interaction.)

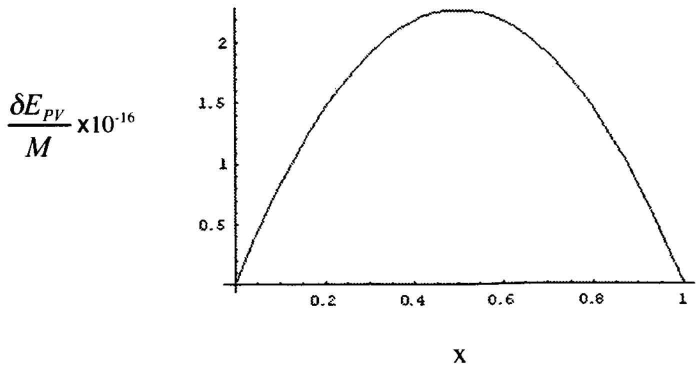

The fraction we have just calculated is very small, and (since we can only compare different nuclei) its variation from nucleus to nucleus is even less--2x10^{-17}, if x varies from 1/2 to 1/3. There are similar smooth empirical formulae for the total mass of a nucleus, but the mass differences are somewhat larger from nucleus to nucleus because the mass depends in a more jagged way on the atomic number. Thus, the plane wave description of the protons and neutrons cannot suggest which nuclei have unusually large or unusually small contributions from the weak force. There are many other contributions to the parity violating energy as well—for example, the interaction V_{PCPV} produces an energy shift at second order in perturbation theory. This can occur only at second order because $<i| V_{PCPV}|i>$ vanishes—after all, $|i>$ is a parity eigenstate since the strong forces which determine the structure of the unperturbed nucleus are parity conserving. However, by introducing an intermediate state of opposite parity and very similar energy, one can hope to obtain the largest possible weak parity violating contribution to the energy. For ^{19}F, Ref [xxvi] estimates $\frac{\delta E_{PV}}{M}$=7x10^{-17}, which is very similar to what we obtained above. Ref. xxvi did not calculate the matrix elements from the theoretical formula for V_{PCPV} but from an experiment mentioned in Ref xxv. The latter reference also calculated the matrix element from a theory based on exchange of pions and other particles, giving a value which was off by only 20%.)

Ref xxvi's calculation did not take the direct exchange of single pions in which both the emitted and absorbed pion have parity violating interactions, leading to an impression that only nuclei with narrowly separated partners of opposite parity have large values of $\frac{\delta E_{PV}}{M}$. However it leads to a very clear case in which one expects a jump in the parity violating energy—choose a nucleus $|i>$ which is close in energy to another nucleus $|i'>$ with the opposite parity. Fluorine is not the only choice. If one were to calculate the matrix element of V_{PCPV} between these states theoretically (the calculation would be similar to the above), one would find that $< i' \mid V_{PCPV} \mid i > \propto volume \propto M$. Thus,

$\frac{\delta E_{PV}}{M} = \frac{1}{M}\frac{|< i' \mid V_{PCPV} \mid i >|^2}{M_i - M_{i'}} \propto \frac{M}{M_i - M_{i'}}$, where the denominator here is just the energy denominator (with energy replaced by mass). (M is either of the two masses.) So we expect an especially large parity violating energy if the mass difference of the nucleus and its excited state is small compared to the mass of the nucleus.

Finally, Ref. [xxvii] calculates the weak-force self-energy of a proton or neutron and finds that its fractional contribution to the mass of a nucleus is 10 times larger than the energy from the interactions of different protons and neutrons in the nucleus calculated in Ref. xxiv. Most likely, the parity violating self-energy of the protons and neutrons is more significant than anything we have already calculated. This returns to one of the most obvious models for equivalence principle violations—assume that gravity couples differently to protons and neutrons. This gives gravitational mass differences which are linear in x (just as we found in the model of a long range force coupled to the total number of baryons in a nucleus). So a simple approach is to choose nuclei with the largest and smallest possible values of x. (Hydrogen and Uranium are suggested in Ref. [xxviii]!)

There are three reasons why it is unlikely that gravity couples differently to the "parity violating part of the weak force." First, this depends on whether one uses the fundamental Lagrangian or the current-current Lagrangian as discussed above. In practice, the definition of the parity violating and parity conserving energies is very technical—a summary of the definition we used is "it is the part of the weak force which is second order in perturbation theory." Second, in the electroweak theory, photons are linear combinations of a W particle and another gauge particle, so if gravity couples differently to the W particles, it probably couples differently to the photon as well. Third, all self-energies are infinite in any case. This is why the self-energy of the protons and neutrons calculated in Ref. xxix is much larger than the energies of the nuclei calculated in Ref. xxiv. The interactions of the quarks inside the protons and neutrons are larger than the interaction energies of different protons and neutrons because the quarks are closer together. If the quarks are point particles, then they contribute infinite self-energies due to the weak force besides these other energies. Fourth, energy cannot be separated into different forms of energies. For example, the energy we calculated above includes the mass of the virtual pions, which is due to the strong force.

Addendum to Theoretical Impact Analysis

In two recent papers[xxix] [xxx], Damour et al., provide a theoretical justification, based on the string theory for expecting violations of the Equivalence Principle at an accuracy above one part in 10^{-12} which is slightly below the present state of the art in EP tests. Their argument centers on the inflationary rate of expansion of the early universe and on the decoupling of scalar fields from matter during the expansion of the universe. When the recent estimates of the early expansion rates are factored into the theory, they conclude that violations of the EP may well occur at accuracy much lower than previously thought.

The conclusion of the analysis by Damour et al. gives strength to EP experiments with improved accuracy even if the improvement is not as dramatic as those promised by the space-based tests (of several orders of magnitude) of the EP. Another implication is that our goal should not be to push the accuracy as high as possible (and consequently increase the difficulty and cost of the experiment) but rather achieve a significant improvement in accuracy with respect to the present state of the art.

CAPSULE/CRYOSTAT DESIGN APPROACH

Introductory Remarks

During the early conceptual development of this experiment, we were focusing our attention mostly on free-fall spans of a few meters to achieve free-fall time as long as possible. This situation, however, precluded the use of a fully cryogenic capsule because of mass considerations and pushed us towards the adoption of a small cryostat at the top of the vacuum chamber to refrigerate the instrument before release. However, the small cryostat creates additional problems which are highlighted by the previous analyses as follows: (1) the small cryostat is a concentrated mass placed very close to the detector and, cosequently, produces relatively strong gravity gradients; and (2) the instrument package spends most of the free-fall time in the vicinity of the small cryostat and moves away from the small cryostat only in the later portion of the fall.

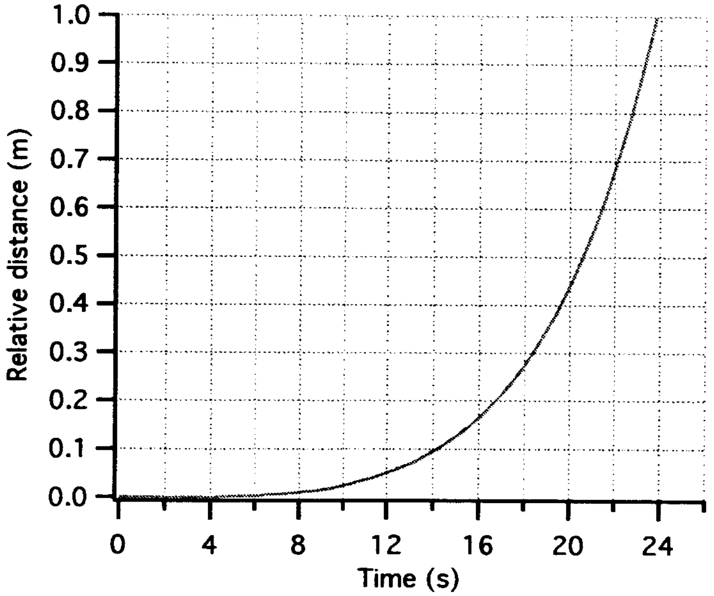

Figure 34 Vertical motion of package relative to capsule for $\beta_0 = 7000$ kg//m^3 (shown for distances < 1 m)

Figure 34 shows clearly that the relative distance between the instrument package and the capsule (for a typical $\beta_0 = 7000$ kg/m^2) is less than 10 cm during the first 14 s, increases to about 1 m at the 24 s mark and becomes greater than 3 m at the 30 s mark (not shown in the figure). In other words, the small cryostat can not be small because it needs to be moved farther away for reducing the self-generated gravity gradients and also for allowing for lateral motions of the capsule with respect to the falling package. The free fall time (once several seconds are spent in attenuating the initial transient motion of the sensing masses after release) affects the experiment accuracy only through its square root (i.e., a weak function). Consequently, it is sensible to sacrifice a few seconds of free-fall time in order to make the experimental area sufficiently short to open up the option of a fully cryogenic vacuum chamber for the detector to fall in.

These considerations are formalized in the next section by developing an optimization process aimed at identifying the size and mass of the experimental chamber and the capsule.

Optimization of Capsule Size and Mass

A design optimization would appear premature at this point of the flight definition study. This optimization process, however, is aimed exclusively at evaluating in a consistent way the size of the capsule and its overall mass. The goal of the optimization process is to devise a mathematical formulation for evaluating capsule sizes and masses that satisfy: (1) geometrical/dynamical constraints and (2) engineering constraints. The first category includes the constraints determined by the strength of the gravity gradient inside the vacuum chamber (generated by the capsule mass itself) and related to the motion of the instrument package with respect to the capsule during free fall. The second category includes size constraint due to transportability and handling of the capsule and also minimum and maximum allowable mass. The minimum mass is determined by the ability of building a vacuum chamber that does not buckle under the atmospheric pressure while the maximum mass is limited by the carrying capacity of the balloon.

The independent variables to work with (as it will become clearer in the following) are the (frontal) low-speed ballistic coefficient of the capsule and the free-fall time. The output variables are the capsule diameter and related capsule length, free-fall span, cryostat mass, and capsule mass.

In more detail, we first need an expression of the free-fall span of the package inside the capsule as a function of the ballistic coefficient β_0 and the free-fall time T_f. The free-fall distances were derived numerically because the relevant functions are not integrable. Consequently, we have to fit the numerically-derived function over the two parameter space (β_0, T_f). The fitting was done successfully over the range of interest of the parameters by starting from the analytical formulation that approximates the solution for a constant ballistic coefficient and then evaluating the fitting coefficients for the general case with variable C_D. The two-parameter fitting process yields:

$$z_f = aT_f^{\,b}\exp(cT_f^{\,2})/\beta_0 \tag{45}$$

where a = 0.149636, b = 3.084, and c = 0.001692 are the fitting parameters. The results are accurate within a few percent for ballistic coefficients varying from 2000 kg/m^2 to 20000 kg/m^2 and free-fall times from 0 to 30 s.

The free fall vertical distance readily determines the minimum length of the experimental chamber which must at least equal the free-fall span plus the vertical size (outer diameter) of the instrument package, that is:

$$L_{min} = \eta z_f + D \tag{46}$$

where D is the outer diameter of the instrument package and η is a safety coefficient (typically equal to 1.5) that takes into account the uncertainties in estimating the drag deceleration due to the rarefied atmosphere.

The next step is to evaluate the minimum internal diameter of the chamber/cryostat that can accommodate the lateral and attitude dynamic of the capsule and also provide low values of the gravity gradients along the free-fall trajectory. In order to keep the equations manageable we adopt for this analysis the constant stand-off distances which were derived previously and boundary values for the capsule attitude dynamics, rather than using an (on-line) numerical computations of the gravity-gradient field as a function of the capsule position (as done in the previous section). The goal is to compute a minimum value of the internal diameter and external diameter (where the two are related through the cryostat thickness) that keep the free-falling package close to the capsule center-line (far away from the cryostat walls) under the action of a maximum wind shear and for reasonable assumptions about the capsule attitude (pitch or roll) dynamics during the fall. The point above can be translated into the following equation for the external capsule diameter:

$$D_{\min}^{ext} = 2\left(y_{pitch} + y_{shear} + y_{gg} + y_{cryo}\right) \tag{47}$$

$y_{pitch} = z_f \sin(\theta_{max})$ where z_f is given by eqn. (45) and θ_{max} can be interpreted as either a limit value of the maximum pitch motion of an uncontrolled capsule or a requirement imposed on the control system of the capsule attitude during the fall. The lateral displacement due to wind shear $y_{shear} = f(\beta_0, T_f)$ is given by eqn. (10) while y_{cryo} is the thickness of the cryostat wall of 10-15 cm (i.e., typical values for large-size helium cryostats). The stand-off distance y_{gg} is the upper bound of the minimum distance between the detector CM and the heavy walls of the cryostat that defines an area (cylindrical and centered at the cryostat center-line) where the gravity gradients generated by the cryostat are sufficiently low. An upper bound of 0.4 m can be adopted across a variety of cylindrical cryostats for sizes and masses of interest to this project.

One obvious consideration is that the internal diameter must be large enough to contain the instrument package. This constraint, however, is already accounted for by the fact that $2y_{gg} > w_P$ where w_P is the width of the instrument package that is presently estimated at about 40 cm. The overall length of the capsule is related to the external diameter through the fineness ratio that, as explained previously, needs to be about 1:4 in order to keep low the value of the drag coefficient, especially in the compressible flow regime.

The next step is to estimate the minimum mass required for the cryostat. Most of the cryostat mass is for the metal of the vacuum chamber that has to withstand the external atmospheric pressure (at ground level). From engineering formulas for the buckling of cylindrical vacuum chambers we obtain that the critical thickness of the vacuum chamber walls (at buckling) is given by:

$$\frac{s_{crit}}{R} = \left[\frac{p_c(L/R)}{0.92E}\right]^{\frac{1}{2.5}} \tag{48}$$

where R and L are the radius and length of the vacuum chamber, s_{crit} is the (minimum) thickness of the load-bearing shell, E is the Young's modulus of the material and p_e the external pressure. The cryostat length is readily computed as:

$$L = \eta z_{ff} + 2y_{gg} \tag{49}$$

The minimum cryostat mass is then computed as follows:

$$M_{cryo}^{\min} = \nu s_{crit} \pi \rho D(D/k + L) \tag{50}$$

where ρ is the density of the material, D the cryostat average diameter, ν is a load safety factor and k is a shape factor that is equal 2 for flat cryostat caps and 1 for hemispherical caps. After adopting $\nu = 3$ and using eqn. (48) to compute the thickness, we find that eqn. (50) provides masses which are in line with actual values of large cryostats (as verified with Janis Research). Since the cryostat is the heaviest component of the capsule, we can estimate the overall (minimum) mass M_{crit} of the capsule as a proportion of the cryostat mass $M = \gamma M_{cryo}$.

The actual mass of the capsule M, however, is defined by the ballistic coefficient β_0 once the external diameter of the capsule is determined as follows:

$$M = \beta_0 C_{D0} A \tag{51}$$

where A is the frontal area of the capsule computed through eqn. (47).

Consequently, we must verify that $M > M_{crit}$. If the inequality is true we can simply add ballast to the capsule in order to preserve the values of the geometrical variables and meet the actual mass requirement. In this case, the vacuum chamber of the ballasted capsule will satisfy the strength requirements captured by eqn. (48). If the inequality is violated, the total mass determined by the ballistic coefficient is too small to build a cryostat that is strong enough to withstand the atmospheric pressure. The violation of this inequality will be dealt with in the optimization process as a (strong) penalty on the cost function as explained later on.

Figure 35 shows an example of a contour plot of two of the key output variables, that is, the capsule mass and the capsule external diameter vs. the low-speed ballistic coefficient and the free-fall time for realistic values of parameters.

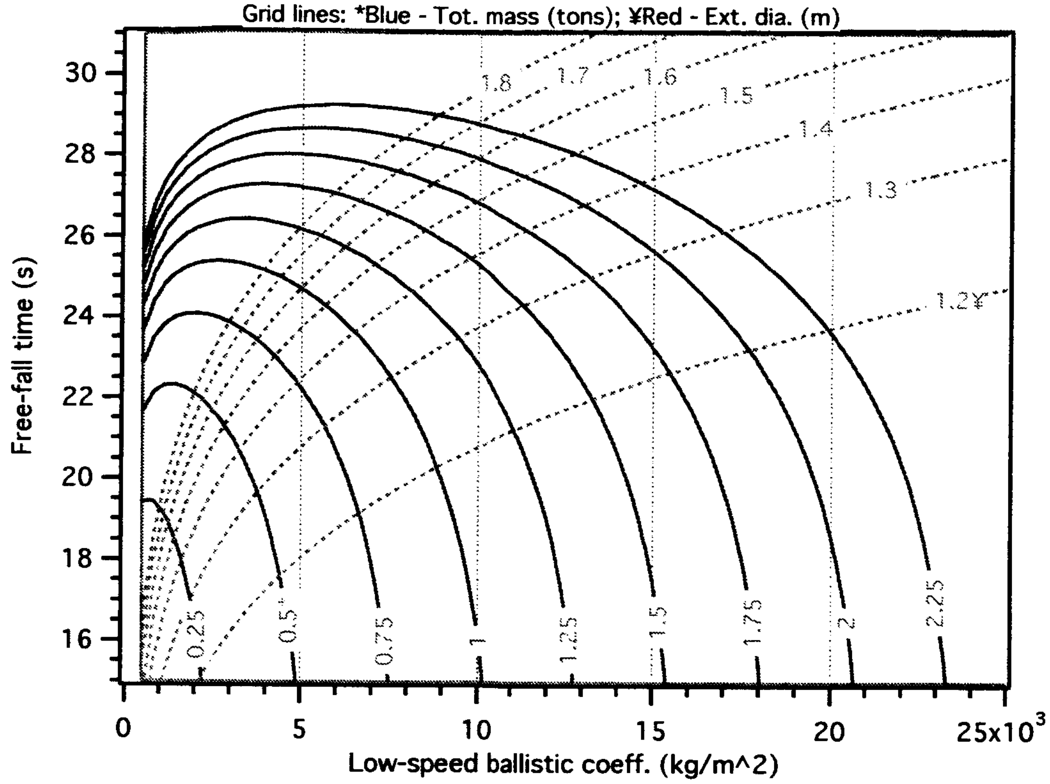

Figure 35 Contour plot with grid lines showing capsule mass and external diameter vs. low-speed ballistic coefficient and free-fall time.

The goal of the optimization process is to define the size and mass of the capsule that minimize the value of a cost function. The cost function consists of the overall capsule mass, the capsule diameter (which is related to the overall capsule length), and the free-fall time. The cost function for this optimization problem can be expressed (and the choice is not uniquely defined) as follows:

$$CF = \frac{a_1 M + a_2 D_{ext}}{\sqrt{t_f - t_{\min}}} + P_M + P_D \qquad with\ t_f \neq t_{\min} \tag{52}$$

where M and D_{ext} are the overall mass and external diameter of the capsule, z_f is the free-fall span inside the capsule (which defines the cryostat length), t_{min} the minimum desired free-fall time, t_f the free-fall time, a_1 and a_2 are weighting coefficients and P_M and P_D are penalty functions. P_M is the penalty function for the total mass and P_D for the external diameter.

The structure of the cost function is readily understood after considering that the experiment accuracy depends on the square root of the integration time. The minimum free-fall time has to include the time required to damp initial transients (a few seconds) and also a minimum number of cycles needed for a reliable extraction of the signal from noise. The weight coefficients adjust the relevant weights of the two quantities at the numerator by making them comparable and/or making one component more important than the other one. By adopting meters for the units of length and metric tons for the units of mass, the two weighting coefficients have the same order of magnitude.

Going back to the penalty functions, obviously the overall mass of the capsule must be greater than the minimum (or critical) mass M_{crit} determined previously and smaller than the maximum mass M_{max} than a reasonable size balloon can carry to an altitude of 40 km. Note that M_{max} is a fixed value while the critical mass depends upon the optimization parameters.

In a similar manner, the external diameter (which also determines the overall length of the capsule according to $L_c = D_{ext}/\delta$) must be large enough to accommodate the instrument package plus the cryostat walls (i.e., larger than D_{min}) and smaller than a maximum value D_{max}. In this case both values are fixed and moreover the first inequality (larger than) is superseded by eqn. (47) if $2y_{gg} > w_P$.

The penalty functions are bowl-shaped functions which are equal to zero for values within the two boundaries of the inequality and whose value rapidly increases as the input variable approaches the boundary values. Figure 36 shows the mass penalty function for two values of M_{crit} = 0.3 ton and 1.0 ton, respectively, and M_{max} = 2.2 tons. The maximum value of the penalty function is quite arbitrary. The value simply needs to be substantially greater than the expected range of values of the first term that appears on the right hand side of the cost function in eqn. (52).

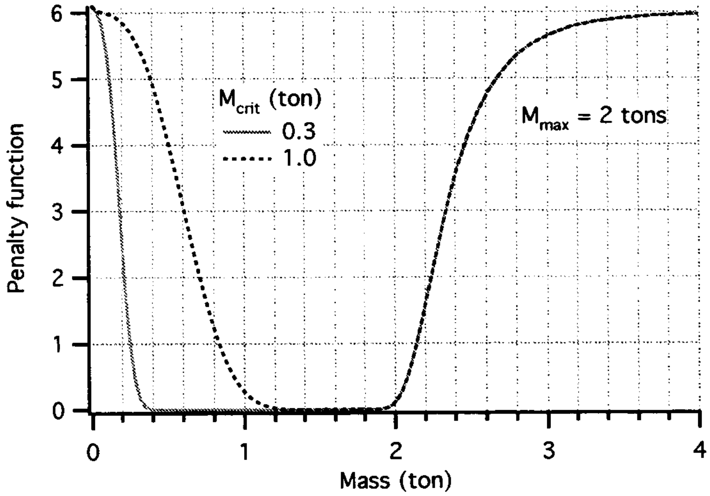

Figure 36 Example of mass penalty function with M_{crit} = 0.3 ton and 1.0 ton, and M_{max} = 2.2 ton.

A similar penalty function with fixed-valued left and right boundaries was derived to penalize the external diameter of the capsule. Without going into excessive details, the penalty functions are obtained from a pair of exponential functions with a set of parameters and power exponents that shapes the function appropriately.

Optimization Results

The optimization routine has been exercised on a large number of cases in order to inspect the influence of any given input parameter on the output/design parameters and the cost function. In the following we will show only the most important results relevant to: (a) a cryostat made of Aluminum and (b) a cryostat made of Steel. The numerical parameters adopted for computing the results shown in Figure 37 and Figure 38 are as follows: instrument package width $w_P = 40$ cm; low-speed drag coefficient of the capsule $C_{D0} = 0.1$; fineness ratio of the capsule $\delta = 0.25$; wind shear = 0.005 m-s^{-1}/m; wall thickness of cryostat = 15 cm; stand-off distance for reducing gravity gradients $y_{gg} = 40$ cm; uncertainty factor on drag deceleration $\eta = 1.5$; strength safety factor for vacuum chamber $\nu = 3$; mass ratio capsule-mass/cryostat-mass $\gamma = 2$; density of material $\rho = 2800$ kg/m^3 (Aluminum) and 7800 kg/m^3 (Steel); Young's modulus E = 80 GPa (Aluminum) and 200 GPa (Steel). Moreover, the maximum capsule mass for a mass penalty in the cost function is equal to $M_{max} = 2200$ kg. The maximum external diameter of the capsule for a penalty is $D_{max} = 2.2$ m (which implies a maximum capsule length of 8.8 m). The weight coefficients have been as follows: $a_1 = 1$ (mass) and $a_2 = 1.5$ (external diameter) in which masses are expressed in metric tons and diameters in meters. More weight has been given to the diameter rather than to the total mass because, as it will be seen later on, there is a fairly large mass margin (large balloons can carry a few tons) while a large external diameter leads to long capsules that are difficult to handle and transport.

The value of the cost function is shown as black contour lines in Figure 37 and Figure 38 and the contour regions are colored with the deep blue color corresponding to the minimum of the cost function. The grid lines of the free-fall span are also added to the figures in green color. The figures provide a host of useful information as the grid lines specify the values of key variables such as capsule mass, external diameter, and free-fall span (of the instrument package inside the capsule) for any point identified by the coordinates β_0 and t_f. The equations shown previously enable us to compute readily other key design parameters: the cryostat length L from eqn. (49) and its mass by dividing the capsule mass by γ.

Figure 37 shows the results for a cryostat made of Aluminum and Figure 38 for a Steel cryostat. The cost function identifies the area on which to focus the selection of the key design parameters. In the (desirable) deep blue area (inside the smaller circular contour lines) the cost function is rather shallow and, consequently, the region for selecting the design parameters is reasonably large. In the dark color region, one of the mass or geometrical constraints has been violated and consequently the penalty functions bound the *design area*. Note that the maximum capsule mass limits the *design area* on the right-hand side of the plots while the (critical) cryostat mass and the maximum external diameter of the capsule limit the *design area* on the left side of the plots. In the Steel-cryostat case the (critical) cryostat mass is the leading boundary condition on the left side of the *design area*. In the lower side of the plot, the *design area* is limited by the minimum free fall time that has been set equal to 15 s in order to allow for a reasonable numbers of signal cycles.

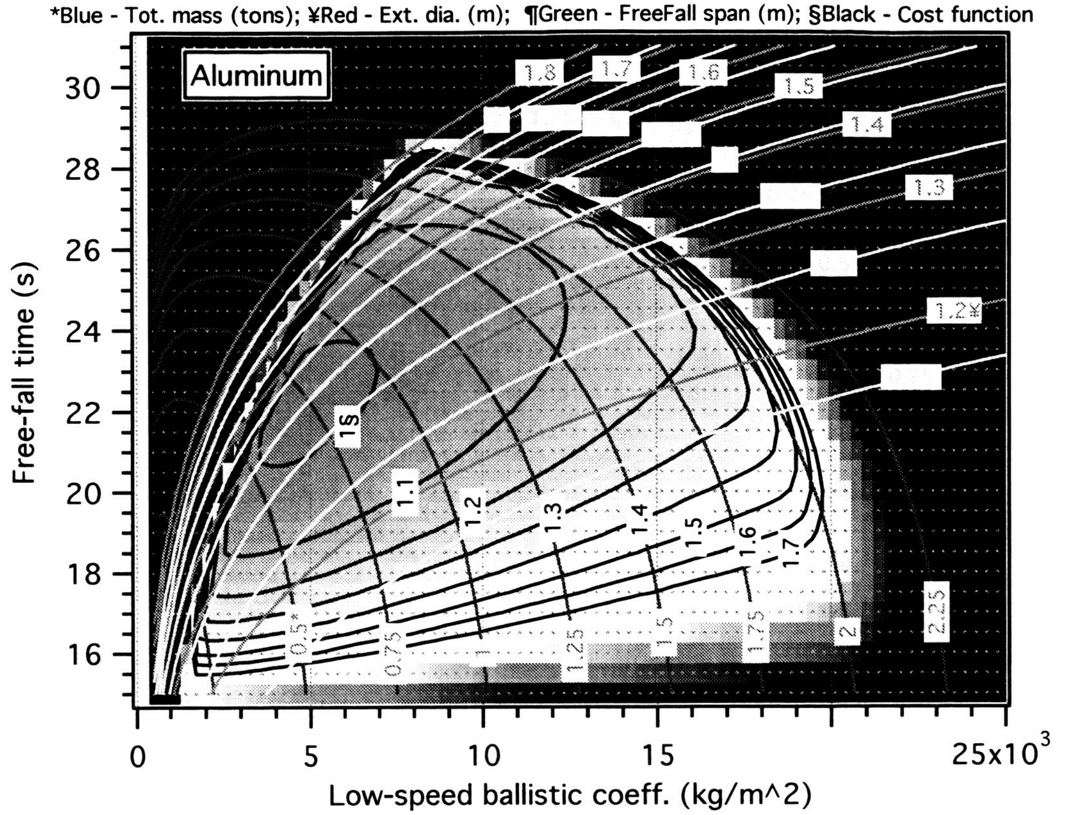

Figure 37 Cost function in the capsule parameter space (Aluminum cryostat)

The figures show that an external diameter in the neighborhood of 1.4 m is a valid selection for the capsule based on the assumptions of this analysis. The 1.4-m diameter contour line cuts across the region of the minimum value of the cost function. Furthermore, the minimum-value region is larger for an Aluminum cryostat than for a Steel cryostat because in the latter case the boundary of the minimum (and critical) cryostat mass encroaches into the low-valued area of the cost function. Consequently, Aluminum is preferable to Steel, from this analysis point of view, as it allows wider margins to work with in the capsule design. However, Steel is also a valid choice and it might be preferable to Aluminum for the vacuum chamber because of the low outgassing. After focusing on Figure 37, an "optimal" design choice could be an external capsule diameter of 1.4 m (with an overall capsule length of 5.6 m). The overall capsule mass could start at a minimum value of about a 1000 kg which provides a free fall time of 23.5 s. Note from the figures that the free-fall span contour line is about parallel to the 1.4-m external diameter line. This situation implies that we could move the design point along those two lines by increasing (with ballast) the capsule mass and increasing the free-fall time. Consequently, a cryostat of given length can provide longer free fall times by simply making the capsule heavier with ballast. The free-fall time can be increased by 1 s for every 250-kg ballast (or other equipment) added to the capsule up to the point where the upper mass limit is reached. The low-speed ballistic coefficient β_0 of the capsule will vary from about 6500 kg/m^2 for a capsule mass = 1000 kg to 13,000 kg/m^2 for a capsule mass of 2000 kg.

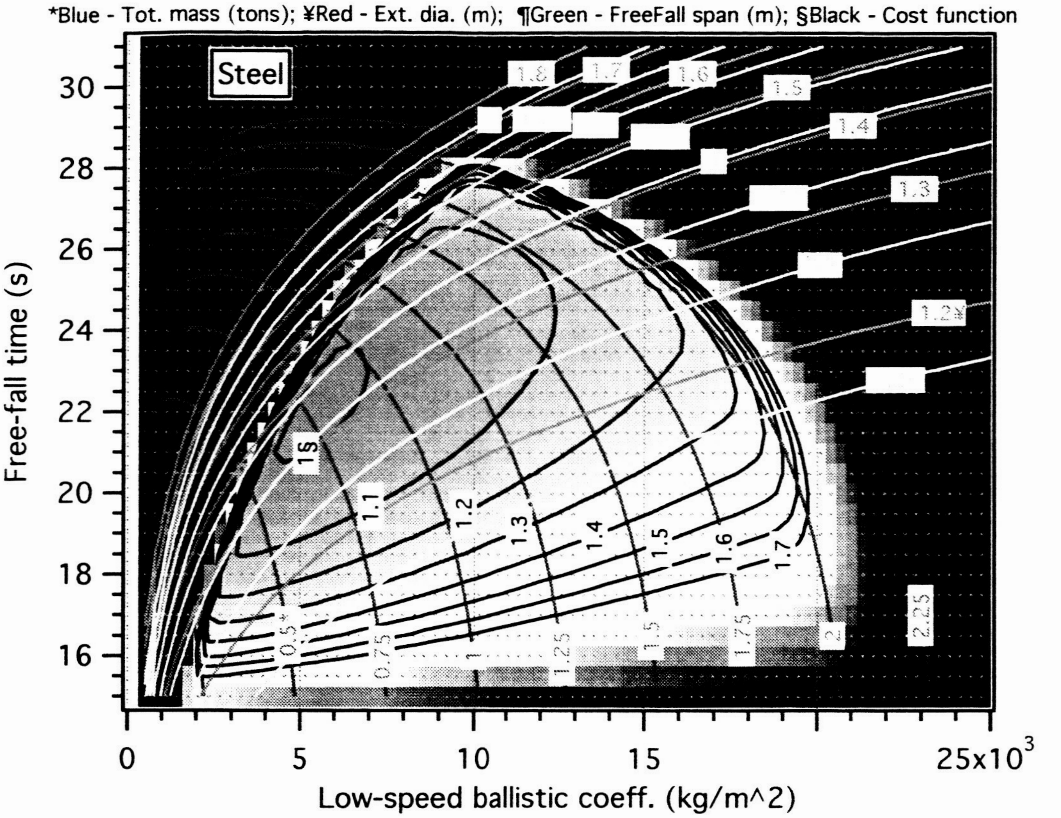

Figure 38 Cost function in the capsule parameter space (Steel cryostat)

The previous choice of parameters is also valid for a Steel cryostat with the only difference that the design point for the lower value of ballistic coefficient (i.e., 6500 kg/m^2 which is associated with a mass of 1000 kg) is closer to the left boundary, defined by buckling. The design point moves away from that boundary for higher values of the low-speed ballistic coefficient.

This "design concept" optimization does not intend to exhaust the design options for the capsule which will have to be revisited many times before the design is frozen based on additional system analyses. However, this process is a valid starting point to provide preliminary numbers for the analysis to be conducted by our cryostat subcontractor. The optimization process also provides a framework that lends itself to future refinements for evaluating system design parameters vis a vis performance input requirements and engineering constraints.

Capsule mass and Size

One of the important results of the analysis carried out is that the small vacuum chamber at the top of the capsule has been eliminated in favor of a fully cryogenic vacuum chamber (see Figure 39). The new solution eliminates the problem of the gravity gradient produced by the small cryostat in the proximity of the detector and also provides more clearance to the instrument package during the early stage of free fall.

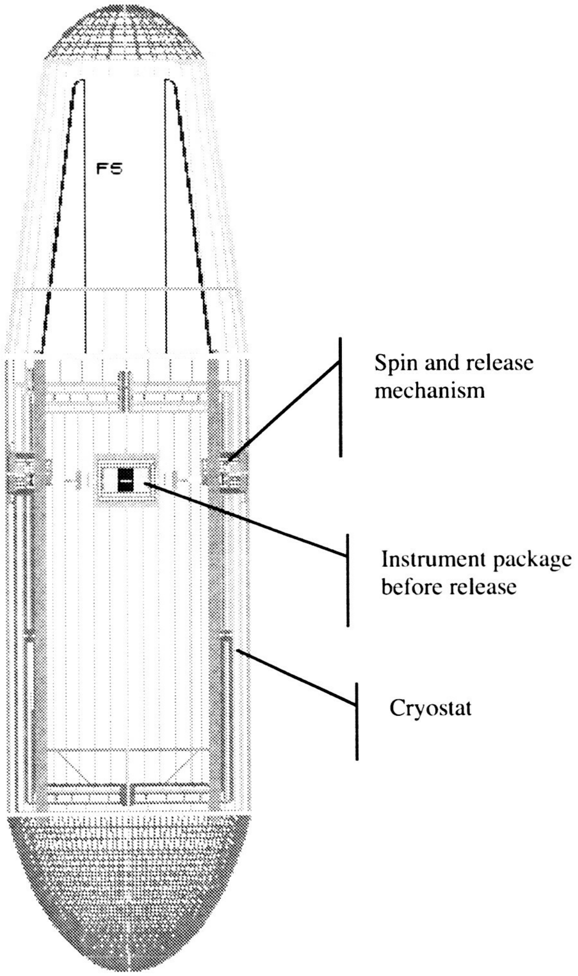

Figure 39 Schematic of capsule with instrument package attached before release

The new configuration also has the advantage of using a more conventional design of the cryostat than the old reference design with the small LHe cryostat.

The preferred size of the vacuum chamber/cryostat was identified as a cylinder with internal diameter of 1 m and an internal height (at the cylinder edges) of 2.1 m which results in an external diameter for the capsule of about 1.4 m and a free-to-chose capsule length of roughly 5.6 m. Preliminary data on large cryostats (from Janis Research), indicate that the mass of a cryostat of the size considered above will fit well within the mass limit of the system. Such chamber/cryostat will allow free fall times in the range 24-28 s depending on the amount of ballast added to the capsule.

The overall capsule mass could start at a minimum value of about a 1000 kg which provides a free fall time of about 24 s. The free-fall time can be increased by 1 s for every 250-kg ballast (or other equipment) added to the capsule up to the point where the a (limit) mass of 2000 kg is reached. The low-speed ballistic coefficient β_0 of the capsule will vary from about 6500 kg/m^2 for a capsule mass = 1000 kg to 13,000 kg/m^2 for a capsule mass of 2000 kg. Correspondingly, the free fall time will vary from about 24 s to 28 s.

Capsule Drop Time

The free fall time of the instrument package inside the capsule was computed for several values of the low-speed ballistic coefficient in the previous sections. Figure 40 depicts (again) the capsule drop distance and Mach number vs. drop time.

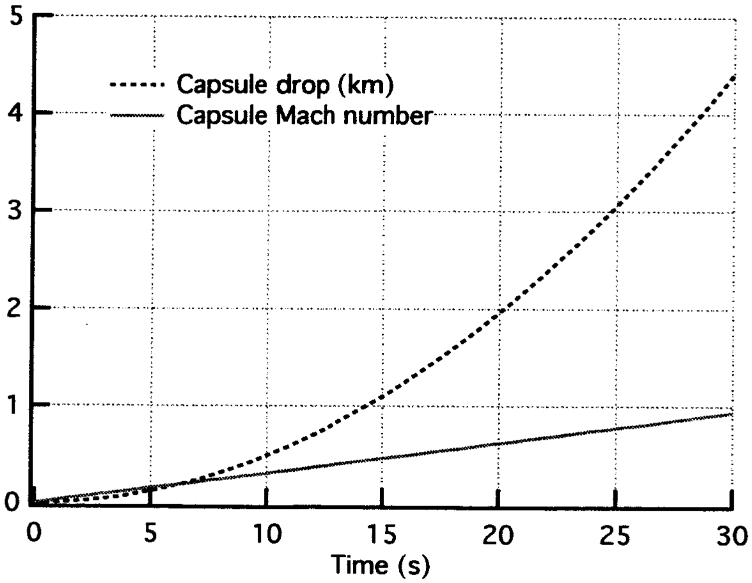

Figure 40 Capsule drop and Mach number vs. drop time

Following the computation of the preferable range of values for the capsule mass and size, Figure 41 shows the relative distance covered by the instrument package during free fall with respect to the capsule for a low-speed ballistic coefficient ranging from 6500 kg/m^2 to 13500 kg/m^2.

These results clearly indicate that a capsule of relatively compact size can provide a free fall time between 24 s and 28 s with a capsule mass ranging from 1000 kg to 2000 kg, respectively. The higher value of the mass is for the same capsule with ballast.

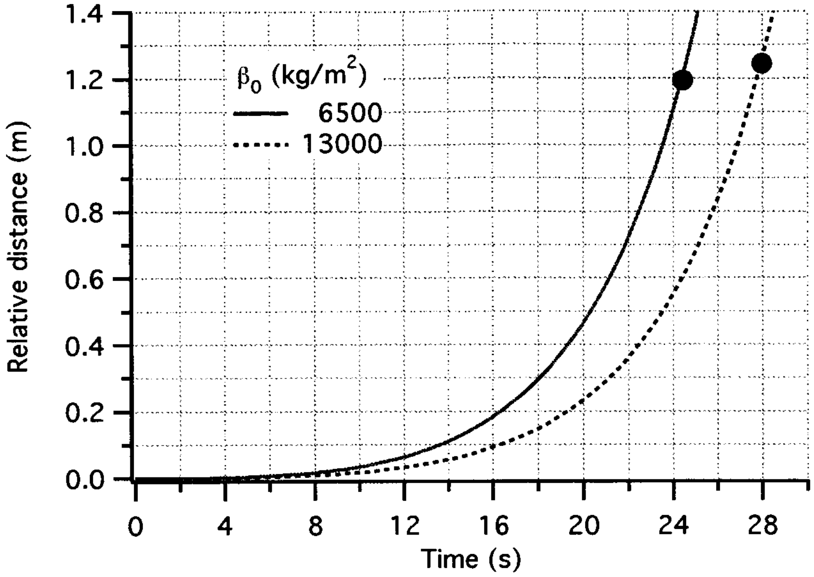

Figure 41 Relative vertical distance vs. free fall time for limit values of interest of ballistic coefficient. Dots mark the expected operating points for the light capsule (M = 1000 kg) and ballasted capsule (M = 2000 kg).

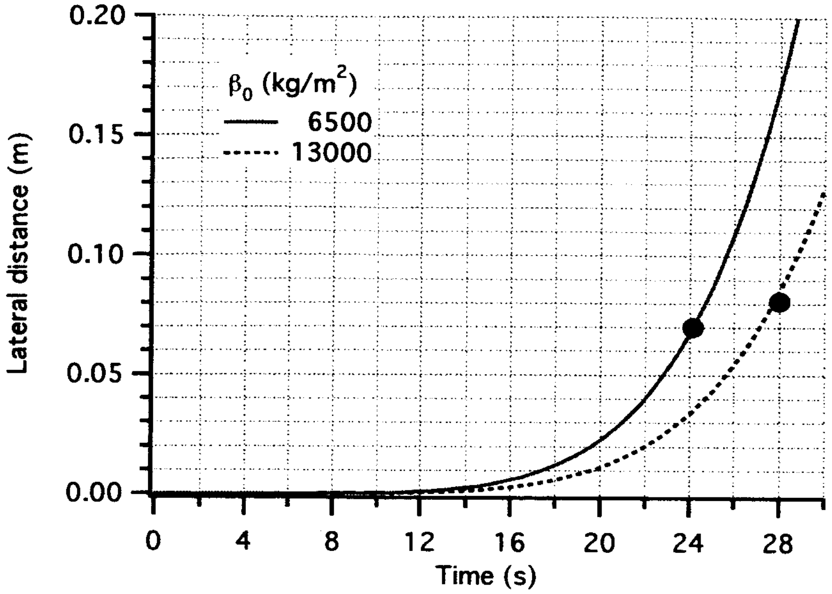

Figure 42 Relative lateral displacement due to wind shear vs. free fall time. Dots mark the expected operating points for the light capsule (M = 1000 kg) and ballasted capsule (M = 2000 kg).

An internal diameter of the capsule of 1 m was also computed from the optimization process. This diameter determines the tolerance to wind shear acting sideways on the capsule. Figure 42 shows the lateral displacement of the capsule with respect to the free-falling instrument package vs. free fall time for the limit values of interest for the low-speed ballistic coefficient. The value adopted for the wind shear of 0.005 s^{-1} is equivalent to a vertical gradient of 10 knots per km. This value is twice as high as the maximum wind shear reported[xxxi] for the Air Force balloon base at Holloman, New Mexico. The lateral displacements due to wind shear are relatively small in the parameter range of interest. Furthermore, if the balloon is launched during the periodically-occurring wind reversal times (in April-May and September-October) the vertical wind gradient is much smaller than the value adopted for the computations shown here.

MODAL ANALYSIS OF DETECTOR

Introduction

The following is the modal analysis of the differential accelerometer for the EP test. The sensor is composed by two masses of different materials constrained to an external case by means of elastic springs. The measurement is performed by monitoring the displacement of the two masses with respect to the external case through the measurement of capacitance variations caused by the displacement.

This analysis evaluates the eigenfrequencies and eigenmodes of the detector and the sensitivity of the modes to variations in the detector parameters.

The model adopts six degrees of freedom, that is, one rotation and one translation for each body. The system parameters considered for the sensitivity analysis are masses and moments of inertia of the bodies, stiffness of the springs and their ratio.

The influence of these parameters is evaluated on both the separation of the natural frequencies and the vibrational modes, particularly for what concerns the differential and common modes of the detector.

Detector Dynamics Model

The detector consists of two sensing masses having their Centers of Mass (CM) coincident with the CM of the external case. In the current detector model, one mass has a dumbbell shape, while the other is a hollow cylinder. The shape of the flight detector sensing masses will likely be different from this early choice. However, the shape of the sensing masses does not affect the generality of this study. The two sensing masses are constrained to the case by means of elastic springs, having a pivot axis parallel to the longitudinal axis of symmetry of the three elements. Figure 43 shows a schematic of the sensor model.

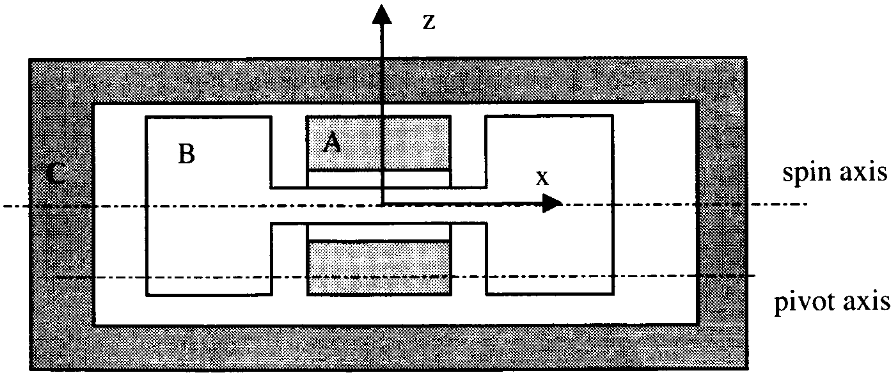

Figure 43 Schematic of detector model.

For this analysis, we assume that the capsule containing the sensor is fixed to the Earth surface, so that only the sensor is falling into it. This assumption does not affect the generality of the modal analysis. The Z axis is the axis of fall and of the Earth's gravity acceleration.

The reference system Cf is a frame parallel to the geographic X, Y, Z axes and displaced by the vector r_Z (see Figure 44). Another coordinate system D is attached to the capsule and having axes parallel to the local normal frame. At this stage of the analysis, reference frame D is assumed to coincide with the local normal frame and the capsule is assumed stationary with respect to the Earth's surface. This assumption doesn't cause any loss of generality for the modal analysis. The coordinate that describes the fall of the case along the z axis is $r_z(t)$, where **r** is the position vector that identifies the body C (external case) with respect to the capsule and, finally, z indicates the axis of fall.

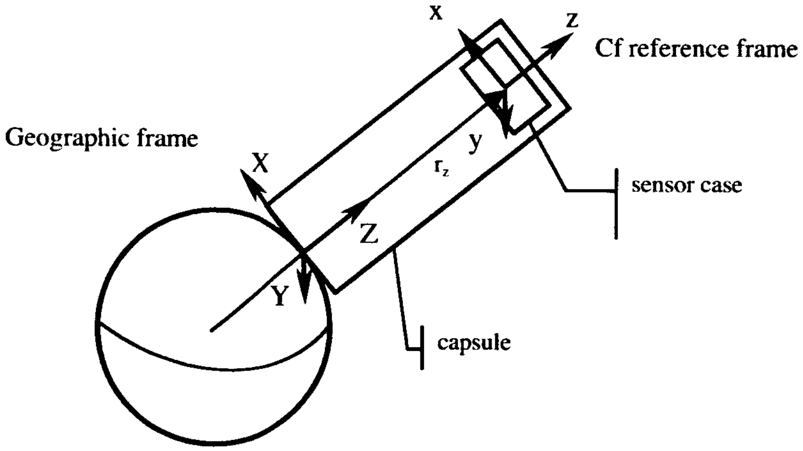

Figure 44 Local normal (geographic) and Cf frames

The body coordinate systems x, y, z are centered at the body CM, and fixed with the body itself. Each system has the x axis along the longitudinal axis of symmetry, corresponding also to the spin axis while the y and z axes are radial axes rotating with the body.

A rotational and translational degrees of freedom have been considered for each mass. More precisely, the x rotation about the CM of each mass, and the y translation referred to the xyz frame. Therefore each body can rotate about the x axis through its CM and can translate along the y axis of our reference frame. Figure 45 shows the possible movements of each body.

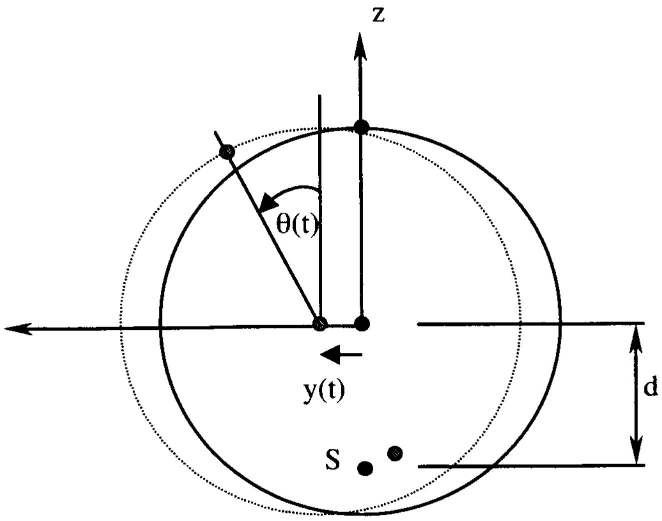

□

Figure 45 Degrees of freedom of each body

External forces

The motion of the sensing mass consists of a rotation θ(t) about the pivot axis (related to the torsional stiffnesses of the springs) and a translation y(t) that depends on the flexural stiffness of the springs. *The flexural stiffnesses are typically much greater than the torsional ones.* The distance *d* in the figure identifies the distance between the CM of the sensing mass and the pivot axis.

The external forces are written in the Cf reference frame, and consist of elastic forces. The elastic forces are produced by the springs connecting the sensing masses to the external case, and consist of a torsional torque and a force. In this analysis we assume that the rotational displacements are small, so that the displacement of the point S along the y axis due to a rotation around the CM is simply equal to θd [i.e., we assume that $\cos(\theta) = \theta$].

The differential displacement of the point S between body A and body C and the elastic force along the y axis are therefore:

$$\Delta y_A = y_A - \theta_A \cdot d_A - (y_C - \theta_C \cdot d_A)$$

$$F_{yA} = -k_{yA} \cdot \Delta y_A = -k_{yA} (y_A - \theta_A \cdot d_A - y_C + \theta_C \cdot d_A)$$

Where y_A and y_C, are the displacements along the y axis with respect to the Cf frame, θ_A and θ_C are the rotations about the x axis of masses A and C, respectively. k_{yA} is the flexural stiffness along y of the spring connecting body A to the case C.

The elastic torque about the CM of A is:

$N_A = -k_{tA}(\theta_A - \theta_C) - k_{yA} \cdot d_A \cdot \Delta y_A = -k_{tA}(\theta_A - \theta_C) - k_{yA} \cdot d_A (y_A - \theta_A \cdot d_A - y_C + \theta_C \cdot d_A)$

Where k_{tA} is the torsional stiffness of the spring connecting A and C.

Similarly, for the other two bodies we have:

$F_{yB} = -k_{yB} \cdot \Delta y_B = -k_{yB}(y_B - \theta_B \cdot d_B - y_C + \theta_C \cdot d_B)$

$N_B = -k_{tB}(\theta_B - \theta_C) - k_{yB} \cdot d_B \cdot \Delta y_B = -k_{tB}(\theta_B - \theta_C) - k_{yB} \cdot d_B (y_B - \theta_B \cdot d_B - y_C + \theta_C \cdot d_B)$

$F_{yC} = -k_{yA}(y_C - \theta_C \cdot d_A - y_A + \theta_A \cdot d_A) - k_{yB}(y_C - \theta_C \cdot d_B - y_B + \theta_B \cdot d_B)$

$N_C = -k_{tA}(\theta_C - \theta_A) - k_{yA} \cdot d_A (y_C - \theta_C \cdot d_C - y_A + \theta_A \cdot d_A) - k_{tB}(\theta_B - \theta_C) - k_{yB} \cdot d_B (y_B - \theta_B \cdot d_B - y_C + \theta_C \cdot d_B)$

These equations will be used in the next section to compute the stiffness matrix.

Modal Analysis

The mass and stiffness matrices are computed in this section. It has to be noted that out of 18 degrees of freedom (DoF) associated with the translational and rotational motion of the three masses only six of them are describing the motion of the degrees of freedom of interest. Specifically, only the translations along the y axis and the rotations about the x axis have to be considered for each body because the other motions do not affect the measurement. The state vector involved is, therefore, as follows:

$$X = [y_A \ y_B \ y_C \ \theta_A \ \theta_B \ \theta_C \ ]^T \tag{53}$$

which contains the translations along y axis and the rotations about the principal x axis of each body.

The mass matrix is a diagonal matrix in a system of rigid bodies as follows:

$$M = \begin{bmatrix} m_A & 0 & 0 & 0 & 0 & 0 \\ 0 & m_B & 0 & 0 & 0 & 0 \\ 0 & 0 & m_C & 0 & 0 & 0 \\ 0 & 0 & 0 & I_{Axx} & 0 & 0 \\ 0 & 0 & 0 & 0 & I_{Bxx} & 0 \\ 0 & 0 & 0 & 0 & 0 & I_{Cxx} \end{bmatrix} \tag{54}$$

The stiffness matrix, obtained from the force and torque equations by using the displacement method, is:

$$K = \begin{bmatrix} k_{yA} & 0 & -k_{yA} & -d_A k_{yA} & 0 & d_A k_{yA} \\ 0 & k_{yB} & -k_{yB} & 0 & -d_B k_{yB} & d_B k_{yB} \\ -k_{yA} & -k_{yB} & k_{yA} + k_{yB} & d_A k_{yA} & d_B k_{yB} & -d_A k_{yA} - d_B k_{yB} \\ -d_A k_{yA} & 0 & d_A k_{yA} & k_{tA} + d_A^2 k_{yA} & 0 & -k_{tA} - d_A^2 k_{yA} \\ 0 & -d_B k_{yB} & d_B k_{yB} & 0 & k_{tB} + d_B^2 k_{yB} & -k_{tB} - d_B^2 k_{yB} \\ d_A k_{yA} & d_B k_{yB} & -d_A k_{yA} - d_B k_{yB} & -k_{tA} - d_A^2 k_{yA} & -k_{tB} - d_B^2 k_{yB} & k_{tA} + k_{tB} + d_A^2 k_{yA} + d_B^2 k_{yB} \end{bmatrix} \tag{55}$$

We can observe that for an external body that is not constrained in its free fall, two rigid motions are possible, that is, the rigid body rotation around the x axis of the Cf frame, and the rigid body translation along the y axis. In order to carry out an analysis of the natural frequencies and natural modes of the system we can eliminate these two rigid motions so as to preserve only the elastic modes. This can be done by expressing one rotational and one translational coordinate of a body as a function of the corresponding coordinates of the other two bodies.

A vector having the three translations equal to a constant and the three rotations equal to zero is a solution of the eigenproblem, so that this vector is an eigenvector. Consequently, all the others eigenvectors must be orthogonal to this one to yield:

$$\{\Phi_0\}^T [M]\{\Phi\} = 0$$

where Φ_0 is a rigid eigenvector, and Φ is another eigenvector. After evaluating the matrix products we obtain:

$$\Phi_0(m_A\Phi_1 + m_B\Phi_2 + m_C\Phi_3) = 0$$

where now Φ_i is the i-th component of a general eigenvector. Because $\Phi_i = fx_i$, where x_i is the i-th component of the vector x and f is a constant equal for all the components, we can also write

$$m_A y_A + m_B y_B + m_C y_C = 0$$

which allows to express one translational coordinate of a body as function of the translations of the other two. It can also be noted that in deriving the former equation we have obtained the conservation of the linear momentum for any elastic motion.

We can obtain similar expressions for the rotational case as follows (from now on we drop the subscript "xx" in the moments of inertia):

$$I_A\,\theta_A + I_B\,\theta_B + I_C\,\theta_C = 0$$

We can now express the coordinates of a body as function of the analogous coordinates of the other two bodies. We can write therefore

$$\{x\} = [C]\{x_c\}$$

where x is the coordinate vector, C is a matrix, and x_e is the new coordinate vector having the two coordinates of a body expressed as function of the others. In our case, we have eliminated the coordinates of body C, obtaining the following matrix [C]:

$$C = \begin{bmatrix} 1 & 0 & 0 & 0 \\ 0 & 1 & 0 & 0 \\ -\frac{m_A}{m_C} & -\frac{m_B}{m_C} & 0 & 0 \\ 0 & 0 & 1 & 0 \\ 0 & 0 & 0 & 1 \\ 0 & 0 & -\frac{I_A}{I_C} & -\frac{I_B}{I_C} \end{bmatrix} \qquad (56)$$

and the vector X_e being

$$X_e = \begin{bmatrix} y_A \\ y_B \\ \theta_A \\ \theta_B \end{bmatrix} \qquad (57)$$

The stiffness and mass matrices can be modified using the new coordinates by

$[K_e] = [C]^T[K]\,[C]$

$[M_e] = [C]^T[M]\,[C]$

where M_e and K_e are the transformed mass and stiffness matrices which are not shown here for the sake of brevity. The dynamical matrix $[D] = [M_e]^{-1}[K_e]$ that is needed to compute the eigenfrequencies of the elastic modes is as follows:

$$D = \begin{bmatrix} k_{yA}\left(\frac{1}{m_A}+\frac{1}{m_C}\right) & \frac{k_{yA}m_B}{m_A m_B} & -\frac{d_A k_{yA}(I_A+I_C)}{I_C m_A} & -\frac{d_A k_{yA} I_B}{I_C m_A} \\ \frac{k_{yB}m_A}{m_B m_C} & k_{yB}\left(\frac{1}{m_B}+\frac{1}{m_C}\right) & -\frac{d_B k_{yB} I_A}{I_C m_B} & -\frac{d_B k_{yB}(I_B+I_C)}{I_C m_B} \\ -\frac{d_A k_{yA}(m_A+m_C)}{I_A m_C} & -\frac{d_A k_{yA} m_B}{I_A m_C} & \frac{(I_A+I_C)\left(k_{tA}+d_A^2 k_{yA}\right)}{I_A I_C} & \frac{I_B\left(k_{tA}+d_A^2 k_{yA}\right)}{I_A I_C} \\ -\frac{d_B k_{yB} m_A}{I_B m_C} & -\frac{d_B k_{yB}(m_B+m_C)}{I_B m_C} & \frac{I_A\left(k_{tB}+d_B^2 k_{yB}\right)}{I_B I_C} & \frac{(I_B+I_C)\left(k_{tB}+d_B^2 k_{yB}\right)}{I_B I_C} \end{bmatrix} \tag{58}$$

Once solved the eigenvalue problem for the constrained system (i.e. with the previous dynamical matrix), the total eigenvector including also the two variables eliminated can be obtained simply premultiplying the eigenvector obtained by the matrix [C].

Eigenvalues and Eigenvectors.

Using the dynamical matrix evaluated before an analysis of the eigenvalues and eigenvectors have been carried out in order to evaluate the influence of parameters on the natural frequencies and modal vectors.

The parameters are the following:

M_A = mass of body A

M_B = mass of body B

M_C = mass of body C

I_A = moment of inertia of body A about the spin axis (x axis)

I_B = moment of inertia of body B about the spin axis (x axis)

I_C = moment of inertia of body C about the spin axis (x axis)

d_A = distance between the CM and the constrained point of body A

d_B = distance between the CM and the constrained point of body B

k_{tA} = torsional stiffness of spring connecting bodies A and C

k_{tB} = torsional stiffness of spring connecting bodies B and C

k_{yA} = bending stiffness of spring connecting bodies A and C

k_{yB} = bending stiffness of spring connecting bodies B and C

Numerical values have been assigned to these parameters to evaluate natural frequencies and eigenvectors. Subsequently, the values of key parameters have been changed while keeping the others constant.

The values used for the first evaluation are as follows:

$m_A = m_B = 5$ kg

$I_A = I_B = 0.009$ kg-m^2 (which corresponds to an external radius of body A of 0.06 m and a mass m_A)

$I_C = 1$ kg-m^2

$d_A = d_B = 0.06$ m

$k_{tA} = k_{tB} = 9.593$ Nm/rad (corresponding to a first torsional frequency for a single-degree-of-freedom system of 3 Hz)

$k_{yA} = k_{yB} = 18000\ \pi^2$ N/m (corresponding to a first lateral frequency for a single-degree-of-freedom system of 30 Hz)

Using these values we obtain the following values:

$f_1 = 2.99$ Hz; $f_2 = 3.29$ Hz

$f_3 = 52.13$ Hz; $f_4 = 55.22$ Hz

and the associated eigenvectors:

$v_1 = \{0.0427736, -0.0427736, 0.705812, -0.705812\}$

$v_2 = \{0.0326524, 0.0326524, 0.706352, 0.706352\}$

$v_3 = \{-0.0209932, 0.0209932, 0.706795, -0.706795\}$

$v_4 = \{-0.0210127, -0.0210127, 0.706795, 0.706795\}$

Remembering that the eigenvector components represent in order y_A, y_B, θ_A, θ_B, we can make a few considerations about the natural modes.

The first vector is composed of a translation of the masses and a rotation about the CM. The sign is opposite for the two masses, so that one moves in opposition to the other while the signs of y_A and θ_A are the same so that the pivot point tends to remain in its original position. In the first mode body C is at rest, the motion being auto-compensating. In summary, the first mode corresponds to a differential mode of the two test masses.

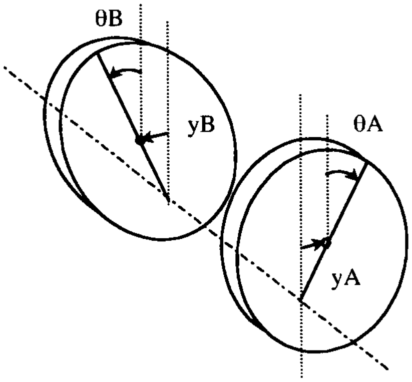

Figure 46 First natural mode (differential)

The second vibrational mode has a similar type of motion, the only difference being that the two proof masses move in the same direction. In this mode body C moves in the opposite direction of the proof masses in order to equilibrate the motion.

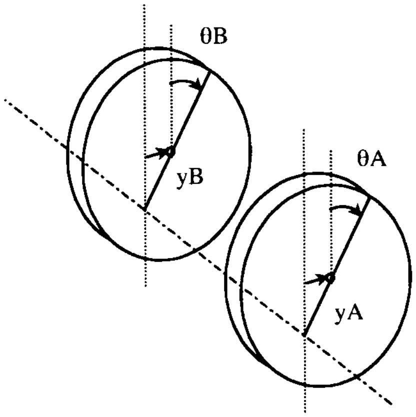

Figure 47 Second natural mode (common)

The third and fourth modes involve the lateral stiffness of the springs as the sign of the rotation and translation of each mass is now opposite, so that the displacement of the constrained point is now the sum of the y translation and of θd_A term (i.e., $y_A - \theta_A d_A$). The y translation depends on the lateral stiffness of the springs that is much higher than the torsional stiffness. The first two modes are analyzed in detail in the following.

Parametric Analysis

K_y influence

The following plots show the variation of the first and second natural frequencies as k_y varies. In each plot the components of the eigenvector is also plotted.

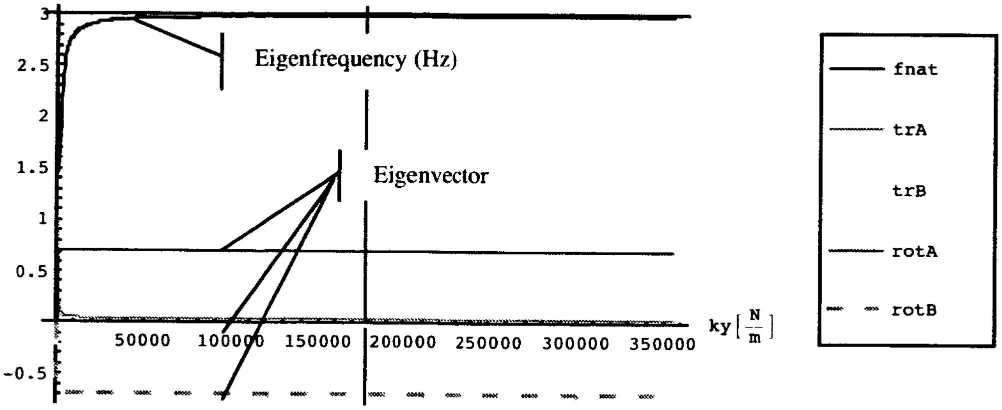

Figure 48 Dependence of first natural frequency on k_y

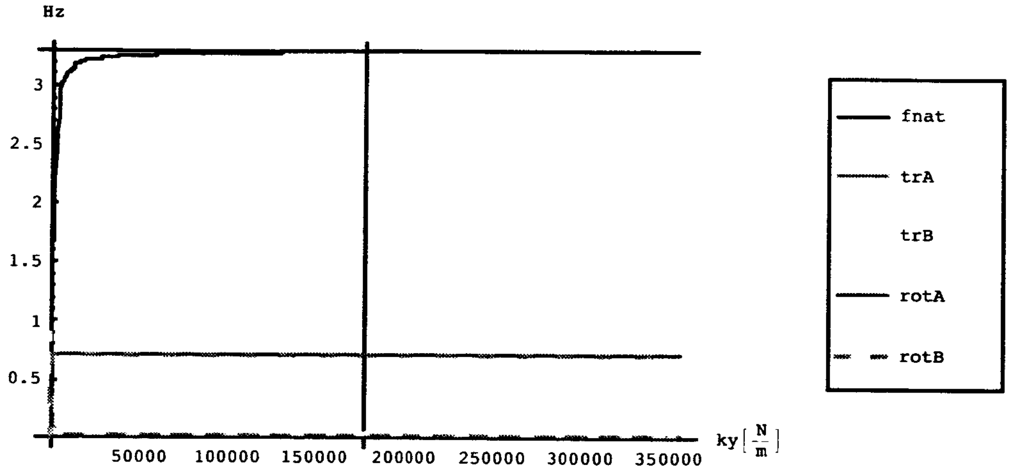

Figure 49 Dependence of second natural frequency on k_y

In the previous plots we can notice that the natural frequencies increase with k_y, having as asymptotes 2.99 and 3.29 Hz respectively. Increasing the value of k_y therefore contributes to separating the two frequencies up to the value of 0.3 Hz. The following plot shows the influence of k_y on the displacement of the constrained point.

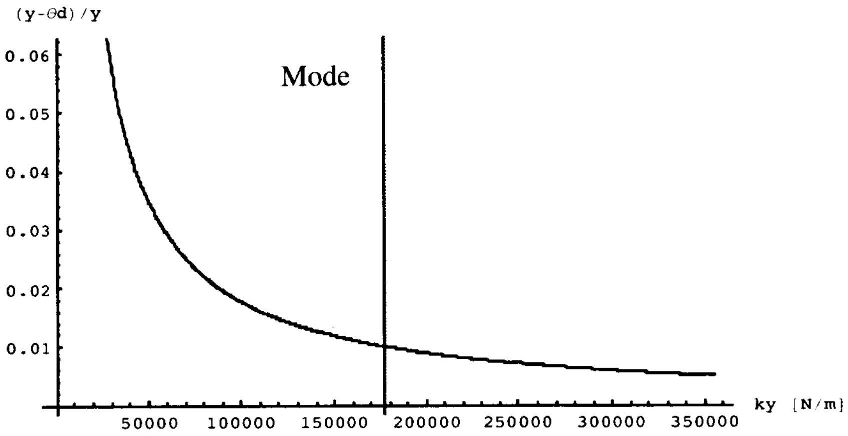

Figure 50 Dependence on k_y of translation of constrained point in first mode

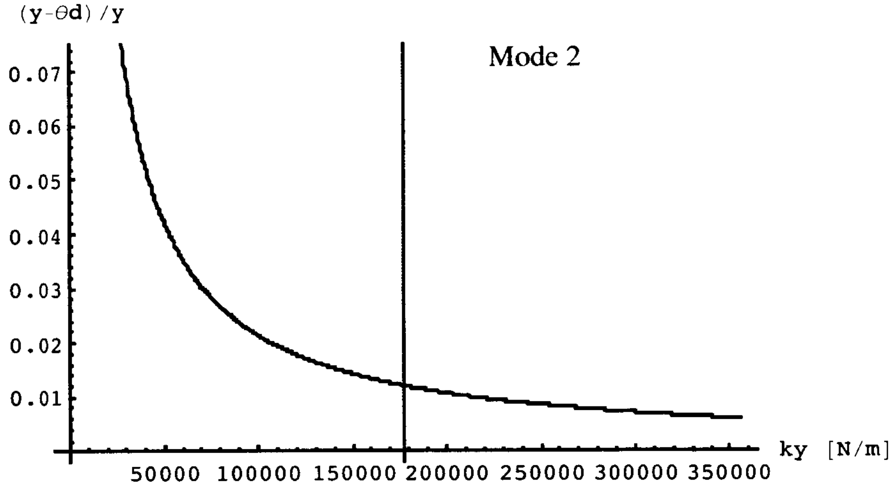

Figure 51 Dependence on k_y of translation of constrained point in second mode

As k_y increases, the displacement of the point S (constrained point) decreases, so that the differential displacement in mode 1 is reduced and likewise for mode 2 (see Figs 50 and 51).

I_C influence

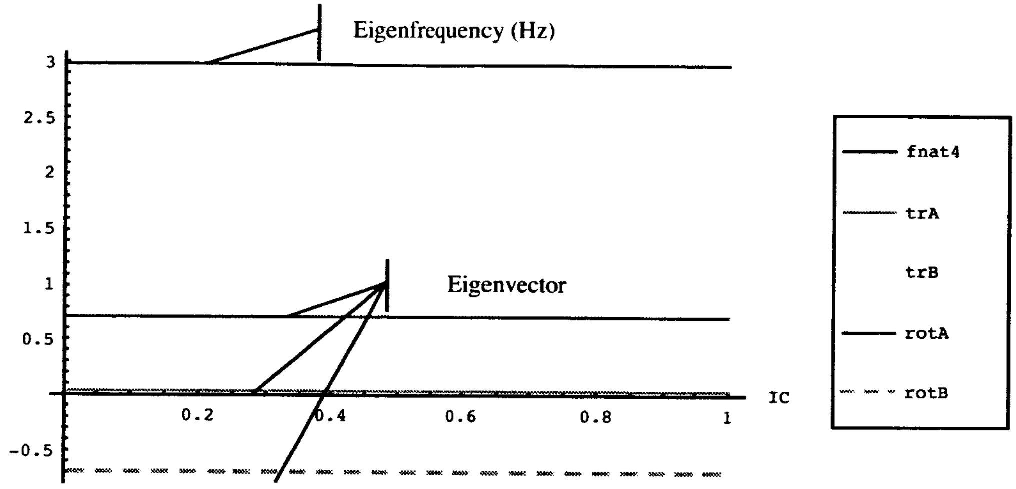

Figure 52 Dependence of first natural frequency on I_C

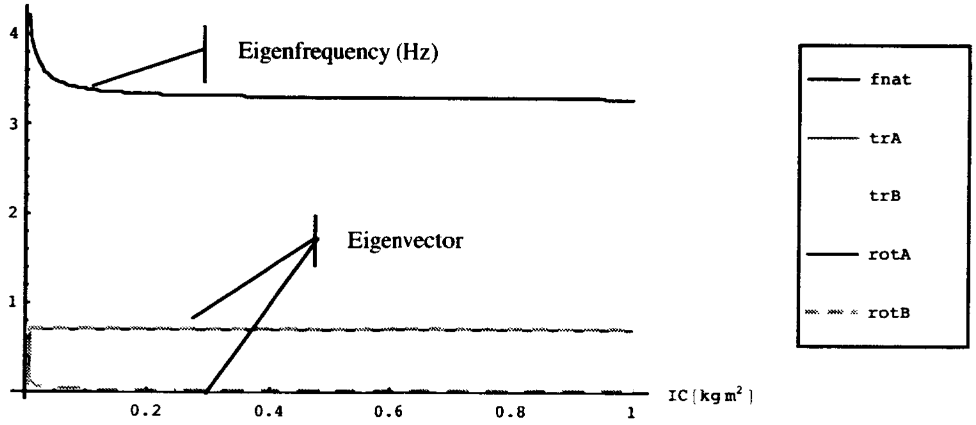

Figure 53 Dependence of second natural frequency on I_C

The value of I_C affects the frequency of the second mode; decreasing the value of I_C the natural frequency increases, yielding also a larger separation between the two first frequencies. I_C has no influence on the displacement of the pivot point.

m_C influence

The effect of m_C on the frequencies considered is to increase the separation of the frequencies as m_C decreases, similarly to the effect of I_C. The plot below shows this effect versus the m_C/m_A ratio.

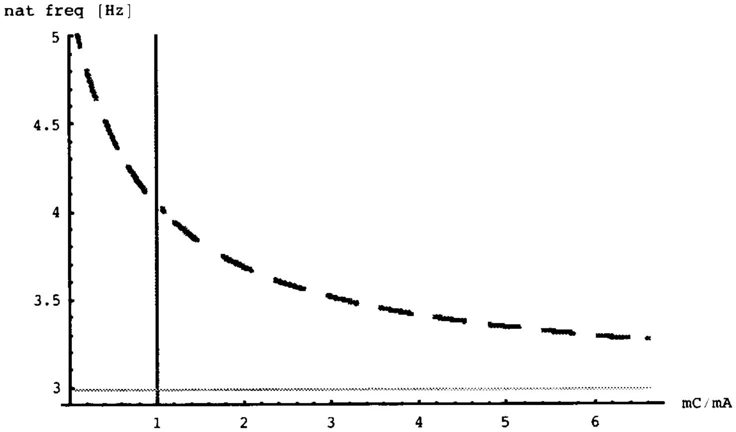

Figure 54 Dependence of natural frequency separation on m_C/m_A

Combining the effect of I_C and m_C, the separation of the frequencies increases from a value of 0.3 Hz when I_C and m_C are much greater than I_A and m_A, to a value of 2.17 Hz when the ratios I_C/I_A approaches unity.

Relative variation of I_A, m_A, k_{yA}, k_{tA}

We perturb the values of the parameters k_{yA}, I_A, k_{tA}, d_A, m_A of the two sensing masses in order to test the influence of possible imperfections in the mechanical and physical characteristics of the sensing masses and springs. The ratios p_A/p_B, where "p" indicates one of the above mentioned parameters have been varied between ±5% of the nominal value.

The main influence of these parameters is on the difference of displacement of the two sensing masses in the common mode (mode 2), resulting in a differential displacement. The plot below shows the differential displacement $(y_A - y_B)/y_A$ versus the p_A/p_B ratio.

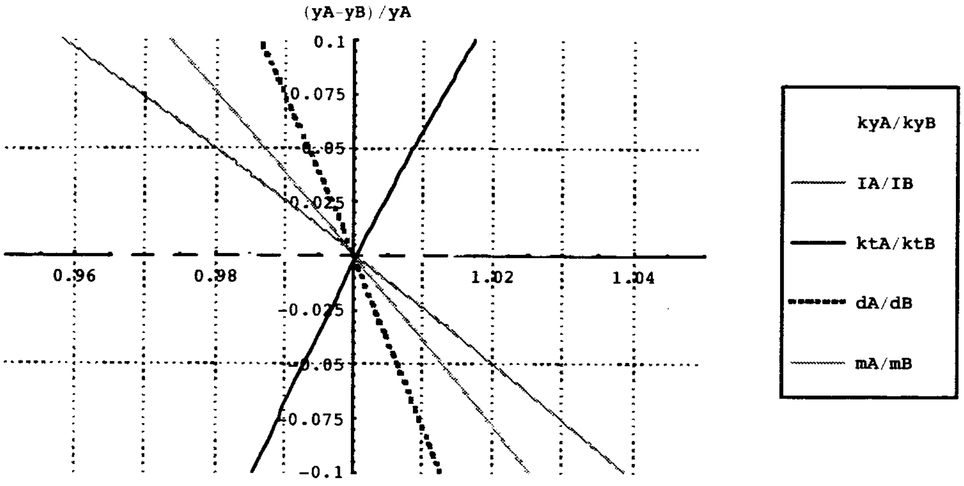

Figure 55 Influence of bodies A and B parameter's ratio on the differential displacement

As it can be seen, the most influent parameter is the distance of the constrained point, and subsequently the mass, and inertia ratio. This kind of dependence is explained by the fact that d_A changes the moment of inertia around the pivot axis with a squared dependence; m_A influences both the translational and the rotational motion, while I_A affects only the rotational degrees of freedom (DoF).

Concluding Remarks

The analysis performed allowed to describe the differential accelerometer's modes and frequencies and their dependence on the inertial and mechanical parameters. The system has been modeled using 6 DoF, the rotation around the x axis and the translation along a radial axis for each body.

The first two frequencies and eigenvectors have been analyzed in detail because these modes of rotation around the pivot axis affect the acceleration measurement the most. The separation of these two frequencies depends mostly on the mass and inertia moment of the C body, and slightly on the lateral stiffness of the springs. The lower C mass and inertia are, the greater the separation between the first two frequencies (if $I_C/I_A = 1 = m_C/m_A$ the difference is 2.17 Hz for a value of $k_y = 18000\pi^2$, while it is only 0.3 Hz if $I_C/I_A = 110$ and $m_C/m_A = 6$). Increasing k_y contributes to reducing the displacement of the pivot axis both for mode 1 and mode 2.

A variation of the parameters ratio between body A and B has also been checked, to evaluate the influence of possible imperfections of the inertial and mechanical characteristics of the proof masses.

The differential displacement of the CM of the sensing masses has been analyzed. The k_{tA}/k_{tB} ratio has the greatest influence, causing a Δy difference of 5% as the previous ratio varies by 0.7%. The k_{yA}/k_{tB} ratio has a similar influence. The ratio m_A/m_B has roughly half the influence of the spring stiffness ratio, causing a 5% Δy difference as the ratio varies by 1.3%. The inertia ratio I_A/I_B produces a 5% variation of the Δy differential displacement as it varies by 2% from the unit value. Finally the lateral stiffness ratio k_{yA}/k_{yB} has a negligible influence compared to the others, i.e., approximately two orders of magnitude less, reaching a 0.025% variation of Δy as the parameter ratio varies by 1%.

DYNAMICS ANALYSIS OF INSTRUMENT PACKAGE/DETECTOR

Introduction

The following analysis is a study of the accelerometer and instrument package dynamics. Two different designs of sensor have been taken into consideration as follows: (1) a sensor with two sensing masses and a case (three bodies); and (2) a sensor with one sensing mass (made of two different materials) and a case. In both types the measurement is carried out by monitoring the differential displacements between masses, through the measurement of capacitance variations caused by those displacements.

In this study we derive the differential equations of motion for each sensor and carry out numerical integrations of cases of interest, starting from different initial conditions of the positions of the centers of mass (CM) and initial rotational velocities of the bodies in order to evaluate the influence of those parameters on the differential output of the accelerometer.

Each body is defined using all its six degrees of freedom (DoF) and elastic forces and torques are applied to each of them at the attachment points of the constraining springs.

Description of sensor configurations

Three-body sensor.

The sensor is composed by two sensing masses having the CM coincident with the CM of the external case. One mass has a dumbbell shape, while the other is a hollow cylinder. These two masses are attached to the case by means of elastic springs, having a pivot axis that is parallel to the longitudinal axis of symmetry of the sensor. All the bodies spin about the symmetry axis x (during the fall). Figure 56 shows a schematic of the 3-body sensor.

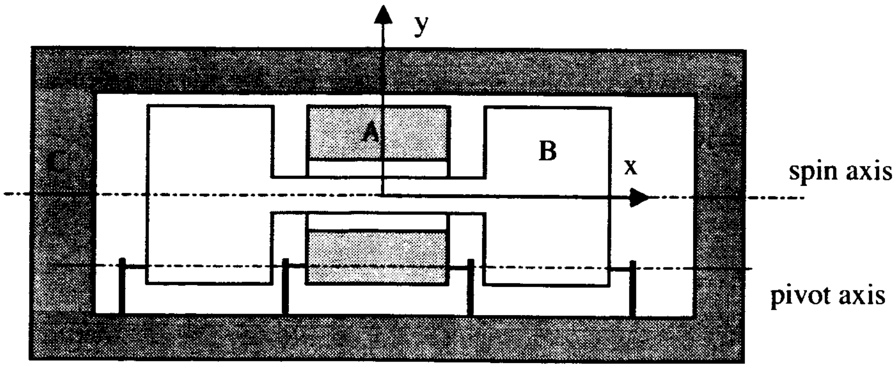

Figure 56 Schematic of three-body sensor

The motion of the sensor is essentially a rotation of the sensing masses about the pivot axis. The translational motion of the sensing masses, which depends on the high lateral stiffness of the springs is much smaller than the rotational motion. A rotation of the mass implies a variation of the distance between the sensing mass and the external case that changes the capacitance of the motion pickup system.

Two-body sensor.

The two bodies sensor consists of an external case (body A) and an internal sensing mass. The internal mass is actually formed by two equal masses of different materials which are rigidly attached so as to behave like a single rigid body. The internal mass is connected to the external mass by means of elastic springs which have a lateral stiffness much higher than the torsional one. All the bodies spin about the symmetry axis x (during the fall).

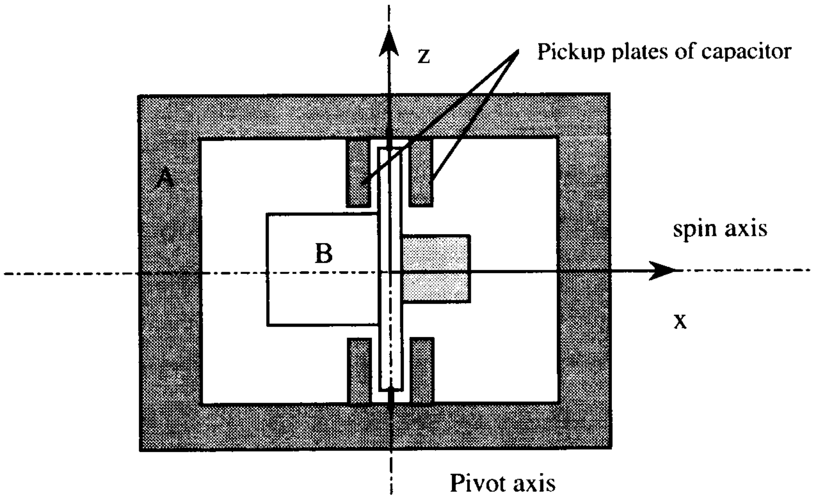

Figure 57 Schematic of two-body sensor

A violation of the EP during the fall would cause a rotation about the pivot axis of the sensing mass with respect to the sensor case. The measurement is then carried out by detecting the differential displacement (and therefore the capacitance variation) of the central disk of body B with respect to the four fixed capacitor plates attached to body A (see Figure 57). The capacitor plates are arranged in such a way that a rotation of B about the pivot axis z unbalances the capacitive measurement bridge and produce an output signal.

Reference frames

A body reference frame has been attached to each body. The attitude of each body is identified by Euler's angles, following the sequence 1-2-3 (i.e., by building the rotation matrix using sequential rotations about x, y, and z axes).

The relationships between the different reference frames have been written by means of rotation matrices and translation vectors. All the matrices are described in details in the following. The R_{0A} matrix transforms the inertial frame (X_0, Y_0, Z_0) into the body A reference frame (X_A, Y_A, Z_A);

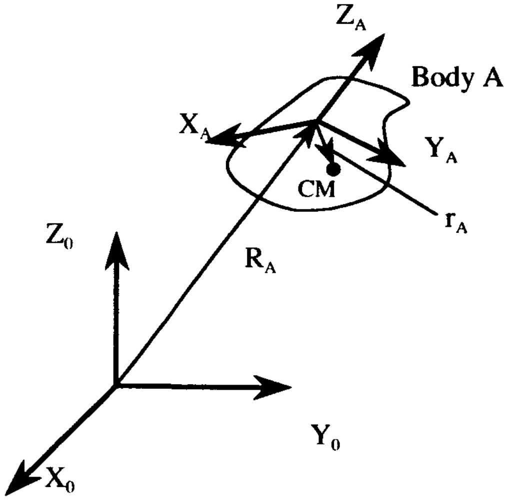

Figure 58 Inertial and body reference frames

The body frame is attached to the geometrical center of the body which, in ideal conditions, coincides with the CM of the body. The position of the CM (of body A for example) in the A reference frame is defined by $\{x_{CMA}, y_{CMA}, z_{CMA}\}$. The coordinates of the origin of the A frame (R_A) with respect to the inertial 0 frame are: $\{x_A(t), y_A(t), z_A(t)\}$.

The matrix yielding the transformation from system X_0, Y_0, Z_0 to X_A, Y_A, Z_A is composed by the following sequence of transformations:

- rotation $\theta_{xA}(t)$ around X axis;

- rotation $\theta_{yA}(t)$ around Y' axis (transformed Y_0 axis after $\theta_{xA}(t)$ rotation);

- rotation $\theta_{zA}(t)$ around Z'' axis (transformed Z_0 axis after $\theta_{xA}(t)$ and $\theta_{yA}(t)$ rotations);

- translation R_A projected along the three axes X_A, Y_A, Z_A.

The rotation matrix $[R_{0A}]$ and the translation vector $\{R_A\}$ from system 0 (inertial) to system A (body A) are the following:

$$[R_{0A}]=\begin{bmatrix} c(\theta_{yA})c(\theta_{zA}) & c(\theta_{zA})s(\theta_{xA})s(\theta_{yA})+c(\theta_{xA})s(\theta_{zA}) & -c(\theta_{xA})c(\theta_{zA})s(\theta_{yA})+s(\theta_{xA})s(\theta_{zA}) \\ -c(\theta_{yA})s(\theta_{zA}) & c(\theta_{xA})c(\theta_{zA})-s(\theta_{xA})s(\theta_{yA})s(\theta_{zA}) & c(\theta_{zA})s(\theta_{xA})+c(\theta_{xA})s(\theta_{yA})s(\theta_{zA}) \\ s(\theta_{yA}) & -c(\theta_{yA})s(\theta_{xA}) & c(\theta_{xA})c(\theta_{yA}) \end{bmatrix}$$

where the superscript identifies the relevant reference frame. The translation vector is the R_A vector, expressed in the A frame. This vector can be computed as follows:

$$R_A = [R_{0A}]\{-x_A \;\; -y_A \;\; -z_A\}^T$$

Where the vector $\{-x_A, -y_A, -z_A\}$ is the opposite of the vector $\{R_A\}$ expressed in the 0 frame.

We have:

$$\{R_A{}^A\}=\begin{Bmatrix} -c(\theta_{yA})c(\theta_{zA})x_A-[c(\theta_{zA})s(\theta_{xA})s(\theta_{yA})+c(\theta_{xA})s(\theta_{zA})]y_A+[c(\theta_{xA})c(\theta_{zA})s(\theta_{yA})-s(\theta_{xA})s(\theta_{zA})]z_A \\ c(\theta_{yA})s(\theta_{zA})x_A-[c(\theta_{xA})c(\theta_{zA})-s(\theta_{xA})s(\theta_{yA})s(\theta_{zA})]y_A-[c(\theta_{zA})s(\theta_{xA})+c(\theta_{xA})s(\theta_{yA})s(\theta_{zA})]z_A \\ -s(\theta_{yA})x_A+c(\theta_{yA})s(\theta_{xA})y_A-c(\theta_{xA})c(\theta_{yA})z_A \end{Bmatrix}$$

For the opposite transformation, which leads from the body A coordinate system to the inertial frame, we use the transpose of the rotation matrix $[R_{A0}] = [R_{0A}]^T$ and the vector is simply the R_A vector expressed in the inertial coordinates $\{x_A, y_A, z_A\}$.

We have

$$[R_{A0}]=\begin{bmatrix} c(\theta_{xA})c(\theta_{yA}) & -c(\theta_{yA})s(\theta_{xA}) & s(\theta_{yA}) \\ c(\theta_{zA})s(\theta_{xA})+c(\theta_{xA})s(\theta_{yA})s(\theta_{zA}) & c(\theta_{xA})c(\theta_{zA})-s(\theta_{xA})s(\theta_{yA})s(\theta_{zA}) & -c(\theta_{yA})s(\theta_{zA}) \\ -c(\theta_{xA})c(\theta_{zA})s(\theta_{yA})+s(\theta_{xA})s(\theta_{zA}) & c(\theta_{zA})s(\theta_{xA})s(\theta_{yA})+c(\theta_{xA})s(\theta_{zA}) & c(\theta_{yA})c(\theta_{zA}) \end{bmatrix}$$

$$\{R_A^0\}=\begin{Bmatrix} x_A \\ y_A \\ z_A \end{Bmatrix}$$

In summary, the transformations are as follows:

Inertial to body A:

$[R_{0A}].\{r^0\} + \{R_A{}^A\}$

Body to inertial:

$[R_{A0}].\ \{r^A\} + \{R_A{}^0\}$

The same procedure is followed for the other bodies.

Degrees of Freedom and equations of motion

The transformation matrices have been written for each body for deriving the equation of motion for the different bodies. The body coordinate systems are centered in the body's geometrical center, and fixed with the body itself. The position of the CM is described using three coordinates (x_{CMA}, y_{CMA}, z_{CMA} for body A). Each system has the x axis along the longitudinal axis of symmetry, corresponding also to the spin axis, the y and z axes are radial axes rotating with the body.

Each body has all the six degrees of freedom, i.e., the three translations of the body frame origin, and the three rotations according to the Euler's angles described above.

To derive the equations of motion the translation accelerations of the CM and elastic forces have been written in the inertial system. The rotational equations are then projected onto the body axes.

Translational accelerations

In the following we describe the procedure for deriving the equations of motion by taking the two-body sensor as an example. The procedure to derive the equations for the three-body sensor is exactly the same with the added complexity of a higher number of equations.

The CM vector in each body's reference frame is:

Body A: $\{r_A\} = \{x_{CMA}\ y_{CMA}\ z_{CMA}\}^T$

Body B: $\{r_B\} = \{x_{CMB}\ y_{CMB}\ z_{CMB}\}^T$

The translational acceleration expressed in the inertial reference is obtained using the formula:

$$\{a_A\} = \left[\ddot{R}_{A0}\right] \cdot \{r_A\} + 2\left[\dot{R}_{A0}\right] \cdot \{\dot{r}_A\} + \left[R_{A0}\right] \cdot \{\ddot{r}_A\} + \left\{\ddot{R}_A^0\right\}$$

Where

$\{a_A\}$ is the acceleration of body A in the inertial frame;

$[R_{A0}]$ is the rotation matrix from A to inertial frame;

$\{r_A\}$ is the coordinates vector of body A CM in the A frame;

$\{R_A^0\}$ is the translation vector expressed in inertial coordinates

$(\dot{\ })$ indicates the time derivative and the dot (.) matrix multiplication.

The same equations are used for the other bodies.

Elastic Forces

To evaluate the elastic forces we define first the points where the springs are attached to each body. The position of these points are expressed in body frame. The distance between connected points is then computed from the actual position during the motion, projected in the A frame, and multiplied by the stiffness vector $\{k_{xA}, k_{yA}, k_{zA}\}$. By following this procedure, it is possible to assign different stiffness to each degree of freedom. Finally the elastic forces are projected onto the inertial coordinate system, and added to the equation of motion. The points connected by the springs are as follows (all distances are in meters):

$$\{p_{A1}\} = \{0, 0, -75\text{x}10^{-3}\}^T$$

$$\{p_{A2}\} = \{0, 0, 75\text{x}10^{-3}\}^T$$

$$\{p_{B1}\} = \{0, 0, -65\text{x}10^{-3}\}^T$$

$$\{p_{B2}\} = \{0, 0, 65\text{x}10^{-3}\}^T$$

The initial lengths of the two springs constraining the motion are as follows:

$$\{l_1\} = \{p_{A1} - p_{B1}\} = \{0, 0, -10\text{x}10^{-3}\}^T$$

$$\{l_2\} = \{p_{A2} - p_{B2}\} = \{0, 0, 10\text{x}10^{-3}\}^T$$

The figure below shows the position of the points where the forces are applied

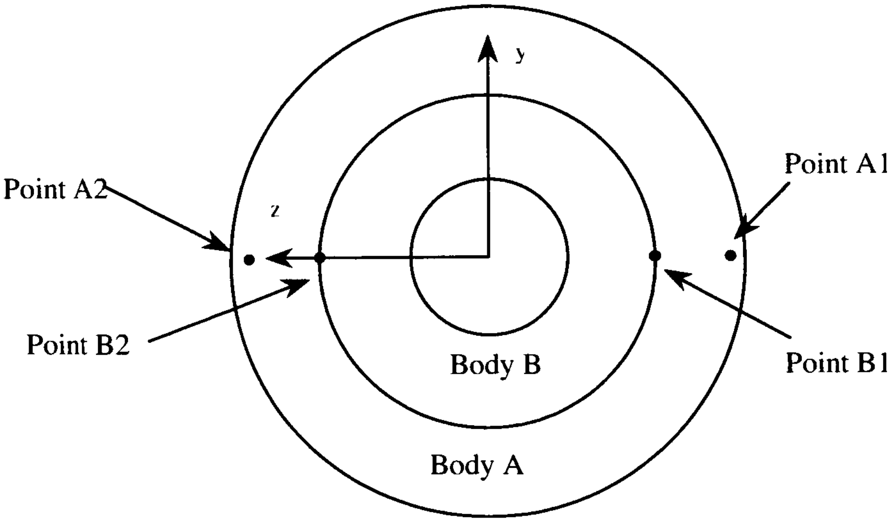

Figure 59 Locations of attachment points

$$\{F_{1A}\} = [\dot{R}_{A0}] \,.\, ([K] \,.\, (\{p_{A1}\} - [T_{0A}].\{T_{B0}.p_{B1}\} - \{l_1\}))$$

$$\{F_{2A}\} = [R_{A0}] \,.\, ([K] \,.\, (\{p_{A2}\} - [T_{0A}].\{T_{B0}.p_{B2}\} - \{l_2\}))$$

$$\{F_A\} = \{F_{1A}\} + \{F_{2A}\}$$

In the above notation the operator "$T_{0A}.x$" indicates the combination of the multiplication by the rotation matrix $[R_{0A}]$ applied to the vector $\{x\}$ plus the translation of the vector $\{R_A{}^A\}$ which yields:

$$\{T_{0A}.x\} = [R_{0A}].\{x\} + \{R_A{}^A\}$$

The expression $T_{0A}.(T_{B0}.p_{B1})$ projects the coordinates of the point p_{B1} (expressed in the body B frame) onto the body A coordinate system. Subsequently, the force is projected onto the inertial frame using the $[R_{A0}]$ matrix. A similar procedure is used to evaluate the forces acting on any other body pairs.

The equations of translational motion for the two bodies A and B are:

$$m_A \{a_A\} - \{F_A\} = 0$$

$$m_B \{a_B\} - \{F_B\} = 0$$

where m_A and m_B are the masses of body A and B, a_A and a_B are the accelerations, and F_A and F_B are the elastic forces:

$$\{F_A\} = \{F_{1A}\} + \{F_{2A}\}$$

$$\{F_B\} = \{F_{1B}\} + \{F_{2B}\}.$$

Rotational accelerations:

The angular velocity of each body is computed by using the rotation matrices that transform the coordinate system from the inertial to the body frame and conversely for the opposite transformation. The rotational velocity matrices of bodies A and B are derived by using the Cartan's formula as follows:

$$[\omega_{\mathrm{A}}] = [R_{0A}] \cdot [\dot{R}_{A0}]$$

$$[\omega_B] = [R_{0B}] \cdot [\dot{R}_{B0}]$$

where $[R_{0A}]$ and $[R_{A0}]$ are the rotation matrices from coordinate system 0 to A and vice-versa. $[R_{0B}]$ and $[R_{B0}]$ are the correspondent matrices for body B.

It should be noted that the former expression lead to the skew symmetric matrix of the angular velocity from which the components of the angular velocity vector $\{\omega_A\}$ can be readily extracted.

The rotational inertia forces are obtained using the formulas:

$$[I_A]\cdot\{\dot{\omega}_A\}+[\omega_A]\cdot[I_A]\cdot\{\omega_A\}$$

$$[I_B]\cdot\{\dot{\omega}_B\}+[\omega_B]\cdot[I_B]\cdot\{\omega_B\}$$

Where $\{\omega_A\}$ and $[\omega_A]$ represent the angular velocity vector and matrix, respectively, for body A (and similarly for body B), $[I_A]$ and $[I_B]$ are the inertia matrices for body A and B which, assuming principal axes, have the form

$$[I_A]=\begin{bmatrix} I_{Axx} & 0 & 0 \\ 0 & I_{Ayy} & 0 \\ 0 & 0 & I_{Azz} \end{bmatrix}; \quad [I_B]=\begin{bmatrix} I_{Bxx} & 0 & 0 \\ 0 & I_{Byy} & 0 \\ 0 & 0 & I_{Bzz} \end{bmatrix}$$

Elastic torques

The elastic torques acting on each body are computed by using the definition of the attachment points and the expression of the elastic forces previously defined. The expressions of the torques in the body reference frame are as follows:

$$\{T_A\} = \{p_{A1}\} \times ([R_{0A}] \cdot \{F_{1A}\}) + \{p_{A2}\} \times ([R_{0A}] \cdot \{F_{2A}\})$$

$$\{T_B\} = \{p_{B1}\} \times ([R_{0B}] \cdot \{F_{1B}\}) + \{p_{B2}\} \times ([R_{0B}] \cdot \{F_{2B}\})$$

where x indicates the external product of vectors.

Finally, the expressions of the rotational equations of motion are:

$$\begin{aligned} &[I_A]\cdot\{\dot{\omega}_A\}+[\omega_A]\cdot[I_A]\cdot\{\omega_A\}-\{T_A\}=0 \\ &[I_B]\cdot\{\dot{\omega}_B\}+[\omega_B]\cdot[I_B]\cdot\{\omega_B\}-\{T_B\}=0 \end{aligned} \qquad (59)$$

The equations of motion for the three bodies sensor are evaluated at the same way as for the two bodies. The same quantities are derived and the same structure for the equations is obtained. Figure 60 shows the positions of the constrained points for the three bodies sensor.

The points p_{CA1}, p_{CA2}, p_{CB1} and p_{CB2} are the points of the external case C connected with the points p_{A1}, p_{A2}, p_{B1}, p_{B2}, respectively. In this case four springs are used to connect the two bodies to the case (two springs per each body).

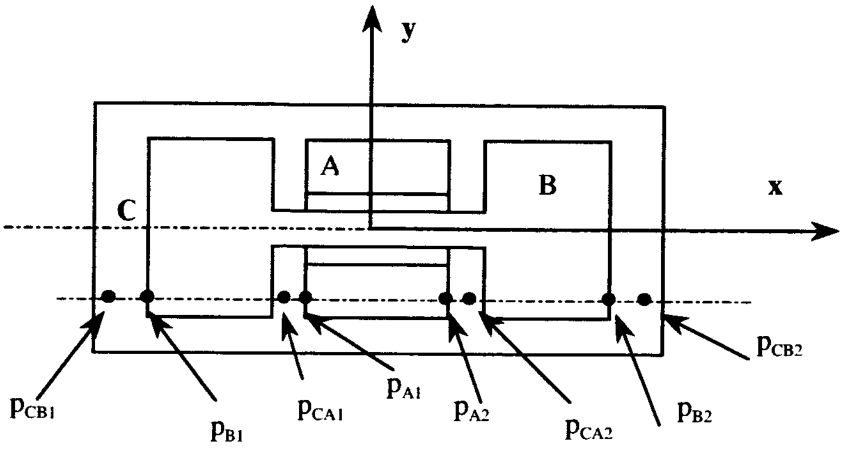

Figure 60 Locations of attachment points

The coordinates of the points are the following (each point is expressed in its own body system):

$\{p_{A1}\} = \{-40\text{x}10^{-3}, -60\text{x}10^{-3}, 0\}^T$

$\{p_{B1}\} = \{-250\text{x}10^{-3}, -60\text{x}10^{-3}, 0\}^T$

$\{p_{CA1}\} = \{-50\text{x}10^{-3}, -60\text{x}10^{-3}, 0\}^T$

$\{p_{CB1}\} = \{-270\text{x}10^{-3}, -60\text{x}10^{-3}, 0\}^T$

$\{l_{A1}\} = \{p_{A1} - p_{CA1}\}$

$\{l_{B1}\} = \{p_{B1} - p_{CB1}\}$

$\{p_{A1}\} = \{40\text{x}10^{-3}, -60\text{x}10^{-3}, 0\}^T$

$\{p_{B1}\} = \{250\text{x}10^{-3}, -60\text{x}10^{-3}, 0\}^T$

$\{p_{CA1}\} = \{50\text{x}10^{-3}, -60\text{x}10^{-3}, 0\}^T$

$\{p_{CB1}\} = \{270\text{x}10^{-3}, -60\text{x}10^{-3}, 0\}^T$

$\{l_{A2}\} = \{p_{A2} - p_{CA2}\}$

$\{l_{B2}\} = \{p_{B2} - p_{CB2}\}$

Two Bodies

The integration of the equations of motion has been performed using different values for the CM position and initial angular velocity of body A.

A frequency analysis has been performed for each result, to evaluate the frequency content of the differential rotation around the z axis, which leads to the detection of a differential signal by the capacitors.

The parameters in the equations are the following:

m_A = mass of body A
m_B = mass of body B
I_{Ax} = moment of inertia of body A about the x axis
I_{Ay} = moment of inertia of body A about the y axis
I_{Az} = moment of inertia of body A about the z axis
I_{Bx} = moment of inertia of body B about the x axis
I_{By} = moment of inertia of body B about the y axis
I_{Bz} = moment of inertia of body B about the z axis
k_x = lateral stiffness of spring connecting bodies A and B (in A coordinates)
k_y = lateral stiffness of spring connecting bodies A and B (in A coordinates)
k_z = lateral stiffness of spring connecting bodies A and B (in A coordinates)
$k_{\theta z}$ = torsional stiffness of spring connecting bodies A and B
x_{CMA} = x position of CM of body A (in body A coordinates)
y_{CMA} = y position of CM of body A (in body A coordinates)
z_{CMA} = z position of CM of body A (in body A coordinates)
x_{CMB} = x position of CM of body B (in body B coordinates)
y_{CMB} = y position of CM of body B (in body B coordinates)
z_{CMB} = z position of CM of body B (in body B coordinates)

The variables for the equations (DoF) are:

$x_A(t)$ = x coordinate of the geometrical center of body A (in inertial coordinates)
$y_A(t)$ = y coordinate of the geometrical center of body A (in inertial coordinates)
$z_A(t)$ = z coordinate of the geometrical center of body A (in inertial coordinates)
$x_B(t)$ = x coordinate of the geometrical center of body B (in inertial coordinates)
$y_B(t)$ = y coordinate of the geometrical center of body B (in inertial coordinates)
$z_B(t)$ = z coordinate of the geometrical center of body B (in inertial coordinates)
$\theta_{xA}(t)$ = x rotation of body A
$\theta_{yA}(t)$ = y rotation of body A
$\theta_{zA}(t)$ = z rotation of body A
$\theta_{xB}(t)$ = x rotation of body A
$\theta_{yB}(t)$ = y rotation of body A
$\theta_{zB}(t)$ = z rotation of body A

Numerical values have been assigned to the parameters and then a study of the influence of the position of the CM with respect to the geometrical center of each body (CM parameters), also combined with an initial angular velocity of body B. The values used for the fixed parameters are in the following.

We analyze in the following representative cases with prograde precession (i.e., ICx > ICy). The reason for favoring prograde precession over retrograde precession is that prograde precession brings about significantly smaller accelerations due to imperfect release (see later on) than retrograde precession.

Two-Body Dynamics Simulation

Prograde precession

IAx < IAy

mA = 30 kg, mB = 1 kg,
IAx = 95/100 kgm^2, IAy = 146/100 kgm^2, IAz = 146/100 kgm^2,
IBx = 17/100, IBy = 17/100, IBz = 17/100,
kx = 45000 N/m, ky -> 35000 N/m, kz -> 35000 N/m,
kx2 = 45000 N/m, ky2 = 35000 N/m, kz2 = 35000 N/m,
kθx = 1000 Nm/rad, kθy = 1000 Nm/rad, kθz = 54 Nm/rad;

spin frequency = 0.3 Hz
initial velocity θ_z of body A = 10^{-2} rad/s
initial nutation angle = 0

xCMA = 0, yCMA = 0, zCMA = 0,
xCMB = 10^{-6} m, yCMB = 0, zCMB = 10^{-6} m

$$\begin{pmatrix} 2.99716 \\ 7.38688 \\ 8.08957 \\ 42.8045 \\ 42.8045 \\ 48.5357 \end{pmatrix}$$

Figure 61 Natural frequencies

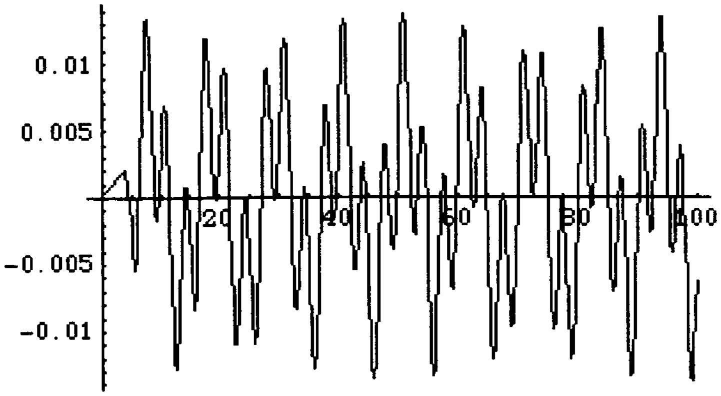

Figure 62 θ_{zA} (rad) vs. time (s)

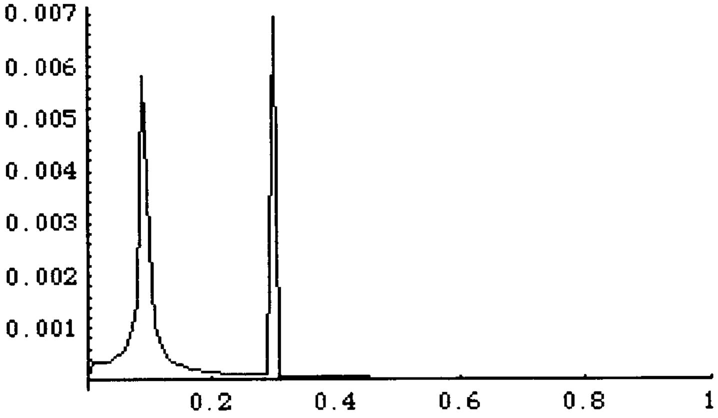

Figure 63 FFT of θ_{zA} vs. frequency (Hz)

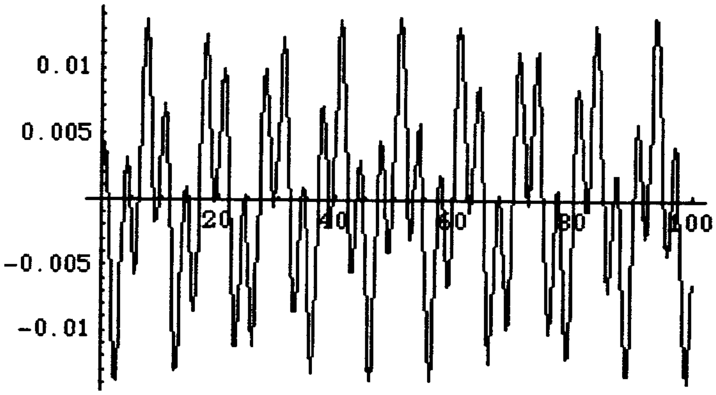

Figure 64 θ_{zB} (rad) vs. time (s)

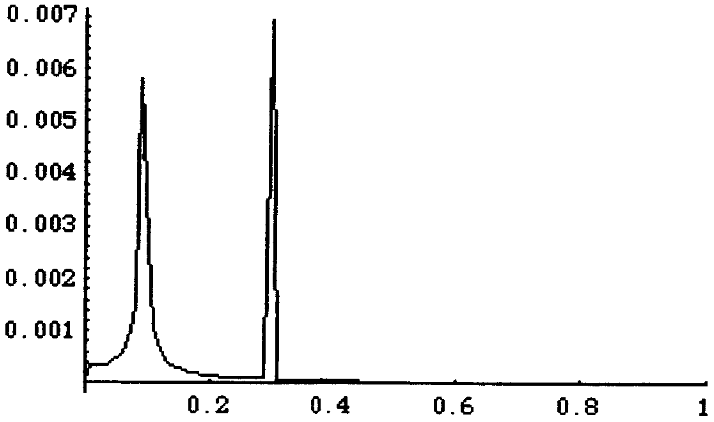

Figure 65 FFT of θ_{zB} vs. frequency (Hz)

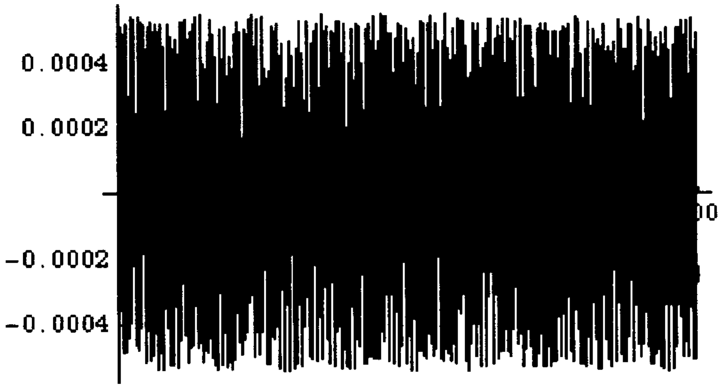

Figure 66 $\theta_{zB} - \theta_{zA}$ (rad) vs. time (s)

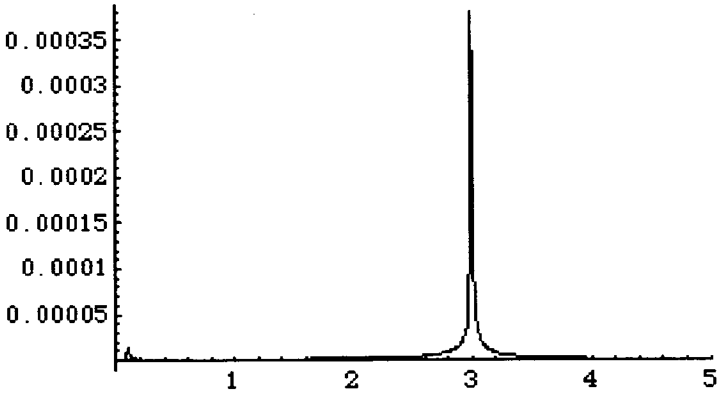

Figure 67 FFT of $\theta_{zB} - \theta_{zA}$ vs. frequency (Hz)

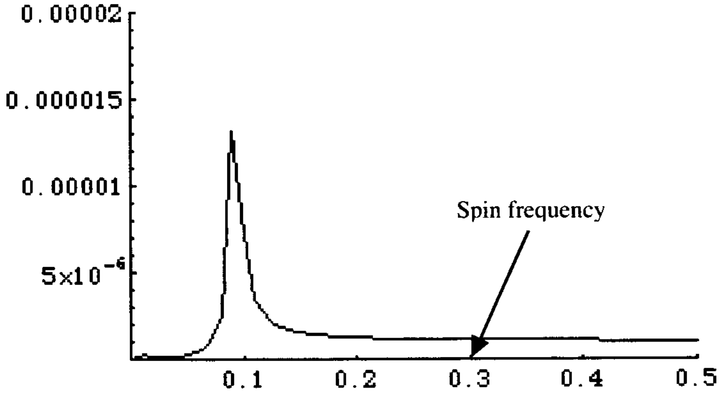

Figure 68 Zoom of $\theta_{zB} - \theta_{zA}$ FFT vs. frequency (Hz)

Three-Body Dynamics Simulations

The parameters in the equations are as follows:

m_A = mass of body A
m_B = mass of body B
m_C = mass of body C
I_{Ax} = moment of inertia of body A about the x axis
I_{Ay} = moment of inertia of body A about the y axis
I_{Az} = moment of inertia of body A about the z axis
I_{Bx} = moment of inertia of body B about the x axis
I_{By} = moment of inertia of body B about the y axis
I_{Bz} = moment of inertia of body B about the z axis
I_{Cx} = moment of inertia of body C about the x axis
I_{Cy} = moment of inertia of body C about the y axis
I_{Cz} = moment of inertia of body C about the z axis
k_{Ax} = lateral stiffness of spring connecting bodies A and C (in C coordinates)
k_{Ay} = lateral stiffness of spring connecting bodies A and C (in C coordinates)
k_{Az} = lateral stiffness of spring connecting bodies A and C (in C coordinates)
k_{Bx} = lateral stiffness of spring connecting bodies B and C (in C coordinates)
k_{By} = lateral stiffness of spring connecting bodies B and C (in C coordinates)
k_{Bz} = lateral stiffness of spring connecting bodies B and C (in C coordinates)
$k_{\theta xA}$ = torsional stiffness of spring connecting bodies A and C
$k_{\theta xB}$ = torsional stiffness of spring connecting bodies B and C
x_{CMA} = x position of CM of body A (in body A coordinates)
y_{CMA} = y position of CM of body A (in body A coordinates)
z_{CMA} = z position of CM of body A (in body A coordinates)
x_{CMB} = x position of CM of body B (in body B coordinates)
y_{CMB} = y position of CM of body B (in body B coordinates)
z_{CMB} z position of CM of body B (in body B coordinates)
x_{CMC} x position of CM of body C (in body C coordinates)
y_{CMC} y position of CM of body C (in body C coordinates)
z_{CMC} z position of CM of body C (in body C coordinates)

The variables for the equations (dof) are:

$x_A(t)$ = x coordinate of the geometrical center of body A (in inertial coordinates)
$y_A(t)$ = y coordinate of the geometrical center of body A (in inertial coordinates)
$z_A(t)$ = z coordinate of the geometrical center of body A (in inertial coordinates)
$x_B(t)$ = x coordinate of the geometrical center of body B (in inertial coordinates)
$y_B(t)$ = y coordinate of the geometrical center of body B (in inertial coordinates)
$z_B(t)$ = z coordinate of the geometrical center of body B (in inertial coordinates)
$x_C(t)$ = x coordinate of the geometrical center of body C (in inertial coordinates)
$y_C(t)$ = y coordinate of the geometrical center of body C (in inertial coordinates)
$z_C(t)$ = z coordinate of the geometrical center of body C (in inertial coordinates)
$\theta_{xA}(t)$ = x rotation of body A

$\theta_{yA}(t)$ = y rotation of body A
$\theta_{zA}(t)$ = z rotation of body A
$\theta_{xB}(t)$ = x rotation of body A
$\theta_{yB}(t)$ = y rotation of body A
$\theta_{zB}(t)$ = z rotation of body A
$\theta_{zC}(t)$ = z rotation of body C
$\theta_{xC}(t)$ = x rotation of body C
$\theta_{yC}(t)$ = y rotation of body C

Prograde precession

ICx < ICy
spin freq = 0.3 Hz

values:

mA = 1 kg, mB = 1 kg, mC = 30 kg,
IAx = 17/100 kgm^2, IAy = 17/100 kgm^2, IAz = 17/100 kgm^2,
IBx = 17/100 kgm^2, IBy = 17/100 kgm^2, IBz = 17/100 kgm^2,
ICx = 95/100 kgm^2, ICy = 146/100 kgm^2, ICz = 146/100 kgm^2,
kA1x = 45000 N/m, kA1y = 35000 N/m, kA1z = 35000 N/m,
kA2x = 45000 N/m, kA2y = 35000 N/m, kA2z = 35000 N/m,
kAqx = 61.68 Nm/rad, kAqy = 1000 Nm/rad, kAqz = 1000 Nm/rad,
kB1x = 45000 N/m, kB1y = 35000 N/m, kB1z = 35000 N/m,
kB2x = 45000 N/m, kB2y = 35000 N/m, kB2z = 35000 N/m,
kBθx = 6168/100 Nm/rad, kBθy = 1000 Nm/rad, kBθz = 1000 Nm/rad

initial θ_z of body C = 10^{-2} rad/s
Initial nutation angle = 0

xCMA = 10^{-6} m, yCMA = 0, zCMA = 10^{-6} m,
xCMB = 0, yCMB = 0, zCMB = 0,
xCMC = 0, yCMC = 0, zCMC = 0

$$\begin{pmatrix} 42.1084 \\ 43.4894 \\ 4.39904 \\ 27.2175 \\ 2.99982 \\ 42.5542 \\ 3.48568 \\ 44.0754 \\ 48.344 \\ 50.0619 \\ 4.34997 \\ 26.7789 \end{pmatrix}$$

Figure 69 Natural frequencies

The simulations have been run for 100 s (which is higher than the actual value) for the sole reason of providing a good frequency resolution for the FFT plots.

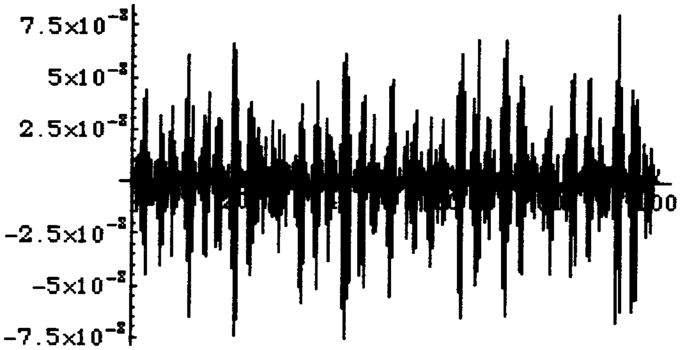

Figure 70 $z_A - z_C$ (m) projected in body C frame vs. time (s)

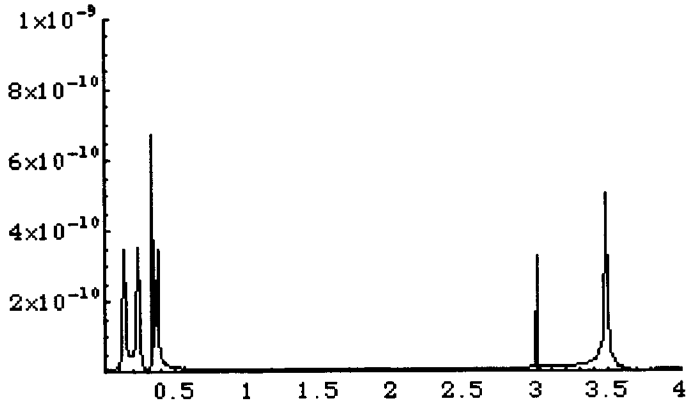

Figure 71 FFT of $z_A - z_C$ vs. frequency (Hz)

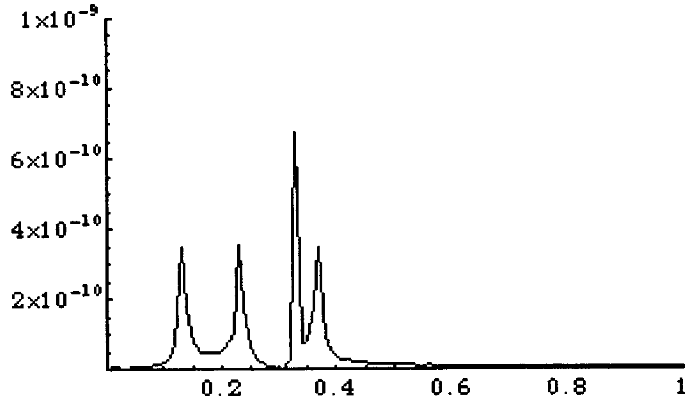

Figure 72 Zoom of $z_A - z_C$ FFT vs. frequency (Hz)

Figure 73 $z_B - z_C$ (m) in C frame vs. time (s)

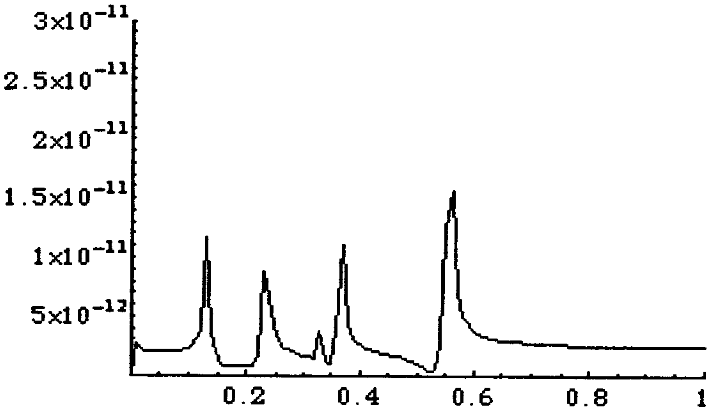

Figure 74 FFT of z_B vs. frequency (Hz)

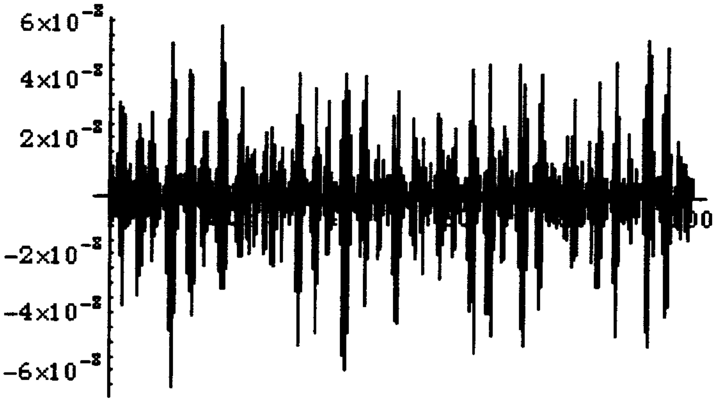

Figure 75 $z_A - z_B$ (m) in C frame vs. time (s)

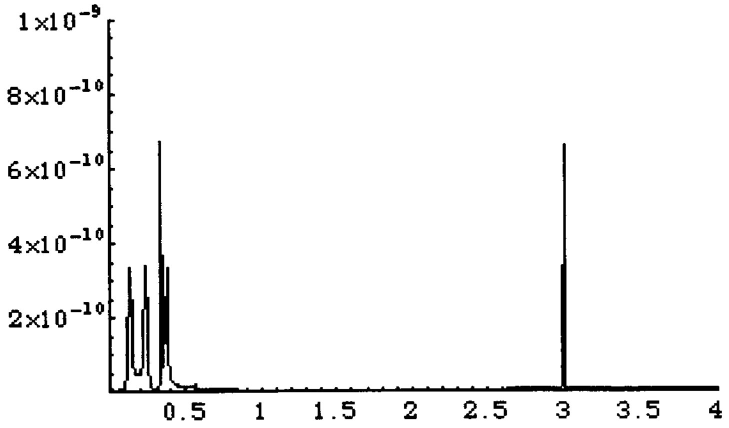

Figure 76 FFT of $z_A - z_B$ vs. frequency (Hz)

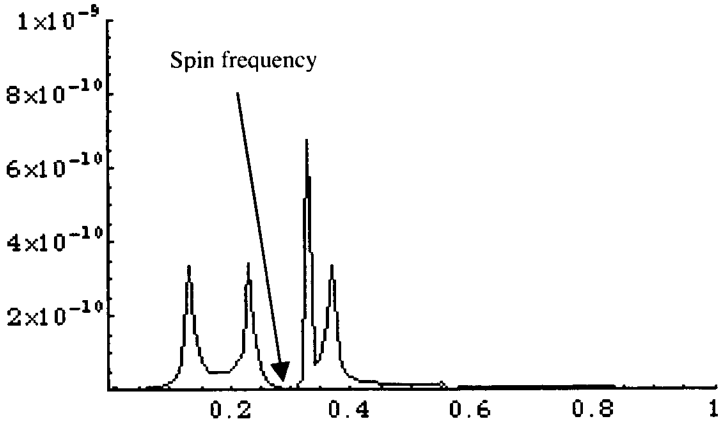

Figure 77 Zoom of $z_A - z_B$ FFT vs. frequency (Hz)

Concluding Remarks

The analysis carried out allowed to evaluate the influence of CM position and initial angular velocity errors in the dynamic of the 2-body and the 3-body sensors. The two systems have been modeled using 12 DoF, and 18 DoF respectively (six dof for each body).

2-body results

The position of the CM for body A (external case) did not affect the rotation about the z axis (measurement axis), while the initial non zero condition on the angular velocity of the same body caused a differential signal to be detected.

Analyzing the frequency content of the signal, though, no frequency peak was noticed at the spin frequency (0.3 Hz), while the natural frequency for the rotation about the z axis (3 Hz) and the precession frequency (0.18 Hz) were present.

These frequencies can easily be changed modifying the torsional stiffness about z axis and changing the inertia ratio (IAz – IAx)/IAz, to which the precession frequency is directly related.

Note that the spin frequency appears in the single θ_{zA} or θ_{zB} starting from an initial angular velocity of body A about y or z axes, but it is rejected when the difference between the two signals is taken.

Applying all the initial conditions together (both CM positions and angular velocities) led to analogous results, resulting in a rejection of the spin frequency in the differential rotation.

3-body results

Likewise, in the three-body detector the position of the CM of the external case (body C) along the spin axis does not influence any of the variables (in the absence of gravity gradients). The displacement of the CM along the axes y and z cause the excitation of the y and z variables only, while the rotations are not affected. Moreover the differential displacement is not excited.

An initial condition on the angular velocity (both along the y or z directions) excites all the dof of the system, both individual and differential; the frequency pattern of the variables doesn't show evidence of peaks at the spin frequency, neither in the individual, nor in the differential component of the displacements.

After applying all the different conditions together, the frequency analysis again shows that the differential signal (along z direction) doesn't show any peak at the spin frequency, even if these peaks are present in the individual variables (y and z) due to initial displacement of the CM of body C along y and/or z directions.

DETECTOR REQUIREMENTS DEVELOPMENT

Model for the Gravitational Perturbations Acting on Proof Masses

Overview

The test body (proof mass), falling inside the capsule, is subjected to non-negligible gravitational attraction by the capsule. In particular, the higher order gravitational potential plays a major role because of the elimination of the zero-order potential due to the equivalence principle.

The model consists of a spinning test body inside a capsule: hollow cylinder covered with flat caps. The test body is released at the axis of the cylinder, and deviates from the axis during its fall. Therefore, our task is to compute the gravitational force and torque acting at the neighborhood of the fall. The fact that both the test mass and the capsule are closed finite bodies, increases the complexity of the problem. We took advantage of the size of the test mass; smaller than the cylinder radius, to derive an asymptotic analytical solution. We are mostly concerned with the force/torque at the modulation frequency. In other words, our model should evaluate the force/torque in a rotating body frame, rather than the static field in the capsule frame of reference. For that purpose we built a semi-analytical model. The main advantage of our model is its flexibility. It can handle any configuration of test mass as well as any additional mass distribution in the test chamber.

The purpose of this work is two folds. We need a working gravitational model for future simulation for the dynamics of the test body. We also need to choose the inertia properties of the test body that minimize the gravitational disturbance.

In the following we presents the analytical approach, analytical results, numerical analyses, and the interpretation of results. Appendices to this section are available in the first Annual Report #2[xxxii] for this grant. Appendix A explains the computer code. Appendix B and C present analytical solutions for the gravitational attraction due to the cylinder and the caps, and check the validity of our numerical model. Appendix D proposes an approximation of the gravitational field and its gradient by using radial basis functions.

General Approach

The purpose of this work is to model and analyze the gravitational attraction between the capsule and the test body. There are at least three ways to approach this problem. The first approach is to compute the force between each capsule mass element and a test body mass element, and to perform a double summation on these forces. If N is the number of capsule mass elements, and N_B is the number of test body mass elements, then the cardinality of the computation is $N \otimes N_B$ (the complexity of the computation is the product of the complexity of a single element computation by the cardinality). The second approach is a double integration over the bodies. The drawback of the first approach is the heavy computational effort, especially if we need, in the future, an online computation in a dynamical process. The weakness of the second approach is in the cumbersome analytical computation. Moreover, the integration will result in an asymptotic series of complicated functions. This will require intense computation. In addition, asymptotic series introduce a truncation error into the computation. We adopted a third approach for this model.

Our computational approach is to consider the capsule as a discrete ensemble of lumped mass, where the resultant force and torque acting on the test body are the cumulative force and torque due to each capsule mass element while the test body is terated with a series expansion. In other words, the interaction is between a finite body and a point mass. This approach is a tradeoff between the previous approaches, its cardinality is N. The main advantage is the flexibility in modeling any capsule shape, according to future requirements.

The purpose of the following computation is to come up with simple closed-form analytical expressions, for the force and torque acting on the spinning test mass due to the capsule gravitational attraction.

Gravitational Model

The gravitational potential for finite size bodies is:

$$V = -G \int_{\Re_o} \int_{\Re_B} \frac{dM_B}{r} dM_o$$

Where in our case $\Re_B$ is the test mass (proof mass), and $\Re_0$ represents the attracting bodies, like the capsule (cylinder and caps) and the Earth.

For the purpose of simplicity we will proceed with a representation of the test body, and a single element of the attracting mass, M_i.

The gravitational potential at a representative element mass M_i due to the test body is: $V(M_i) = -GM_i \int_{M_B} \frac{dM_B}{r}$, where $\bar{r}$ is the radius vector between an element mass of the test body and dM_oas shown in Figure 78.

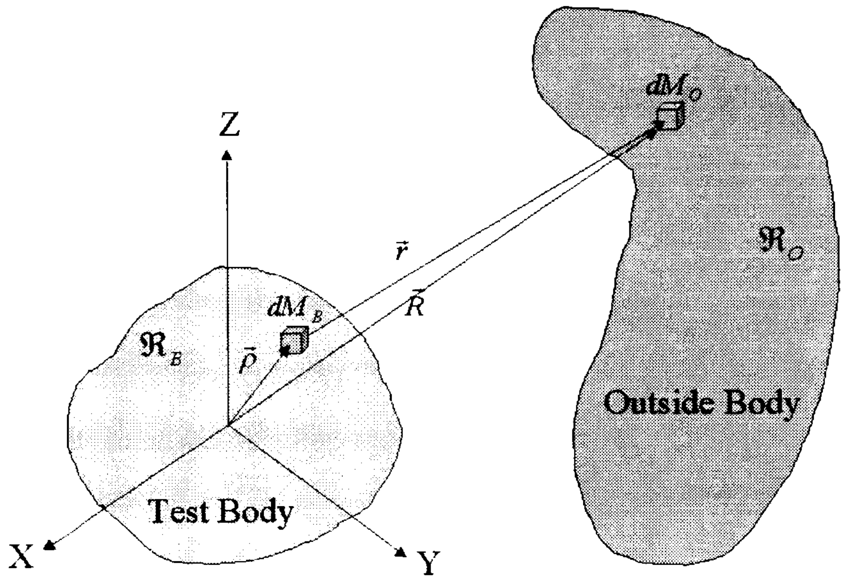

Figure 78 Gravitation model for test mass and outer attracting bodies

Assuming a sufficient discretization, the total force acting on the test body due to all outer mass elements is: $\vec{F}_B \cong \sum_{i=1}^{N} \nabla V(M_i)$, where N is the number of outer mass elements.

The model utilizes two coordinate systems. The first is the capsule frame, denoted by: $\{X,Y,Z\}$. X,Y are so far arbitrary, while Z coincides with the symmetry axis of the main cylinder. The test body frame, denoted by $\{x,y,z\}$, is attached to the test mass. So far, the origin and the orientation of the coordinate system are arbitrary. The gravitational potential will be expressed in body frame. The inertia coefficients of the body are constants in this frame.

The analytical procedure is to express $\vec{r}$ as $\vec{r} = \vec{R} - \vec{\rho}$, and to expand the potential by the following power series: $\frac{1}{r} = \frac{1}{R} \sum_{n=0}^{\infty} \left(\frac{\rho}{R}\right)^n P_n\left(\frac{\vec{R} \cdot \vec{\rho}}{R\rho}\right)$.

Here P_n is the Legendre polynomial of degree n.

The derivation consists of the following steps. Substituting the inverse radius approximation into the potential, carrying out the integration, while expressing vectors in body frame, as follows. $\bar{R} = (l\bar{e}_x + m\bar{e}_y + n\bar{e}_z)R$ and $\bar{\rho} = x\bar{e}_x + y\bar{e}_y + z\bar{e}_z$, where $\{e_x \ e_y \ e_z\}$ are body unit directions, and $l, m. n$ are direction cosines between $\bar{R}$ and the body axes. The resulting potential is a summation over all mass elements M_i:

$$V = \sum_{i=1}^{N}\{-\frac{GM_1M_2}{R} - \frac{GM_1M_2}{R^2}[l\bar{x} + m\bar{y} + n\bar{z}]$$

$$-\frac{GM_1}{2R^3}[(3l^2-1)\mathrm{J}_{xx} + (3m^2-1)\mathrm{J}_{yy} + (3n^2-1)\mathrm{J}_{zz} + 6(lm\,\mathrm{J}_{xy} + ln\,\mathrm{J}_{xz} + mn\,\mathrm{J}_{yz})]$$

$$-\frac{GM_1}{2R^4}[l(5l^2-3)\mathrm{J}_{xxx} + m(5m^2-3)\,\mathrm{J}_{yyy} + n(5n^2-3)\mathrm{J}_{zzz}$$

$$+ 3m(5l^2-1)\mathrm{J}_{xxy} + 3n(5l^2-1)\,\mathrm{J}_{xxz} + 3l(5m^2-1)\,\mathrm{J}_{xyy}$$

$$+ 3n(5m^2-1)\,\mathrm{J}_{yyz} + 3l(5n^2-1)\mathrm{J}_{xzz} + 3m(5n^2-1)\mathrm{J}_{yzz}$$

$$+ 6lmn\,\mathrm{J}_{xyz}] + \mathrm{O}(\frac{1}{R^5})\}$$

where $j_{x^p y^q z^r}$ are the inertia integrals defined as:

$$j_{x^p y^q z^r} = \int_{M_B} x^p y^q z^r \, dm$$

For the second order, it is common to use the moment of inertia. The following relations relate them to the inertia integrals:

$$J_{xx} = \frac{1}{2}(\mathrm{I}_{yy} + \mathrm{I}_{zz} - \mathrm{I}_{xx})$$

$$J_{yy} = \frac{1}{2}(\mathrm{I}_{xx} + \mathrm{I}_{zz} - \mathrm{I}_{yy})$$

$$J_{xx} = \frac{1}{2}(\mathrm{I}_{xx} + \mathrm{I}_{yy} - \mathrm{I}_{zz})$$

$$J_{xy} = I_{xy}$$

$$J_{xz} = I_{xz}$$

$$J_{yz} = I_{yz}$$

We define $\vec{\delta} = \{\bar{x}, \bar{y}, \bar{z}\}$ as the offset between the origin of the frame and the center of mass. It should be emphasized at this point that the origin does not necessarily coincide with the center of mass. Although the test bodies are typically axisymmetric, and ideally the geometrical center is the center of mass, mass and/or mounting imperfections can displace the center of mass from the geometrical center.

Note that if the origin is at the center of mass, the body frame coincides with the principal axes, and $O(1/R^4)$ is neglected, then the resulting potential is the so-called MacCullagh formula:

$$V \cong -\frac{GM_1M_2}{R} - \frac{GM_1}{2R^3}\left(tr\mathrm{I} - 3\mathrm{I}_R\right),$$

where $\mathrm{I}_R = e_R \cdot \bar{\mathrm{I}} \cdot e_R = l^2\mathrm{I}_{xx} + m^2\mathrm{I}_{yy} + n^2\mathrm{I}_{zz}$ is the projection of the second order inertia tensor $\bar{\mathrm{I}}$ on $\vec{R}$.

The force acting on the body is the gradient of the potential (the negative gradient is the force acting on M_i).

The resulting total force components, in body frame, are:

$$\begin{aligned}
F_x = G \sum_{i=1}^{N} M_i \{ & \frac{M_B l}{R_i^2} + \frac{M_B}{R_i^3}\left[(3l_i^2 - 1)\bar{x} + 3l_i m_i \bar{y} + 3l_i n_i \bar{z}\right] \\
& + \frac{1}{R_i^4}[(\frac{5}{2}\Gamma_i - \mathrm{I}_{yy} - \mathrm{I}_{zz} + 2\mathrm{I}_{xx})l_i + 3m_i(5l_i^2 - 1)\mathrm{I}_{xy} + 3n_i(5l_i^2 - 1)\mathrm{I}_{xz} + 15l_i m_i n_i \mathrm{I}_{yz}] \\
& + \frac{1}{R_i^5}[\frac{1}{2}(35l_i^4 - 30l_i^2 + 3)\mathrm{J}_{xxx} + \frac{5}{2}(7m_i^2 - 3)l_i m_i \mathrm{J}_{yyy} + \frac{5}{2}(7n_i^2 - 3)l_i n_i \mathrm{J}_{zzz} \\
& + \frac{15}{2}(7l_i^2 - 3)l_i m_i \mathrm{J}_{xxy} + \frac{15}{2}(7l_i^2 - 3)l_i n_i \mathrm{J}_{xxz} + \frac{3}{2}(35l_i^2 m_i^2 - 5l_i^2 - 5m_i^2 + 1)\mathrm{J}_{xyy} \\
& + \frac{15}{2}(7m_i^2 - 1)l_i n_i \mathrm{J}_{yyz} + \frac{3}{2}(35l_i^2 n_i^2 - 5l_i^2 - 5n_i^2 + 1)\mathrm{J}_{xzz} + \frac{15}{2}(7n_i^2 - 1)l_i m_i \mathrm{J}_{yzz} \\
& + 3(7l_i^2 - 1)m_i n_i \mathrm{J}_{xyz}] + H.O.T\}
\end{aligned}$$

$$
\begin{aligned}
F_y &= G\sum_{i=1}^{N} M_i\{\frac{M_B m_i}{R_i^2}+\frac{M_B}{R_i^3}\left[3l_i m_i\bar{x}+(3m_i^2-1)\bar{y}+3m_i n_i\bar{z}\right] \\
&+\frac{1}{R_i^4}[(\frac{5}{2}\Gamma_i-\mathrm{I}_{\mathrm{xx}}-\mathrm{I}_{zz}+2\mathrm{I}_{\mathrm{yy}})m_i+3l_i(5m_i^2-1)\mathrm{I}_{xy}+15l_i m_i n_i\mathrm{I}_{\mathrm{xz}}+3n_i(5m_i^2-1)\mathrm{I}_{yz}] \\
&+\frac{1}{R_i^5}[\frac{5}{2}(7l_i^2-3)l_i m_i\mathrm{J}_{\mathrm{xxx}}+\frac{1}{2}(35m_i^4-30m_i^2+3)\mathrm{J}_{\mathrm{yyy}}+\frac{5}{2}(7n_i^2-3)m_i n_i\mathrm{J}_{\mathrm{zzz}} \\
&+\frac{3}{2}(35l_i^2 m_i^2-5m_i^2-5l_i^2+1)\mathrm{J}_{\mathrm{xxy}}+\frac{15}{2}(7l_i^2-1)m_i n_i\mathrm{J}_{xxz}+\frac{15}{2}(7m_i^2-3)l_i m_i\mathrm{J}_{\mathrm{xyy}} \\
&+\frac{15}{2}(7m_i^2-3)m_i n_i\mathrm{J}_{yyz}+\frac{15}{2}(7n_i^2-1)l_i m_i\mathrm{J}_{xzz}+\frac{3}{2}(35m_i^2 n_i^2-5m_i^2-5n_i^2+1)\mathrm{J}_{\mathrm{yzz}} \\
&+3(7m_i^2-1)l_i n_i\mathrm{J}_{\mathrm{xyz}}]+H.O.T\}
\end{aligned}
$$

$$
\begin{aligned}
F_z &= G\sum_{i=1}^{N} M_i\{\frac{M_B l}{R_i^2}+\frac{M_B}{R_i^3}\left[3l_i n_i\bar{x}+3m_i n_i\bar{y}+3(n_i^2-1)\bar{z}\right] \\
&+\frac{1}{R_i^4}[(\frac{5}{2}\Gamma_i-\mathrm{I}_{xx}-\mathrm{I}_{yy}+2\mathrm{I}_{zz})n_i+15l_i m_i n_i\mathrm{I}_{\mathrm{xy}}+3l_i(5n_i^2-1)\mathrm{I}_{xz}+3m_i(5n_i^2-1)\mathrm{I}_{yz}] \\
&+\frac{1}{R_i^5}[\frac{5}{2}(7l_i^2-3)l_i n_i\mathrm{J}_{xxx}+\frac{5}{2}(7m_i^2-3)m_i n_i\mathrm{J}_{yyy}+\frac{1}{2}(35n_i^4-30n_i^2+3)\mathrm{J}_{zzz} \\
&+\frac{15}{2}(7l_i^2-1)m_i n_i\mathrm{J}_{xxy}+\frac{3}{2}(35l_i^2 n_i^2-5l_i^2-5n_i^2+1)\mathrm{J}_{xxz}+\frac{15}{2}(7m_i^2-1)l_i n_i\mathrm{J}_{xyy} \\
&+\frac{3}{2}(35m_i^2 n_i^2-5m_i^2-5n_i^2+1)\mathrm{J}_{yyz}+\frac{15}{2}(7n_i^2-1)l_i n_i\mathrm{J}_{xzz}+\frac{15}{2}(7n_i^2-3)m_i n_i\mathrm{J}_{yzz} \\
&+3(7n_i^2-1)l_i m_i\mathrm{J}_{xyz}]+H.O.T\}
\end{aligned}
$$

where

$$
\Gamma_i=(\mathrm{I}_{yy}+\mathrm{I}_{zz}-2\mathrm{I}_{xx})l_i^2+(\mathrm{I}_{xx}+\mathrm{I}_{zz}-2\mathrm{I}_{yy})m_i^2+(\mathrm{I}_{xx}+\mathrm{I}_{yy}-2\mathrm{I}_{zz})n_i^2
$$

Note that the force has the following order of magnitude:

$$
F\propto\sum_i G\frac{M_i M_B}{R_i^2}\{O(1)+O(\frac{\bar{\rho}}{R_i})+O(\frac{L_B^2}{R_i^2})+O(\frac{L_B^3}{R_i^3})+H.O.T\}
$$

Where L_B is a typical length of the test body, $\frac{L_B}{R_i}<<1$, and $\frac{\bar{\rho}}{R_i}<<1$.

Gravity Torques

The torque, acting on the test body, can be computed with respect to the center of mass or with respect to the geometrical center. Both coincide when the body has perfect symmetries. In reality there are mass imperfections that cause the center of mass to deviate from the geometrical center. Since we have no a-priori knowledge of the imperfections, our reference point for computing the torque is the geometrical center.

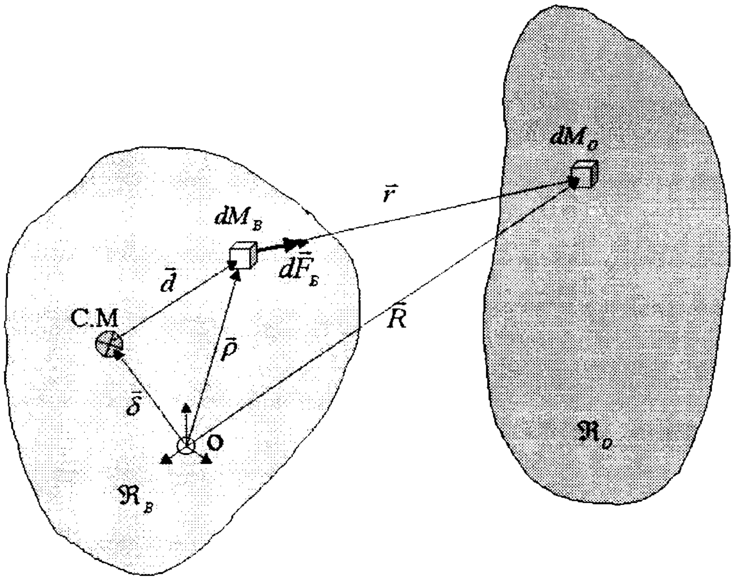

Figure 79 A Model for the Torque

There are few approaches for computing the gravity torque. Our approach is to integrate the torque due to mass element in each body. The torque with respect to an arbitrary point is, therefore:

$$\vec{T}_o = \vec{T}_{C.M} + \vec{\delta} \times \vec{F}_B$$

where,

$$\vec{T}_{C.M} = G \int_{\Re_O} \int_{\Re_B} \vec{d} \times \frac{\vec{r}}{r^3} dM_B \, dM_O \cong G \sum_{i=1}^{N} m_i \int_{\Re_B} \frac{\vec{d} \times \vec{R}}{r^3} dM_B$$

$$\vec{F}_B = G \int_{\Re_O} \int_{\Re_B} \frac{\vec{r}}{r^3} dM_B \, dM_O = G \sum_{i=1}^{N} m_i \int_{\Re_B} \frac{\vec{r}}{r^3} dM_B$$

There are three approaches to compute the integrals. The choice of the approach depends on the size of each body. If both $\Re_B$ and $\Re_O$ are small compared with R, than we can expand r, and obtain an analytical approximation. If only $\Re_B$ is small, as in our case, we can approximate $\Re_B$ but have to integrate numerically in $\Re_O$. If both are large relative to r, then the only way is to perform a double numerical integration. In our case, not only $\Re_O$ is large, it is also surrounded by $\Re_B$, so there is no topological way to expand r in $\Re_O$.

$$\begin{aligned}
T_x = 3G \sum_{i=1}^{N} M_i \{ & \frac{1}{R_i^3} [m_i n_i (I_{zz} - I_{yy}) + l_i n_i I_{xy} - l_i m_i I_{xz} + (n_i^2 - m_i^2) I_{yz}] \\
& + \frac{1}{2R_i^4} [n_i (5m_i^2 - 1) J_{yyy} - m_i (5n_i^2 - 1) J_{zzz} + n_i (5l_i^2 - 1) J_{xxy} + 10 l_i m_i n_i J_{xyy} \\
& - m_i (5l_i^2 - 1) J_{xxz} - 10 l_i m_i n_i J_{xzz} + m_i (10n_i^2 - 5m_i^2 + 1) J_{yyz} \\
& - n_i (10m_i^2 - 5n_i^2 + 1) J_{yzz} + 10 l_i (n_i^2 - m_i^2) J_{xyz}] + \mathrm{H.}O.T \}
\end{aligned}$$

$$\begin{aligned}
T_y = 3G \sum_{i=1}^{N} M_i \{ & \frac{1}{R_i^3} [l_i n_i (I_{xx} - I_{zz}) - m_i n_i I_{xy} + l_i m_i I_{yz} + (l_i^2 - m_i^2) I_{xz}] \\
& + \frac{1}{2R_i^4} [-n_i (5l_i^2 - 1) J_{xxx} + l_i (5n_i^2 - 1) J_{zzz} - 10 l_i m_i n_i J_{xxy} - n_i (5m_i^2 - 1) J_{xyy} \\
& - l_i (10n_i^2 - 5l_i^2 + 1) J_{xxz} + n_i (10l_i^2 - 5n_i^2 + 1) J_{xzz} + l_i (5m_i^2 - 1) J_{yyz} + 10 l_i m_i n_i J_{yzz} \\
& + 10 m_i (l_i^2 - n_i^2) J_{xyz}] + \mathrm{H.}O.T \}
\end{aligned}$$

$$T_z = 3G\sum_{i=1}^{N} M_i\{\frac{1}{R_i^3}[l_i m_i(I_{yy} - I_{xx}) - (m_i^2 - l_i^2)I_{xy} + m_i n_i I_{xz} - l_i n_i I_{yz}]$$

$$+ \frac{1}{2R_i^4}[m_i(5l_i^2 - 1)J_{xxx} - l_i(5m_i^2 - 1)J_{yyy} + l_i(10m_i^2 - 5l_i^2 + 1)J_{xxy}$$

$$- m_i(10l_i^2 - 5m_i^2 + 1)J_{xyy} + 10l_i m_i n_i J_{xxz} + m_i(5n_i^2 - 1)J_{xzz} - 10l_i m_i n_i J_{yyz}$$

$$- l_i(5n_i^2 - 1)J_{yzz} + 10n_i(m_i^2 - l_i^2)J_{xyz}] + \mathrm{H.}O.T\}$$

The order of magnitude of the torque is:

$$T \propto \sum_i G\frac{M_i M_B}{R_i}\{O(\frac{L_B^2}{R_i^2}) + O(\frac{L_B^3}{R_i^3}) + H.O.T\}$$

If the origin is at the center of mass and the body frame coincides with the principal axes, then the resulting torque is reduced the well-known expression (based on MacCullagh formula):

$$T_x \cong 3G(\mathrm{I_{zz}} - \mathrm{I_{yy}})\sum_{i=1}^{N}\frac{M_i}{R_i^3}m_i n_i$$

$$T_y \cong 3G(\mathrm{I_{xx}} - \mathrm{I_{zz}})\sum_{i=1}^{N}\frac{M_i}{R_i^3}l_i n_i$$

$$T_z \cong 3G(\mathrm{I_{yy}} - \mathrm{I_{xx}})\sum_{i=1}^{N}\frac{M_i}{R_i^3}l_i m_i$$

Proposal for frequency decomposition

We would like to propose a more general approach for a closed-form solution of the force/torque in terms of their frequencies.

Let us expand the force in potential orders as well as a Fourier series in the spin angle, assuming a pure spin around the axial axis of the test body.

$$\vec{F} = G\int_{\Re_o}\frac{1}{R^{d+2}}\sum_{d=0}^{d_{\max}}\{\vec{a}_0^{(d)} + \sum_{n=1}^{d+1}[\vec{a}_n^{(d)}\cos n\varphi + \vec{b}_n^{(d)}\sin n\varphi]\}dM_0$$

where d is the degree of the inertia. Let $J_{x^i y^j z^k} = \int x^i y^j z^k dM_B$ than $d = i + j + k$. Assuming that we have carried out the integration (analytically or by numerical means), $\vec{F}$ can be expressed as:

$$\vec{F} = G \sum_{d=0}^{d_{\max}} \{\vec{A}_0^{(d)} + \sum_{n=1}^{d+1} [\vec{A}_n^{(d)} \cos n\varphi + \vec{B}_n^{(d)} \sin n\varphi]\}$$

where $\vec{A}_n^{(d)} = \int\limits_{\Re_0} \frac{\vec{a}_n^{(d)}}{R^{d+2}} dM_o$, and $\vec{B}_n^{(d)} = \int\limits_{\Re_0} \frac{\vec{b}_n^{(d)}}{R^{d+2}} dM_o$.

These coefficients may be viewed as a generalization of the inertia coefficients of $\Re_O$. If $\Re_O$ is topologically connected (i.e., $\Re_B$ is outside $\Re_O$), and if $\Re_O$ is sufficiently small, then one may asymptotically expand these integrals. This will result in the inertia coefficients of $\Re_O$. In our case, these coefficients can be computed numerically, or sometimes analytically, when $\Re_O$ is simple enough.

For a more general rotation, one needs to express the direction cosines in terms of the general transformation matrix (rather than the single-axis rotation).

Order of Magnitude and Similarity Analysis

The dominant sources of the gravitational attraction are the capsule, the Earth, and to a lesser degree the Moon. Let us perform a qualitative comparison of each source. First, we should note that the force acting on the test mass is not a homogeneous function of the mass and the radius (as a force acting on a point mass). This is because the parameters R and M_B contribute as:

$$F \propto O\left(\frac{M_B}{R^2}\right) + O\left(\frac{M_B}{R^3}\right) + O\left(\frac{M_B}{R^4}\right) + O\left(\frac{M_B}{R^5}\right), \text{ or}$$

$$F \propto F^{(0)} + F^{(1)} + F^{(2)} + F^{(3)},$$

where $F^{(0)}$ represents the 2-Body term, and so on (the order enumeration is according to the corresponding Inertia order). Therefore, it is impossible to express the ratio of forces from different sources as $F(M1,R1)/F(M2,R2) \propto f((M1/M1)^m, (R1/R1)^n)$.

On the other hand, each order is homogeneous, that is

$$F^{(k)}(M1,R1)/F^{(k)}(M2,R2) = (M1/M2)(R2/R1)^{(k)}$$

Therefore, in order to compare different sources of attraction, we must consider each order separately.

The following qualitative discussion concerns the force difference between the two test bodies. Let us denote $f()$ as a generic function, then a generic expression for the force acting on test mass B_j is:

$$F^{B_j} = f(M_j;)O\left(\frac{1}{R^2}\right) + f(\bar{\rho}_j;)O\left(\frac{1}{R^3}\right) + f(I_{2j};)O\left(\frac{1}{R^4}\right) + f(I_{3j};)O\left(\frac{1}{R^5}\right)$$

We present two models for the force difference. In the first model the two test bodies are centered, and the inertia components of the bodies are different. In the second model, the bodies have equal inertia, but are not centered. These two models are idealization of the two sources of difference, while the reality is probably a combination of these.

The force difference for the first model is:

$$\Delta F = F^{B_2} - F^{B_1} = f(\Delta M;)O\left(\frac{1}{R^2}\right) + f(\Delta\bar{\rho};)O\left(\frac{1}{R^3}\right) + f(\Delta I_2;)O\left(\frac{1}{R^4}\right) + f(\Delta I_3;)O\left(\frac{1}{R^5}\right)$$

The force difference for the second model is represented by a differential. For central deviation ε, the force differential is:

$$dF \cong F^{B_2} - F^{B_1} \cong \nabla F \cdot \varepsilon = f(M;)O\left(\frac{1}{R^3}\right) + f(\bar{\rho};)O\left(\frac{1}{R^4}\right) + f(I_2;)O\left(\frac{1}{R^5}\right) + f(I_3;)O\left(\frac{1}{R^6}\right)$$

The ratio between force terms of order k from two different sources 1 and 2, is:

$$\frac{F^{(k)}(M_1, R_1)}{F^{(k)}(M_2, R_2)} = \frac{M_1}{M_2}\left(\frac{R_2}{R_1}\right)^k$$

The following table compares the force order of magnitude due to different sources. Note that we eliminated order 0 (2-Body), since the test body is in free fall.

Table 1 Ratio of force terms for few orders for the dominant gravitational sources

Inertia order	Capsule / Earth	Capsule / Moon	Earth / Moon
1	$4*10^{-3}$	$8*10^{4}$	$2*10^{7}$
2	$3*10^{4}$	$3*10^{13}$	$1*10^{9}$
3	$2*10^{11}$	$1*10^{22}$	$6*10^{10}$
4	$1*10^{18}$	$4*10^{30}$	$4*10^{12}$

It is obvious that the effect of the Moon is negligible. The Earth is dominant only with respect to the gravity gradient. Again, as the order under consideration becomes higher, the effect of the capsule increases.

To gain more insight into the nature of gravitational attraction let us examine the force. It can be rewritten in the following form:

$$F = O\left(\frac{1}{R^2}\right)O(c) + O\left(\frac{1}{R^3}\right)O(c^E) + O\left(\frac{1}{R^4}\right)O(c^O) + O\left(\frac{1}{R^5}\right)O(c^E)$$

Where c represents the direction cosines. The notations c^O and c^E show the nature of the degree of the direction cosines (odd or even). For example, a square of a particular direction cosine has an even degree, while a product of the three direction cosines has an odd degree. Now, suppose that the test mass is at the center of the cylinder. Since for each direction cosine to a mass element there is an opposite direction cosine, all the odd terms are cancelled out. Therefore, the only non-zero contribution is due to the even terms.

Another important issue is the role of the test body mass and size. For this purpose we perform a similarity analysis, as shown in the following.

We formulated the gravitational potential as an asymptotic series in $1/R^n$. Each term in the series has an inertial tensor of degree $n - 1$. For example, the first term is of order n = 1 and its inertia tensor is of order 0 (the test body mass). The third term is of degree n = 3 and its inertia tensor is of order 2. This non-uniformity introduces a problem, as mentioned earlier, when one computes the forces for a particular test mass, and wants to deduct the forces for a different scale of test mass. Mathematically speaking, if $F(M_{B1})$ and $F(M_{B2})$ are the forces due to two different test masses, then the ratio between the forces is not a homogeneous function, that is, $F(M_{B1})/F(M_{B2}) \neq g((M_{B1}/M_{B2})^m)$ where g is a function and m is the degree of the homogeneity. Note however that each term of the series is homogeneous by itself. For example, the first term is homogeneous of degree one, that is, the ratio between forces equals the ratio between the masses.

We will distinguish between two cases. In both, the mass distribution of the different test masses can be scaled. The first case is when the difference in masses is due to a different density. Since the forces are homogeneous of degree one in density, the ratio between the forces is equal to the ratio between the masses. In the second case the density is the same, and the different mass is due to different sizes. In this case we will apply a different similarity to each term. Let L and M be scaling factors for the length and the mass, respectively. If the density of different test bodies is the same, then $L \propto M^{1/3}$. Let $m = n - 1$ be the order of the moment of inertia. Its similarity dimension is $L^m M$, or $M^{1+m/3}$, or L^{m+3}. The acceleration similarity is $M^{m/3}$ or L^m. The following table summarizes the similarity dimension for each term in the potential.

Table 2 Similarity relations for the gravitational potential terms

Potential Order $n: 1/R^n$	Inertia Order $m = n - 1$	Inertia Similarity	Acceleration Similarity
1	0	$M \quad (L^3)$	$1 \quad (1)$
2	1	$M^{4/3} \; (L^4)$	$M^{1/3} \; (L)$
3	2	$M^{5/3} \; (L^5)$	$M^{2/3} \; (L^2)$
4	3	$M^2 \quad (L^6)$	$M \quad (L^3)$
5	4	$M^{7/3} \; (L^7)$	$M^{4/3} \; (L^4)$

To summarize, given the force (or the acceleration) due to a particular test body, we can deduct the force (acceleration) due to another geometrically scaled test mass. The acceleration ratio (of two different test masses) versus similarity dimensions (mass and length) is illustrated in the following plot.

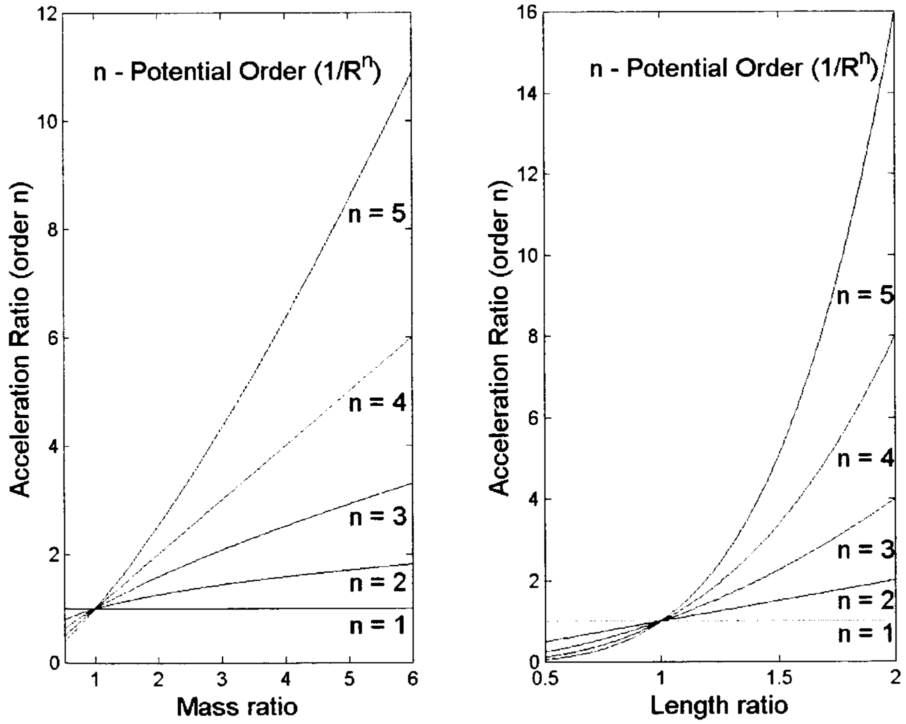

Figure 80 Scaling of Acceleration of Test Mass

The maximum potential order considered in this analysis is the hexadecapole (n = 5) which involves the fourth-order inertia integrals. We computed numerically the forces associated with the hexadecapole for a body with equal second-order inertia integrals (in order to minimize the quadrupole term). The results show that, at the worst expected location inside the capsule, the maximum acceleration associated with the hexadecapole term for a 1-kg proof mass are less than 10^{-16} g. In other words, for the accuracy goal of this experiment there is no need for belted cylinders (which would reduce the hexadecapole component even further). Proof masses with equal second-order inertia integrals (or alternatively moments of inertia) and construction accuracy of order ten microns are sufficient to make the contributions of all the higher-order gravity terms negligible.

EFFECT OF INERTIA IMPERFECTION ON A SPINNING TEST MASS

Our goal is to minimize the gravitational forces acting on the test mass. The force equations reveal that the dominant term under our control is the term corresponding to the second order inertia. The CM offset effect may be bigger to start with but it can be reduced by centering. The direct way to minimize the forces is to require equal second moments of inertia. The residual forces then are due to mass imperfection, and to higher order inertia integrals. The purpose of the following discussion is to explore the effect of each term for a spinning test body.

First we will evaluate the mixed-inertia terms due to the imperfection.

We assume that the imperfection is due to disturbance in mass and in length. The nominal test body is a perfect cylinder, with radius R_B and length L_B. In order to minimize the force we require that $I_{XX} = I_{YY} = I_{ZZ}$. This constraint results in a given aspect ratio of the cylinder as follows: $L_B = \sqrt{3}R_B$. Given the mass density, the mass or the sizes of the cylinder are now functions of a single free parameter. For example, given the mass, M_B, and the density, ρ_B, the length is: $L_B = \left(\frac{3M_B}{\pi\rho_B}\right)^{\frac{1}{3}}$

The similarity dimension of the k-order inertia is: $[I] = ML^k$. Thus, the perturbed k-ordered inertia is: $[\delta I] = L^k\,\delta M + kML^{k-1}\delta L$, or

$$\left[\frac{\delta I}{I}\right] = \left[\frac{\delta M}{M}\right] + k\left[\frac{\delta L}{L}\right]$$

Next we consider the effect of the spin. The test body is spinning about its x-axis with a frequency that will be regarded as a fundamental frequency, or P1 (period one). We are primarily concerned with P1 which is the period of the measured signal. For that purpose we will analyze F_Y by substituting the direction cosines, shown below, into the force expression (note that y is the sensitive axis of the accelerometer).

$$l_i = l_i(t;P1);\quad m_i = m_i(t;P1);\quad n_i = n_i(t;P1)$$

It is important to note that the forces are expressed in body frame. The direction cosines are P1-periodic. Moreover, if the body fall such that the body x-axis is parallel to the capsule X-axis, only m and n are periodic, as will be seen from the following discussion.

The periodicity in time is introduced through the direction cosines that represent the orientation of the body frame relative to the capsule frame. The transformation between the two is:

$$\begin{bmatrix} x \\ y \\ z \end{bmatrix} = \begin{bmatrix} 1 & 0 & 0 \\ 0 & c\theta & s\theta \\ 0 & -s\theta & c\theta \end{bmatrix} \begin{bmatrix} X \\ Y \\ Z \end{bmatrix}$$

The resulting direction cosines are:

$$l = \frac{x}{R} = \frac{X}{R} \neq l(\theta)$$

$$m = \frac{y}{R} = \frac{Y c\theta + Z s\theta}{R}$$

$$n = \frac{z}{R} = \frac{-Y s\theta + Z c\theta}{R}$$

l is a cyclic function only if the body deviates from the X-axis. If the test body is perfect, then only the point mass term and the first term of $O(1/R^4)$ contribute to Fy. Otherwise, m, n introduce higher harmonics. If the power of the direction cosines is even (N_E), than the additional harmonics are: $P_0, P_2, \cdots, P_{N_E}$. For odd power ($N_O$) the additional harmonics are: $P_1, P_3, \cdots, P_{N_O}$. The dominant time dependency of a perfect body is introduced through the first order attraction on a point mass. It results in a fundamental frequency, because the gravitational attraction is static in the capsule frame, while the measurement is in the rotating body frame.

The expected frequencies are the following. P1 from the point mass term $O(1/R^2)$. P1 and P2 from the offset term $O(1/R^3)$. Since Γ_i contributes P2, the term of $O(1/R^4)$ contributes P1 and P2. However, because of the almost axial-symmetricity of the test body, Γ_i is almost a constant, so the dominant frequency of $O(1/R^4)$ should be P1. The term of $O(1/R^5)$ contributes P1, P2, P3 and P4, where P2 should be dominant.

The analysis above is for the x-axis parallel to the X-axis, that is, for $l = \text{constant}$. Otherwise $l = l(\theta)$ and higher frequencies are involved. The explicit orientation dependency of period one (P1) becomes:

$$F_y^{Body}(\theta;P_1) = G\sum_{i=1}^{N} M_i \left\{ \frac{1}{R_i^2}\tilde{F}_y^{(2)} + \frac{1}{R_i^3}\tilde{F}_y^{(3)} + \frac{1}{R_i^4}\tilde{F}_y^{(4)} + \frac{1}{R_i^5}\tilde{F}_y^{(5)} \right\}$$

where

$$\tilde{F}_y^{(2)} = M_B(\hat{Y}_i\cos\theta + \hat{Z}_i\sin\theta)$$

$$\tilde{F}_y^{(3)} = 3M_B\hat{X}_i(\hat{Y}_i\cos\theta + \hat{Z}_i\sin\theta)\bar{x}$$

$$\begin{aligned}\tilde{F}_y^{(4)} &= \left\{\frac{5}{2}[A\hat{X}_i^2\hat{Y}_i + \frac{1}{4}(3B+C)(\hat{Y}_i^3 + \hat{Y}_i\hat{Z}_i^2)] - B\hat{Y}_i\right\}\cos\theta \\ &+ \left\{\frac{5}{2}[A\hat{X}_i^2\hat{Z}_i + \frac{1}{4}(3B+C)(\hat{Y}_i^2\hat{Z}_i + \hat{Z}_i^3)] - B\hat{Z}_i\right\}\sin\theta\end{aligned}$$

$$\tilde{F}_y^{(5)} = \frac{5}{2}(7\hat{X}_i^2 - 3)(\hat{Y}_i\cos\theta + \hat{Z}_i\sin\theta)\hat{X}_i I_{xxx}$$

and $\hat{X}_i = X/R$, $\hat{Y}_i = Y/R$, $\hat{Z}_i = Z/R$ are the direction cosines in the capsule frame.

An interesting case is the effect of the attraction of a point mass located on the Z-axis. It may represent the Earth attraction on horizontally falling body, or the caps on the top or the button of the capsule.

Let the attracting mass M_1 be at $Z1 = \mp R_1$ in the plane $X = Y = 0$. Using the relations: $Z_1 = R_1\,\mathrm{sgn}(Z_1), \hat{Z}_1 = \mathrm{sgn}(Z_1)$, $\hat{Z}^2 = 1$, and substituting the attracting mass coordinates results in the following simple equation:

$$F_y^{Body}(\theta;P_1,I=0) = GM_i\left\{\frac{M_B}{R_i^2} + \frac{1}{8}\frac{1}{R_i^4}(7B+5C)\right\}\mathrm{sgn}(Z_1)\sin\theta$$

Again, the relations above are the terms corresponding to P1. The other frequencies may be observed from analytical expansions, or from a numerical frequency analysis, as demonstrated in the next section.

Numerical Investigation of an Imperfect Spinning Test Body

The scenario under investigation is shown in Figure 81. The capsule consists of a hollow cylinder, covered by two flat caps and a total mass of 500 kg. The test body mass is 1 kg with sizes: $R_B = 0.0412m$ and $L_B = 0.0713m$. The geometrical and mass inhomogeneity errors are: $\delta L/L = 10^{-4}$ and $\delta M/M = 10^{-5}$. Consequently, the offset components are: $\bar{x} = 1.7\times10^{-6}m$, $\bar{y} = 2\times10^{-6}m$, $\bar{z} = 1.7\times10^{-6}m$. The components of the inertial matrix are: $I_{XX} = 8.5\times10^{-4}$ kg-m^2, $I_{YY} = 8.501\times10^{-4}$ kg-m^2, $I_{ZZ} = 8.5015\times10^{-4}$ kg-m^2. Note that the nominal values of those are the same. The mass perturbations prevent the elimination of the following inequalities: $I_{XX} + I_{YY} - 2I_{ZZ} \neq 0$, $I_{XX} + I_{ZZ} - 2I_{YY} \neq 0$, $I_{YY} + I_{ZZ} - 2I_{XX} \neq 0$.

$I_{XY} = 3\times10^{-8}$ kg-m^2, $I_{XZ} = 3\times10^{-8}$ kg-m^2, $I_{YZ} = 4\times10^{-8}$ kg-m^2. The components of the third-order inertia tensor are: $I_{XXX} = 5\times10^{-10}$, $I_{YYY} = 8\times10^{-10}$, $I_{ZZZ} = 8\times10^{-10}$, $I_{XXY} = 6\times10^{-10}$, $I_{XXZ} = 6\times10^{-10}$, $I_{XYY} = 7\times10^{-10}$, $I_{YYZ} = 8\times10^{-10}$, $I_{XZZ} = 6\times10^{-10}$, $I_{YZZ} = 8\times10^{-10}$, $I_{XYZ} = 7\times10^{-10}$ (all in kg-m^3).

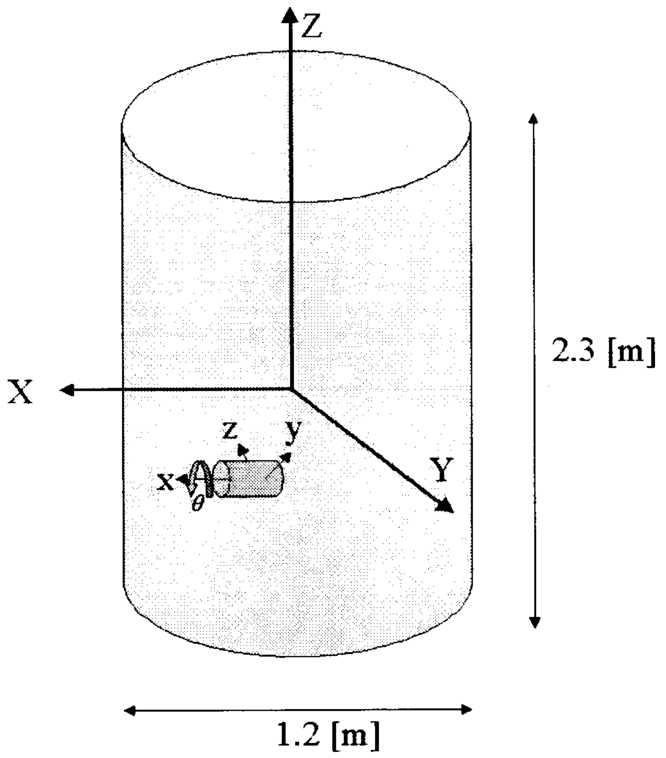

Figure 81 Coordinate systems for the test body and the capsule (dimensions account for the thickness of the capsule walls)

The gravitational force and the torque acting on the test mass were computed at 9 points inside the capsule. Three points along the axial axis, three points along an axis deviated by 0.1 m from the axial axis, and three points along an axis deviated by 0.2 m from the axial axis. The ninth point is the farthest away, thus representing the worst case.

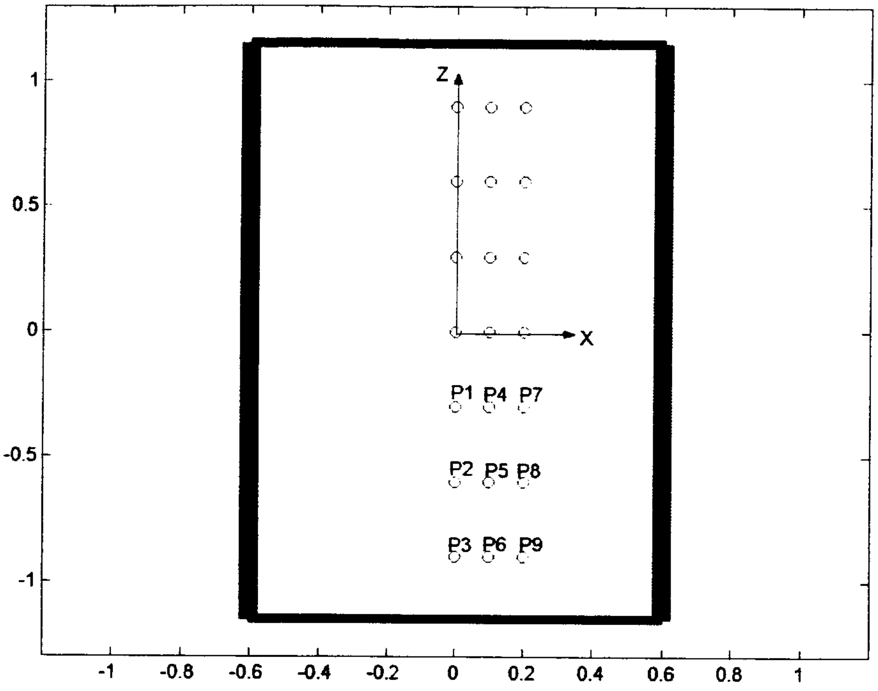

Figure 82 Tested Points inside the Capsule

We are mostly interested in F_Y (F_Y is in phase with F_Z) and in T_X. Because of the free fall, we exclude the 2-Body terms. The following plots show the angular history of the force/torque for a single revolution with respect to the x-axis, and the corresponding spectra. The latter are normalized, such that the highest amplitude is equal to one. The results are given in the following 18 plots. The analysis of the frequency spectrum requires a closed look at the equations for the force and torque, considering the particular location of the test mass relative to the capsule. Some of the results are non intuitive. The general approach to estimate the results is to specify each term according to the degree of the direction cosines (odd or even), and consider possible cancellations due to anti-symmetricity with respect to the radius vector between the test mass and each capsule element. The results are shown in the following figures.

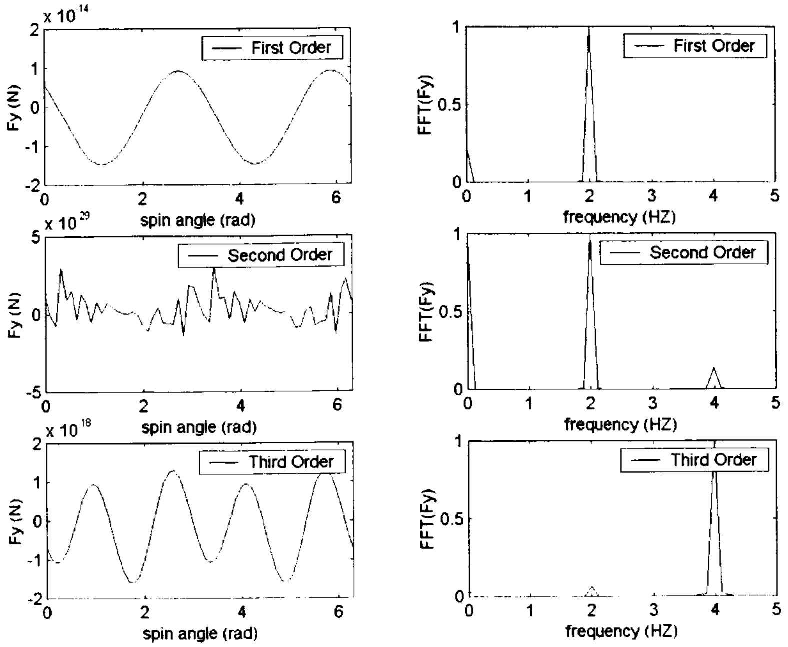

Figure 83 Ordered Force and harmonics at Point 1 due to Capsule Attraction

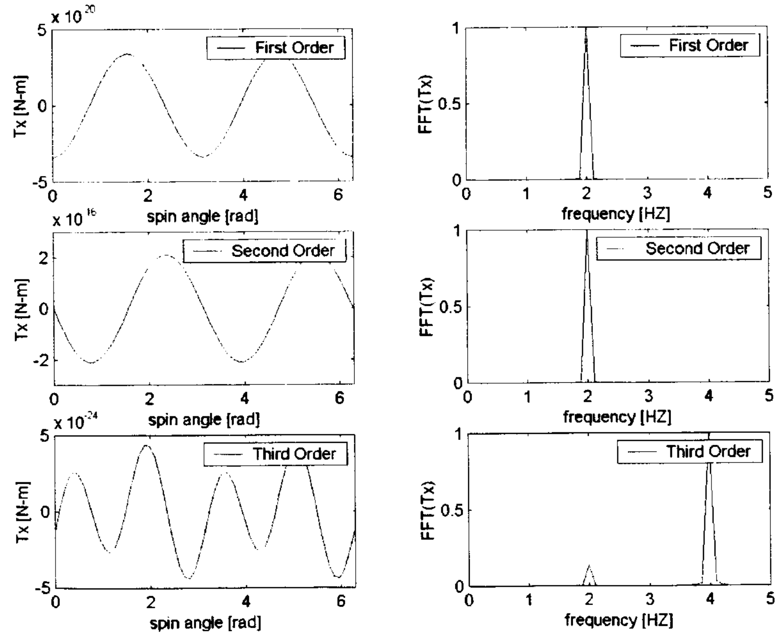

Figure 84 Ordered Torque and harmonics at Point 1 due to Capsule Attraction

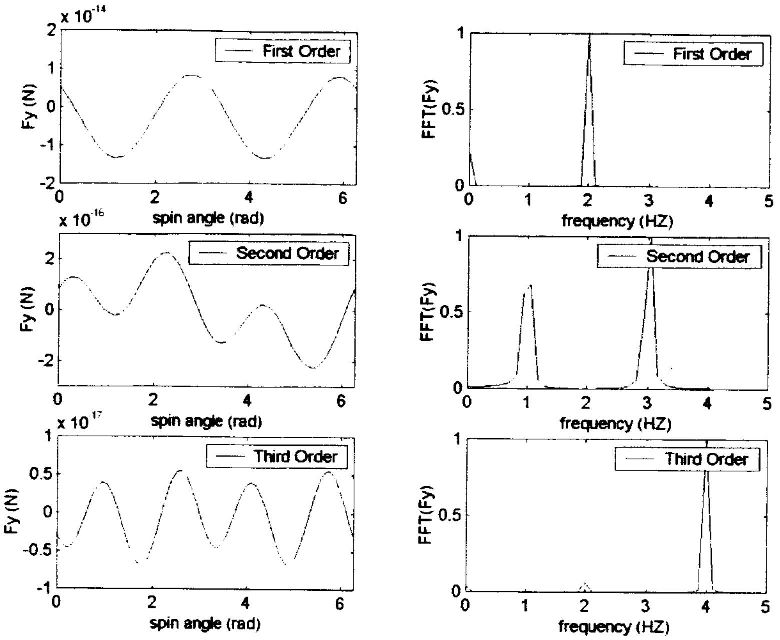

Figure 85 Ordered Force and harmonics at Point 2 due to Capsule Attraction

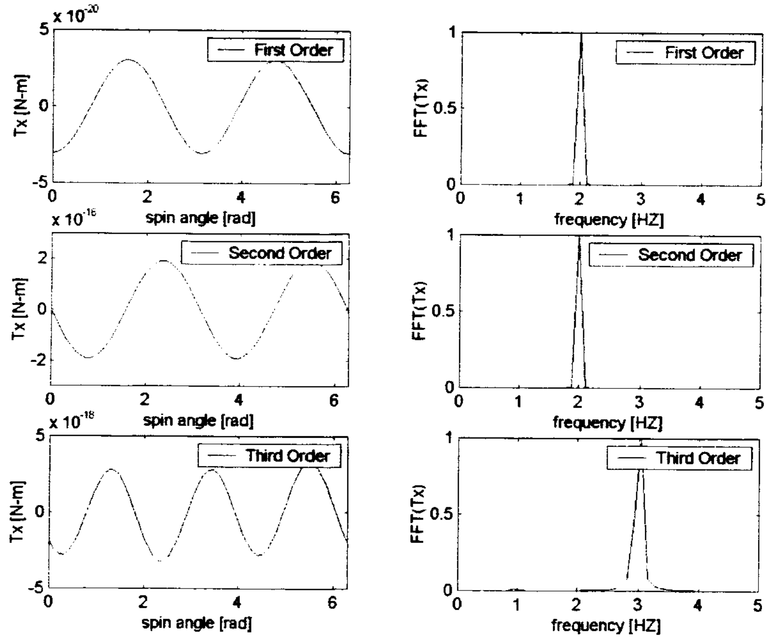

Figure 86 Ordered Torque and harmonics at Point 2 due to Capsule Attraction

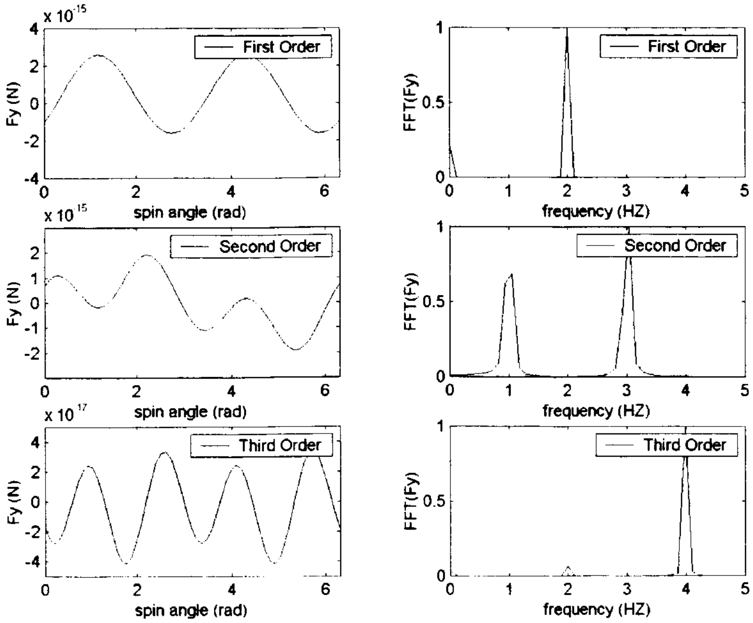

Figure 87 Ordered Force and harmonics at Point 3 due to Capsule Attraction

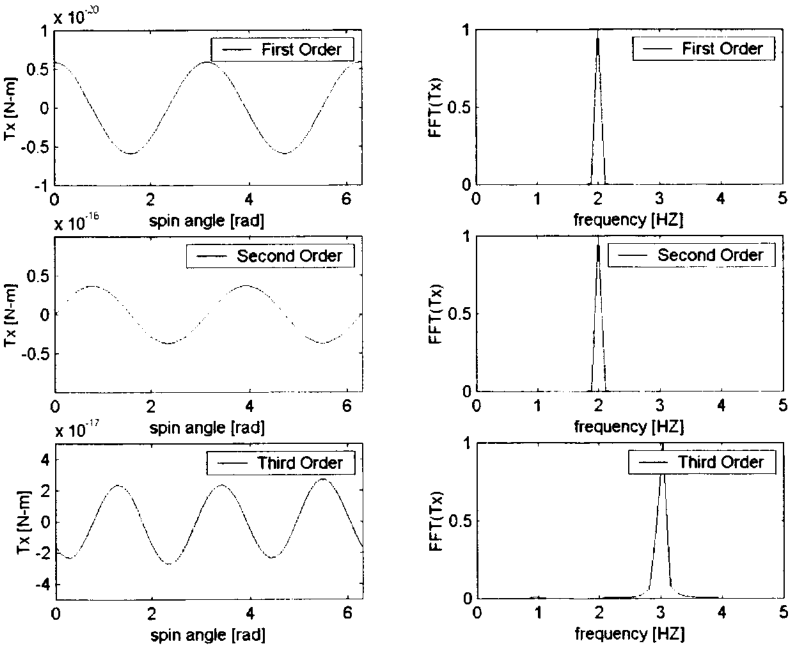

Figure 88 Ordered Torque and harmonics at Point 3 due to Capsule Attraction

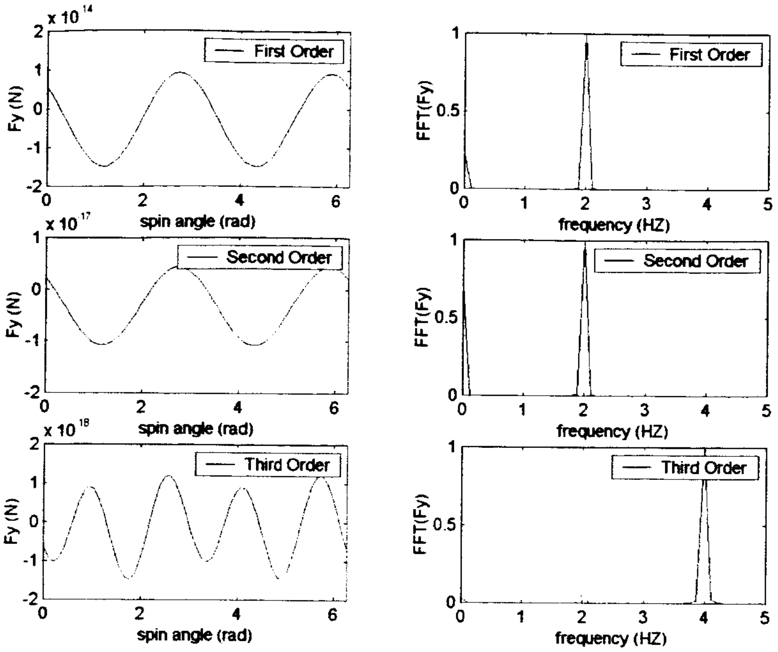

Figure 89 Ordered Force and harmonics at Point 4 due to Capsule Attraction

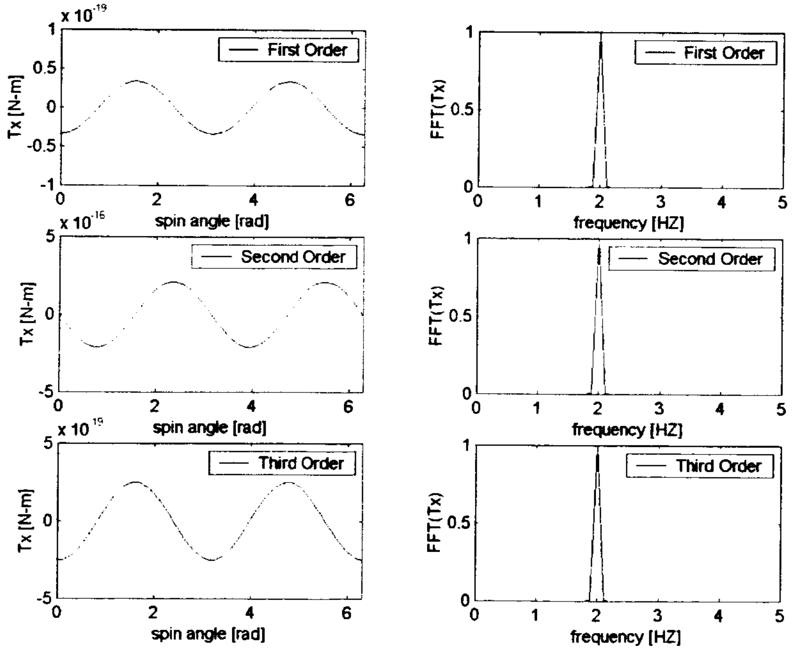

Figure 90 Ordered Torque and harmonics at Point 4 due to Capsule Attraction

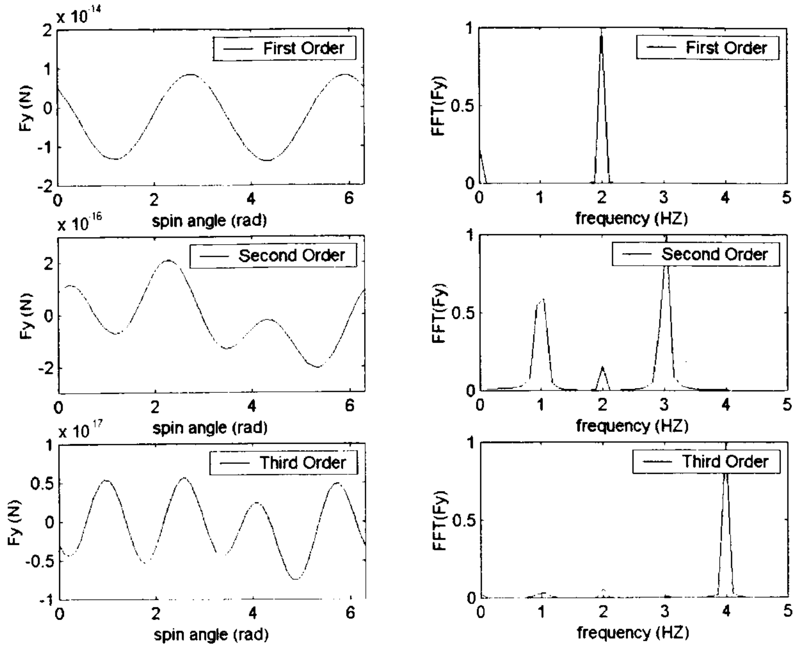

Figure 91 Ordered Force and harmonics at Point 5 due to Capsule Attraction

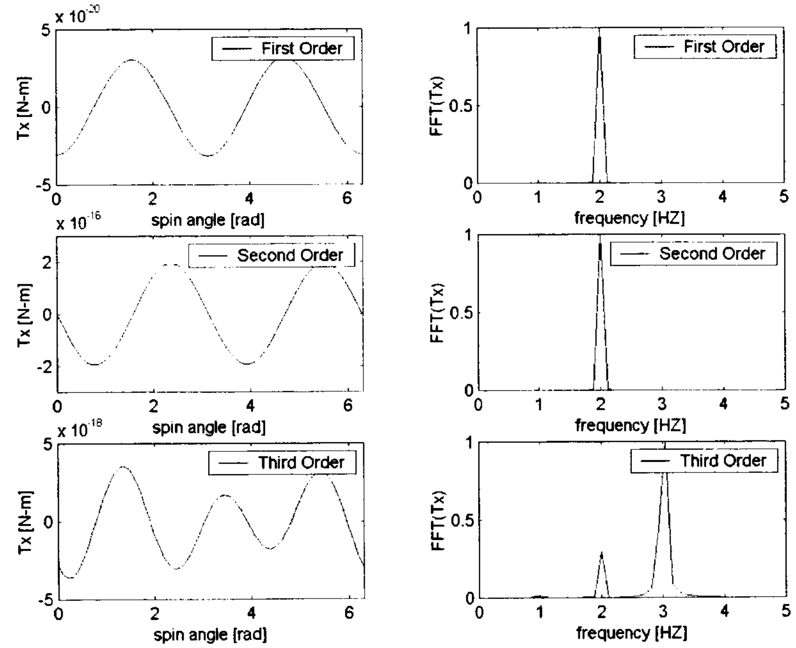

Figure 92 Ordered Torque and harmonics at Point 5 due to Capsule Attraction

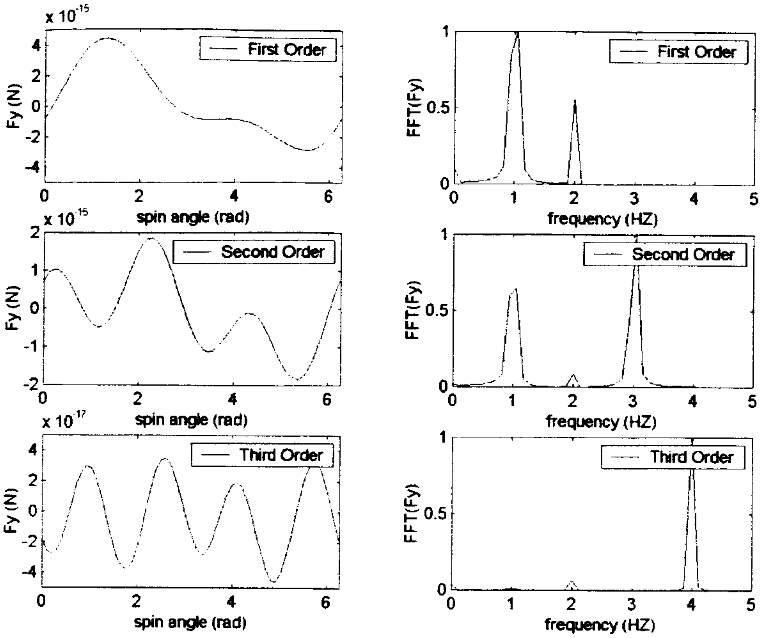

Figure 93 Ordered Force and harmonics at Point 6 due to Capsule Attraction

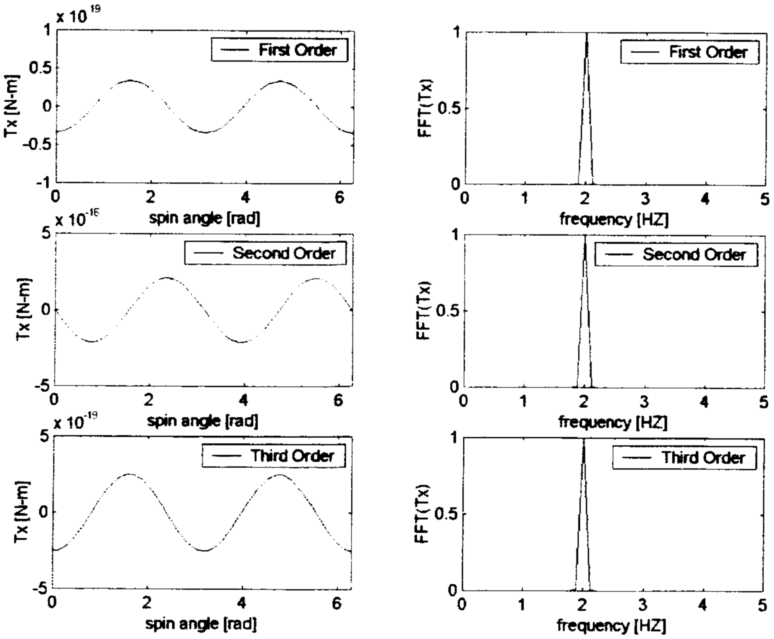

Figure 94 Ordered Torque and harmonics at Point 6 due to Capsule Attraction

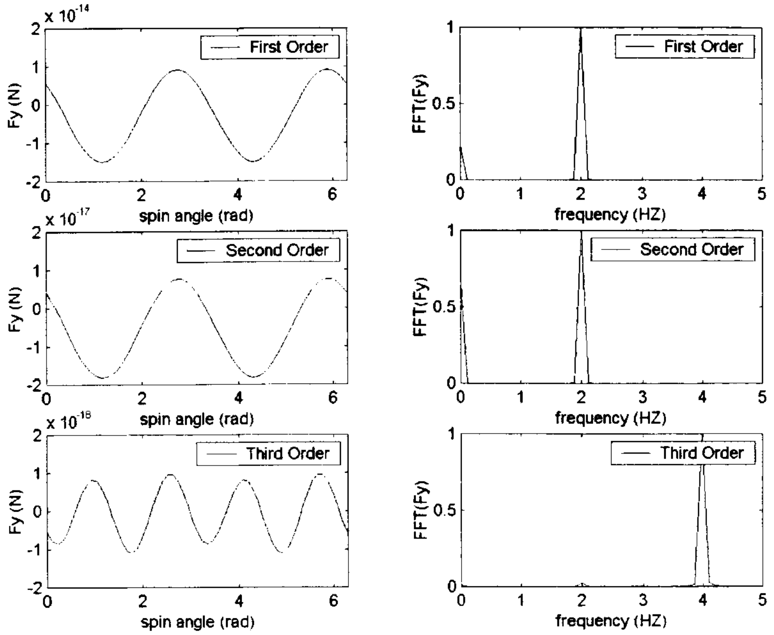

Figure 95 Ordered Force and harmonics at Point 7 due to Capsule Attraction

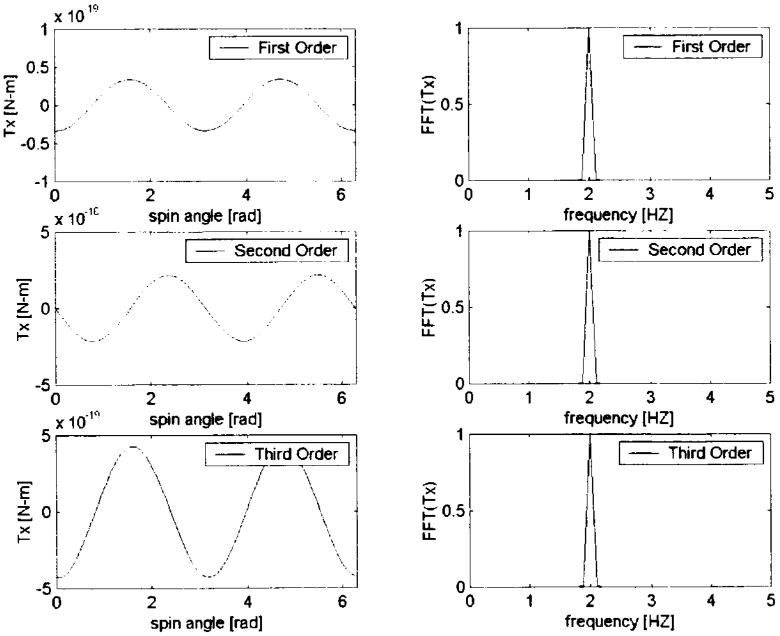

Figure 96 Ordered Torque and harmonics at Point 7 due to Capsule Attraction

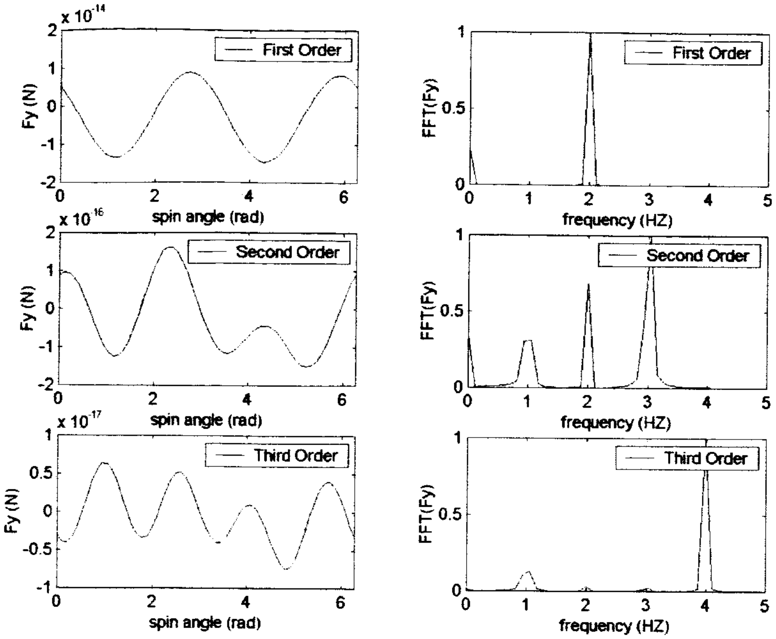

Figure 97 Ordered Force and harmonics at Point 8 due to Capsule Attraction

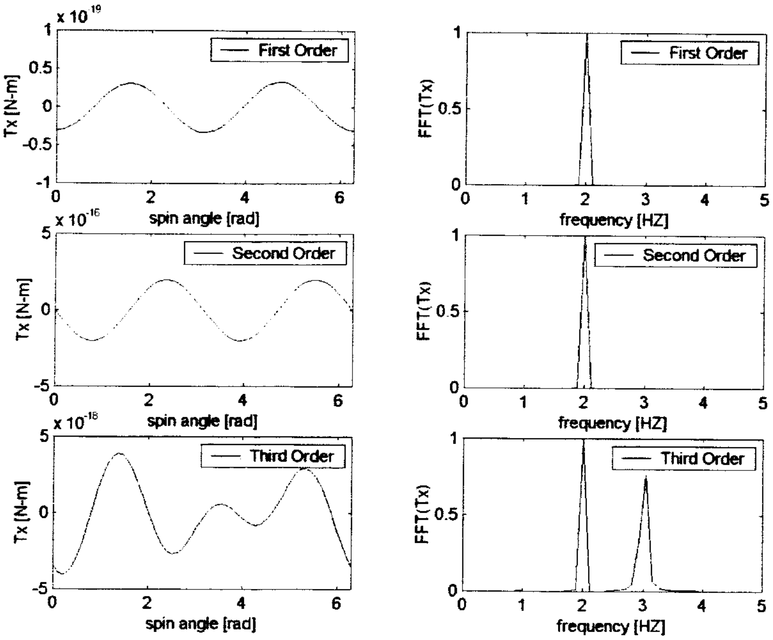

Figure 98 Ordered Torque and harmonics at Point 8 due to Capsule Attraction

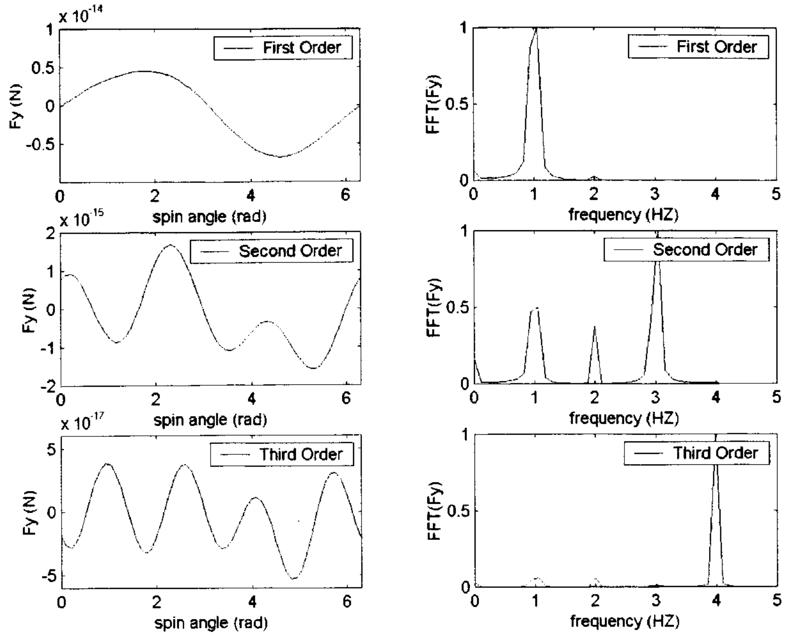

Figure 99 Ordered Force and harmonics at Point 9 due to Capsule Attraction

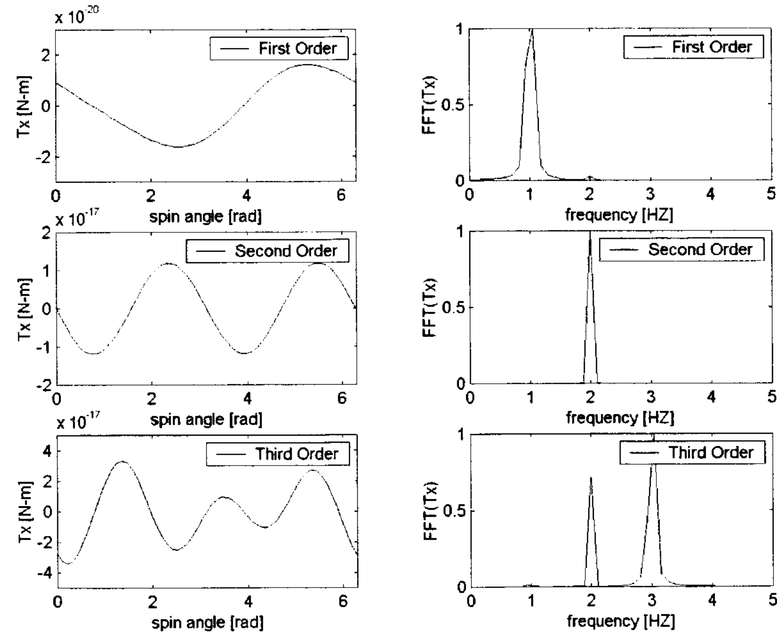

Figure 100 Ordered Torque and harmonics at Point 9 due to Capsule Attraction

The frequency spectrum for the force and the torque are shown in the following tables. The dominant frequencies are in bold face.

Table 3 Frequency spectrum along the capsule axis

	First Order	Second Order	Third Order
F_y	P0, **P2**	P0, P1, **P2**, **P3**	P2, **P4**
T_x	**P2**	**P2**	P2, **P3**, P4

Table 4 Frequency spectrum to the side of the capsule axis

	First Order	Second Order	Third Order
F_y	P0, **P2**	P0, P1, **P2**, **P3**	P1, P2, P3, **P4**
T_x	**P2**	**P2**	P1, **P2**, **P3**

Table 5 Frequency spectrum close to the cap

	First Order	Second Order	Third Order
F_y	**P1**, **P2**	P1, P2, **P3**	P1, P2, P3, **P4**
T_x	**P1**, **P2**	P2	P1, **P2**, **P3**

The orders in the above tables are the following. Order 1- offset or inertia order 1, $O(1/R^3)$ for the force. Order 2- inertia order 2, degenerates to MacCullagh formula for a perfect body (or with respect to the principal axes), $O(1/R^4)$ for the force. Order3- inertia order 3. $O(1/R^5)$ for the force.

It is important to emphasize that the relative orders depend on the mass imperfection. For example, we should not rush to a conclusion regarding the contribution of the offset.

The dominant contribution for a perfectly symmetrical body is from the second order. In this case the torque is in agreement with the MacCullagh formula. The spectrum associated with the second order can be obtained by noticing that the direction cosines, m and n, have period one: $m \rightarrow P1$, $n \rightarrow P1$. Therefore,

$$Tx \approx (Izz - Iyy)\,m\,n \rightarrow P2\,,\ Ty \approx (Ixx - Izz)\,n \rightarrow P1\,,\ Tz \approx (Iyy - Ixx)\,m \rightarrow P1.$$

Note that Iyy ≈Izz, thus both the offset term and MacCullagh term are amplified by the offset. Tx is null for a perfectly symmetrical body. Ty and Tz show various frequencies. However, Ty and Tz acting on a perfectly symmetrical body contribute P1 according to MacCullagh formula. Also note that order 4 may play a role as well, because we assumed equal principal inertia of order 2. This assumption nulls the perfect body contribution of the second order but it does not cancel completely the term of order 4.

The frequency P1 is dominant only at the extreme location (point 9 inside the capsule), due to the offset. We investigated the vicinity of this point, and found that the amplitude of P1 decreases as we move farther from the cap.

Concluding Remarks

We presented an analytical and a numerical analysis of the gravitational perturbations acting on the test mass due to the capsule. The outcome of this work is a closed-form formulation for the force/torque as well as a flexible and interactive computer code.

Our analysis predicts that the gravitational perturbations, acting on the test mass due to the capsule attraction, are safely within the limit required by the experiment if construction criteria, outlined below, are followed.. Moreover, along most of the test mass trajectory, the perturbations are far smaller than the limit, and their frequencies are different from the modulation frequency.

The conclusions from our investigations concerning the construction of the test masses are:

- The test masses should be smaller than about 10 cm and lighter than about 2 kg.
- The second-order principal moments of inertia should be all equal within construction tolerances, i.e., $\delta L/L < 10^{-4}$.
- There is no need for belted cylinders (as used in the STEP satellite experiment) for the accuracy target of our experiment.
- The mass distribution of the test masses should be as uniform as possible within $\delta M/M < 10^{-4}$.

The investigation carried out is essential for the definition of the tolerable sizes, masses, inertia characteristics, and construction accuracy of the sensing masses.

RELEASE/LEVELING MECHANISM DEVELOPMENT

Introductory remarks

The leveling and release mechanism must be able to release the detector with initial conditions that do not impair the accuracy of the science measurement. Once the effects of the higher-order mass moments on the proof masses are made negligible through the right shapes and sizes, the most important external perturbation is the Earth's gravity gradient. Other perturbations are of course present but they can be made negligible through suitable thermal design, reducing the pressure inside the detector, and shielding the detector from magnetic disturbances.

The noise components associated with the Earth's gravity gradient manifest themselves at twice the spin frequency and (depending on the orientation of the spin axis) at the spin frequency. The latter are the damaging components. The gravity component of importance to us is the g_{xy} where x is the spin axis and y the sensitive axis of the accelerometer. As shown previously, this component is proportional to the product $\sin(\phi)\delta_x$ where ϕ is the elevation angle of the body symmetry axis with respect to the horizontal plane (defined by the local gravity) and δ_x is the centering error along the spin axis between the CMs of the proof masses. The formulas derived previously for the Earth's gravity gradient components will be utilized at the end of this section to set a limit on the tolerable tilt angle at release.

Additional harmonic components come from the rotational dynamics of the instrument package. These harmonics are related to the inertia characteristics of the package and the rotational velocity errors at release. In summary, the leveling and release mechanisms must provide an orientation of the spin axis close to horizontal (to reduce the Earth's gravity gradient component) and rotational velocity errors sufficiently low to avoid saturation of the accelerometer output.

The detector has also its own elastic dynamics (as shown in a previous section) which is excited by the conditions at release. We can conservatively assume that the release will excite the elastic dynamics of the detector up to its end of scale. The experiment strategy is to damp the elastic oscillations through electrical dissipative forces (see later on for experimental results) exercised for a few seconds after release. Once the elastic (natural) oscillations are abated to a level well within the dynamic range of the instrument, the electrical dissipative forces are removed and the detector operates as a high-Q detector. After the natural oscillations are abated, the oscillations of the proof masses will be forced by the rotational dynamics of the detector during the fall.

In order to understand the effects of initial errors at release upon the differential accelerometer output, we need to develop a simplified model of the accelerometer. This model must contain the key dynamical elements but must also have a sufficiently simple formulation that shows analytically the origin and frequency content of the proof masses acceleration.

Simplified dynamical model

The differential accelerometer consists of proof masses that are about twenty times lighter than the mass of the instrument package. Moreover, the proof masses are expected to move with respect to the CM of the whole package by only microns during the early transient phase and by nanometers during the measurement phase of the fall. Consequently, the rotational dynamics of the package is unaffected (and this will be confirmed in follow-up analyses) by the tiny motions of the proof masses. On the contrary, the rotational dynamics of the package drives the motion of the proof masses. In summary and with a good degree of approximation, the rotational dynamics of the package can be assumed to be steady. The solution of the attitude motion of the rigid body is available in close form for a free spinning body. Consequently, we need to write the equation of a proof mass that is mechanically constrained to the rotating (and wobbling) instrument package in order to understand the origin and frequency content of the acceleration output of a single proof mass. The analysis can be extended to two proof masses.

The general expression for the acceleration of a test mass at point **P** with respect to **O** in a rotating system F can be written in matrix form as:

$$[\dot{\omega}]\begin{Bmatrix} x \\ y \\ z \end{Bmatrix} + [\omega][\omega]\begin{Bmatrix} x \\ y \\ z \end{Bmatrix} + 2[\omega]\begin{Bmatrix} \dot{x} \\ \dot{y} \\ \dot{z} \end{Bmatrix} + \begin{Bmatrix} \ddot{x} \\ \ddot{y} \\ \ddot{z} \end{Bmatrix} = \{a_P - a_O\} \tag{60}$$

where $[\omega]$ is the angular rate matrix of the reference system and $\{x\ y\ z\}^T$ the position of the point **P** with respect to the center of the reference system **O** (placed at the instrument package CM).

For a rigid body the equations are projected onto the axes attached to F itself (body axes) where the position vector is assumed fixed with respect to the center of F.

Consequently, eqn. (60) transforms into:

$$[\dot{\omega}]^B \cdot \begin{Bmatrix} x \\ y \\ z \end{Bmatrix}^B + [\omega]^B[\omega]^B\begin{Bmatrix} x \\ y \\ z \end{Bmatrix}^B = \{a_P - a_O\}^B \tag{61}$$

Where the angular rate matrix projected onto the body axes can be computed from the rotation matrix that relates the body axes to an inertial system:

$$[\omega]^B = R_{IB}\dot{R}_{BI} = \begin{bmatrix} 0 & -\omega_z & \omega_y \\ \omega_z & 0 & -\omega_x \\ -\omega_y & \omega_x & 0 \end{bmatrix} \tag{62}$$

After substituting eqn. (62) into (61), we derive the well-known acceleration matrixes that provide the acceleration gradient at the point **P** with respect to **O** as observed by the rotating observer (or equivalently a proof mass of the detector):

$$[C] = \begin{bmatrix} \omega_y^2 + \omega_z^2 & -\omega_x\omega_y & -\omega_x\omega_z \\ -\omega_x\omega_y & \omega_z^2 + \omega_x^2 & -\omega_y\omega_z \\ -\omega_x\omega_z & -\omega_y\omega_z & \omega_x^2 + \omega_y^2 \end{bmatrix} \quad \text{centrifugal acceleration matrix}$$

$$[E] = \begin{bmatrix} 0 & \dot{\omega}_z & -\dot{\omega}_y \\ -\dot{\omega}_z & 0 & \dot{\omega}_x \\ \dot{\omega}_y & -\dot{\omega}_x & 0 \end{bmatrix} \quad \text{Euler acceleration matrix}$$

Consequently, the (apparent) acceleration gradient tensor (in body axes) between a point **P** and the package CM at **O** is:

$$[A] = [C] + [E] \tag{63}$$

In order to compute the expression of ω_x, ω_y, ω_z we need to consider the dynamics of the instrument package that houses the detector. In other words, we must solve the Euler equations for the torque-free case of a rigid body. We will consider an inertially axisymmetric body and regard x as the longitudinal axis of inertial symmetry. The non-symmetric body also has a known solution but it is more complicated as it involves elliptic integrals.

After setting v = component of the angular rate along the axis of symmetry, the well-known solution of the Euler equations is obtained as follows:

$$\begin{cases} \omega_x = v \\ \omega_y = -\omega_t \cos(\Omega t) \\ \omega_z = \omega_t \sin(\Omega t) \end{cases} \tag{64}$$

in which the origin of t is at the time when ω_y attains its maximum value and where:

$$\Omega = \frac{I_t - I_x}{I_t} v \qquad \text{body precession rate}$$

$$\omega_t = \sqrt{\omega_y{}^2 + \omega_z{}^2} = \sqrt{\omega_{y0}{}^2 + \omega_{z0}{}^2} \qquad \text{transverse angular velocity}$$

The quantities ω_{y0} and ω_{z0} are the initial components of the angular velocity orthogonal to the symmetry axis. In our case, they can be interpreted as the rotational velocity errors at release of the instrument package.

After substituting eqn. (64) into the matrices [C] and [E], we obtain the component of the overall acceleration gradient matrix:

$$a_{xx} = -\omega_t^2$$

$$a_{xy} = a_{yx} = -\omega_t \cos(\Omega t)(\Omega - v)$$

$$a_{xz} = a_{zx} = -\omega_t \sin(\Omega t)(\Omega - v)$$

$$a_{yy} = \frac{1}{2}\omega_t^2\left[1 - \cos(2\Omega t)\right] + v^2$$

$$a_{yz} = a_{zy} = -\frac{1}{2}\omega_t^2 \sin(2\Omega t)$$

$$a_{zz} = \frac{1}{2}\omega_t^2\left[1 + \cos(2\Omega t)\right] + v^2$$

The acceleration vector *a* measured at P and projected onto the body axes, is simply:

$$\{a\} = [A]\{d\} \tag{65}$$

where $\{\delta\} = [\delta_x, \delta_y, \delta_z]^T$ is the position vector from **O** to **P** (we have changed the notation to the δs to highlight the fact that we are dealing with very small distances). The component of the acceleration along the sensitive axis (ie, z-axis in this formulation) of the accelerometer is as follows:

$$a_z = -\omega_t(v - \Omega)\cos(\Omega t)\delta_x + \frac{1}{2}\omega_t^2 \sin(2\Omega t)\delta_y + \left[v^2 + \frac{1}{2}\omega_t^2\left(1 + \cos(2\Omega t)\right)\right]\delta_z \tag{66}$$

This acceleration is the dominant acceleration experienced by the proof mass once the natural oscillations have been abated. In fact the amplitude of the residual natural oscillations can be made orders of magnitude smaller than the magnitude of the δ vector through initial damping. Equation (66) highlights several important points as follows: (1) the rotational velocity errors at release (encapsulated into ω_t) combine with the displacement error δ to produce an acceleration output along the sensitive axis; and (2) this acceleration component is modulated by the body precession rate *and not by the spin frequency*. This fact was observed previously in the results of the general elastic model of the detector. The conclusion is very important because it implies that the errors at release do not impact directly a possible EP signal violation (that appears at the spin frequency). The overall advantage of the gyroscopic body (with non-spherical inertia ellipsoid) is that the precession rate is different from the spin rate. Moreover, the precession rate can be chosen at will by selecting the ratio of the moment of inertia of the instrument package in order to maximize the ability of extracting the signal from the dynamics-related noise. Since both ω_p and 2 ω_p appear in the expression of the acceleration, it is advisable to make ω_p non commensurate with v (the spin rate). The selection of the moments of inertia ratio (and hence ω_p) and the ability to extract a signal with a strength at the threshold sensitivity of the detector will be carried out in next year analysis.

Derivation of requirements

The first requirement derives directly from the analysis carried out previously and it is related to the strength of the components of the Earth's gravity gradient at the spin frequency. The resulting acceleration component [from eqn. (43)] is

$$\begin{aligned}\delta a_z < {} & 3\frac{\mu}{R^3}\cos(\phi)\sin(\phi)\sin(\nu t)\delta_x + \frac{3}{2}\frac{\mu}{R^3}\cos^2(\phi)\left[\sin(2\nu t)\delta_y + \cos(2\nu t)\delta_z\right] \\ & + \frac{\mu}{R^3}\left[\frac{3}{2}\cos^2(\phi) - 1\right]\end{aligned} \qquad (67)$$

for an instrument package spinning about x, a sensitive axis along z, and ϕ the elevation angle of the symmetry axis with respect to the horizontal plane defined by the local (gravity) vertical. Equation (67) highlights the three components produced by the Earth's field at the spin frequency, at twice the spin frequency, and a dc term. The strength of the gravity gradient component at the spin frequency must be substantially less (say 10^{-15} g) than the signal at threshold. A product $\phi\delta_x$ of 0.1 deg-micron will safely meet the previous condition. Consequently, we can either be more relaxed on the leveling/release mechanism (i.e., $\phi < 1$ deg and $\delta_x < 0.1$ micron) or on the centering between the two proof masses along the spin axis (i.e., $\phi < 0.1$ deg and $\delta_x < 1$ micron). Both options will be kept open for the time being because they involve several technical considerations related to the mechanization of the leveling/release mechanism and the calibration of the differential accelerometer. A choice between the two options will be searched for after a dynamic analysis of the release mechanism and laboratory tests on the differential accelerometer prototype to assess the difficulties involved with the accurate centering of the proof masses along the spin axis.

The requirement on the rotational velocity errors at release can be readily obtained from the following considerations. First, the rotational velocity error must be sufficiently small not to saturate the instrument output. In this case we do not have to worry about the instrument sensitivity because with appropriate inertia characteristics there will be no components at the spin frequency related to the precession dynamics of the instrument package. In this case the stronger component is associated with the first term of eqn. (66).

A rotational velocity of 1 deg/s will only produce a signal of order 10^{-9} g which is well within the dynamic range for the expected values of spin and precession frequencies.

However, we must also worry about the amplitude of the precession (i.e., the nutation angle) because through coning of the body axis the accelerometer will sense the Earth's gravity gradient. The frequency sensed through coning is not exactly the spin frequency because the coning adds a frequency modulation at the precession frequency. Nevertheless, we will assume conservatively that the amplitude of the nutation angle must be less than previously indicated for the gravity gradient related noise. For an axisymmetric body the amplitude of the body-axis coning (i.e., the nutation angle) is as follows:

$$\tan(\theta) = \frac{I_t}{I_a}\frac{\omega_t}{v} \tag{68}$$

where ω_t is the transverse angular velocity at release, I_a and I_t are the moments of inertia about the transverse and the symmetry axis (x-axis in our case), respectively. If we assume an upper bound for the nutation angle of 1 deg, a spin frequency of 0.5 Hz and a (worst-case) inertia ratio $I_t/I_a \approx 3$, we obtain $\omega_t < 1$ deg/s. Likewise, if we had assumed a maximum $\theta < 0.1$ deg then we would have obtained $\omega_t < 0.1$ deg/s. In summary, we will establish the following two sets of requirements

a) $\delta_x < 1\ \mu$m (centering error between proof masses CMs along the spin axis)
   $\phi < 0.1$ deg (horizontality of detector)
   $\omega_t < 0.1$ deg/s (angular rate error at release)

b) $\delta_x < 0.1\ \mu$m (centering error between proof masses CMs along the spin axis)
   $\phi < 1$ deg (horizontality of detector)
   $\omega_t < 0.1$ deg/s (angular rate error at release)

We will start by base lining the release and leveling mechanism according to option *a* while keeping option *b* open if the tight centering of the proof masses of the detector turns out to be feasible.

THERMAL ANALYSIS/ISSUES

Following the procedure of the *STEP* project, we have estimated the pressure requirement inside the detector for keeping the radiometer effect and the damping due to residual gas to tolerable levels.

Radiometer effect

The tolerable pressure inside the detector is related to the maximum allowable thermal gradient through the radiometer effect, i.e., the acceleration produced by gas molecules emitted from regions with different temperatures[xxxiii]. This effect is likely to produce an acceleration error modulated at the signal frequency because, as the detector rotates, it could see (static) regions with slightly different temperatures. The acceleration produced by the radiometer effect is $a = p\,(\Delta T/\Delta L)/(2\rho T)$ where p is the pressure, T the temperature and ρ the density of the sensing mass. For $\rho = 2800$ kg/m^3 (Aluminum) and an acceleration error of 10^{-15} g, we could have for example: $p = 10^{-9}$ Pa and a temperature gradient of 0.3 K/m, or a higher pressure and proportionally lower temperature gradient. As a result, we can place a requirement on the product of the two as follows $p \bullet (\Delta T/\Delta L) < 3 \times 10^{-10}$ Pa-K/m. In other words, the requirement on the pressure can be traded for the requirement on the temperature gradient. Early estimates of temperature gradient across the detector diameter are very small and, consequently, a higher detector pressure can be tolerated in a detector that is well thermally shielded.

A thermal gradient across the detector also affects the resonant frequencies of the sensing masses through variations of: the Young's modulus of the material, the geometry of the torsional springs, and the moments of inertia of the sensing masses. Consequently, a thermal gradient changes differentially the resonance frequencies of the sensing masses and ultimately affects the common mode rejection factor.

The common-mode rejection factor is related to the temperature variation ΔT across the detector as follows $\text{CMRF} \approx |\alpha + \alpha_E|\Delta T$ where α is the thermal expansion coefficient and α_E the thermal coefficient of the Young's modulus. For Aluminum at low temperatures $\alpha << \alpha_E$, $\alpha_E \approx -3.5 \times 10^{-4}\ \text{K}^{-1}$ [xxxiv] while CMRF is required to be $\leq 10^{-4}$. Consequently, the tolerable temperature gradient for suspensions of the proof masses that are separated by many centimeters is of order 1 K/m. This value is less stringent than the tolerable value of the thermal gradient dictated by the radiometer effect and, consequently, is superseded by the previous effect.

Thermal configuration of instrument package

There are 3 elements that operate at different internal temperatures in the instrument package, namely, the detector, the preamplifier and the electronic box. The detector should be at the lowest possible temperature with an upper limit of 10 K. The Gallium Arsenide FET preamplifier can operate from low temperature (> 10 K) up to room temperature with slightly reduced performance at high temperature. The electronic box must be kept close to room temperature. The three boxes also dissipate different amounts of power. The power dissipated by the detector W_1 is in the nW range which is negligible. The power dissipated by the preamplifier and the electronic box are typically $W_2 \approx 100$ mW and $W_3 \approx 500$ mW which are both non negligible. A simplified thermal scheme of the three elements is shown in Figure 101.

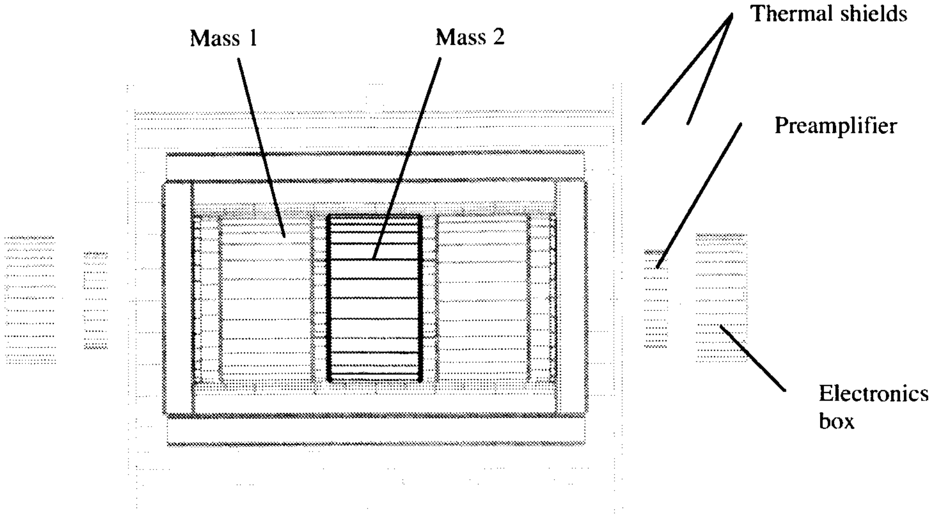

Figure 101 Simplified thermal scheme

Thermal issues and design

Thermal issues are not solved by simply meeting the thermal gradient requirement and lowering the pressure. The experiment has two cold parts, that is, the proof masses plus casing (i.e., the sensor) and the preamplifier and a component at almost room temperature (inside its case), that is, the electronics box which includes battery and various housekeeping functions.

The sensor has negligible thermal dissipation while the preamplifier and electronic boxes have non-negligible thermal dissipations. We need to evaluate the following: (1) cooling down time for the sensor and preamplifier before launching the balloon; (2) the tolerable temperature drifts of the detector, the preamplifier and the electronics during the measurement phase after release; and (3) the tolerable temperature drifts of the same units before release during the check out phase.

Experimental data was provided by our partners at IFSI on the power consumption of the units involved and their sensitivity to temperature variations. Not surprisingly, the sensor and the preamplifier have the highest temperature sensitivity (expressed as change of acceleration output per degree K), of order 10^{-8} g/K and 10^{-9} g/K, respectively, followed by the electronics which is a few orders of magnitude less sensitive. If the two sensitivities quoted above are taken at face value, the temperature variation over the measurement time should be less than 0.1 μK! In reality, the sensor and preamplifier will be grounded to the cryostat temperature before release and then they will rely on their own thermal inertia during the 25-30 s measurement phase. The temperature drift is slow, with a time constant that is typically two orders of magnitude bigger than the measurement time. Since variations of less than μK are unrealistic to obtain, the question can be put as follows: how well an acceleration signal at the expected sensitivity can be extracted from a slow varying background (dependent on the temperature drifts) which increases by several orders of magnitude over the measurement time?

Answering this question is important to define more realistic requirements for the thermal design, in general, and for solving point 2 outlined above, in particular. In order to answer this question we have investigated techniques of signal extraction from a noisy signal which also drifts by a very large amount due to temperature variations.

This exercise is not meant to be a comprehensive work on the techniques that will be adopted for extracting the signal from noise but rather it is limited to the issue described previously. In summary, we have taken a sample 0.5-Hz signal with a strength of 2×10^{-15} g (at 95% confidence level), added to a random noise with $\sqrt{30}x10^{-15}$ g rms and to a double-exponential (other functions have also been tested) drifting acceleration that ramps up to an acceleration intensity many orders of magnitude bigger than the signal. The double exponential (or similar function) represents the different heating rates of the sensor and the preamplifier with two different time constants TC_1 and TC_2 where we have assumed $TC_1 > TC_2$ to account for the sensor's bigger thermal inertia We have practiced a basic technique to extract the signal, without assuming any knowledge of the functional expression of the thermal drift, for increasing steepness of the thermal ramp (that is the rates of change of the two temperatures).

Figure 102 shows a conservative situation in which the thermal-induced acceleration ramps up to 2×10^{-8} g, that is, its maximum value is 7-orders of magnitude bigger than the expected signal. The signal was extracted with reasonable ease by detrending the signal + noise with a 6-order polynomial and computing the FFT of the detrended signal. This extraction process would not succeed for much stronger thermal drifts, although no additional effort was devoted to improving the process because the results obtained were already satisfactory. After considering these results, we can establish thermal drift requirements for the relevant units as follows:

Sensor temperature drift: < 0.0067 K/s (i.e., ~0.2 K in 30 s)

(69)

Preamplifier temperature drift: < 0.017 K/s (i.e., ~0.5 K in 30 s)

For the temperature of the electronic box we can safely assume that it is sufficient to keep the temperature variation below a few degrees over a 30 s maximum free-fall time.

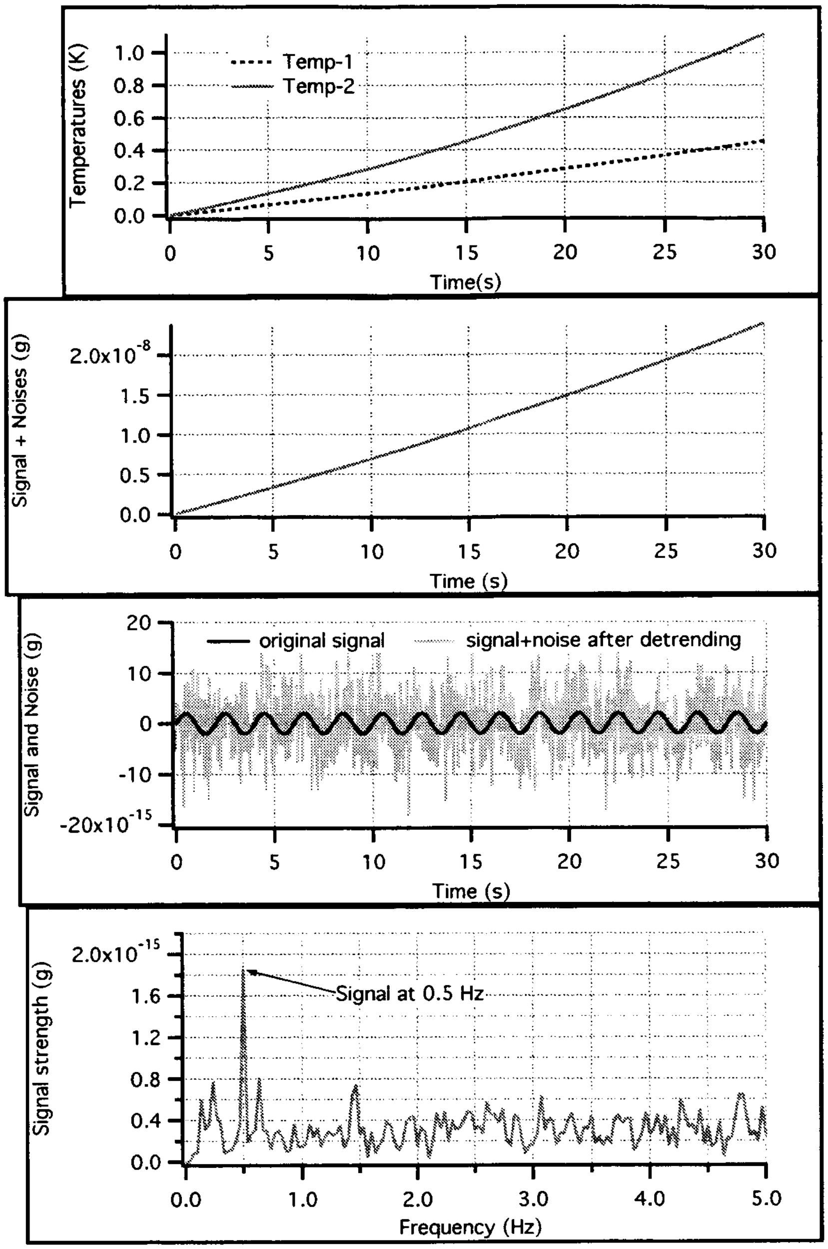

Figure 102 Example of extraction of signal from random noise plus a strongly-dominant slow-drifting acceleration noise (Temp-1 = sensor and Temp-2 = preamplifier).

Preliminary Thermal Results

A preliminary thermal analysis was carried out by using a finite-difference thermal analysis code to address the two more critical thermal issues, that is: (a) the cooling down of the detector and (b) the temperature rise of the preamplifier during the measurement phase.

Results of the cooling down are shown in Figure 103 under different assumptions of radiation and conduction through a cold strap with a conductance of 0.02 W/K connecting the case of the detector to the cryostat. The most relevant results are those shown in Fig. 103(a) while Figs. 103(b) and 103(c) represent cases that were run to assess the relative contributions of radiation and conduction, respectively. As shown by Fig. 103(a) the cooling time needed, with the cold strap, to reduce the temperature below 10 K is shorter than a week.

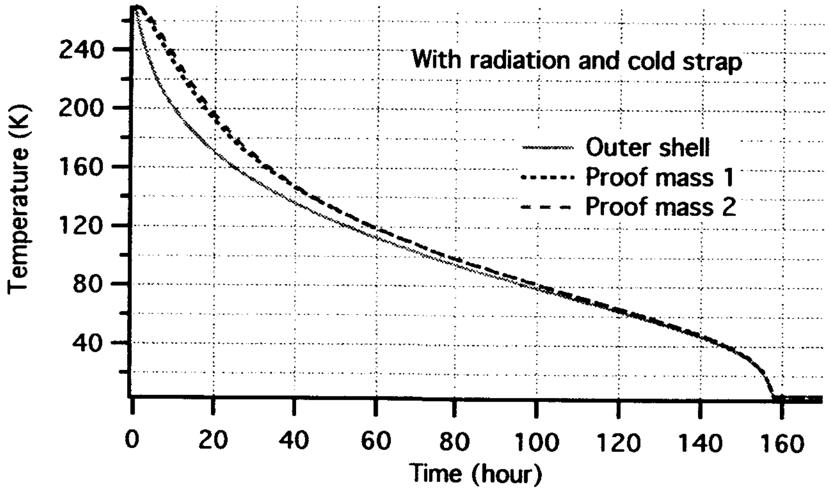

(a)

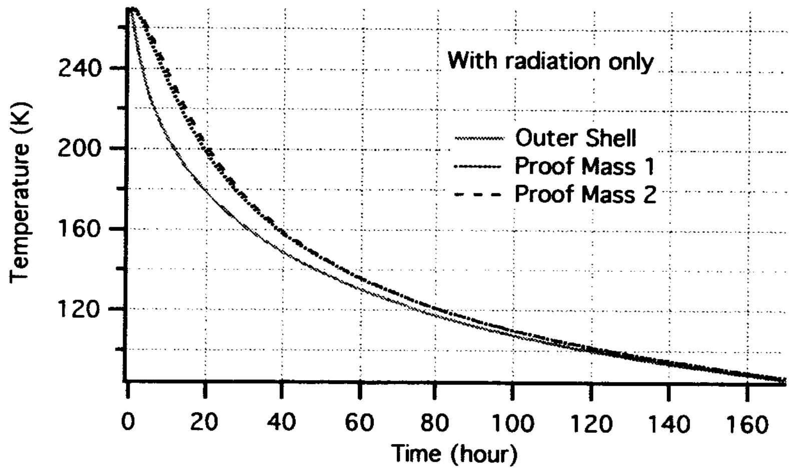

(b)

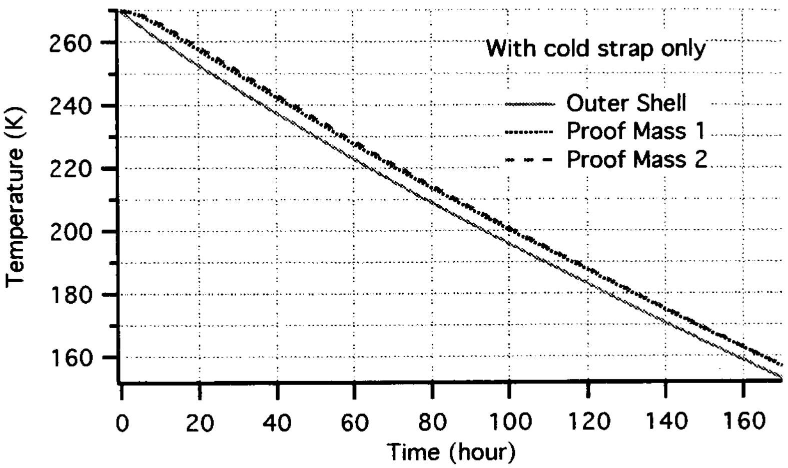

(c)

Figure 103 Temperatures of detector during cool down under various assumptions

The second critical issue that we addressed is the temperature rise of the preamplifier during free fall (i.e., the measurement phase). The preamplifier was singled out as more critical, from the thermal point of view, than the detector because it has high power and low mass while the detector has negligible power dissipation and higher mass. We assumed that the preamplifier is at its desired temperature value (ie, 10-20 K) before the instrument package release and that a thermal shield is interposed between the preamplifier box, which is attached to a thermal radiator, and the detector.

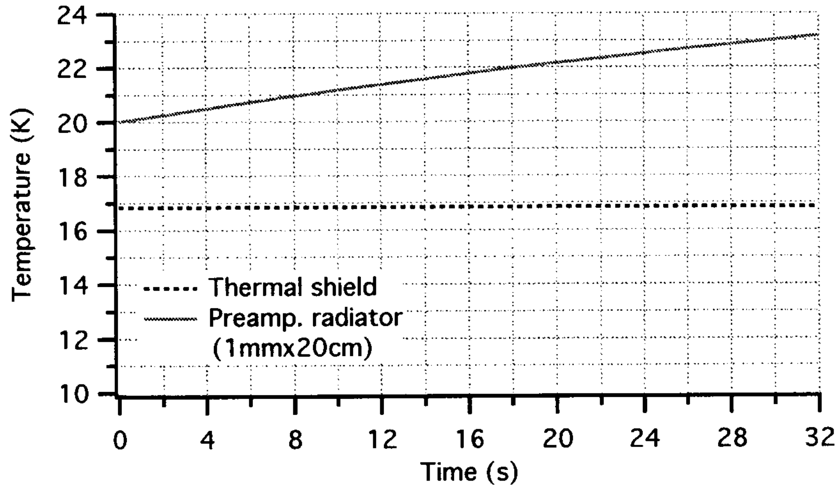

(a)

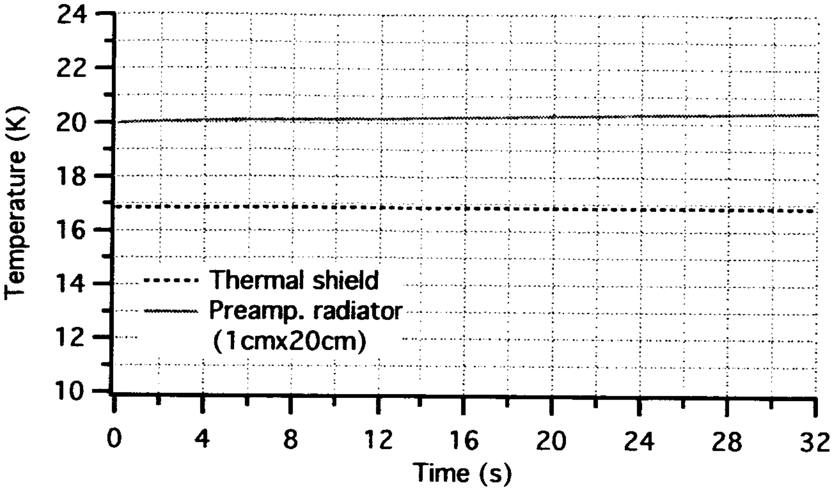

(b)

Figure 104 Temperature of preamplifier and thermal shield during free-fall phase

Figure 104 shows the results for different thicknesses of the thermal radiator. Clearly, in order to keep the temperature variation below 0.5 K during a 30-s time, a 1-cm (thick) x 20-cm (dia.) radiator is required. Additional thermal analyses will be performed to compute temperature variations of the three connected boxes and, consequently, define in more detail the thermal design beyond this preliminary analysis of critical issues.

MECHANICAL REPORT

Release sequence

The release of the package takes place in 2 stages. Initially the capsule is released from the balloon. Then, very soon after, the sensor package is released, in two steps, within the vacuum chamber.

Capsule Release

The combination of wind shear during ascent, the extremely low air resistance at float, and the limited time at float make it necessary to assume that the balloon will be rocking at the time of package release. Since it is required that capsule is vertical and non-rotating before release, the release strategy must account for this. The present concept, developed thus far, is to actively separate the orientation dynamics of the capsule from the behavior of the balloon. That is, we have placed a 3-axis gimbals between the capsule release mechanism and the portion of the gondola that stays with the balloon (capsule leveling/release mechanism).

As the balloon rockets back and forth, and rotates, the gimbals will be driven to ensure that the capsule angular orientation is unchanged. The sole effect being that the capsule will be translating back and forth, and moving up and down slightly. During this process the linear motion will be tracked from the ground. In order to ensure that we release the capsule when it is as close to unaccelerated as possible, we will release it at one of the extremes of the balloon pendular swing.

Since the sensor release does not have any orientation adjustment capability, the capsule release mechanism must be designed to meet all the alignment and stability requirements that cover the release of both the capsule and the sensor.

Sensor Release

The sensor release concept involves a two stage support (sensor release mechanism). The first stage is a simple spit that holds the sensor package through release of the capsule from the balloon. Once the capsule is in free-fall the sensor release mechanism pulls back far enough to disengage the spit, and draw it to a position that the sensor will not hit it on the way down. At this point the sensor is held between 6 springs, 3 on each side. These springs will be sized so that they can not impart more force than is allowed by the rotation stability requirements. Any transient sensor motion induced in the spit-support release will be allowed to damp out in the 6 spring. Once the instrument package is spinning at a stable rate, and oscillation from the initial stage of the release have damped, the mechanism second stage will pull back further, and the instrument will drop. The next stage of the work on this design will be to create a detailed simulation of the entire system, in order to examine its behavior in detail.

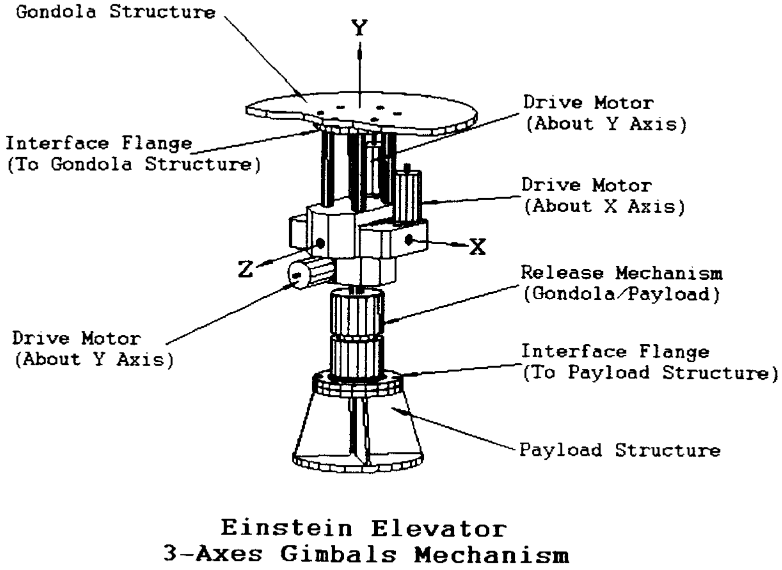

Figure 105 Schematic of leveling mechanism

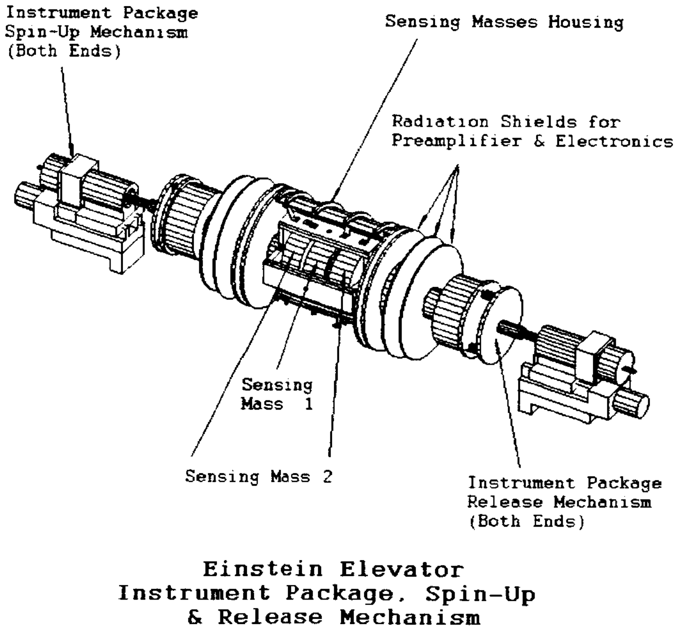

Figure 106 Instrument package spin-up and release mechanism

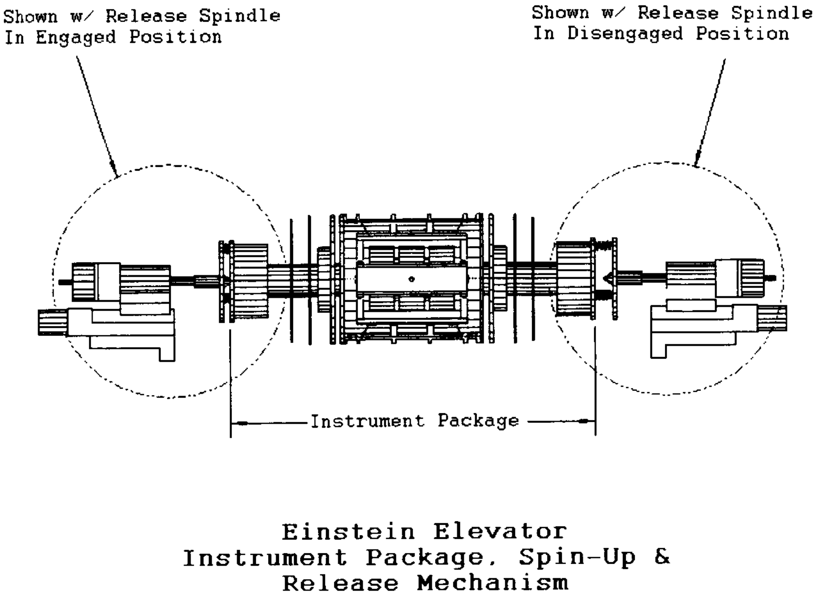

Figure 107 Front view of release mechanism

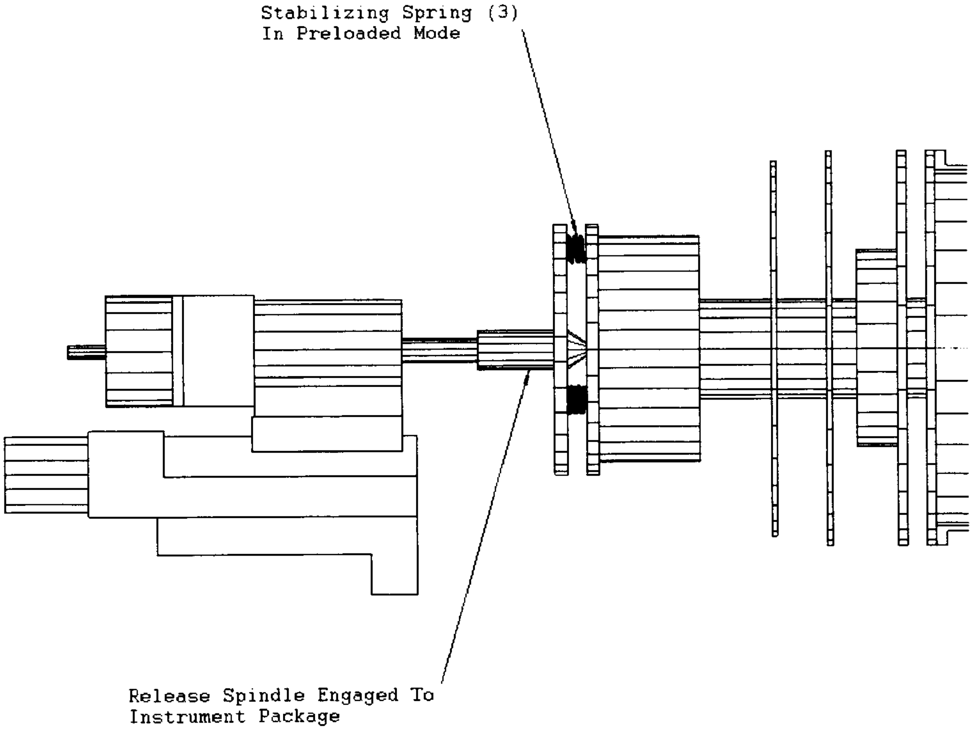

Figure 108 Detail of release mechanism (with spindle engaged)

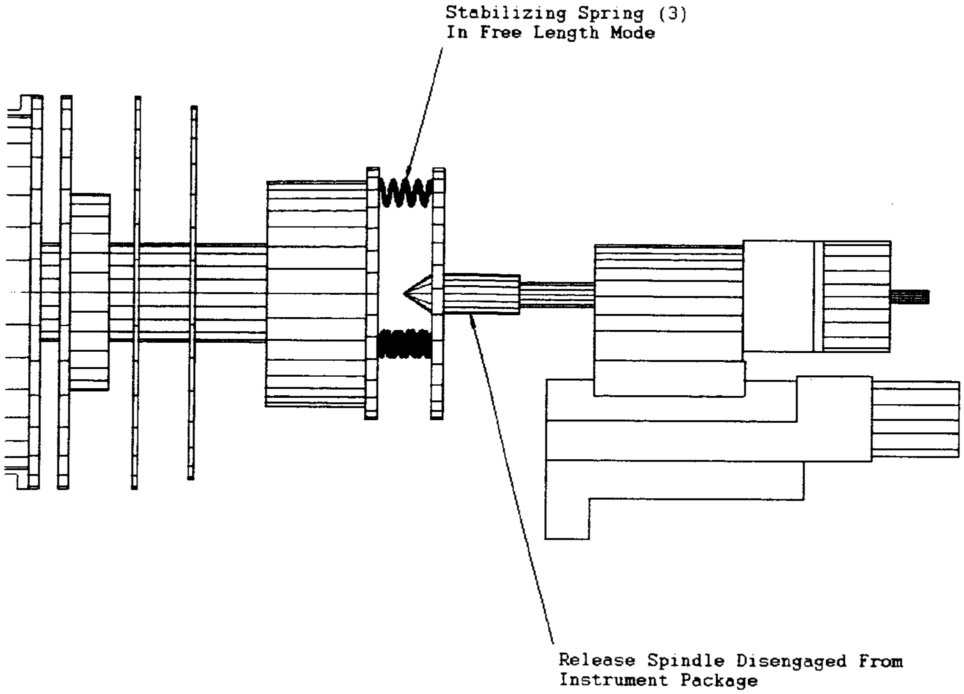

Figure 109 Detail of release mechanism with spindle disengaged and springs still engaged

Mechanical/Thermal Design

One of the key advances this year was in the area of the thermal design and increased detail in the thermal model. In order to assist in this area the main supporting structure for the sensor package had to be sized. Though most of the instrument design remains at the concept level, it became important to examine the design forces that controlled this component's dimensions. The sizing involved balancing the need to minimize the heat transfer, and therefore the support's cross sectional area, while at the same time minimize the support deflection, or therefore the support's structure moment. Studies of viable cryogenic materials suggested that a Kevlar composite would be the best material to use. Since we intent to use a composite material, and by the nature of the design, one with a thin wall, a further constraint on the design was a limitation on the allowable compression load. Coupling these requirements we were able to size the main shaft in such a way that is can support the instrument without allowing out-of-spec instrument deflection, while dropping thermal conductivity well below the allowable level.
Below are the present support parameters:

- Length = 0.12m
- Diameter = 0.05m
- Wall thickness = 0.0012m
- Kt/m = 1.9×10^{-5} W*m/K, at 10°K

Cool down Techniques

Though this will be covered in more detail in the thermal section, the preferred method for lowering the instrument to cryogenic temperature has been re-examined and changed. Initially we had examined using radiation alone to reduce the instrument operation temperature to below 10 K. It was quickly clear that this approach was inadequate. Next we examined having a cold strap in place prior to launching the balloon. We would then rely on just radiation from the cold Dewar walls to maintain the temperature. Though this is effective, it introduces issues related to manipulating the cold strap.

To avoid this we have since base lined a third approach, one involving cooling the instrument down by flowing cooled gaseous helium (Ghe) through the vacuum chamber until the instrument is cool. We would then pumping out the remaining GHe from the inside of the Dewar. This give us a fast way to cool the instrument without having to manipulate a cold strap.

Dewar Operation Techniques

One of the larger instrument dynamics stability issues that needs to be addressed is the effects of the liquid cryogens during free fall:

- the fact that they may slush during the fall
- the fact that they will continue to boil during the fall
- the fact that they needs to be vented, which will cause a propulsion effect.

In order to avoid these effects we are beginning to examine novel Dewar operation techniques. The standard approach for maintaining temperatures at this level is a Dewar with a vacuum shroud and 2 cryogen shrouds, LN2 and LHe. But the LN2 is heavy. It can slush, it tends to boil similarly to water, and when it is vented it produces some propulsion, all of which will cause some dynamic reaction in the Dewar that could disrupt the experiment. The LHe, on the other hand is quite light and is far less likely to cause a dynamic disturbance.

For these reasons we have decided to examine operating the Dewar, at least through the experiment phase, without LN2. The first approach that we examined was allowing the LN2 to completely vent prior to dropping the experiment package from the balloon. This is an acceptable approach, though it does produce some limitation on system timing. We would rather be able to begin the experiment when the system is settled, rather than waiting longer for the LN2 to boil off. Instead we are going to examine the possibility of allowing the LN2 boil off on the ground, and then flowing the boiled off LHe into LN2 shroud.

Dewar Layout

We have moved the Dewar opening from the top of the chamber to the bottom. The initial Dewar design had the opening for inserting the instrument package into the top of the Dewar. This meant that all the feedthroughs into the system, as well as all the service feedthroughs for the Dewar itself were broken anytime the Dewar was opened. In addition, the load path from the balloon to most of the instrument mass goes through this connection. By moving the opening to the bottom, all the feedthroughs remain intact when loading the system, and only the instrument crash protection is supported through the Dewar cover (bottom plate).

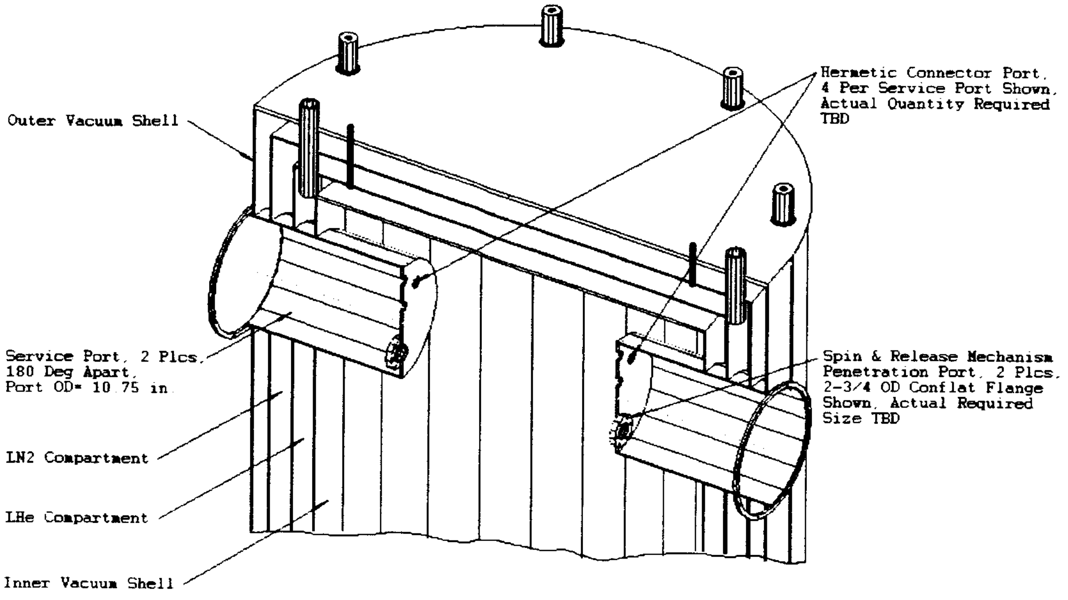

Figure 110 Cryostat top detail with feedthrough interfaces

THERMAL ANALYSIS

The simplified model discussed previously has been further developed, particularly in the area of isolation of the sensor from the (relatively) warmer preamp and electronics module. In fact, the electronics has to be kept above a minimum temperature (for this model, we have assumed –65C) to prevent damage to the components, and possibly needs to be warmed further to a "cold-start" temperature at the initiation of experiment calibration.

The design consists of a sensor supported by a Kevlar-reinforced shaft (discussed previously) that is suspended by the rotation fittings across the dewar diameter. We have assumed the electronics module and preamp are balanced disks supported by this same shaft, both to one side of the centrally located sensor module. Between these various elements we have places radiation shields to minimize views of the warmer elements to the sensor. The model representation is shown in Figure 111. The electronics are shown in red as a result of their maintained temperature; the preamp is just visible between the two largest disks.

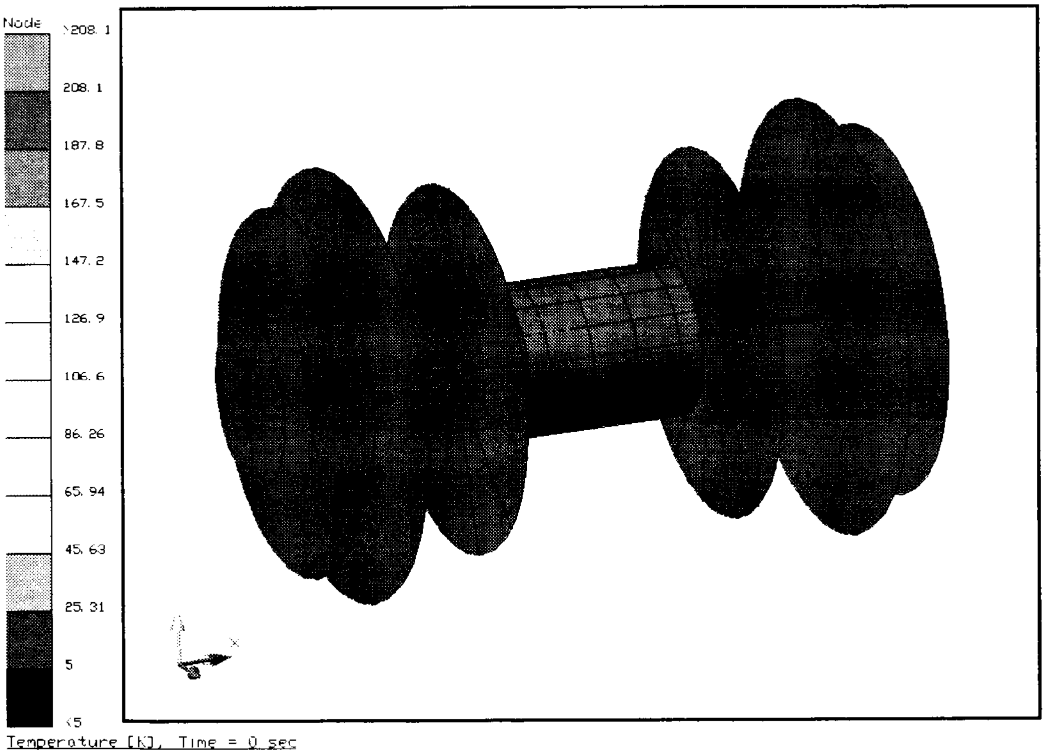

Figure 111 Thermal model representation

We have assumed that during the entire process (including cool down of the experiment) that the electronics is maintained above -65C, as illustrated by the red disk at the left end of the figure.

There are two fundamental conductive paths between the various elements in the model: the supporting shaft and the wires connecting the electronic elements. The hollow shaft has been sized to support the masses with sufficient stiffness to allow the experiment to be balanced. The wires (currently assumed to be 4 pairs between each module) have been sized to provide less than 1-ohm resistance per circuit. Pure-metal wire like copper or silver have sharply peaked thermal conductivity in this temperature regime (10-25K) as well as rapidly changing electrical conductivity, so we have assumed for this analysis that the wires are Constantan, which has very little change in electrical characteristics from room temperature down to 4K, but its thermal conductivity drops by a factor of 100, providing effective thermal isolation at the experiment temperature. The conductors in the model have been sized to accurately represent the shaft and wires, and all the important materials are modeled with temperature-varying conductivity and specific heat.

It has been shown in earlier studies that the experiment cannot be cooled effectively by radiative exchange with the dewar alone – it requires the addition of a thermal strap to achieve the desired starting temperature in a reasonable period of time. However, a mechanical strap (or straps) adds several complications to the design. The largest mass is the sensor itself, yet this is the least desirable location to affix a strap. We are currently considering an alternative approach: to flow gaseous helium over the experiment to cool it. This has the advantage that after starting conditions are achieved; the helium can be pumped out, allowing us to take advantage of the effective isolation of the mechanical hardware.

We have run a study of the warm-up of the preamp and experiment with nominal power inputs and the previously mentioned initial condition of the electronics module at 208K (-65C). Using an assumed cooling of the preamp based on area ratio to the sensor and heat flow through the wires, the equilibrium temperature of the preamp prior to startup is approximately 20K. Using these initial conditions, and wires and support tube modeled as described above, the temperature rise of the preamp and the temperatures and estimated gradients in the sensor are shown in Figures 112 and 113.

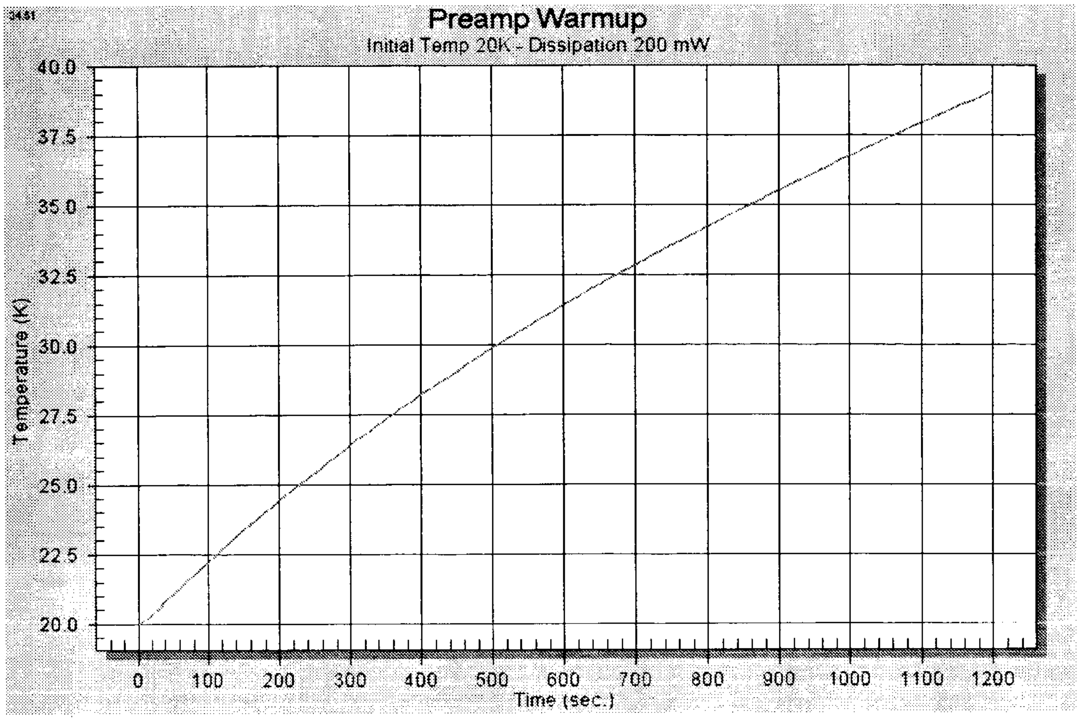

Figure 112 Temperature rise of preamplifer during calibration

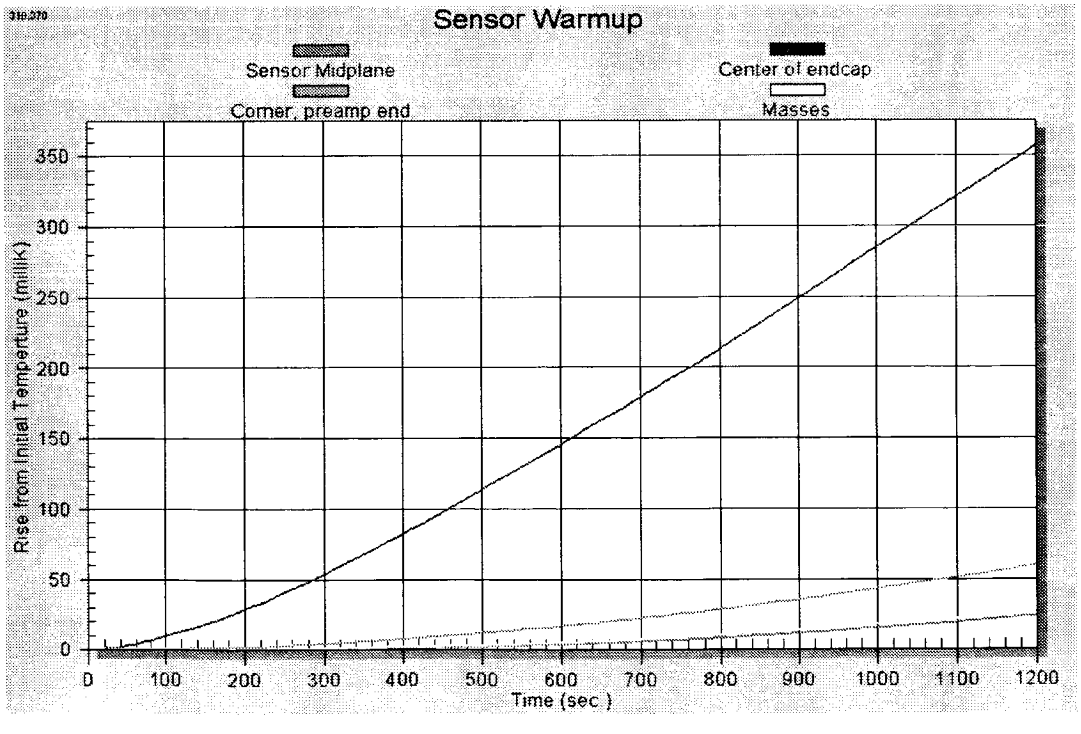

Figure 113 Temperature rise at various locations of sensor

This study has yielded several significant conclusions for the design of the experiment:

- Properly sized alloy wires provide sufficient electrical conductance without significant impact on the thermal performance
- The most significant thermal conductance is the shaft supporting the sensor and other modules.
- Radiative heating of the sensor can be well controlled with concentric disks between modules. These disks, if of significant thickness, also provide thermal mass to slow the heating of the sensor.
- Temperature gradients across the sensor package at the end of the preamp warmup phase appear to be quite small (see Fig. 114).

It should be noted that while the temperature rates of change fall within the previously described limits (current estimate of maximum temperature in sensor is 0.0004 K/sec), improvements can be contemplated which would control these rates better. For example, the model currently has the shaft connected directly to the center of the aluminum endcap of the sensor module, essentially a worst-case solution. A set of Kevlar straps between the shaft and the sensor could provide high stiffness with lower conductance. However, such improvements, as well as better fidelity modeling of the inner structure of the sensor, require more sensor design detail.

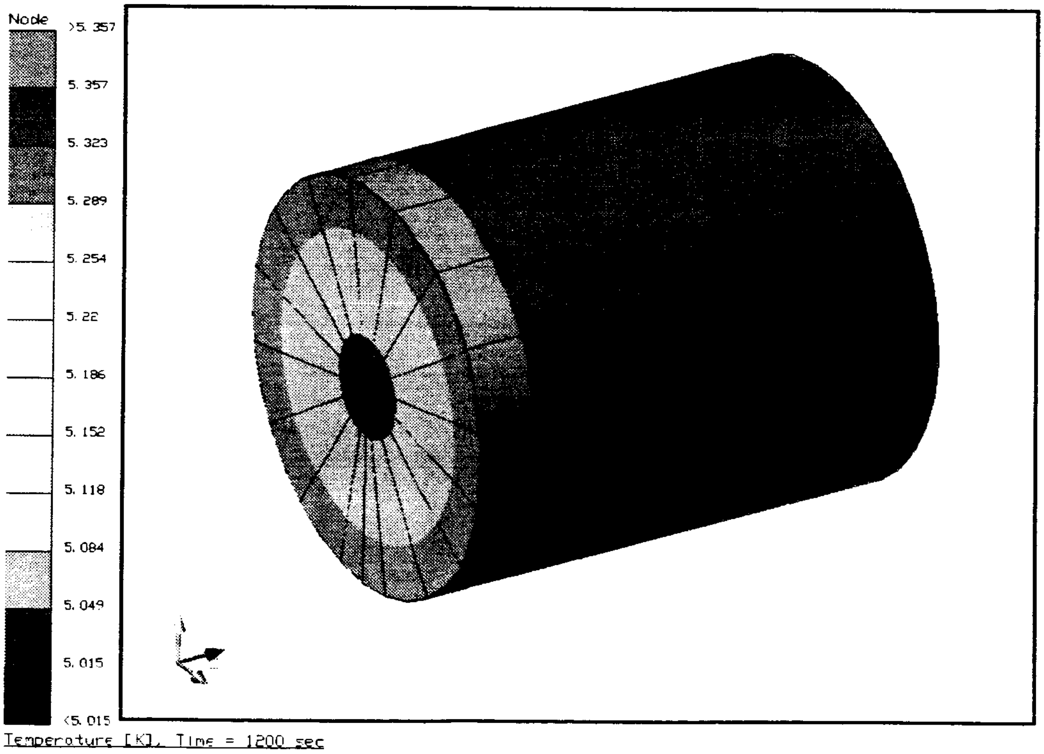

Figure 114 Sensor temperature distribution at end of 20 min.

INSTRUMENT ELECTRONICS OVERVIEW

The overall communication and control system for the experiment is shown below. Minimum electronics beyond that already in the detector are added to provide a data collection and status link to electronics mounted outside the vacuum chamber. The link electronics on the detector is a battery-powered RS-232 to IR transceiver comprised of a 110° field of view IR emitter-detector pair driven by an IR encoder-decoder and linked to an identical pair on the side of the chamber. The total power required for this portion of the interface should be less than 100mW. Presently the electronics will need to run at -40 °C, but we will investigate if we can go lower.

The power and telemetry control box will be a comprised of a Book-sized PC with an Ethernet interface to a procured telemetry radio, such as the Freewave FGR1115RE 900MHz spread spectrum radio. A small IR to RS-232 module provides the interface to the IR transceiver inside the capsule. The externally mounted system will run from a single +12VDC 85W power source. The unit is expected to occupy a volume of 40cm x 30cm x 25cm.

The gondola will contain a standard SIP module for ground communication and control. We will need to provide an interface between the SIP telemetry interface and a radio that links to the experiment. This interface will essentially be the same design as the power and telemetry control box in the instrument.

Other means of communication within the capsule were considered, including a low power 2.4 GHz radio link, and this option could be a viable alternative if the IR link is not feasible. The major advantage to this approach would that the link does not depend on position, and the power would be about the same.

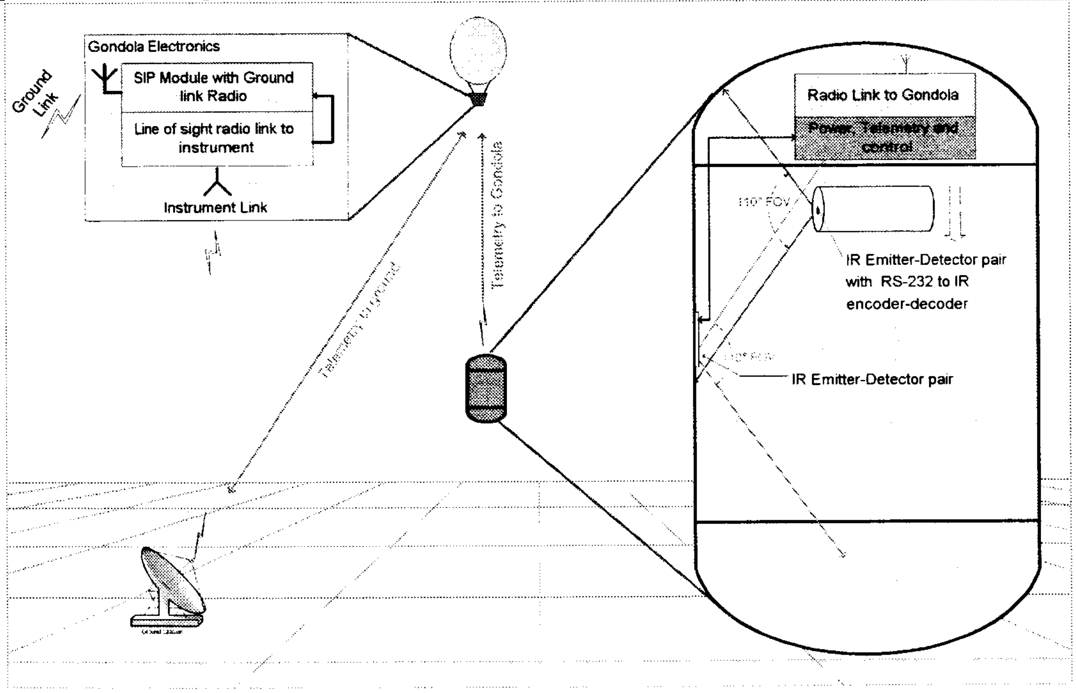

Figure 115 Schematic of telemetry links

SYSTEM REQUIREMENTS DEVELOPMENT

Table 6 summarized key requirements of major subsystems derived thus far.

Table 6 Development of Requirements vs. Design Drivers

Design Driver	**Science-originated Reqmt.**	**Engineering Requirements**		
	Tolerable differ. acceleration	**Detector/ Package**	**Cryostat**	**Drop System**
Free-fall (time > 20 s)	N/A	Transient damping time < 5 s;	N/A	Low-speed ballistic coeff. $\beta_0 > 5000$ kg/m^2
Amplifier noise (white)	$< 10^{-14}$ g/$\sqrt{\text{Hz}}$	Preamp. $T_N < 60$ mK	N/A	N/A
Brownian noise (white)	$< 10^{-14}$ g/$\sqrt{\text{Hz}}$	$\omega_0/Q < 6\pi/10^5$ rad/s $T < 10$ K	LHe cryostat	N/A
Temperature gradients [Radiometer effect]	$< 10^{-15}$ g	$p(\Delta T/\Delta x) <$ $3\text{x}10^{-10}$ Pa-K/m	TBD	N/A
Acceleration noise inside capsule in free fall	$< 10^{-12}$ g	CMRF $< 10^{-4}$	Pressure inside capsule $p_c < 10^{-6}$ mBar	Structural and attitude freqs. $\gg \omega$
Earth's gravity gradients	$< 10^{-12}$ g (2ω) $< 10^{-15}$ g (ω)	Centering of proof masses (δ_x) along spin axis within 1 μm	N/A	Verticality before release $\delta_x\phi < 0.1$ μm-deg
Cryostat's gravity gradients (distributed mass)	$< 10^{-12}$ g (2ω) $< 10^{-16}$ g (ω)	Centering of proof masses within 10 μm	Cryostat internal diameter ≥ 1 m	N/A
Gravity gradients of lump masses on board capsule	$< 10^{-12}$ g (2ω) $< 10^{-16}$ g (ω)	Centering of proof masses within 10 μm	N/A	Mass-distance exclusion zones (see pp. 53-54)
Magnetic disturbances	$< 10^{-16}$ g	Use Niobium alloy blanket around detector. Degauss proof masses	Temperature of package $T < Tc$ (T_c = critical temperature)	Limit magnetic moments outside sensor package $M_m <$ TBD A-m^2 and $r >$ TBD m
Higher-order mass moments	$< 10^{-16}$ g	Proof masses with almost equal moments of inertia ($\delta M/M \sim \delta L/L < 10^{-4}$)	Mass of cryostat < 500 kg, Intern. dia. ≥ 1 m	N/A
Centrifugal gradients due to skewed spin axis	$< 10^{-15}$ g	Centering of proof masses $\delta_x \leq 1$ μm	N/A	Verticality within 0.1°; rate errors at release ≤ 0.1 °/s

ω = signal angular frequency; ω_0 = detector resonant angular frequency

EXPERIMENTAL ACTIVITY (IFSI/CNR)[1]

Our partners have been working very hard in carrying out experimental activity on critical aspects of the detector development. The team at the Institute of Space Physics (IFSI/CNR) has already built a differential accelerometer prototype and carried out significant laboratory measurements on the prototype.

The prototype was designed with the goal of exploring key aspects of a differential accelerometer and not for carrying out a preliminary test of the Equivalence Principle in the laboratory. As such, the prototype has two sensing masses of the same material with their centers of masses close together but not perfectly coincident. The prototype has several features in common with the instrument that we expect to develop for the flight experiment as follow: same capacitive pick-up system; same elastic suspension of the sensing masses; same measurement chain to extract the differential signal from the accelerometer.

Figure 116 and Figure 117 show schematics of the differential accelerometer prototype. Each sensing mass (blue and orange elements in the figure) is shaped to compenetrate (with leeway) into the opposing one so as to bring the two CMs close together (perfect coincidence is not a requisite for this prototype).

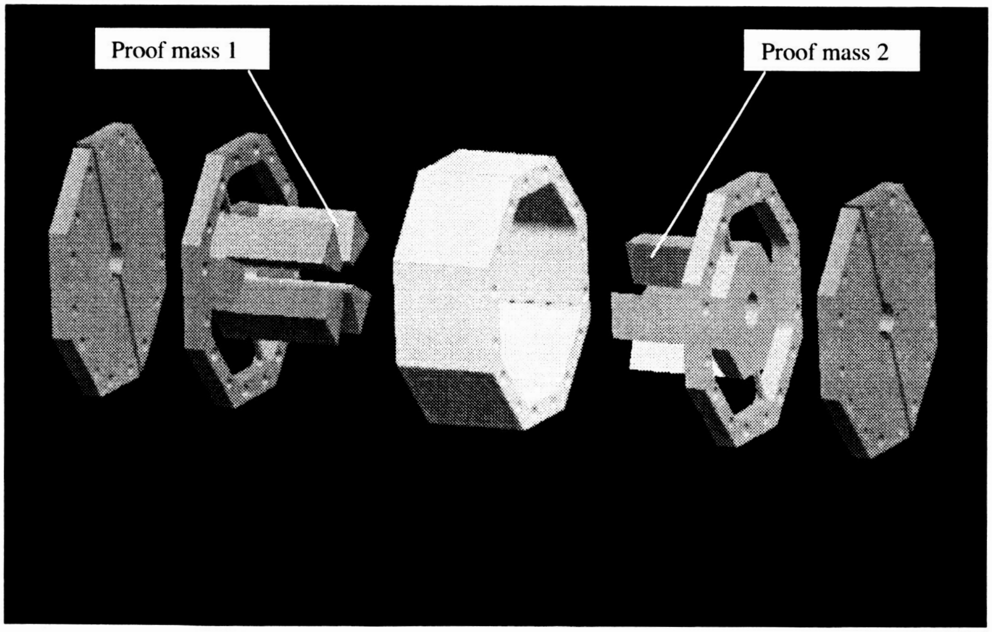

Figure 116 Exploded view of differential accelerometer prototype

---

[1] Section contributed by V. Iafolla S Nozzoli and M. Fiorenza of IFSI/CNR funded through Italian Space Agency (ASI).

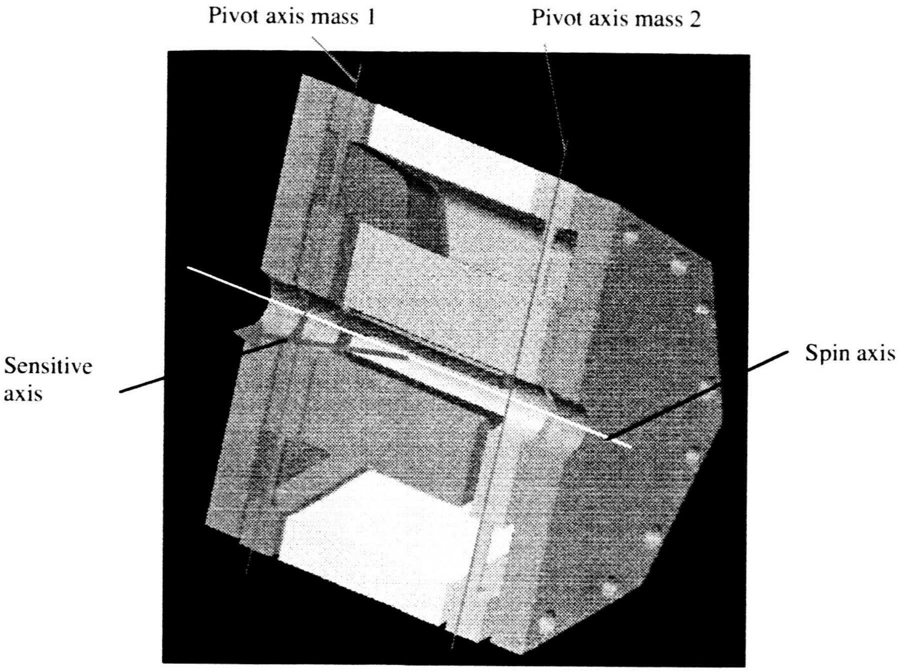

Figure 117 Cross section of (assembled) differential accelerometer prototype

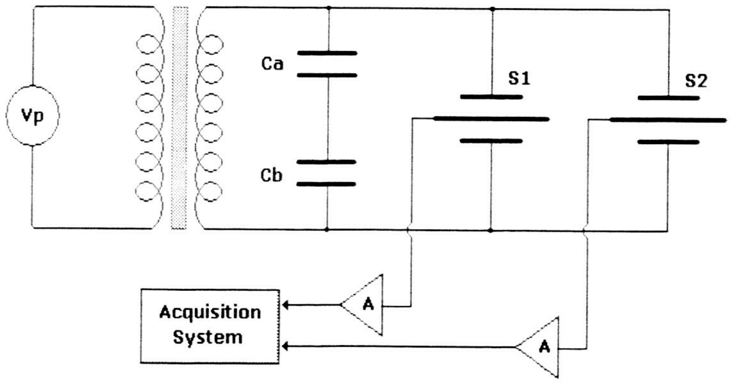

Figure 118 Simplified electrical diagram of signal pick-ups

Each sensing mass can rotate (through elastic restraints) about the pivot axis on each side of the accelerometer. The two pivot axes are parallel to one another. The sensitive axis of the differential accelerometer is perpendicular to the pivot axes and to the longitudinal axis of the instrument (spin axis). Each sensing mass has two fixed capacitor plates for signal pickup.

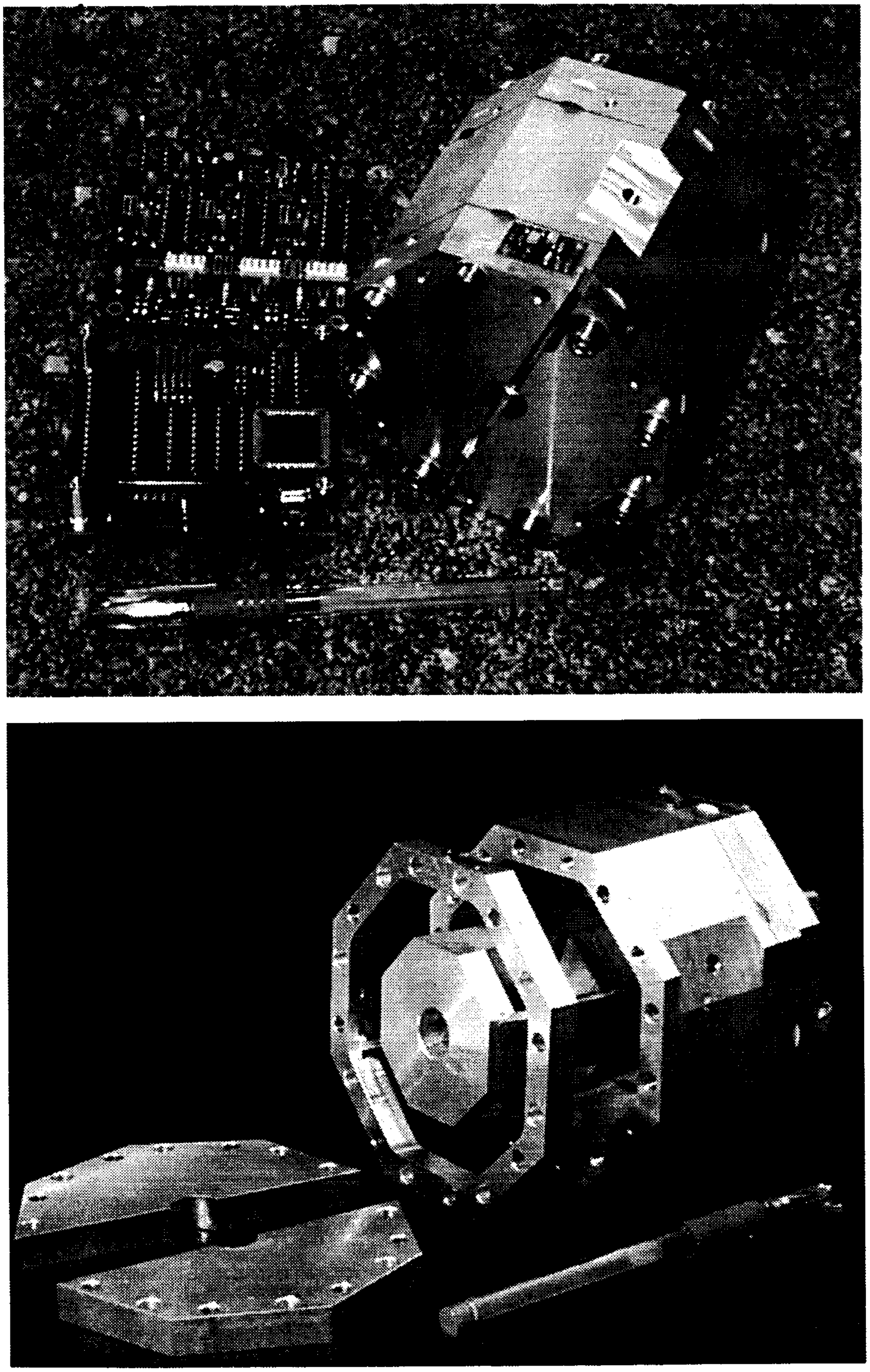

Figure 119 Pictures of differential accelerometer prototype

The output signals of the sensing masses are independently amplified and sent to the data acquisition system for conditioning, filtering and comparing. This prototype differential accelerometer builds on the heritage of (single) high-sensitivity accelerometers that were built at IFSI through the years. These accelerometers were tested extensively in the laboratory and in the field[xxxv]. Key characteristics of the differential accelerometer prototype are summarized in Table 7.

Table 7 Key characteristics of differential accelerometer prototype

Item	
Sensing mass	0.22 kg
Quality factor	2900
Resonance frequency	18.12 Hz
Preamplifier noise temp. (K)	0.76
Preamplifier type	AD743 (commercial)

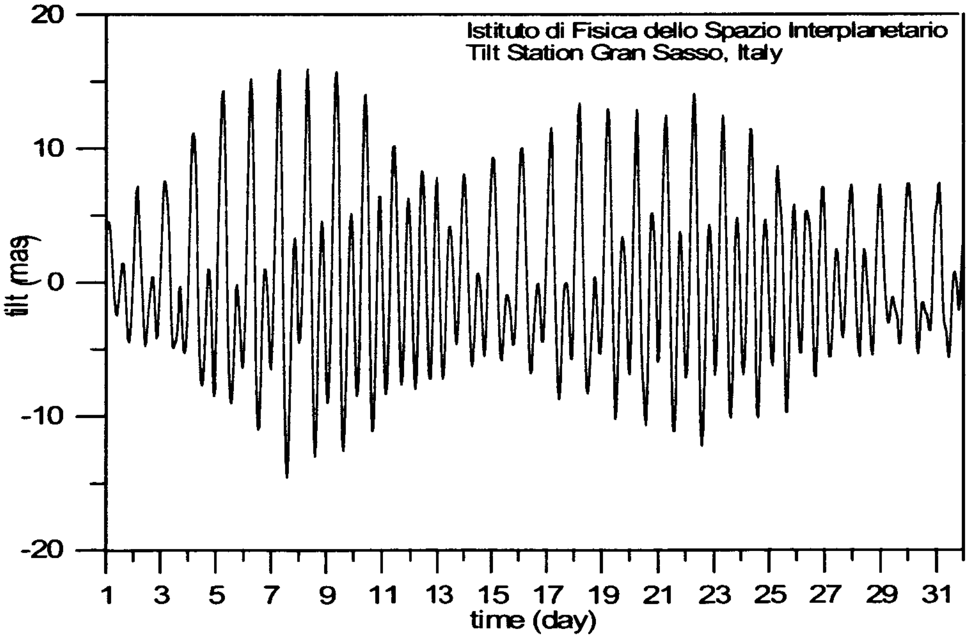

Figure 120 Luni-solar tide signal filtered with 49-hour filter (1 mas = 2.78×10^{-7} g) and measured with single accelerometer in August 1998.

The single accelerometer, in its various implementations, has demonstrated a remarkable sensitivity and repeatability. The accelerometer was able to resolve a modulated gravity signal (at 0.3 Hz) with a strength of less than 10^{-9} g in the presence of seismic noise. Another single accelerometer is used to measure the Luni-Solar tides (working as a tilt meter) in the Gran Sasso laboratory (Italy). Excellent tidal signal over periods of months have been measured by the IFSI team. A month-long sample of a Luni-Solar tide in August 1998 is shown in Figure 120 as an example of the performance of the single accelerometer in the field.

Damping of transient oscillations

The differential accelerometer prototype was developed and built to test, among others, key aspects of differential acceleration measurements as follows: (a) abatement of the natural dynamics excited by the instrument release into the capsule; and (b) rejection of the common-mode signals. Point (a) above is critical for the success of our experimental scheme. For an instrument that is required to resolve acceleration of 10^{-14} g, the release is an abrupt event that pushes the detector well beyond its saturation point. Moreover, in a (flight) instrument with a Quality factor (Q) of order 10^5 and a resonance frequency of a few Hz, the transient oscillations would take a very long time to decay to within the instrument's dynamic range. The strategy that we plan to follow in the experiment is to reduce the Q factor during the first few seconds of fall from 10^5 down to a few units. The reduction of the Q factor is accomplished by inserting a resistance in the feedback control loops of the accelerometer (see Fig. 121). The technique has been tested successfully on the prototype accelerometer.

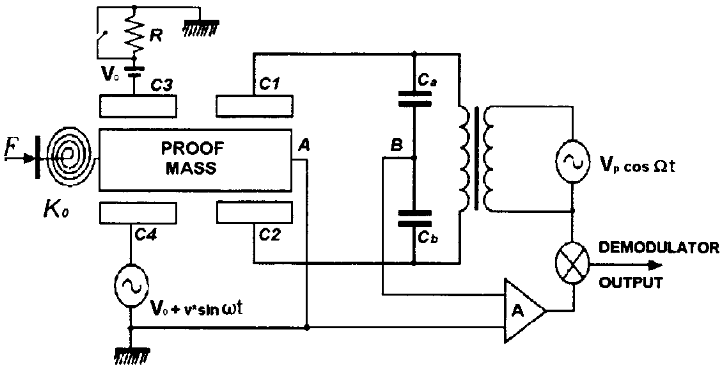

Figure 121 Electrical diagram of one test mass pickup system with resistance added to the feedback loop

Figure 122 shows the oscillation amplitude (from the oscilloscope output) of the accelerometer after an excitation. The accelerometer has a resonant frequency of 18.5 Hz and an (undamped) Q_t = 2900. The introduction of a 50 Mohm resistive load in the feedback loop, reduces the Q from its undamped value to Q_t' = 441 and, consequently, the oscillation amplitude decays much more rapidly. Subsequently, the resistance is removed to demonstrate that this operation does not re-excite the oscillation amplitude.

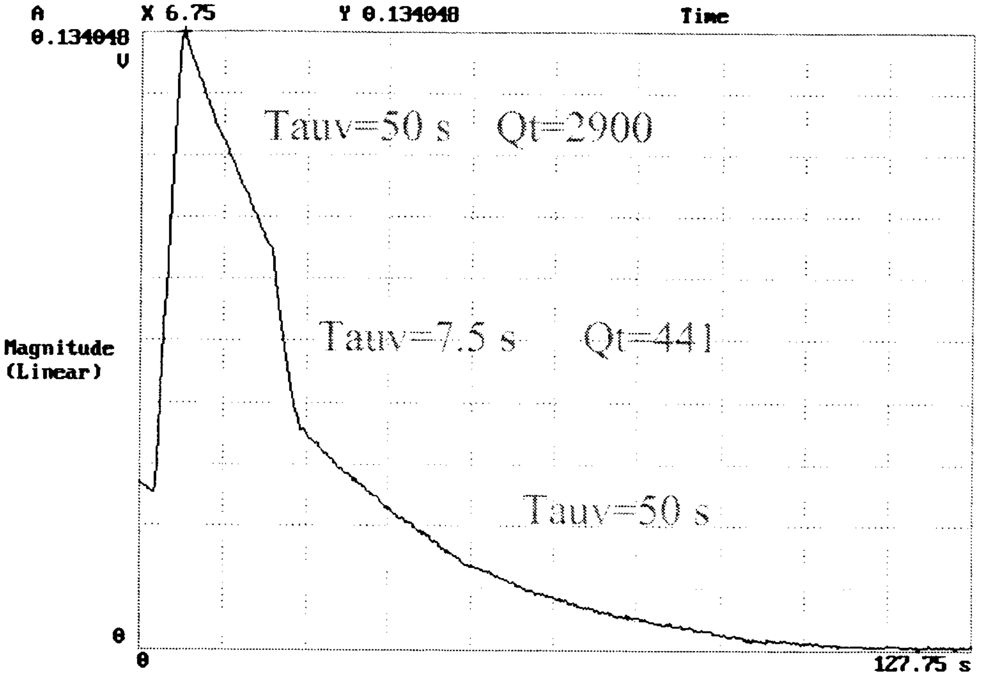

Figure 122 Oscillation amplitude decay vs. time with and without resistance inserted in the feedback loop

It is worth reminding that the decay of the proof mass oscillations is driven by the total quality factor of the electro-mechanical system which is as follows:

$$\frac{1}{Q_t} = \frac{1}{Q_m} + \frac{1}{Q_e} \quad with \quad \frac{1}{Q_e} = \lambda \frac{\omega_0 RC}{1 + (\omega_0 RC)^2} \tag{70}$$

where λ is the electro-mechanical coupling factor

$$\lambda = \frac{CE^2}{m\omega_0^2}$$

that is the ratio of electrical energy to mechanical energy of the oscillator. The electro-mechanical coupling factor of the instrument prototype is a low $\lambda = 0.01$. The flight instrument will have a value much closer to unity thanks to a lower value of ω_0 and higher value of the capacitance C. Consequently, an electrical resistance of the value adopted for this test coupled into the feed-back loop of the flight instrument will imply a reduction of the value of Q_t to a few units. In summary, this damping technique is able to provide the desired damping performance.

Common-mode rejection factor

One important characteristic of a differential accelerometer is its ability to reject perturbations that are not differential, i.e., common-mode disturbances. This ability is quantified by the common-mode rejection factor (CMRF).

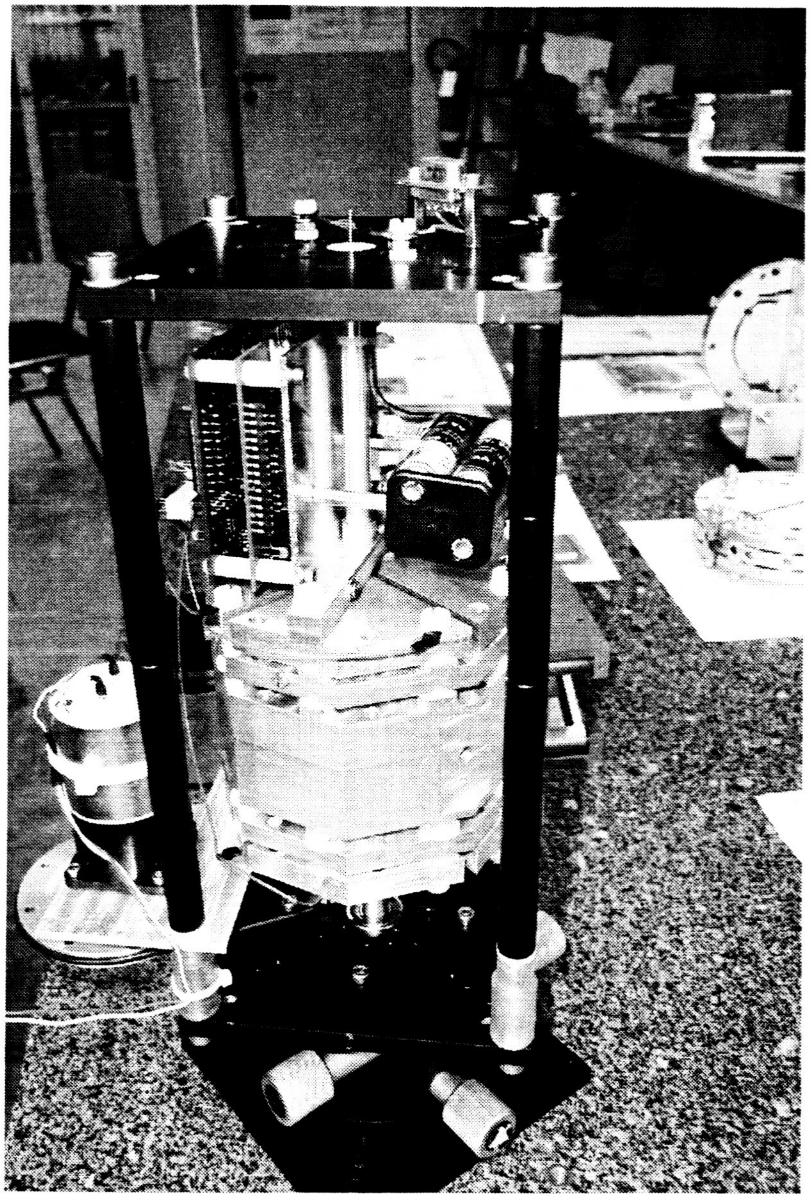

Figure 123 Experimental setup to perturb differential accelerometer with periodic common-mode disturbances.

The IFSI laboratory has built a rotating system whose rotation axis can be accurately tilted off the vertical (see Fig. 123). The accelerometer is mounted inside the rotating device with the sensitive axis orthogonal to the spin axis. The rotating outfit is tilted by about 10^{-3}rad away from the vertical and spun at a slow rotation with a frequency of 0.15 Hz. As the differential accelerometer slowly rotates, it measures a small component (proportional to the tilt) of the Earth's gravity field at the rotation frequency. This perturbation is a common-mode disturbance which affects equally the two proof masses.

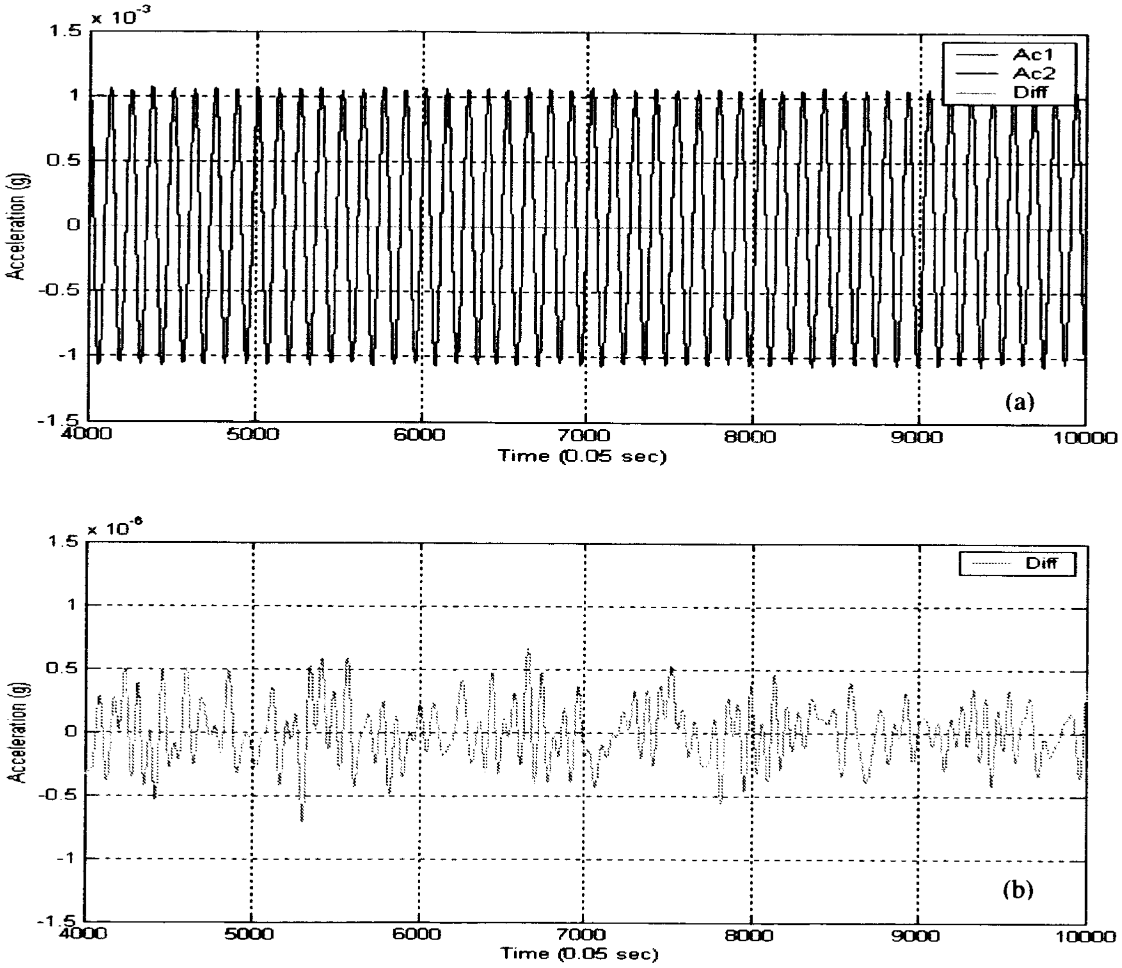

Figure 124 Accelerometer outputs: (a) single acceleration from proof mass 1 and 2 and (b) differential acceleration.

The differential output generated by the calibration signal is then treated by the software through spectral analysis of the individual signals to adjust the proportionality factors of the two sensing masses and the phase differences of their responses.

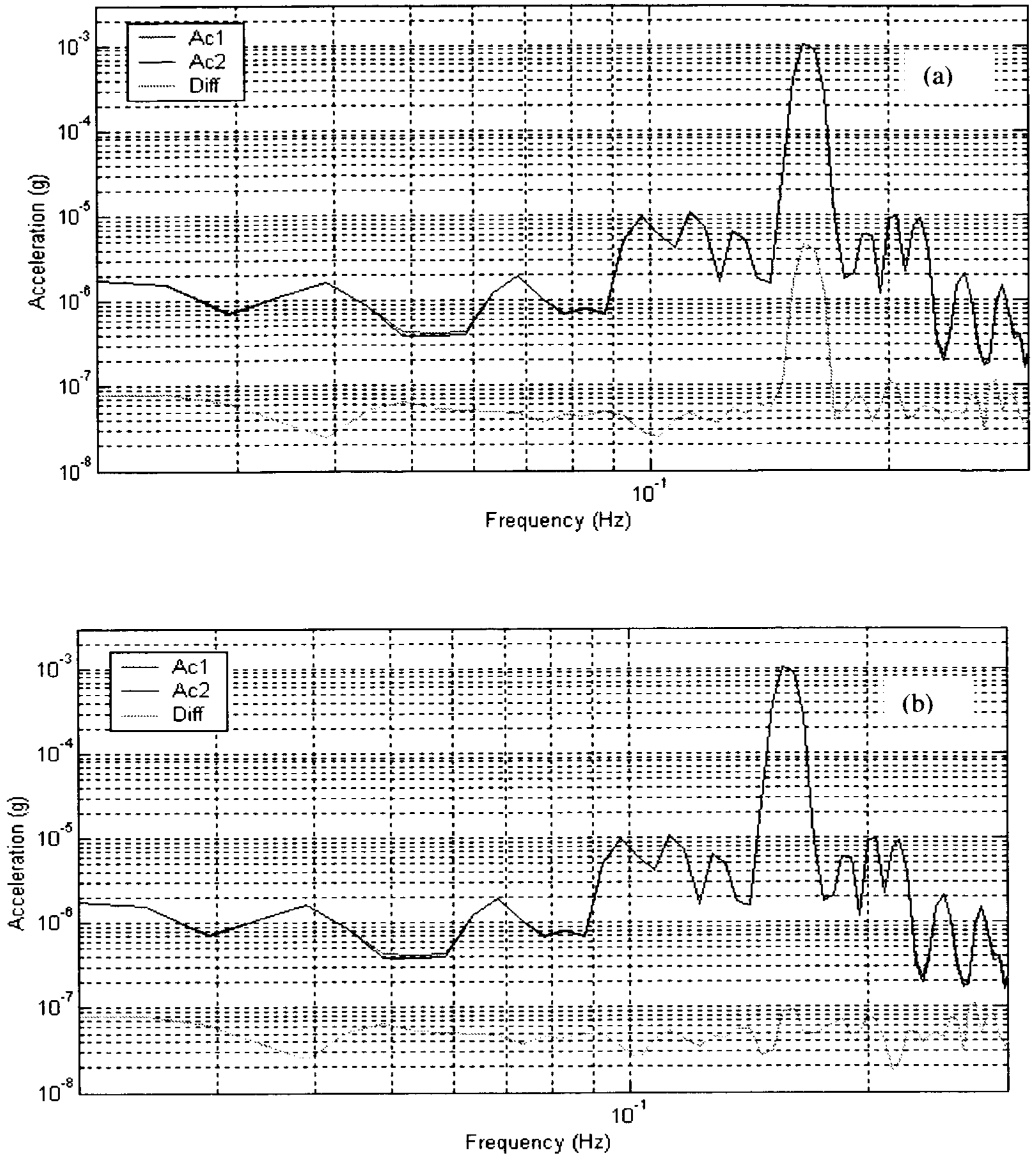

Figure 125 Spectra of individual and differential acceleration outputs: (a) after amplitude calibration only and (b) after amplitude and phase calibration.

Figure 125 shows that after calibrating for amplitude and phase a 10^4 attenuation is readily obtained for the differential signal. This level of attenuation is effective not only at the perturbation frequency of 0.15 Hz but also over a larger frequency band. An attenuation of 10^4 or equivalently a common-mode rejection factor of 10^{-4} meets the present requirement on the CMRF for the proposed tests of the Equivalence Principle.

Concluding Remarks

The laboratory activity consisted in the construction of a laboratory prototype of a differential accelerometer. The laboratory prototype has been used to conduct key tests on the differential instrument. The team at IFSI demonstrated the ability of the detector to damp quickly transient oscillations by utilizing a resistive load in the feedback loops and then removing that load to reestablish a high quality factor of the detector. A rotating device with tilt control was also built at IFSI. This device was utilized to impart (through the Earth's gravity) common-mode perturbations to the differential accelerometer. These calibration disturbances have been used to trim the acceleration outputs of the individual proof masses in order to obtain a common-mode rejection factor better than 10^{-4} in a sufficiently large frequency band centered at the spin frequency.

REFERENCES

---

[i] R.V. EÖTVÖS, Math. u. Naturw. Ber. aus Ungarn Vol. 8, 65 (1890).

[ii] R.V. EÖTVÖS, V. PEKAR AND E. FETEKE, "Beitrage zum Gesetze der Proportionalität von Trägheit und Gravität," *Annalen der Physik*, Vol. 68, 11-66 (1922).

[iii] P.G. ROLL, R. KROTKOV AND R.H. DICKE, *Annals of Physics*, Vol. 26, 442 (1964).

[iv] I.I. SHAPIRO, C.C. COUNSELMAN AND R.W. KING, *Phys. Rev. Lett.* Vol. 36, 555 (1976).

[v] J.G. WILLIAMS ET AL., *Phys. Rev. Lett.* Vol. 36(11), 551 (1976).

[vi] Williams, J.G., X.X. Newhall and J.O. Dickey (1996), Relativity parameters determined from lunar laser ranging, *Phys. Rev. D*, 53, 6730.

[vii] Baessler S., Heckel B., Adelberger, E. Gundlack J., Schmidt U. and Swanson E. (1 Nov. 1999), *Phys Rev Lett.*, Vol. 83.

[viii] Touboul P.,"µScope, Satellite á traineé Compenseé pour l'Observation du Principe d'Equivalence." ESA-CERN Workshop – Fundamental Physics in Space and Related Topics, 5-7 April 2000.

[ix] Nobili, A.M. et al., "*Galileo Galilei* Flight Experiment on the Equivalence Principle with Field Emission Electric Propulsion." *Journal of the Astronautical Sciences*, Vol. 43, No. 3, 219-242, 1995.

[x] STEP team, "STEP Satellite test of the equivalence principle report on the Phase A study." ESA SCI(96) 5, 1994.

[xi] Lorenzini, E.C., M.L. Cosmo, M.D. Grossi and T. Rothman, "A method for testing the principle of equivalence with improved accuracy." Smithsonian Astrophysical Observatory, Technical Note TP91-001, Cambridge, Massachusetts, 1991.

[xii] Dittus, H., et al., "Testing the weak equivalence principle at the Bremen drop tower: report on recent developments." *Classical And Quantum Gravity*, Vol. 13, No. 11, A43-A51, 1996.

[xiii] Gullahorn, G.E., F. Fuligni and M.D. Grossi, "Gravity gradiometry from the tethered satellite system." *IEEE Trans. On Geoscience and Remote Sensing*, Vol. GE-23, 531-540, 1985.

[xiv] Lockerbie, N.A., X. Xu, A. Veryaskin, "Spherical harmonic representation of the gravitational coupling between a truncated sector of a hollow cylinder and an arbitrary gravitational source: Relevance to the STEP experiment." *Classical and Quantum Gravity*, Vol. 27, No. 11, 1215-1229, 1995.

[xv] Lazarevich, A. et al., "Balloon-borne, high altitude gravimetry: the flight of Ducky Ia." Report AFGL-TR-0342, Air Force Geophysics Laboratory, Hanscom AFB, MA, 1985.

[xvi] Lorenzini, E.C., I.I. Shapiro, F. Fuligni, V. Iafolla, M.L. Cosmo, M.D. Grossi, P.N. Cheimets and J.B. Zielinski, "Test of the Weak-Equivalence Principle in an Einstein Elevator." Il Nuovo Cimento, Vol. 109B, No. 11, 1994.

[xvii] Kretzschmar, Mikroba unpublished acceleration data, 1999.

[xviii] Staff of John Hopkins University APL and Staff of Stanford University, "A Satellite Freed of all but Gravitational Forces: "TRIAD I". J. Spacecraft, Vol. 11, No.9, (1974).

[xix] Braginsky, V.B. and A.B. Manukin, "Measurement of Weak Forces in Physics Experiments." The University of Chicago Press, p. 7, 1974,.

[xx] Giffard, R.P., *Phys. Rev. D* 14, 2478, 1976.

[xxi] Iafolla, V., A. Mandiello and S. Nozzoli, "The High Sensitivity Italian Spring Accelerometer (ISA) for Fundamental Physics in Space" Advances in Space Research, Vol. 25, No. 6, 1241-1244, 2000.

[xxii] Haugan, Mark P. and Clifford M. Will. "Weak Interactions and Eötvös Experiments," Phys. Rev. Lett. 37, 1 (1976).

[xxiii] Adelberger, E.G. and W.C. Haxton. "Parity Violation in the Nucleon-Nucleon Interaction," Ann. Rev. Nucl. Part. Sci. 35 (1985).

[xxiv] Desplanques, B., J. F. Donoghue, B.R. Holstein. Ann. Phys. 124, 449 (1980).

[xxv] Bethe, H.A. and P. Morrison. Elementary Nuclear Theory, New York: Wiley (1956).

[xxvi] Haugan, Mark P., Ephraim Fischbach, and Dubravko Tadic. "The Equivalence Principle and Weak Interactions," 1993 STEP symposium.

[xxvii] Chamoun, N. and H. Vucetich, "Weak Interactions Effect on the P-N Mass Splitting and the Principle of Equivalence," hep-ph/9909384.

[xxviii] Damour, T. and A.M. Polyakov, "The String Dilaton and a Least Coupling Principle," Nuclear Phys. B423 (1994).

[xxix] Damour, T., F. Piazza, and G. Veneziano, "Violations of the Equivalence Principle in a dilaton-runaway scenario." Phys. Rev. D66, 046007:1-15, 2002.

[xxx] Damour, T., F. Piazza, and G. Veneziano, "Runaway dilaton and Equivalence Principle violations." Phys. Rev. Letters, Vol. 89, No. 8, 081601:1-4, 2002.

[xxxi] Lazarevich, A. et al., "Balloon-borne, high altitude gravimetry: the flight of Ducky Ia." Report AFGL-TR-0342, Air Force Geophysics Laboratory, Hanscom AFB, MA, 1985.

[xxxii] I.I. Shapiro et al. "Test of the Equivalence Principle in an Einstein Elevator." Annual Report #2 on NASA grant NAG8-1780, June 2003.

[xxxiii] P.W. Worden Jr, C.W.F. Everitt and M. Bye, "Satellite Test of the Equivalence Principle." Stanford University Report (Palo Alto, California, 1990).

[xxxiv] F.J. Lavoie (Editor), "Materials Engineering: *Materials Selector 1987.*" Penton Publication, p. 72 (1986).

[xxxv] Iafolla et al., "Measurements at Gran Sasso laboratory", see web site http://iafosun.ifsi.rm.cnr.it/~iafolla/gravsper.html.